On-Demand Electricity from Future Fission Energy Systems

Thesis

On-Demand Electricity from Future Fission Energy Systems

Thesis submitted for the degree of Doctor of Philosophy (PhD)

in Engineering and Innovation

Andy Robert Wilson

Original submission of thesis: 28th May 2020

Resubmission following post-examination corrections: 7th December 2020

Acknowledgements

I would like to give my heartfelt thanks to my supervision team of William J. Nuttall, Bartek A. Glowacki, John Bouchard and Satheesh Krishnamurthy for their support throughout the course of my studies. A special thanks to Bill and John who advocated for my interests in November 2019.

To Bill, who pushed me to do things of which I had not previously considered myself capable, I owe an extraordinary debt of gratitude. Thank you for all those times I needed support, discussion, or steering. I could not have made it to this point without you.

My wife Hannah deserves a special thanks. Without her support, I could not have finished this thesis. Thank you for being a light in the darkness. For being everything. Your name might not be on the front of this document, but it is as much yours as it is mine.

Thank you to my mother and father, without whom nothing would be possible. Thanks to my brother Dave who has always been my hero.

I would like to thank Charles W. Forsberg and Nikolaos K. Kazantzis who both inspired the ideas in this thesis.

Thank you to my examination team whose insights and advisory comments have helped to improve the content of this thesis.

For my friend Minnie. Always missed, never forgotten. To my friend Timmy. Always my support.

This work was supported by the Engineering and Physical Sciences Research Council (EPSRC) and the Imperial College, Open University and Cambridge University Centre for Doctoral Training (ICO CDT) in Nuclear Energy under award 1653547.

Table of contents

Table of Abbreviations

Abbreviation	Meaning
1DFV	One-dimensional finite volume
ABWR	Advanced boiling water reactor
AGR	Advanced gas-cooled reactor
AIC	Akaike information criterion
AR	Auto-regressive
ARCH	Autoregressive conditional heteroskedasticity
ARMA	Auto-regressive moving average
BMMR	Brownian motion mean reversion
BWR	Boiling water reactor
CAES	Compressed air energy storage
CCGT	Combined cycle gas turbine
CfD	Contract for difference
CPI	Consumer prices index
Cu-Cl	Copper-chlorine
DCF	Discounted cash flow
EES	Engineering equation solver
EPR	European pressurised (water) reactor
ESDU	(formerly) Engineering Sciences Data Unit
ESS	Energy storage system
FIRES	Firebrick resistance-heated energy storage
FOAK	First of a kind
FV	Finite volume
GARCH	Generalised autoregressive conditional heteroskedasticity
HX	Heat exchanger
IFR	Integral fast reactor
J-T	Joule-Thomson
LAES	Liquid air energy storage
LAES	Liquid air energy storage
LCOE	Levelized cost of electricity
LCOS	Levelized cost of storage
LNG	Liquefied natural gas
LTE	Low-temperature electrolysis
LWR	Light water reactor
MA	Moving average
MIT	Massachusetts Institute of Technology
MSR	Methane steam reformation
NOAK	n^{th} of a kind
NPP	Nuclear power plant
NPV	Net present value
O&M	Operation and maintenance
ORC	Organic Rankine cycle
PERT	Performance evaluation and review technique
PHES	Pumped hydroelectric energy storage
PWR	Pressurised water reactor
RNG	Random number generator
S-I	Sulphur-iodine
SMR	Small modular reactor
S-PRISM	Super power reactor innovative small module
STOR	Short-term operating reserve
HTE	High-temperature electrolysis
UTES	Underground thermal energy storage
VBA	Visual basic for applications
VHTR	Very high temperature reactor

Abstract

This thesis details a novel methodological approach to assessing the relative economic viability of a combined power generation and energy storage plant. The approach optimises the given system from both a process engineering and a financial perspective and this is the key novel contribution that this work provides to the field.

The thesis utilises two key pieces of software. The first is Modelica code used within the Dymola simulation environment for engineering process modelling of the energy storage plant. The second is the Palisade @RISK plugin used within Excel for economic evaluation of the plant performance in a simulated UK electricity spot market, using a Monte Carlo approach for evaluating plant designs in the face of uncertainty.

The first two technical sections of the thesis following the literature review comprise a detailed description of the engineering model and the financial model, respectively. The former describes the equations that are used in each component of the engineering process model. The latter describes not only the equations that make up the financial model, but also the approach taken to estimating energy storage plant capital costs.

This thesis builds on previous work on liquid air energy storage, particularly the substantial body of engineering studies and the smaller but increasing body of economic studies. The market-led approach to engineering design remains, at the time of writing, the only example of a detailed study of how plant design parameters impact the economic viability of the plant in question.

Results are presented in two sections. The first discusses the initial engineering-focused modelling in which the bulk of the plant engineering design work was performed. This begins with a deep dive into the effect of design parameters on plant performance and goes on to compare different plant configurations with a focus on the number of compression and expansion stages. The second result section discusses the initial results of the financial modelling using the plant performance results from both the engineering and financial models.

The closing sections discuss the successes and limitations of the project and speculate on other fields in which this novel approach might prove enlightening. Whilst a nuclear power plant coupled with energy storage was the chosen example for demonstration of this work, the methodology could be equally well applied to other energy storage plants and is particularly well-suited to asymmetrical energy storage systems.

Chapter 1 - Introduction

1.1. Overview

This thesis details a novel methodological approach to assessing the relative economic viability of different configurations of a combined power generation and energy storage plant. The approach optimises the given system from both a process engineering and a financial perspective and this is the key novel contribution that this work provides to the field.

In this study, the methodology is applied to a hypothetical combined NPP (nuclear power plant) and LAES (liquid air energy storage) plant. The study is performed in two stages using the engineering model discussed in Chapter 3 and the financial model discussed in 0. The different options for plant configuration are assessed via the engineering model in Chapter 5 and the early part of Chapter 6 is devoted to assessing the relative risk of different plant configurations and deciding upon an optimal configuration given this information. The second stage involves investigating the effect of spot market conditions on the relative risk of the chosen configuration and is detailed in the latter part of Chapter 6.

The intention of this particular thesis is to demonstrate the methodological approach by determining whether the inclusion of LAES in the plant detailed herein can be used to provide a load-following output from an NPP to the UK electricity grid. The plant is considered to sell power to two markets; the non-variable output is sold on the basis of a strike price under a CfD (contract for difference) agreement and the variable output is sold on the spot market. The study quantifies how high a strike price and how volatile the spot market must become to make a given proposition financially viable. With this information, it then assesses the relative financial risk of different system sizes to optimise the system from a financial perspective for the different market scenarios.

1.2. Study specifics

The engineering model is a plant process model written in the Modelica language and simulated within the Dassault Systèmes Dymola simulation environment. The model is built in a modular sense from a range of components. Broadly, these comprise two types of component; thermodynamic models of turbomachinery and finite volume flow models that are used in heat exchangers and thermal store components. The detailed approach to heat exchangers allows them to be sized and costed while the modular approach to modelling facilitates the rapid modelling of multiple competing configurations. Both of these features are essential to the

overall approach of this study, which is reliant on the simulation and sizing of a variety of plant design configurations.

The financial model was developed in Excel using the Palisade @RISK plugin. @RISK is a Monte Carlo simulation plugin that allows modelling to be performed in the face of uncertain input parameters. There are two sets of input parameters; initial parameters such as plant capital cost and construction time are defined using probability distributions and provide a single starting value for each iteration of the simulation. Time series are used to model electricity prices and cost indices as these values vary over time. The model is run for several thousand iterations and provides a probability distribution of the NPV (net present value) and the payback period of a given proposition. Using these distributions, the relative investment risk of different plant sizes and configurations may be assessed.

1.3. Methodological applicability

As discussed above, the key contribution of this work to the field is the methodology used, which combines engineering and financial modelling in a much more detailed way than previous work in the field. The application of this methodology is detailed in the specific example of a combined NPP and LAES plant system (hereafter referred to as a hybrid plant), however the methodology and the models themselves can be extended to other systems. This applicability and a number of ways in which the work could be extended are discussed in more detail in Chapter 7.

Work on such a hybrid plant represents a significant gap in the available literature, with only a single paper performing a detailed engineering assessment of such a system, as far as this author is aware. Financial modelling work on energy storage systems has become an emergent topic in the years the work in this thesis has been developed and the development of an important metric for this, in LCOS (levelized cost of storage), is at the forefront of this work. In contrast to LCOS, which defines the average electricity sale price required for a given energy storage proposition to become profitable, this thesis presents an alternative methodology by which the required market conditions for plant profitability might be explored. In addition, it provides a means by which the performance of alternative system designs might be compared within the context of a hypothetical electricity market.

The crux of this thesis is the question of whether engineering and financial modelling can be combined in such a way that an engineering system for energy storage can be optimised from a market-led perspective. This thesis will discuss the development of a novel methodological

approach that attempts to achieve precisely that, and of the modelling framework that supports it. This is demonstrated and applied within the context of a coupled LAES and NPP design but has potentially far broader reaching applications within the context of energy storage systems as a whole.

1.4. Objectives and methodology

This thesis is intended to explore the economic viability of a combined LAES and NPP design through completion of the following objectives:

- Develop an engineering model and library of components in the Modelica language for plant process modelling of the combined NPP and LAES system.
- Use the engineering model to determine operating parameters for a range of proposed plant configurations.
- Size components for the given plant configurations and use these to evaluate asset costs for the LAES plant.
- Develop a financial model for determining relative economic performance of the plant designs in the face of uncertain market conditions using Excel and the Palisade @RISK plugin.
- Use the financial model to determine the relative economic performance and investment risk of the plant design outputs from the engineering model.

In achieving these objectives, this work would provide a novel scientific contribution to the field of economic assessment of energy storage systems in the form of a methodology for assessing the economic performance of engineering storage systems within uncertain market conditions. At the time that this study was conceived, no such methodology had been applied to the described system, or indeed to any energy storage system, in this level of detail. During the development of the methodology supporting this thesis, the LCOS approach emerged for the analysis of ESSs (energy storage systems). As discussed in section 1.3, in Chapter 7 and in 0, this thesis provides an alternative to the LCOS approach, providing additional insights into plant performance.

Chapter 2 - Literature Review

2.1. Introduction

In recent decades, investment costs of nuclear power plants have risen, however pricing incentives for baseload clean energy have been elusive, largely due to the favouring of renewables for direct subsidy (Newbery, 2016). This has left nuclear power in a difficult situation in the UK; with investment costs on the rise and public and political support wavering, there is a very real possibility of not only nuclear losing its relevance to the future of UK electricity generation, but a loss of the associated skills. This project aims to explore whether nuclear can vary its power output to act as a backup for intermittent renewable sources by incorporating some form of energy storage. This chapter attempts to discuss the role of nuclear in a future energy grid.

Section 2.2 aims to contextualise the role of nuclear within a power grid with increasing penetration of renewable generators and section 2.3 discusses the difficulties associated with using nuclear energy in a load-following role. Section 2.4 examines a few of the available technologies for energy storage and discusses any potential synergies they might have with nuclear power. Section 2.5 discusses LAES (liquid air energy storage) in detail and examines the expanding base of literature available on the subject in detail. Sections 2.6 and 2.7 discuss the various options and software packages available for the two forms of modelling that have been performed in this project and discusses the reasoning for the approach taken to modelling seen in later chapters.

2.2. Nuclear power and renewables

A fundamental assumption in this work is that the world, and more specifically the UK, will work towards large-scale decarbonisation of not only electricity generation, but all forms of energy use. This would mean, broadly, either large-scale transition to sources of low carbon intensity, such as renewables and nuclear, significant development and application of carbon capture and storage technologies and continued use of fossil fuels, or a combination of the two. This section studies the literature available on the role of nuclear in the future of energy supply. It aims to study the question of whether or not nuclear energy has a place in a power grid with significant quantities of renewable generators.

A key feature of modern electricity grids is that demand for electricity varies significantly throughout the day. Figure 2-1 (data from (Smith and Halliday, 2016)) shows the daily electricity profile for a Wednesday in January, April, July, and October for 2014. As might be expected, electricity use is at its lowest overnight, between the hours of 23:00 and 06:00, when most of the population is asleep. There is a rise in the morning which typically plateaus around 09:00 by which time most people are at work. There is a peak in consumption in evenings during the winter months. This is presumably a result of the fact that people are beginning to arrive at home, but industry, offices and schools are still occupied and consuming power. With the exception of unplanned plant outages, it seems that it is demand that drives the electricity price.

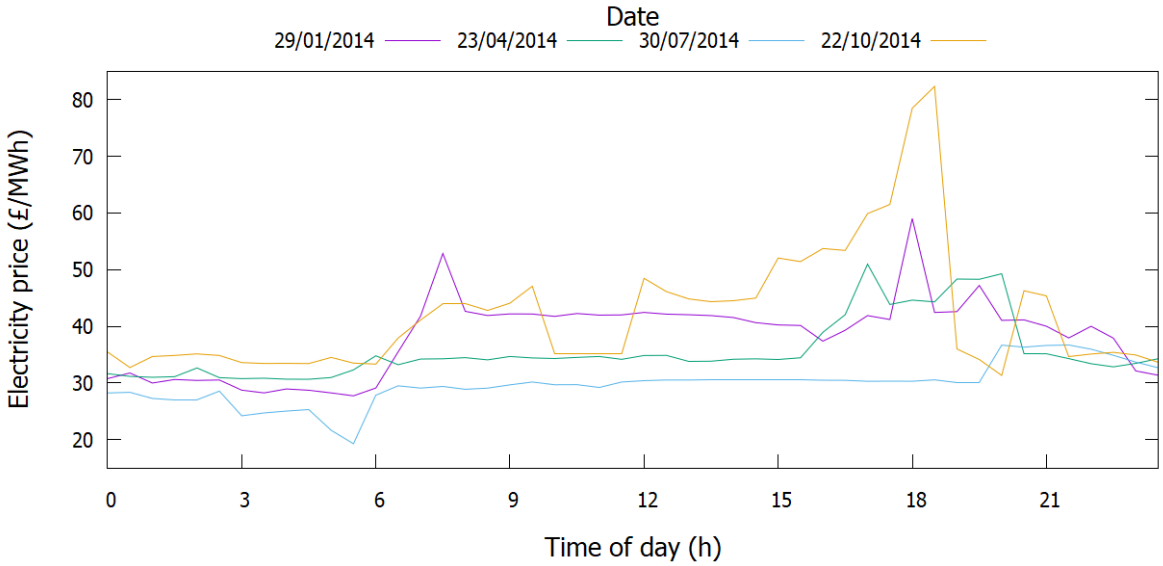

Figure 2-1: Day electricity price profiles in 2014

The discussions in the previous paragraph are highly generalised, superficial, and only consider a tiny portion of the dataset (Smith and Halliday, 2016). In actuality, the dataset exhibits complex daily, weekly, and seasonal variation and is highly unpredictable. A significant part of this project was dedicated to the detailed analysis of this dataset and its use in constructing a model to predict electricity prices. This process is discussed in far greater detail in section 4.4.

As renewables become more integrated into electricity grids, the need for provision of energy storage, demand-side management, or dispatchable (load-following) plants will come to the fore, and indeed has already begun to do so. Nascent energy storage has a number of drawbacks; in the case of batteries it remains expensive for grid-scale capacity (Strbac et al., 2012); in the case of flywheels capacity is limited and the storage is itself more suitable for frequency stability (Strbac et al., 2012); and in the case of PHES (pumped hydroelectric energy storage), it requires specific terrain. Large scale deployment of electric vehicles may provide significant additional storage within the grid however study of this suggests that significant subsidy will

likely be required (Richardson, 2013) and that such schemes are likely better suited to frequency regulation than actual load following (White and Zhang, 2011). In addition, some form of centralised control will likely be required to ensure that the vehicles are charged at the right time (Khayyam et al., 2012).

Demand-side management has the potential to make a significant contribution to power grid balancing and some policies have been proposed for the UK (Warren, 2014). Ultimately, however, the use of electricity is liable to increase dramatically in the near future as a result of the electrification of systems that are typically powered by fossil fuels. Transportation and heating (both domestic and industrial) are the two most significant examples of primary energy consumers that are likely to see conversion to electrification (Waters, 2019). As a result, the disparity between the peaks and the average shown in Figure 2-1 is likely to increase. Demand-side management is unlikely to be sufficient to fully manage this without either changing public behaviour, externally controlling the population's power consumption or, most likely, offering some kind of financial incentive, as (Warren, 2014) notes.

Dispatchable power generation is a key contributor to grid balancing, and currently by far the most important (Alexander et al., 2015). The term 'dispatchable power plant' has a somewhat nebulous definition and in this text will be used to describe a power plant that can be ramped from zero to full power in a matter of minutes. The only plants that can currently do this without ancillary energy storage are PHES and natural gas power plants. It should be noted that this is a definition similar to the National Grid's requirement for provision of fast reserve (National Grid, 2020a), which specifies a ramping rate of 25 MW per minute for a given participating plant and whose most recent report (National Grid, 2019a) exclusively contains PHES, hydroelectric and natural gas plants. Such plants are primarily used for load following and peak matching, that is ensuring that the supply of electricity into the grid matches the demand on an instantaneous basis. A second type of balancing service in the UK is STOR (short-term operating reserve), whose plants, in contrast to fast reserve, are required to supply small changes in output for periods of a few hours (National Grid, 2020b). There are myriad providers to the UK STOR service ranging from small diesel generation units to distributed provisions supplied by multiple plants (National Grid, 2019b)

The economics of dispatchable power generation is important to discuss briefly at this stage. Natural gas power plants require a relatively small capital investment but have high fuel costs (Ponciroli et al., 2017). Due to these characteristics, it is preferable to an operator that these plants are run only at times when the electricity price is high in order to maximise profit. This

contrasts with nuclear plants which, as discussed in section 2.3, require high capital investments and have small fuel costs necessitating that they operate in a baseload capacity.

The economics of running a power grid with increasing renewable capacity has been explored in countless studies. The role of nuclear in such a grid is a subject of no small debate. Some studies argue that correctly designed and managed renewable grids require no nuclear power and no backup from fossil fuels, arguably the most extreme approach to decarbonisation. Perhaps the most vocal proponent of this idea is Mark Z Jacobson, whose two-part 2010 paper makes an argument for such a grid (Jacobson and Delucchi, 2011, Delucchi and Jacobson, 2011). These papers have some significant shortcomings, not least their qualitative treatment of both renewable intermittency and seasonal storage, their ignorance of the investment required for energy storage, and their limited discussion of the socio-economic impacts of the chosen approach to grid management.

A paper published a few years later by the same lead author (Jacobson et al., 2015) provided a more quantitative analysis. This comprises a combination of weather modelling to determine energy supply and stochastic modelling to determine demand during 30s intervals over a six-year period. The key conclusions state a total energy requirement of over 92,000 TWh over a six-year period. Of this, 7% is lost to transmission, distribution and maintenance and a mere 4% is lost in storage media. A shift away from thermal fuels and energy generation is indeed likely to reduce the amount of energy rejected from transport, electricity generation and heating, however a reduction from around 70% energy rejection today (Lawrence Livermore National Laboratory, 2019) to a mere 11% is incredibly ambitious.

The paper's appendices detail the modelling assumptions as regards storage round-trip efficiencies and go some way to explaining how this conclusion was reached. Thermal storage round-trip efficiencies are all in excess of 70%, with some approaching 100% - these assumptions are very high, as will be discussed in more detail in section 2.4. The conversion of concentrated solar heat to electricity is also very high, exceeding 70% - well in excess of current highly efficient combined cycle gas turbine capabilities. As a result of the deficiencies in the paper, a rebuttal paper was published a few years later (Clack et al., 2017), refuting many of the conclusions drawn. Despite this, Jacobson remains confident and continues to publish papers on a transition to a 100% wind, water and solar grid.

Despite their shortcomings, these papers do make some important points relevant to this study, and to the topic of power grid decarbonisation as a whole. All of these Jacobson-authored papers (Jacobson et al., 2015, Jacobson and Delucchi, 2011, Delucchi and Jacobson, 2011) emphasise

the importance of hydrogen in energy production. Whilst clean hydrogen production remains difficult, hydrogen is likely to be an important fuel in the future, as discussed in section 2.4. Published work (Jacobson et al., 2015) highlights lithium ion battery degradation over repeated charge/discharge cycles and the resulting difficulties associated with using them as grid-scale storage or using electric vehicles as a storage medium, in contrast to the suggestions in the early work (Jacobson and Delucchi, 2011). The related paper (Delucchi and Jacobson, 2011) mentions the potential grid reliability issues associated with unplanned outages in large, centralised plants, and the fact that their size means such outages will have a greater impact on the grid. Whilst this is not a particularly novel point, it remains an important point for consideration in future grid planning. These papers also provide a cautionary tale; this study is a large-scale model of global energy generation and demand. The fallacy of a one-size-fits-all solution aside, such a far-reaching study will inevitably require a vast number of assumptions and these must always be treated with vigilance.

Less common is the view that nuclear could dominate a future decarbonised energy mix. Published work (Barry et al., 2018) promotes such a view, arguing that next-generation nuclear technologies combined with fuel synthesis technologies, with a little niche support from renewables, could support a decarbonised future. These are two major flaws with this paper that stem from the same fundamental issue; their reliance on technologies without proven commercial applicability. A central focus of the paper is the IFR (Integral Fast Reactor) system and its associated waste reprocessing techniques, along with some mention of MSR (Molten Salt Reactor) technologies. The IFR was a sodium-cooled fast reactor technology developed in the United States in the 80s and the genesis of the S-PRISM (Super power reactor innovative small module) which GE Hitachi have attempted to commercialise (GE Power & Water, 2015). Despite interest from both the US and UK governments, the reactor design remains without a prototype. The vision in (Barry et al., 2018) also relies on the use of synthetic fuels, another technology without any commercial demonstration to date.

Ultimately, the assertion that a baseload generator should dominate the energy mix presents issues with grid balancing and requirements for substantial provision of electricity storage that mirror those of renewables. It is worth noting however, that energy storage profitability is broadly reliant on having multiple charge-discharge cycles, something which a mix with a lot of baseload generation might be better suited to than a mix with a lot of intermittent generation by providing more opportunities to charge the system. This point is expanded on further in section 2.4.6. As is the case with the authors of the paper disputing the Jacobson work (Clack et al., 2017), the prevailing view in the field of grid management and planning is that a grid

with a diverse portfolio of generators provides the most inexpensive and secure route to decarbonisation.

An old paper (Roques et al., 2008) studies the ways liberalised electricity markets dictate the constituent parts of the energy mix. Unfortunately, this study is somewhat dated and completely omits renewables. Despite this, it still makes some interesting points. Its primary argument is that the UK's liberalised market exhibits a strong correlation between electricity, gas and carbon prices. This in turn incentivises construction of CCGT (combined cycle gas turbine) plants because the margin between revenues (in the form of electricity sales) and costs (in the form of gas and carbon credits) is largely fixed due to the correlation between their prices. The high capital costs and lack of fixed revenue increases the perceived risk of nuclear and coal plants, resulting in a lack of diversity in generators. It highlights access to low-cost capital and long-term energy purchase contracts as means to incentivise investment in a more diverse mix of generators. The rise of CfD pricing in the UK for nuclear goes some way to address this latter point, however capital investment remains, for the most part, private and hence higher-cost than public funding.

An interesting report from MIT (Massachusetts Institute of Technology) (Buongiorno et al., 2018) studies the cost of decarbonisation to different target emissions levels for a number of scenarios; one for a world without nuclear power, and four for nuclear power at various cost levels relative to the projected 2050 cost from the US Department of Energy (high, nominal, low and extremely low). This is achieved via modelling in MIT's GenX model. With inputs of generator costs and characteristics, this model optimises the generator mix by minimising the system cost for a given scenario, whilst still matching supply with demand on an hourly basis and meeting the emissions criteria set.

In the six geographical cases considered, the model shows that generation cost, even in the no nuclear scenario, increases only modestly as decarbonisation approaches 90%; the most dramatic increases are seen beyond this point. In all but the high cost scenario for nuclear, the inclusion of nuclear in the energy mix represents a substantial system cost saving. Indeed, for the low and extremely low cases, full decarbonisation can be achieved with only modest system cost increases.

There is however one important caveat to these results. In all cases where nuclear contributes to significant system cost savings, nuclear contributes the lion's share of the system's generation capacity. The model itself does not appear to take into account market effects, in particular the increase in cost of nuclear fuel as a result of the significant expansion of nuclear

generation. Whilst this is not necessarily an issue for the nominal cost scenarios, as fuel does not contribute a large amount to nuclear power's overall cost, as the cost of nuclear falls fuel costs will become a larger fraction of the whole and changes in the market will have an increasing effect on overall system cost. This is not to discount the results of the study as a whole, which appears to be a well thought out and thorough study of energy markets, but rather to say that the results for the most optimistic scenarios for nuclear cost should be treated with caution.

Broadly, the report emphasises that large-scale decarbonisation of electricity generation cannot be achieved without either significant cost increases (by factors of 3-6 depending on location), or increased construction of NPPs. Despite this conclusion, the report does concede that a key problem with the construction of NPPs is cost. The authors propose six ways to address these cost concerns:

- improving project/construction management techniques,
- serial plant manufacture,
- using NPP designs that incorporate passive safety,
- enacting decarbonisation policies that favour CO_2 reduction rather than specific technologies,
- establishment of sites for prototype reactor testing, and
- increased funding of prototype plants.

Whilst the latter three are important points in their own right, this study will not directly consider policy issues. The first three points are important considerations for this study and each will be discussed in turn.

The report highlights a key issue with both current and historical nuclear power plants; the breakdown of the construction management process. Many of these failures, particularly the lack of an experienced supply chain and construction workforce, and the mismanagement of projects, can be best seen very recently in the issues experienced with the construction of the new EPR (European Pressurised Water Reactor) plants (World Nuclear News, 2018) and there is little question that these failings have contributed to budget and schedule overruns. Others, such as the tendency to redesign plants either during construction, or between plant iterations, can be seen as far back as the UK's AGR (Advanced Gas-cooled Reactor) plants, which saw repeated redesigns as more iterations were built (Rush et al., 1977, Chesshire, 1992).

The use of standardised manufactured units for NPPs presents considerable opportunities for cost reduction by learning, something which the nuclear industry has historically not achieved. On the contrary, nuclear costs have risen over time. A recent book (Lévêque, 2015) cites an array of contributing factors, stemming from a lack of both the learning effect and economies of scale. The latter is exemplified by the very same iterative redesign with each generation of plant that plagued the AGRs, where larger plants are not simply larger in capacity; they are more complex and take significantly longer to build per kW. The learning effect has traditionally been elusive to nuclear new build, but there is some evidence of it in the French construction programme.

The French programme was largely seen as the most successful worldwide in terms of iterative learning, however (Grubler, 2010) disputes this using publicised financial records from EDF to analyse the cost escalation, and finding a negative learning effect. Dissenting work (Rangel and Lévêque, 2015) argues that this negative learning arose due to errors in the extrapolation of the EDF financial reports and that cost escalation can largely be attributed to attempts to scale up, rather than a negative learning effect in iterations of identical plant designs. There remains contention as two which of these two papers has the right of it (Berthélemy and Rangel, 2015, Perrier, 2018) and the original paper (Grubler, 2010) continues to be cited regularly.

Whilst standardised manufacturing is a characteristic most commonly associated with SMRs (Small Modular Reactors), (Buongiorno et al., 2018) asserts the opportunities are also present in larger current-generation LWRs (Light Water Reactors). This assertion is largely dependent on deference to the successes of the French programme. This opportunity for cost reduction remains a key hallmark and selling point of SMRs (Roulstone, 2015), but whether such savings will actually materialise remains unproven and a somewhat contentious issue (Kidd, 2010, Wearing, 2017, Boldon et al., 2014).

The aforementioned book (Lévêque, 2015) asserts that the key driving factor for escalating nuclear costs is the effect of safety regulation. This is not simply the effect of regulation increasing the complexity and hence cost of plants, but also due to the difficulty in assessing plant designs for adherence to regulation prior to their approval. Many plant in the US were simply not up to regulation at the time of their construction and had to be retrofitted for compliance (Cooper, 2010). One way to reduce the additional costs is the introduction of passive safety, that is designing reactors that can tolerate accident conditions with no emergency power and minimal operator intervention. This reduces the cost of regulatory compliance by relying on physics and plant designs rather than costly engineering safety systems. Whilst passive safety is again a hallmark of SMRs (Boldon et al., 2014), some passive safety features

have already been incorporated into newer current-generation LWRs, such as the AP-1000 (Cummins, 2013). Even the AGRs had passive safety systems of which modern plants might be envious (Wilson, 2015), however the nascent regulatory environment in the UK at the time was likely not a major contributing factor to cost.

All of the papers mentioned so far have a common discussion point to a greater or lesser degree: cost. It is easy to understand why; large-scale decarbonisation of global electricity generation is a gargantuan task in itself, even before considering the wholesale electrification of end uses that would typically be fulfilled by fossil fuels, such as transportation and heating. A pair of studies (McCombie and Jefferson, 2016, Kis et al., 2018) provide a comparison of nuclear and renewable generation (and in the latter, fossil generation) that stand out because of their focus on characteristics aside from cost. (McCombie and Jefferson, 2016) compares energy return, resource requirements, emissions, health effects, accidents, waste and public perception for nuclear and a variety of renewable generators by way of a qualitative literature review. (Kis et al., 2018) provides a more quantitative analysis of material use, energy return, job creation and carbon dioxide emissions by way of numerical modelling.

A pertinent point is that the energy returned for nuclear as a factor of the energy invested in construction is significantly greater than that for renewables. The data for renewables in (McCombie and Jefferson, 2016) is particularly damning, however the supporting data is sourced from an article that is not peer-reviewed, dated and somewhat disputed by (Kis et al., 2018). Nevertheless, this is a vital consideration as the world decarbonises; the energy input into construction today is carbon intensive and the smaller the ratio of energy yield to energy investment, the less tangible an energy source's contribution to that decarbonisation.

The papers take different approaches to material requirements. (Kis et al., 2018) provides a numerical analysis of material used per unit electricity output with a focus on cement and steel. Surprisingly, nuclear's cement and steel usage is comparable to that of many renewables and is ultimately less in many cases. This is presumably a result of the quantity of material being calculated as a factor of the energy produced, which due to nuclear's capacity factor and lifespan is inevitably higher than that of renewables. (McCombie and Jefferson, 2016) chooses to focus more on the rare elements associated with renewable generation, which whilst a tiny fraction of the whole, are still an important consideration. The paper cites reliance on China, which controls a significant proportion of the currently available materials, and the toxicity of these materials and their processing wastes as potential pitfalls. The paper does however concede that nuclear wastes are likely more expensive and more difficult to manage appropriately in the long run.

Social considerations are a feature of both papers. (McCombie and Jefferson, 2016) places emphasis on the fatalities per unit energy produced by the various sources considered. In this paper, three figures are used to make this comparison. The first two place nuclear and renewables on a similar footing and greatly below that of fossil fuelled generators. The third compares fatalities resulting from accidents with Chernobyl painting an unflattering picture for nuclear. Whilst focusing on accidents is perhaps not the most considered approach to social impacts – these events are rare in the extreme for both nuclear and renewables – the paper makes an important point in stating that these are events that capture the public imagination and likely have a greater impact on public sentiment than any statistical analysis. (Kis et al., 2018) focuses on the jobs created per unit electricity output per year, with far more jobs created in renewables than in nuclear. Once again, the figures are likely skewed somewhat by the energy density of nuclear, this time in the favour of renewables.

In summation, the discussions above highlight important considerations for any work that studies the performance of an engineered system in a real-world market. (Delucchi and Jacobson, 2011, Jacobson and Delucchi, 2011, Jacobson et al., 2015) highlight the potential pitfalls of making assumptions too broad and how difficult this is to avoid where a study attempts to be too generally applied. (Buongiorno et al., 2018) highlights the importance of construction costs to nuclear power and the risks associated with considering only the effect of a market on a proposition, not said proposition's effect on the market. It also provides a strong argument for potential cost reductions in future nuclear projects.

One point that most of these studies consider, to a greater or lesser degree, is the intermittency of renewable generators and the requirement for balancing technologies in the form of either load-following generators, or energy storage. The former will be discussed in the context of nuclear in section 2.3, whilst the latter will be discussed in section 2.4. In answering the fundamental question of this section, there is an argument that baseload nuclear power can provide backup for renewable intermittency up to a point, however as the penetration of renewables increases, power plants capable of flexibly adjusting their electricity output will become more and more valuable.

2.3. Load-following with nuclear

Broadly, NPPs are typically seen as baseload generators; plants with a fixed power output that does not vary over time. Whilst this is indeed a role these plants have historically filled in the UK, some nuclear plants have provided variable output power to the grid, particularly those in France, Canada and, historically Germany (Ingersoll et al., 2016a, Ingersoll et al., 2016b,

Ponciroli et al., 2017, Kidd, 2009, Lokhov, 2011b). In the former two cases this is largely a result of the high percentage of nuclear generated capacity, while in the latter it was a result of the high penetration of intermittent wind power.

Load-following in nuclear is often seen as having an adverse effect on the lifetime of NPP components, however this can be refuted to some degree (Lokhov, 2011b). Whilst cycling will surely affect the lifetime of some components, particularly valves and high temperature pipework, and increase O&M (operation and maintenance) costs, larger components are, for the most part, unaffected by this accelerated ageing – provided that the ramping rate and operational power ranges remain within specified limits (Lokhov, 2011b), as discussed below.

Previous study (Ponciroli et al., 2017) highlights several key operational considerations for varying the output power of a nuclear reactor; chiefly xenon poisoning. Xenon-135 is a decay product and acts as a strong neutron absorber, essentially slowing the nuclear reaction. After power reductions, the concentration of xenon rises over the following 7-8 hours due to the decay of Iodine-135, leading to a reduction in the reactivity of the core if the power is ramped back up too soon afterwards (Lokhov, 2011b). The former work (Ponciroli et al., 2017) also cites axial power variations over the height of the core, and fuel integrity and reliability as factors discouraging the operation of NPPs in anything other than baseload, whilst the latter (Lokhov, 2011b) notes the limitations on reactor manoeuvrability late in the fuel cycle due to the reduced core reactivity and increased fuel damage resulting from core temperature cycling.

The effect of load-following on profitability is modelled in detail in one study (Ponciroli et al., 2017). The factors mentioned above are found to be of minimal consequence compared to the potential revenue loss. Given the correct market conditions, the flexible operation proposed can actually increase plant profits. It is important to note that by the authors' own admission, the market study is too limited to prove this conclusively. It should also be noted that this study assumes that the NPP is operated within a market that already has regulatory acceptance of load-following with NPPs and makes no consideration of operation in markets where this is not the case. The previously mentioned paper (Lokhov, 2011b) compares the LCOE (Levelized Cost of Electricity) for various generators depending on load factor. At lower load factors of around 60%, gas performs best, followed by coal, with nuclear performing poorest. At 85%, the LCOE of these generators is similar. Above 85%, nuclear performs best and gas performs poorest.

Whilst not a viability consideration, the ramping rate of an NPP speaks to its usefulness in a load following capacity. Gas turbines are a key component of backup and load following power

supply and are capable of ramping at a rate of up to 15% of their nominal power each minute (Hentschel et al., 2016, Kumar et al., 2012). They also have the advantage of being able to cold start in minutes. Adding a steam power cycle to this, as with CCGT (Combined Cycle Gas Turbine) plants, reduces the ramping rate to a maximum of 8% of nominal power per minute with cold start time increasing into the range of hours rather than minutes. Steam-only cycles reduce the potential ramping rate to a maximum of 5% of nominal power each minute.

The paper discussing ramping rates (Kumar et al., 2012) also goes into great detail on the costs of cycling non-nuclear thermal power plants, which are primarily due to the early failure of components and the associated increase in O&M costs. An important point this report makes is the substantial difference in ramping rates between steam and gas turbines. Broadly, it would seem that gas turbines can start up and ramp more quickly than steam turbines. On the other hand, the power range of 40-90% of nominal power in which ramping is viable is similar for gas and steam turbines. In most cases of load following NPPs, the regulator sets the maximum power ranges and limitations on the ramping rates. In France, for example, NPPs are typically allowed to vary power by 5% of rated power per minute in the range of 50-100% of rated power (Lokhov, 2011b).

Reasons for operating NPPs in a baseload capacity are arguably driven by economic factors to a much greater extent than technical ones. As touched on in section 2.2, NPPs contrast with, say, natural gas plants because NPPs have high capital costs and low fuel costs. In such a scenario, it is preferable to an operator to maximise profits by running the plant at its maximum capacity throughout its working lifetime. Where fuel costs are negligible, this provides the greatest possible revenue to the operators. This is especially true in the UK where electricity prices are set years in advance of operation by CfD arrangements.

Recent work (Loisel et al., 2018) provides an interesting study into market effects of load-following with nuclear. Perhaps its most interesting conclusion is that the economic performance of such a proposition is, for the most part, market dependent. Like many other studies, it asserts that NPP components perform best in a load following role when power output is between 50 and 100% of the rated output, largely in line with the steam-driven turbines as mentioned above. As a result, such a system performs better in markets with modest intermittent renewable penetrations. (Lokhov, 2011a) places the minimum operational level even lower, with French plants occasionally operating at levels below 30% of nominal power.

This paper's (Loisel et al., 2018) market treatment is also interesting; the paper models market energy prices under the expectation that whilst prices will continue to increase up to 2030 as a

result of decarbonisation efforts, that prices will decrease approaching 2050 as a result of maturation of renewable technology and diversification of generation technologies. It is worth pointing out, however, that the paper does not appear to consider that renewables have a shorter lifespan than conventional plants. The effect of reliable load-following technology on market conditions is an important consideration; it is not unreasonable to assume that as more load-following capacity is made available (either through generators or commission of energy storage systems), that overall spot market volatility and price swings will fall.

The considerations in this section can be broadly placed into two categories; operational and economic. Operational considerations are those associated with reactor reactivity and control, increased fuel damage, and the reduction of efficiency in optimised systems, such as the turbomachinery and generators. One way of mitigating these issues is to use an energy storage system. This allows the NPP to run in a baseload capacity whilst the coupled energy storage system can absorb or output additional power to vary to output power of the hybrid plant. Such energy storage systems are discussed in section 2.4.

The key economic consideration is that running an NPP in anything other than a baseload capacity can have an adverse effect on revenues, especially in a market such as the UK's, where electricity prices for new NPPs are fixed prior to construction. Despite this, some in this field see this as a potential opportunity (Stack et al., 2016, Stack and Forsberg, 2015), especially if future spot markets provide sufficient volatility for a combination of variable plant power output and energy arbitrage to capitalise on energy prices. This last point is discussed in more detail in section 2.4.

2.4. Energy storage options

This section will detail and discuss a number of the energy storage options available today. There is a plethora of ESSs available today, at various stages of technological development and application within the electricity grid. It will discuss a number of potential ESSs:

- PHES, where electricity is converted to potential energy.
- Batteries and chemical stores, where electricity is converted to chemical energy.
- Thermal stores, where electricity is converted to heat.
- Air storage, where electricity is used to compress or liquefy air.

The objective of this study is to determine whether nuclear power can provide variable electricity to the grid. The discussions of ESSs herein thus focus on whether these systems might contribute to achieving this objective.

2.4.1. Pumped hydroelectric energy storage

The most prevalent and important ESS to date is PHES. The basic principle is simple; when electricity is in abundance (and prices are low), power is used to pump water uphill from a lower to an elevated reservoir. When electricity is in demand (and prices are high), the water is allowed to run downhill through turbines, generating electricity which is in turn sold back to the grid. It is important to note, however, that arbitrage is not sufficient to turn a profit from PHES and that current systems are reliant on ancillary service payments to maintain economic viability (Ela et al., 2013). The potential capacity of PHES plant is sizeable; Dinorwig, the UK's largest PHES plant, can store up to 9 GWh and has an output capacity of 1.7 GW. The overall PHES capacity in the UK is around 26 GWh (Barbour et al., 2012). The ramping rate for PHES is extremely fast, allowing them to ramp from zero to full power in a matter of seconds and the round-trip efficiency is in excess of 75%.

The economic viability of PHES is partially reliant on maximisation of the number of charge-discharge cycles (Forsberg, 2015, Barbour et al., 2012); the greater the number of cycles, the greater the opportunity for generating revenue through arbitrage. This arguably makes PHES more compatible with grids with large installed capacity of baseload generators, as this provides more guaranteed opportunities to charge the system than a grid with a large installed capacity of intermittent renewable sources. Detailed financial modelling (Connolly et al., 2011, Barbour et al., 2016, Barbour et al., 2012) has shown that PHES is unlikely to make sufficient profit from arbitrage, with payback periods exceeding 40 years (Barbour et al., 2016), a period prohibitive to potential investors. Installation costs of PHES are highly variable (Lazard, 2015, Dames and Moore, 1981, Karl Zach, 2012), primarily due to their dependence on large structures and suitability of terrain. Whilst the UK's capacity for pumped storage remains considerable, it is insufficient for large penetrations of renewables and other ESSs need to be considered (Guittet et al., 2016).

2.4.2. Batteries

Perhaps the next most developed ESS is batteries, of which there are a variety of types, as summarised in Table 2-1. A review paper (Aneke and Wang, 2016), whilst not exhaustive, provides a thorough summary of the different types of battery in use and in development today. Conventional chemical storage batteries such as sodium-sulphur, lead-acid or lithium-ion batteries, whilst by far the most well-understood, have the disadvantage of degradation of the electrodes over time (Wang et al., 2016). Flow batteries have an advantage over conventional batteries in that electron exchange takes place in the electrolyte rather than the electrodes,

preventing physical and chemical degradation (Aneke and Wang, 2016). Flow batteries are however more complex and much larger than conventional batteries and are thus best suited to grid-scale energy storage. They have the potential to be cheaper than conventional batteries, but most designs remain in the development stage (Koohi-Kamali et al., 2013). Air batteries utilise an anode made of an easily oxidised metal, such as zinc, which is oxidised by the air in the presence of a catalyst to generate electricity (Koohi-Kamali et al., 2013). Air batteries can be highly compact but suffer from a difficulty recharging and a low number of operating cycles before electrode degradation. These issues must be solved before these batteries become viable for grid-scale energy storage.

Technology	Efficiency	Primary use	Notes
Sodium sulphur	~85%	Grid energy storage	
Sodium nickel chloride		Electric vehicles	
Vanadium redox flow battery	~85%	Grid energy storage	
Iron chromium flow battery	-	Currently in development	
Zinc bromine flow battery	-	Currently in development	
Zinc air battery	50%	Currently in development	Short lifespan
Lead acid	85-90%	Household	
Nickel cadmium		Household	Toxicity issues

Table 2-1: Comparison of battery energy storage systems (Aneke and Wang, 2016, Koohi-Kamali et al., 2013)

2.4.3. Hydrogen

Hydrogen is such an important commodity that it deserves to be discussed in its own context, separately from batteries. It is widely used today in the production of fertiliser and in the refinement of petroleum (Sharma and Ghoshal, 2015, Ramachandran and Menon, 1998). It is also viewed by many as a cornerstone of a future low carbon economy by merit of its potential use as an energy storage medium (Gorensek and Forsberg, 2009, Hanley et al., 2015), and as a chemical reducer to replace carbon in processes such as steel making (Forsberg, 2009, Forsberg, 2004). It could furthermore be used as a feedstock for the production of synthetic fuels (Takeshita and Yamaji, 2008), or the upgrading of conventional hydrocarbon fuels or biofuels (Brown et al., 2015).

The current industry standard for hydrogen production is the MSR (methane-steam reformation) process. This is a multi-stage chemical process that first combines natural gas with steam in the presence of a nickel catalyst at temperature in excess of 700°C:

$$CH_4 + H_2O \leftrightarrow CO + 3H_2 \qquad (2\text{-}1)$$

Additional hydrogen is produced in the shift reaction, where steam is added to the reactants:

$$CO + H_2O \leftrightarrow CO_2 + H_2 \qquad (2\text{-}2)$$

The reaction in equation (2-1) is highly endothermic. The reaction heat is typically provided by combusting natural gas, adding to both the quantity of feedstock consumed and the overall carbon dioxide produced by the system (Hori, 2008). The process itself releases significant quantities of unreacted methane, nitrogen oxides and sulphur oxides (Spath and Mann, 2001). These are all important greenhouse gases.

If methane-steam reformation is to contribute to low-carbon hydrogen production, significant reductions in emissions will have to be made, potentially by providing the heat for reaction (2-1) from a clean heat source, such as a nuclear reactor (Hori et al., 2005), or by reducing the temperature of this reaction by using alternative catalysts (Zeppieri et al., 2010, Matsumura and Nakamori, 2004, Nieva et al., 2014). In 2014, the Gen IV International Forum reduced the target temperature of the VHTR (Very High Temperature Reactor) from 1000°C to 750°C (Gen IV International Forum, 2014), reducing its potential process heat applications and making the former unlikely. The catalysts mentioned are some way from commercial application, making the later unlikely for the time being.

There are alternative hydrogen production processes to methane-steam reformation. The most developed of these is arguably electrolysis, but thermochemical cycles are potentially an important future technology. LTE (Low-temperature Electrolysis) involves the electrolysis of liquid water to split it into hydrogen and oxygen and is a technology that has some small-scale use today. Its main drawbacks are its low efficiency and difficulties with scaling up to production of industrial quantities. It is seen by some as ideal for coupling with wind energy as it can assist with intermittency by acting as an energy sink during times of high supply and low demand (Lee, 2012, Orhan et al., 2012). It is important to consider that the value of intermittently producing hydrogen in this way is potentially somewhat limited, since the uses for hydrogen mentioned above require continuous supply of industrial quantities.

HTE (High-temperature electrolysis) is a development of LTE in which the water is heated to produce steam before it is electrolysed. As (Fujiwara et al., 2008) shows, increasing the temperature of the steam reduces the required electrical energy input. Provided an efficient source of heat is available, less energy will be lost in heating water than in the conversion of that heat to electricity (Fujiwara et al., 2008). Once again, however, the 750°C temperature of the VHTR is at the lower end of economic viability for HTE.

The final important method of hydrogen production that will be discussed here is thermochemical. These are series of chemical reactions that are used to split water into hydrogen and oxygen. They are characterised by the reuse of all the chemical reactants except

water. These involve endothermic reactions and an efficient source of heat. Some are hybrid cycles and also require a supply of electricity. There are many such processes; here, the S-I (sulphur-iodine) cycle will be given as an example of a pure thermochemical cycle and the Cu-Cl (copper-chlorine) cycle will serve as an example of a hybrid cycle.

The S-I cycle has seen plenty of small-scale testing in Japan (Zhu et al., 2012, Zhang et al., 2010). This is a purely thermochemical cycle and only requires heat supplied to each of its three steps.

Step 1 (at 120°C):

$$SO_2 + I_2 + 2H_2O \rightarrow H_2SO_4 + 2HI \qquad (2\text{-}3)$$

Step 2 (at 830°C):

$$H_2SO_4 \rightarrow SO_2 + H_2O + \frac{1}{2}O_2 \qquad (2\text{-}4)$$

Step 3 (at 450°C):

$$2HI \rightarrow H_2 + I_2 \qquad (2\text{-}5)$$

This process is summarised diagrammatically in Figure 2-2 (diagram taken from (Wilson, 2015)).

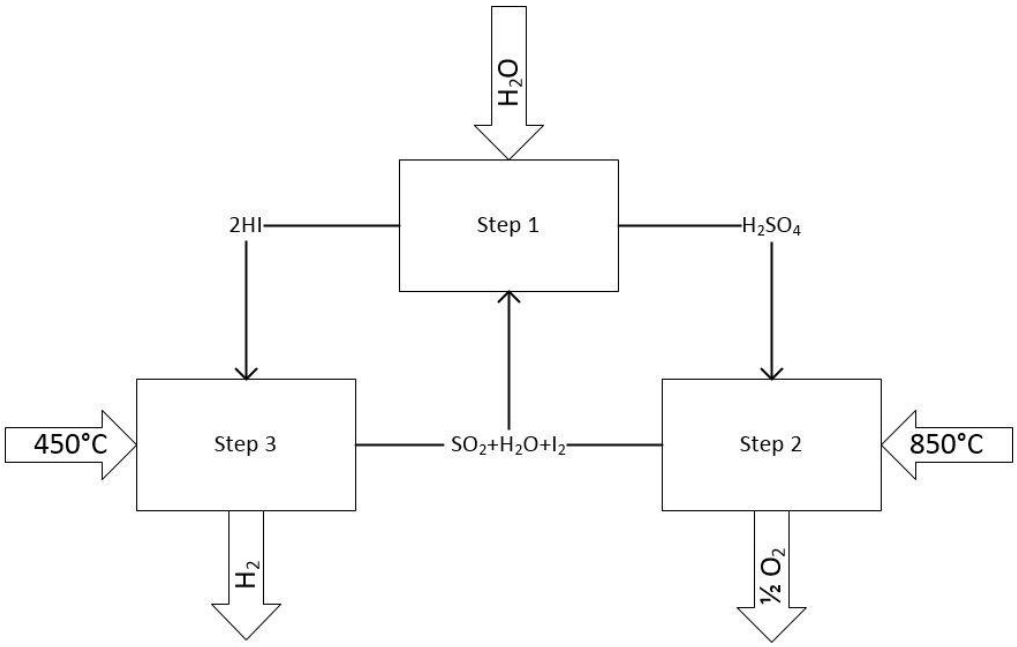

Figure 2-2: S-I cycle process diagram

The Cu-Cl cycle has also seen a great deal of development, this time primarily in Canada (Naterer et al., 2010, Naterer et al., 2013, Naterer et al., 2009). This has the advantage of a lower temperature requirement than the S-I cycle, however it requires an electrical input into one of its reactions.

Step 1 (at <100°C with electrolysis):

$$2CuCl_{(aq)} + 2HCl_{(aq)} \rightarrow H_{2(g)} + 2CuCl_{2(aq)} \qquad (2\text{-}6)$$

Step 2 (at <100°C):

$$2CuCl_{2(aq)} \rightarrow 2CuCl_{2(s)} \qquad (2\text{-}7)$$

Step 3 (at 400°C):

$$2CuCl_{2(s)} + H_2O_{(g)} \rightarrow Cu_2OCl_{2(s)} + 2HCl_{(g)} \qquad (2\text{-}8)$$

Step 3 (at 500°C):

$$Cu_2OCl_{2(s)} \rightarrow 2CuCl_{(l)} + {}^{1}/_{2}\, O_{2(g)} \qquad (2\text{-}9)$$

This process is summarised diagrammatically in Figure 2-3 (diagram taken from (Wilson, 2015)).

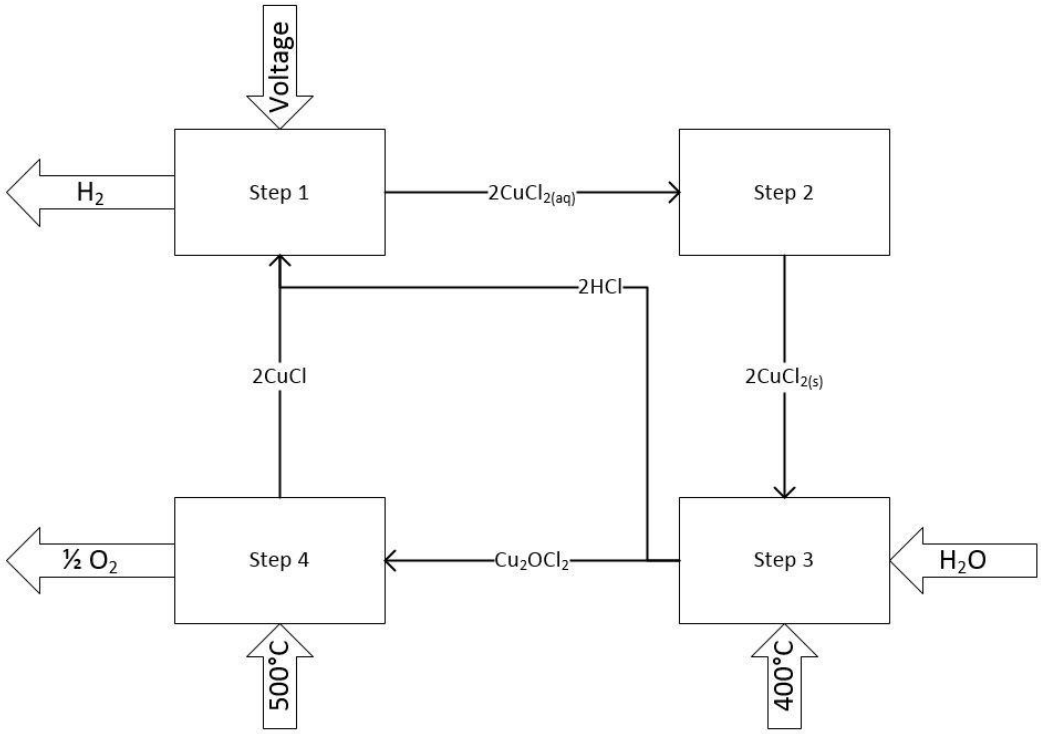

Figure 2-3: Cu-Cl cycle process diagram

As mentioned above, there are many other water-splitting chemical cycles available, as well as variants of both the Cu-Cl and S-I cycles, but these two have seen the most development. There has been significant interest in these cycles as a means to produce hydrogen with nuclear heat (Barbooti and Al-Ani, 1984, Wang et al., 2009, Wang et al., 2010, Norman et al., 1982). Clearly, however, the S-I cycle has a major disadvantage in its extremely high temperature requirement, especially with the aforementioned limitations of the VHTR. The Cu-Cl cycle goes some way to reduce this requirement, however the requirement for electrical input will reduce its overall efficiency for thermal power plants. In terms of energy input to energy output, both of these cycles have a round-trip efficiency of approximately 55%. This does not take into account the losses in generation of electricity, so the effective thermal round-trip efficiency will be lower for the Cu-Cl cycle. The reactants used in these cycles include highly corrosive materials and would add to the considerable thermal strain on the equipment used.

It is important to consider whether hydrogen generation could contribute to the development of a output-flexible NPP. For this, there are two options; either producing hydrogen for sale to industry and reducing NPP output at time of low electricity demand, or as an internal energy

store, absorbing power at times of low demand and releasing it at times of high demand, either using a gas turbine or a hydrogen fuel cell. As discussed, industrial hydrogen users require continuous production of pipeline quantities of hydrogen. It is thus not unreasonable to think that the best use for these systems in the context of an NPP would be as an internal energy store for time-shifting power output.

Nuclear-assisted MSR, HTE and the thermochemical cycles require too high temperatures for currently available LWR designs. Ultimately, all of these applications will require significant development of next generation designs and are unlikely to be commercially viable for decades. Of the hydrogen production options discussed, only LTE is compatible with current-generation reactor designs and a candidate for this study. Given its high cost and difficulties scaling, it is better suited to generators of low-cost electricity, such as wind power, than nuclear.

2.4.4. Thermal energy storage

Storing energy from thermal power plants as heat would arguably seem to make a lot of sense from an efficiency perspective. This is because it negates the energy losses associated with the conversion of one form of energy to another. The basic concept of any thermal store is to use power plant heat to increase the temperature of a medium, typically a fluid with a high heat capacity, and store this is an insulated container for later use.

Steam accumulators are one of the oldest forms of heat storage and consist of an insulated pressure vessel containing a mixture of hot water and steam. To charge the system, steam is blown into the tank and raises the temperature of the water inside as well as the overall pressure. During discharge, steam is drawn off for power generation or, more commonly, process heat purposes. This reduces the pressure in the tank, allowing more water to boil and producing additional steam. This would, on the face of it, seem highly suited to an LWR, which uses steam as a working fluid.

Heat-to-heat round-trip efficiencies for steam accumulators are in excess of 90% (O'Brien and Pye, 2010). Steam accumulators have a key drawback in that they are a high-pressure store and, as such, require a strong pressure vessel. This has been a major cost in nuclear power plants, especially PWRs, and could make steam accumulators prohibitively expensive when compared to other ESSs (Kuravi et al., 2013). Their energy density is also relatively low compared to chemical options. At this stage, however, it is important to point out that one of the main reasons nuclear reactor pressure vessels have been so expensive is their size; steam accumulators as an energy store could benefit from having multiple small vessels rather than a single large one as

in a PWR. Steam accumulators are still used and actively marketed, however studies in coupling them to thermal power plants are either quite old (Fritz and Gilli, 1970, Gilli and Beckman, 1973), or in need of further development (Ryu et al., 2012).

Molten salts have been put forward as a potential thermal storage medium. A molten salt ESS would be charged by heating the salt using a thermal power source and storing it in an insulated tank. On discharge, it would then be pumped through a heat exchanger to supply heat to a working fluid which would then be used to generate electricity.

This is a promising energy storage technology which is capable of achieving high heat-to-heat round-trip efficiencies in excess of 80%. It is important to note, however that the requirement for heat exchange with their coupled thermal plant's working fluid will result in additional losses in the conversion of heat to electricity. This is because the temperature gradients required by heat exchangers will require that the working fluid produced during discharge be of a lower temperature than that used during charge, reducing the efficiency of the power cycle. For this reason, it has primarily been associated with high-temperature thermal power plants such as concentrated solar-thermal (Slocum et al., 2011), or high temperature nuclear reactors (Green et al., 2013). There has been significant research into the molten salts themselves, but the materials required for resistance to these corrosive materials are still in development (Forsberg, 2011).

UTES (underground thermal energy storage) involves storing hot water in geological features such as aquifers or underground caverns (Eames et al., 2014, Forsberg, 2015). Because the energy density of UTES is very low, finding the right geological conditions are highly important to limit costs. Because rock is a particularly poor conductor of heat, UTES could provide highly efficient energy storage over seasonal timescales (Pavlov and Olesen, 2012). Whilst there has been some success with UTES in Europe, experience in the UK is limited (Sanner et al., 2003). The slow response of UTES limits its value as a means of providing variable electricity to the grid and it is better suited as a grid-scale seasonal ESS.

Heat can be stored in solid media, such as ceramics. Perhaps the most common example is that of storage heaters which allow homes with potentially expensive electrical heating to take advantage of low electricity prices by storing the resultant heat for when it is needed. More recently, the same idea has been developed into a potential ESS in the form of FIRES (firebrick resistance-heated energy storage) (Stack et al., 2016, Stack and Forsberg, 2015).

FIRES consists of a high heat capacity solid energy storage medium and some form of resistance heating. When charging, the medium would be heated using a thermal power source, electricity via the resistance heaters, or by a combination of the two. The system would be discharged by blowing air through the medium and using the resulting hot air to either supply process heat or to drive an air power cycle.

The system is highly flexible in that it allows designers to vary capacity, charge rate and discharge rate simply by altering the volume, heating element resistance and the air throughput of the system respectively (Stack et al., 2016). Its development has been associated with the FHR (fluoride-salt-cooled high-temperature reactor) design (Forsberg et al., 2015) and the intention of the developers to increase nuclear power's economic viability by increasing revenues rather than decreasing costs has been a major inspiration for this project.

FIRES shares the same drawbacks as molten salt storage in that the overall efficiency of the system is associated with the efficiency of the output power cycle. As a result, FIRES is specifically designed to be coupled with high temperature reactor systems. One particularly interesting feature of the design is the designers' suggestion that natural gas could be used to increase power cycle temperatures (Forsberg et al., 2015). This not only improves the efficiency of the coupled power cycle, but also allows it to provide peaking power when the FIRES storage has been completely exhausted. Whilst using natural gas as part of a topping cycle does reduce the associate carbon dioxide emissions over a purely natural gas power cycle, it does lessen the green credentials of what would otherwise be a highly environmentally friendly system.

2.4.5. Air storage

Thermal storage systems need not necessarily be high temperature; cold systems can also effectively and efficiently store energy. CAES (compressed air energy storage) and LAES (liquid air energy storage) have seen significant development and have both been demonstrated in pilot-scale plants (Institution of Mechanical Engineers, 2012). Both systems operate in a similar way. When charging, energy is used to compress air, which is then stored in a tank. LAES takes this one step further and liquefies the air using a process similar to commercial liquefaction plants, as discussed in section 2.5. Discharge involves heating the air (following vaporisation in LAES) and expanding it through turbines.

Two CAES plants have been built; the first in Germany and the second in the United States (Luo and Wang, 2013, Nakhamkin et al., 2010, Rouindej et al., 2020). Both are gas turbine plants that store the compressed air in underground salt domes. Air is compressed using

electrically driven compressors at times of low electricity demand and is heated by natural gas combustion and expanded during times of high demand. These plants achieve round-trip efficiencies of around 50% and significantly reduce the carbon dioxide emissions associated with the natural gas that they consume (Energy Storage Association, 2016). Improvements can be made on overall system efficiency by storing the heat of compression and using this to heat the discharge air, eliminating the need for natural gas. Work is underway to commercialise such systems (Rouindej et al., 2020, RWE Power, 2010) and they are expected to achieve efficiencies of 70% or higher.

A great deal of experience in LAES systems has been gained from the pilot plant demonstrated by Highview Power Storage (Highview Power Storage, 2016). Whilst round-trip efficiency at the pilot plant was less than 10%, two important features of a commercial plant were highlighted (Morgan et al., 2015b). Firstly, cooling a storage medium with the air during discharge and using it to cool the incoming compressed air during the subsequent charge phase is paramount to improving round-trip efficiency. This is most commonly known as cold recycle (Li, 2011). Secondly, reserve service trials were favourable with the plant showing excellent ramping ability and rapid start up.

Coupling LAES with a nuclear plant has been suggested (Li et al., 2014). Highview suggest an expected round-trip efficiency of 50% might be improved to in excess of 55% with the use of a source of waste heat or potentially even higher by storing the heat of compression during the charging phase (Peng et al., 2018). It is in this area that LAES truly shines as an ESS; the low temperatures of its working fluid allow it to utilise heat that would otherwise be considered waste. Furthermore, this makes LAES uniquely suited to coupling with an LWR NPP, which has low- and medium-grade heat in abundance. LAES is discussed in significantly greater detail in section 2.5.

2.4.6. Discussion of revenue generation

Revenue generation and profits for ESSs are a vital consideration. Section 2.3 discusses a study, (Loisel et al., 2018), whose market treatment assumes that spot market prices will fall as more energy storage technologies are integrated into the grid. (Roques et al., 2008) would seem to support this assumption. As discussed in section 2.2, this paper (Roques et al., 2008) posits that electricity and gas prices are strongly correlated. This makes intuitive sense; CCGT plants provide the bulk of variable electricity sold into the spot market and will presumably bid to ensure their margins are sufficiently high. The necessity to fulfil power demand and the bidding

nature of the UK spot market will drive electricity prices sufficiently high to allow CCGT operators to make a profit. In this way the generators, and their costs, are driving the market.

The case of energy storage, however, is more complicated. The revenues from energy storage are likely to be based on a combination of arbitrage and ancillary service payments (Mauricio et al., 2017, Dunbar et al., 2016, Ela et al., 2013) and the cost to charge the store is much more difficult to predict. The minimum spot market price is likely to be driven by an excess of electricity supply. Currently, this takes place overnight (Smith and Halliday, 2016) and is driven by a combination of reduced demand at night and the fact that baseload generators are still running. A grid with significant quantities of renewables could increase supply (at least from wind generation) and if demand were to remain the same, this could reasonably be expected to drive down the electricity price. Like a CCGT plant's gas price, the cost to charge energy storage is driven by factors external to the plant itself.

The revenue from energy storage is generated in the same way as that for CCGT peaking plants; by bidding into the spot market. Here however, a new bidder is being introduced into a market already dominated by another generator. As discussed in the previous paragraph, cost drivers for CCGT and energy storage systems are entirely independent from one another. It is not hard to envisage a situation where a saturation of energy storage systems results in a decreased reliance on natural gas, reducing gas demand and prices. This, in turn, could allow CCGT to bid lower into the spot market, essentially undercutting energy storage systems. This thinking would seem to support the market treatment in the aforementioned paper (Loisel et al., 2018).

Predicting the effect of an increasing share of renewables in the grid is thus important in attempting to model electricity price and revenue for energy storage. One hypothesis is that increasing intermittent generation in the energy mix will result in greater price volatility. Considering the lowest electricity prices first, some expect that high concentrations of renewables could result in negative electricity prices (Grünewald et al., 2011, Barbour et al., 2014). Broadly, the reasoning behind this is that renewables are typically subsidised, and it is preferable to an operator that they bid into the day-ahead market with a negative price of magnitude on par with their subsidy. This minimises their risk of curtailment, which would result in zero revenue for energy generated. Others (Dunbar et al., 2016) suggest that negative prices will not transpire as renewables expand and subsidies shrink.

The possibility of negative electricity prices has major implications for energy storage. As (Barbour et al., 2014) notes, the presence of negative prices means that an energy store generates revenue on both the charging and discharging phases, meaning that even systems of

low efficiency can become viable. When electricity prices are always positive, the ratio of the electricity prices during charging to those during discharge must be greater than the storage system's round-trip efficiency if that system is to turn a profit. As far as analysing arbitrage revenue goes, this latter scenario would be the more conservative.

2.5. Liquid air energy storage

2.5.1. System basis

The basis of LAES lies in the liquefaction of air. Gas liquefaction has seen significant development over the past century. The first liquefaction technique was cascade liquefaction and relied on the ability to liquefy gases by compression (Kerry, 2007). This is possible where the gas has a sufficiently high critical temperature that the temperature of the compressed gas does not exceed. This first liquid can then be used to cool a second gas (one with a lower critical temperature), allowing this second fluid to be liquefied by compression.

The critical temperature and critical pressure define the critical point of a fluid; the point above which the boundaries between the liquid and gaseous states of the fluid are no longer clearly

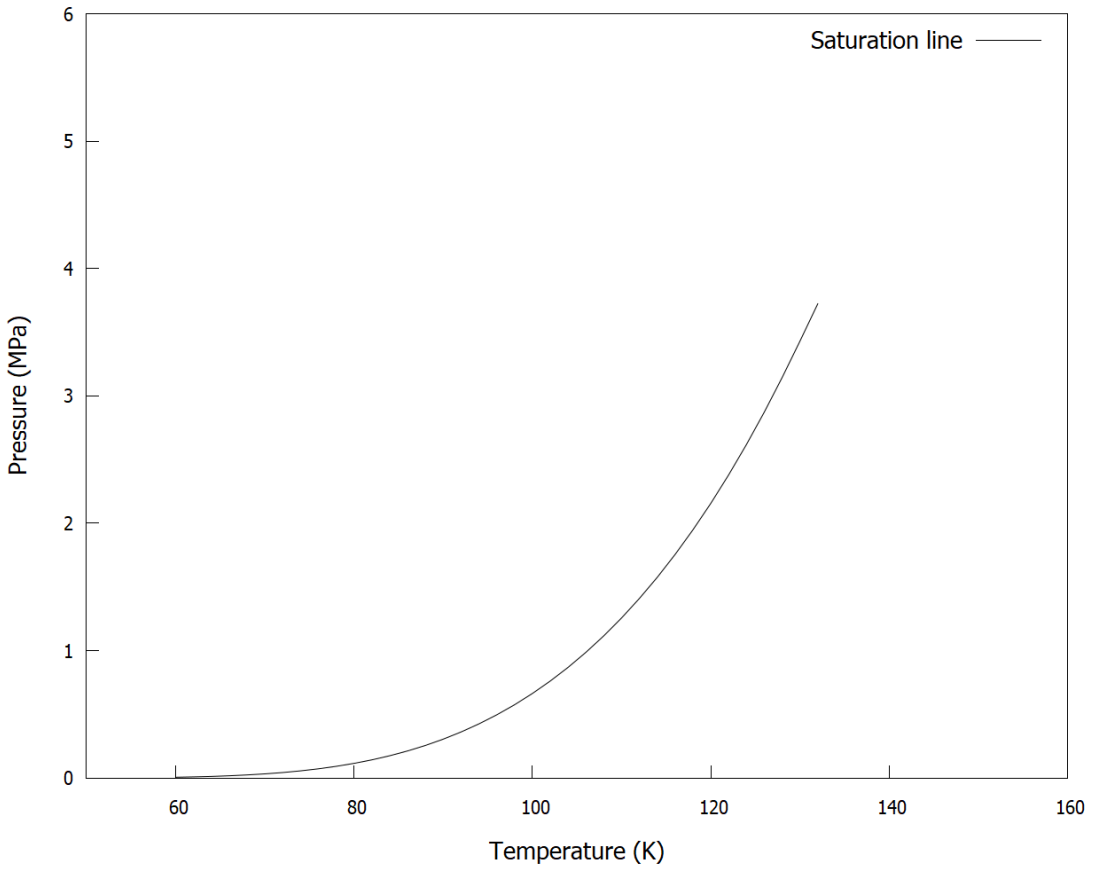

Figure 2-4: p-T diagram showing saturation points for air

defined. This critical point is shown by the end point of the saturation line (the line connecting all points at which a phase transition between liquid and gas occur) on the p-T diagram for air in Figure 2-4 (data taken from (Lemmon et al., 2000)) and shows that the critical temperature for air is 132.6 K. Above the critical temperature, it is impossible to liquefy a fluid no matter how much it is compressed. It is this quality that makes the critical temperature so important for cascade liquefaction; the temperature of the fluid prior to compression must be sufficiently low that the temperature rise of compression does not exceed the critical temperature, otherwise liquefaction will be impossible.

Cascade liquefaction is poorly suited to continuous production. The majority of processes that have been developed since then rely on the J-T (Joule-Thomson) effect. This effect occurs when a fluid that is below its inversion temperature is expanded through an insulated valve (subsequently known as a J-T valve) in an adiabatic process (Kerry, 2007). An adiabatic process is one in which there is no transfer of heat to or from the process (i.e. a process that occurs at a constant enthalpy). The inversion temperature for a fluid is the temperature below which that fluid will fall in temperature during expansion and above which it will increase in temperature when expanded.

Expansion at a constant enthalpy below the inversion temperature results in the cooling of the gas. If the starting temperature is sufficiently low and the pressure drop sufficiently large, the fluid in question will reach its saturation line and experience a phase transition from the gaseous to liquid state. This process was first exploited for gas liquefaction in the Linde-Hampson system, as shown in Figure 2-5 (Kerry, 2007).

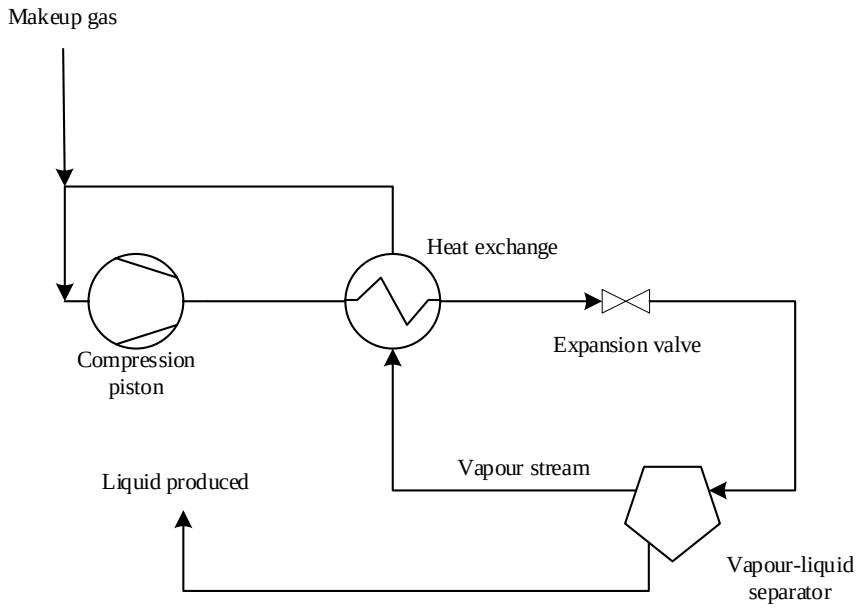

Figure 2-5: Linde-Hampson air liquefaction

In the L-H system, the gaseous fluid is compressed (and cooled) in a piston. It is then cooled via heat exchange with the return vapour stream before being expanded in a J-T valve to be partially liquefied. The liquid is separated as a product while the vapour is returned via the heat exchanger to be mixed with makeup gas and restart the cycle. This process was used for some 50 years (Kerry, 2007) and was improved by adding some cooling via a separate refrigeration process immediately following the compression stage. Incidentally, this process was the basis for the original proposal for the original LAES system design (Smith, 1977).

The expansion valve is the key disadvantage of the L-H system. Adiabatic processes are irreversible and are by definition less efficient than reversible processes. Improvements can be made to the process by expanding some of the working fluid in a work-producing expander, a device that approximates a reversible isentropic process. Unlike a J-T valve where the enthalpy of the working fluid is kept constant, in an ideal expander, entropy is kept constant and enthalpy falls as energy is extracted from the system. This not only provides an additional cooling effect but also produces some useful mechanical work, improving the efficiency of the overall process. A reciprocating expansion engine was included in a liquefier in the Claude system, as shown in Figure 2-6 (Kerry, 2007).

In the Claude process, a portion of the compressed fluid (typically around 75%) is diverted to a reciprocating expander following the first heat exchanger. Once expanded, the cooled exhaust is mixed with the return fluid stream and used to cool the incoming stream. The development of large amounts of liquids in reciprocating expanders would damage them, so this expansion

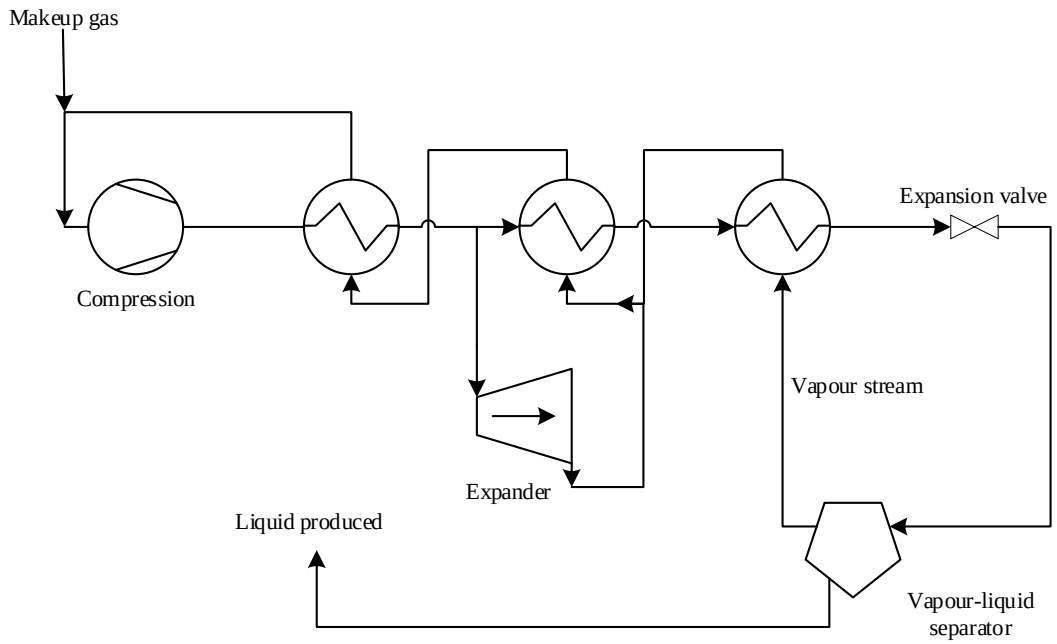

Figure 2-6: Claude liquefaction process

must take place at an early stage. The ultimate liquefying expansion still takes place in a J-T valve following cooling by heat exchange with the return fluid stream.

Multiple alternatives to the Claude process have been used commercially in the intervening years. The Kapitza and Heylandt cycles both replaced the reciprocating expander with a centrifugal turbine and used one fewer heat exchanger. The former replaced the first heat exchanger with a regenerator for initial cooling of the compressed fluid (Kerry, 2007), allowing operation of the cycle at far lower pressures than previously used, at less than 1 MPa. The latter diverted gas flow to the turbine immediately following compression but did not use regenerative heat exchange, requiring significantly higher pressures of 20 MPa. Another alternative, the Collins cycle, used additional heat exchangers and multiple expanders with similar pressures and is capable of helium liquefaction (Thomas et al., 2012).

LAES further complicates the issue by including both liquefaction and power cycles. The fact that stored air is discharged, vaporised and used to drive turbines provides a unique opportunity; the discharged air can be used to cool a thermal medium, thereby offering a free and passive source of cooling during subsequent liquefaction. Whilst 'cold' is not technically an energy so much as the absence of one, the term 'cold store' will be used herein to discuss the medium that the discharge air cools and 'cold recycle' will be used to discuss the process of cooling this medium and the subsequent cooling of the charge air stream. This both facilitates ease of discussion and brings the terminology in line with that used in literature on the subject. There have been several modelling studies into LAES, but almost all of the literature that will be discussed below uses some form of cold recycle.

2.5.2. Engineering studies

The literature available on LAES is substantial, but the majority of published papers are engineering studies. Highview Power has a patented LAES design and built the first pilot plant in Slough in the UK. The company has co-authored several papers (Morgan et al., 2015b, Morgan, 2016) discussing the pilot plant. (Morgan et al., 2015b) discusses the lessons learned from this plant and compares its performance to theoretical performance of a grid-scale plant.

A Highview study (Morgan et al., 2015b) discusses two models; a basic model studying the maximum theoretical efficiency of the plant and a more detailed cycle performance model that uses Aspen HYSYS. The former calculates theoretical round-trip efficiencies in excess of 75% that increases with charging pressure. The latter incorporates second-law losses associated with heat transfer processes and yields some interesting results that inform process design. Firstly, while increasing the peak pressure of the discharge cycle improves the energy yield, so too does

it reduce the available cold recycle. This results in diminishing returns on round-trip efficiencies for peak discharge pressures in excess of 15 MPa. Secondly, the specific energy of production has a minima at a pressure of around 5.4 MPa at the expansion valve above which the increased work of compression offsets improvements in liquid yield. Finally, the model demonstrates that increased turbine inlet pressures and temperatures improve energy yield during discharge and the paper notes the importance of using waste heat from nearby industry to improve power, as well as the particular suitability of LAES to capturing low-grade waste heat. Whilst the modelling assumptions of compressor and turbine efficiencies of 90% is potentially a little high, this is a sensible and thorough engineering study with some results that usefully inform process design. Furthermore, the authors have access to data from the pilot plant and state that their model predictions provide a good match with experimental data.

In addition to its engineering study, (Morgan et al., 2015b) discusses the commercialisation of the technology. It cites being able to vary the discharge rate of the cold store as allowing the system to respond to electricity prices. When prices are low, the paper suggests limiting cold store use during charging, retaining some of the cold stored and subsequently allowing the system to produce air a high efficiency when electricity prices rise again. Whilst this is an interesting idea, it is of dubious value in today's market, where there are long periods at night during which the behaviourally-driven prices are low as discussed in section 2.4.6. Nevertheless, this point highlights an aspect of design flexibility that could be advantageous in changing markets.

The paper (Morgan et al., 2015b) also discusses additional means of revenue generation in the UK; reserve and response services. Reserve service requires plant to be able to bring its generators on-load within 15 minutes of a call from the grid operator. The pilot plant achieved reliability sufficient to provide this service but the paper notes that the higher rotational inertia of turbomachinery in a larger-scale plant would increase ramping times. Conversely, it notes that the operational temperature range is significantly lower than for a natural gas turbine, limiting the effect of fast ramping on thermal fatigue damage. Response service requires plant to able to load-follow in response to an instruction from the operator. The pilot plant excelled in this trial.

This paper (Morgan et al., 2015b) also discusses practical lessons learned from operating the pilot plant. It discusses potential oxygen enrichment in the air storage tank by preferential evaporation of nitrogen, whose boiling point is lower than that of oxygen and the potential hazard of this coming into contact with hydrocarbons, such as turbine lubrication oil. The paper emphasises the importance of a cold store in improving efficiency whist noting that the cold

store is the sole system component that was not available off the shelf and highlighting the importance of minimising its cost.

Another paper co-authored by Highview Power (Morgan, 2016) provides discussion of the modelling work performed in their preceding work (Morgan et al., 2015b) but provides a less detailed study of the engineering system results. However, (Morgan, 2016) does discuss some potentially useful design options for the cold store. It discusses an early system proposal (Smith, 1977) that used an inline cold storage system that is cooled directly by the discharge air stream and directly cools the charge air stream. The paper notes that whilst this design reduces heat transfer losses, a high-pressure storage vessel is required that will increase cost. A further paper by the same group (Morgan et al., 2015a) goes into greater detail of the results of the Aspen HYSYS model from (Morgan et al., 2015b). Perhaps the most important part of this paper is the discussion of a 'warm recycle' system; a corollary of cold recycle that stores the heat of compression when charging and uses it to heat the air prior to expansion during discharge. The paper highlights a trade-off between the number of compression stages and the temperature of the recycled heat. Despite the reductions in the energy cost of production for more compression stages, the reduced warm recycle temperature resulted in a lower overall round-trip efficiency. This paper also provides a basic cost analysis that is discussed in section 2.5.3.

Highview's pilot plant was relocated from Slough to the University of Birmingham 2014, and the team involved in its study published a number of papers. (Sciacovelli et al., 2017a, Sciacovelli et al., 2017b) detail the engineering modelling work they performed. With sufficient levels of cold and warm storage, the group asserts that round-trip efficiencies in excess of 60% are achievable. (Sciacovelli et al., 2017a) provides an overview of the group's engineering model and provides a thorough account of their attempts to validate their process model against experimental data from the Highview pilot plant. Their results show a strong match to the thermodynamic states seen in the actual system. This paper also predicts the theoretical round-trip efficiency limit for the pilot plant at around 35%. This is about half the theoretical limit of a commercial system as a result of the low pressure of the liquefaction system and the limited cold recycle in the pilot plant.

(Sciacovelli et al., 2017b) provides a more rigorous discussion of the dynamic process model developed using EES (engineering equation solver) software (F-Chart Software) by the University of Birmingham group. The bulk of this paper, however, is dedicated to the modelling of a commercial plant design. This is the intended mature design for LAES and features two-stage compression, both warm and cold recycle systems, and a liquefier design most similar to the Heylandt cycle discussed in section 2.5.1. The account of their modelling is detailed and

depicts a credible system design with feasible modelling assumptions of isentropic turbine and compressor efficiencies of 85%.

One of the triumphs of (Sciacovelli et al., 2017b) is its detailed treatment of the cold store. The model uses empirical relationships to estimate both heat transfer coefficients and axial pressure drops to dynamically calculate temperatures along the axis of the gravel bed during the charge and discharge of the system. These provide an excellent match to experimental data and highlight an important consideration; the temperature of the air from the cold store rises towards the end of the charge cycle as the cold box temperature rises. As a consequence of this, the specific energy of liquefaction rises towards the end of the charging cycle as the temperature of the air prior to expansion rises. This is a similarly important consideration for this work and is one that is discussed in detail in sections 5.2.2 and 5.2.6.

This feature of cold recycle also represents an important consideration in the applicability of LAES to grid-scale storage. Despite the effectiveness of modern insulation techniques, the cold store will inevitably be warmed by the environment over time. Since the specific energy of liquefaction is highly dependent on the quantity of cold recycled, the longer the system is allowed to idle, the greater the energy cost of liquefaction. As a result, even if sufficient storage were available for the liquefied air, the system would be wholly unsuitable for seasonal storage, given the large time delay between the discharge and subsequent charge cycles that would result.

Members of the same group went on to publish papers focused on further improvements of the round-trip efficiency of the LAES design. The first of these was a detailed assessment of the effect of cold and warm recycle on the performance of LAES (Peng et al., 2018). Using the same model as (Sciacovelli et al., 2017b), the authors study the improvements available by utilising cold and warm recycle systems, as well as considering the opportunities of capturing additional waste heat using an ORC (organic Rankine cycle). This paper highlights the importance of the cold store in an LAES plant's round-trip efficiency, noting that even small reductions in the efficiency of the cold store can have significant ramifications for the efficiency of the overall plant. The effect of inefficiencies in the warm store, although non-negligible, is significantly less. The inclusion of ORCs is discussed in more detail below.

Other papers focused on the coupling of LAES with LNG (liquefied natural gas) regasification (Peng et al., 2019, Kim et al., 2018). This is a particularly interesting idea. Cooling of the compressed air is done by heat exchanging the incoming air stream with the return air stream (the vapour fraction separated from the post-expansion air) and a second cold stream (air or

hydrocarbon) from the cold store in most of the papers already discussed. (Peng et al., 2019, Kim et al., 2018) augment this cooling by using the cold stream form an LNG store prior to vaporisation. (Peng et al., 2019) considers a system that supplies the resulting natural gas to the grid, generating some additional power during its expansion, whereas (Kim et al., 2018) combusts the gas onsite. Both studies yield expected round-trip efficiencies in excess of 70%, with (Peng et al., 2019) claiming an efficiency of 88%. The latter paper does not burn the gas onsite so the associated inefficiencies have been discounted and neither paper considers the energy losses associated with the natural gas liquefaction process, however, it may well be that this cold would otherwise be waste. It should be noted that (Kim et al., 2018) also mixes the natural gas with the discharged air stream from the LAES plant.

Burning natural gas in the discharge cycle is an interesting concept that is studied in other papers (Antonelli et al., 2017, Kim et al., 2018). Doing so provides benefits to both the LAES discharge cycle, in the form of an increased turbine inlet temperature, and to the gas turbine cycle, as the discharge air is compressed by a pump in its liquid state and the requirement for a gas compressor is negated entirely. Predicted round-trip efficiencies are typically in excess of 70%. Natural gas combustion allows the LAES plant greater flexibility in its power output during discharge. Burning natural gas is an interesting proposition as discharge air from an LAES plant will likely be higher in oxygen than atmospheric air due to preferential boil-off of nitrogen in the liquid air tank, improving combustion efficiency. Such a proposal must be treated with caution, however due to the safety concerns associated with oxygen-enriched combustion. The implications for the low-carbon credibility of the plant are obvious. However, as the natural gas is mixed with the discharge air following vaporisation in most cases, removing the natural gas supply at a later date is not out of the question. It is furthermore arguable that if natural gas is to be burnt somewhere in the world, it is best to do so as efficiently as possible.

A unique paper (Wu et al., 2020) discusses a thermochemical energy storage system coupled with an LAES plant. The paper asserts that the requirement for warm recycle significantly reduces the energy density of LAES. It explores synergies between thermochemical energy storage and LAES as a means to eliminate this. Thermochemical ESSs rely on two reversible chemical reactions; one endothermic:

$$\mathrm{Me}_x\mathrm{O}_y \rightarrow \mathrm{Me}_x\mathrm{O}_{y-1} + \frac{1}{2}\mathrm{O}_2 \qquad (2\text{-}10)$$

and one exothermic:

$$\mathrm{Me}_x\mathrm{O}_{y-1} + \frac{1}{2}\mathrm{O}_2 \rightarrow \mathrm{Me}_x\mathrm{O}_y \qquad (2\text{-}11)$$

Here, Me is taken to be a metal used in the oxidation reaction. The endothermic reaction allows the system to store heat for later release by the exothermic reaction. This energy is released in the form of heat and requires a power cycle, typically an air cycle, in order to generate electricity. The study notes that the energy required for compressing air is one a detriment to the round-trip efficiency of the system and posits that coupling such a system with an LAES/CAES presents opportunities to reduce the losses associated with compression. The paper performs process simulation of the overall plant. Overall, the engineering approach is detailed and rigorous, although it should be noted that its assumption that pressure drops are negligible is perhaps overly optimistic. The real bulk of the paper, however is in its financial modelling, which is discussed in section 2.5.3.

One paper highly relevant to this thesis (Li et al., 2014) provides a study into the use of LAES for load-shifting with NPPs. This models an LAES system that uses a simplified Claude cycle for liquefaction during charge and uses steam from an NPP to heat the air during discharge. The diversion of steam from the NPP is obviously detrimental to the NPP's power output and efficiency and is a core consideration of sections 5.2.1 and 5.2.3. This paper is a thorough and detailed engineering study, but some assumptions are arguably overly optimistic. Perhaps the most glaring of these is the use of air compressors approximated to an isothermal process with an isothermal efficiency of 90%. The isentropic efficiencies of turbines are also a little high. Finally, the steam is provided at 7 MPa by the NPP, approximately double the pressure of a standard PWR. The implications of these assumptions will now be discussed in turn.

A gas is compressed by reducing its volume, increasing both its pressure and its temperature. The best thermodynamic approximation of this process is that it is isentropic – both adiabatic and reversible. This means that no heat is transferred to or from the system, which is broadly accurate for an industrial compression process; when gases are compressed quickly, the heat is not able to diffuse quickly enough, and the temperature rises. In isothermal compression, the reduction of volume is performed sufficiently slowly to allow heat to dissipate, significantly reducing the required energy input. The implication of this is shown in Figure 2-7.

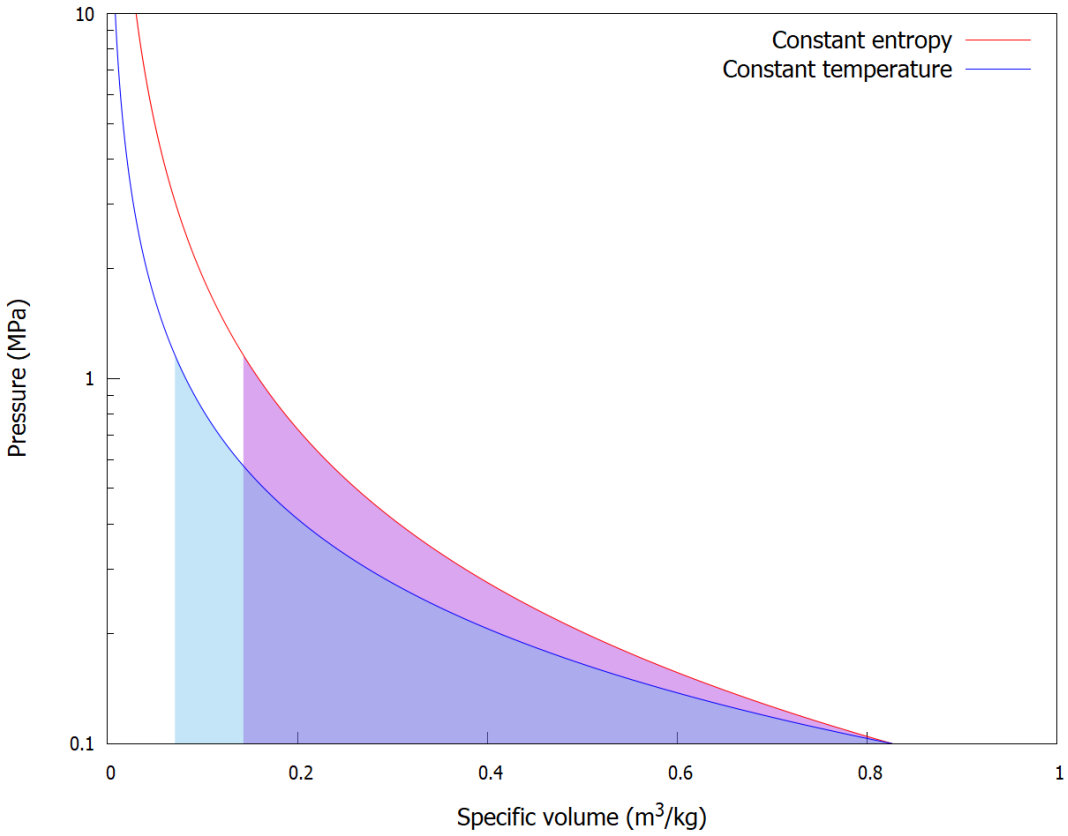

Figure 2-7: p-v diagram for air

Figure 2-7 is a p-v (pressure-specific volume) diagram showing a line of constant temperature in blue and a line of constant entropy in red. An ideal compression process would follow a path along the relevant line. In a p-v diagram, the work done by compression is proportional to the area under the curve, shown for compression from 101 kPa to 1159 kPa, as in the first compression process in (Li et al., 2014). The line of constant entropy has an area about 4% larger underneath it than the line of constant temperature, equating to a higher energy input requirement, even in ideal conditions. At first glance then, isothermal compression would seem to be reasonably similar to isentropic.

The exact effect of this can be quantified using the compressor model described in section 3.2.6. In (Li et al., 2014), incoming air is compressed twice. The details of these process are shown in Table 2-2, along with a comparison of the same processes modelled as isentropic with an isentropic efficiency of 90% (a little high but on par with other assumptions in the paper). The discrepancies in this table are significant; modelling the compression process as isentropic increases the power consumption by nearly 50%. Significant temperature increases are also evident. Clearly, simply modelling as isothermal is not sufficient to explain such discrepancies

in the modelling results. The exact modelling equations used in (Li et al., 2014) are not given, but assuming isothermal compression, the work done per unit mole could be calculated using:

$$W = RT \ln\left(\frac{p_2}{p_1}\right) \qquad (2\text{-}12)$$

where p_1 and p_2 are the inlet and outlet pressures, T is the operating temperature and R is the molar gas constant. This provides results that are very close to the paper under discussion and is presumably the equation that has been used to model compression. The compressor model detailed in section 3.2.6 disagrees with the compression powers in (Li et al., 2014) but produces results consistent with other literature reviewed.

Variable	**Stage 1 90% isothermal**	**Stage 2 90% isothermal**	**Stage 1 90% isentropic**	**Stage 2 90% isentropic**
Mass flow rate (kg/s)	150		150	
Inlet pressure (kPa)	101.3	1159.0	101.3	1159.0
Inlet temperature (K)	282		282	
Outlet pressure (kPa)	1159.0	13409.0	1159.0	13409.0
Outlet temperature (K)	288	288	592	596
Power consumption (MW)	40.03	39.83	57.93	57.91

Table 2-2: Comparison of compression processes from literature and this thesis

Some work has been done on the approximation of an isothermal compression process in a real-world compressor. (Teng et al., 2019) discusses a piston compressor whose compression chamber is partially filled with a liquid that is cooled via a heat exchanger loop and against which the gas is compressed. As the paper notes, this setup results in dissolution of the gas in the liquid in question, which is significant, even at the low pressures demonstrated and does reduce the efficiency gains. Despite the gas lost in this way, the work demonstrates an reduction of compression work of nearly 20% over a standard piston compressor. (Jia et al., 2018) describes an alternative piston compressor where water is injected during compression via a water spray to cool the air during compression. This again results in a significant reduction in the work done.

It should be noted that (Teng et al., 2019, Jia et al., 2018) rely on piston compression; these techniques are inappropriate for centrifugal compressors which must operate using dry air to prevent damage. Both piston compression techniques would humidify the resulting compressed air which would require drying prior to expansion in order to prevent damage to equipment (in the case of cryoturbine expansion) and the presence of ice in the expanded air. Both studies model and demonstrate peak pressures in the sub-megapascal range, an order of magnitude lower than that required for air liquefaction, and neither implies that the technology can be

scaled to higher pressures and industrial throughputs. Finally, the isothermal efficiency of the process is significantly less than 90% in both cases. The conclusion here must be that the assumption of being able to compress air at an isothermal efficiency of 90% made in (Li et al., 2014) is invalid.

As discussed above, (Li et al., 2014) uses isentropic efficiencies of 92% for turbines, slightly higher than the value of 85% used in the bulk of similar work. Whilst only a small difference, this still makes a non-negligible difference to the work output by the turbines. The paper also makes the assumption that steam is supplied by the NPP at approximately 7 MPa, rather than the 3.5 MPa peak pressure more typical of PWRs. The supply pressure of steam is important, as it affects the saturation temperature of water, which in turn affects the pinch point temperature in a heat exchanger. Using steam of a higher pressure means that it stays at a higher temperature during its phase change from vapour to liquid. This in turn increases the air temperature that it is possible to achieve following heat exchange and the inlet temperature of the turbines. Higher inlet temperatures result in improved power generation by the turbines for the same pressure ratio and hence the assumption of high steam pressures has the potential to result in overcalculation of the discharge power of the system.

The steam pressure delivered by the NPP is thus an important point. As mentioned, most PWR designs output steam at a pressure of around 3.5 MPa (NuScale Power LLC, 2018b, AREVA, 2013). This is not exclusively true, however; the AP-1000 outputs steam at a pressure of 5.7 MPa (Westinghouse Electric Company, 2011). BWRs (boiling water reactors) are capable of higher still steam outputs, with the ABWR (advanced boiling water reactor) operating at a pressure of 6.8 MPa (GE Nuclear Energy, 1997). The paper under discussion (Li et al., 2014) is explicit in stating that a PWR is used.

An LAES study from Italy (Antonelli et al., 2017) is an unusual one; it studies different configurations of the discharge side from an LAES using an Aspen HYSYS model but does not model the liquefaction cycle at all. Instead, it simply takes the specific energy of liquefaction to be 0.35 kWh/kg, significantly higher than other papers (Sciacovelli et al., 2017a). This is, however, a reasonable assumption, since the power cycles used do not appear to include a facility for cold recycle. The discharge cycles modelled include a baseline case where the discharge air is simply vaporised and expanded through turbines and additional cases all of which combust natural gas in the discharge air stream. Some of the cycles modelled also couple ORCs or cold Brayton cycles to capture and utilise additional waste heat from the process. This is an attractive proposition; the modelling, whilst somewhat superficial, uses reasonable turbomachinery efficiencies and achieves round-trip efficiencies in excess of 75%. The lack of

detailed engineering modelling, and the reliance on either natural gas combustion or on power cycles that have yet to be commercially proven means that this paper has little to contribute to this thesis.

One particular issue with many of the LAES papers is the use of cryoturbines for the final expansion before storage in the tank. Such a design is present in (Li et al., 2014, Guizzi et al., 2015, Sciacovelli et al., 2017b). The purpose of the final expansion is to partially liquefy the compressed and cooled air prior to separation of the liquid and vapour phases. In all of these papers, the air is over 80% liquid at the turbine outlet; such low vapour quality would certainly cause damage to the turbine. The Claude process shown in Figure 2-6 shows how turbines are typically used; air is drawn from the main stream and sent to the turbine before it is cooled sufficiently to cause liquefaction. This technique is similar to that used by Highview Power (Morgan et al., 2015b). The implications of using final stage cryoturbine expansion are non-trivial. Expansion is typically performed in a J-T valve, an insulated valve which approximates an adiabatic expansion process, keeping gas enthalpy constant. When expansion is performed in a cryoturbine, the process is closer to an isentropic process.

The difference is best visualised using a p-h (pressure-enthalpy) diagram, as shown in Figure 2-8. This shows the process of expanding air from 105 K and 15 MPa to atmospheric pressure. The red line shows air expanded in a J-T; the vertical line shows that enthalpy is fixed. The blue line shows cryoturbine expansion, showing a significant reduction in enthalpy. The reduction in enthalpy is due to the air's internal energy being removed by the turbine. The results of this are two-fold; the fluid leaves at a lower vapour quality than it would from a J-T valve (0.17 for the cryoturbine compared to 0.29 for a J-T valve), and the cryoturbine performs useful work. The use of a cryoturbine then represents an increased yield and a power saving, potentially producing misleading results.

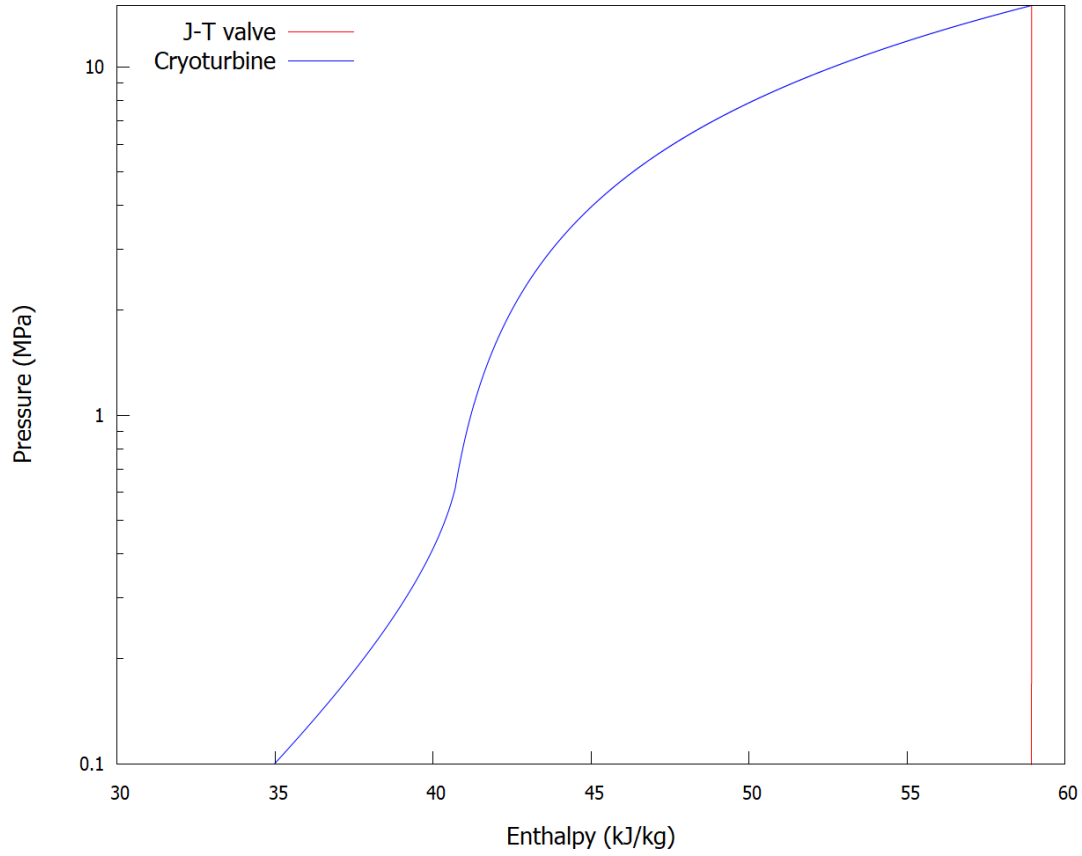

Figure 2-8: p-h diagram for two different expansion processes

Another potential issue with many studies is the use of liquid hydrocarbon cold stores. The cold store is a vital piece of equipment for LAES. As (Morgan et al., 2015b) states, limited cold recycle is part of the reason Highview Power's pilot plant's round-trip efficiency was so low. It is however, treated differently by the studies discussed herein. Whilst some studies (Sciacovelli et al., 2017b, Morgan et al., 2015b) model a cold store that uses a solid medium like a gravel bed, others (Guizzi et al., 2015, Li et al., 2014) use a liquid hydrocarbon cold store. These use heat exchangers to cool hydrocarbons with the discharged air, storing the cooled liquid in tanks ready to be used to cool the incoming air during the following charge cycle. In

(Guizzi et al., 2015, Li et al., 2014), two such loops are used; a low temperature loop containing propane and a high temperature loop containing methanol. The use of two liquids prevents phase changes and ensures that both fluids remain liquid throughout the cycle temperature ranges.

A hydrocarbon cold store has its advantages; where a solid media store's temperature will change over the course of a charge or discharge cycle, a hydrocarbon store's tank temperature will be continuous, mitigating a production rate drop-off towards the end of the charge cycle. On the other hand, there is a potentially serious safety issue. At atmospheric pressure, nitrogen liquefies at 77.4 K while oxygen liquefies at a higher temperature 90.2 K. This potentially leads to oxygen preferentially condensing on the outside of system pipework. If the hydrocarbons used in the cold store were to leak, this could create an extremely hazardous situation with a fire in an oxygen-rich environment. Whether or not this would be too much of a risk for regulators remains to be seen but hydrocarbon cold stores are a nascent technology, whereas solid media cold stores have been successfully demonstrated by Highview Power (Morgan et al., 2015b, Sciacovelli et al., 2017b, Sciacovelli et al., 2017a, Morgan, 2016). Pertinent to this discussion, one of these papers (Sciacovelli et al., 2017b) discusses a warm recycle where the heat of compression is stored when charging the system and utilised to heat the discharge air stream. The proposed system that uses a hot oil loop, however such a loop would be separate from exchange with fluids in the cryogenic temperature range and is perhaps of less concern.

(Tafone et al., 2019) provides an interesting study. Noting the complexity of the plant and of thermodynamic modelling, this paper uses existing gas turbine data to develop performance maps for different system configurations. These maps allow designers to determine the effect of modifying plant operating parameters, such as charging pressure or the quantity of cold or warm recycle, on overall plant performance. These maps, validated against actual data from the Highview power pilot plant, provide designers a shorthand means of evaluating the performance of an LAES system depending on their design choices.

Other papers (Antonelli et al., 2017, Tafone et al., 2018, She et al., 2017, Peng et al., 2018) suggest making use of ORCs (organic Rankine cycle) to capture additional energy from the discharge air stream. An ORC uses an organic working fluid with a saturation point lower than that of water, which allows it to make use of low-grade heat that would otherwise be wasted. LAES has a potentially useful synergy with such systems; many of the proposed working fluids have a boiling point below 0°C and thus the low temperature air of an LAES discharge cycle provides an effective heat sink for the ORC condenser. As (Tafone et al., 2018) notes, ORCs

remain in early stages of development and it remains to be proven whether they can be commercially competitive.

These papers provide a variety of potential system configurations, some more realistic than others. This study is intended to explore what can be done with operable processes and current technology. Highview Power and their literature (particularly (Morgan et al., 2015b, Morgan, 2016)), as well as the University of Birmingham group and theirs (Sciacovelli et al., 2017b, Sciacovelli et al., 2017a) provide the best basis with which to develop a realistic model of the liquefaction side of the plant. The plant configurations taken forward for further modelling are largely based on the pilot plant and grid scale plant designs discussed in (Morgan et al., 2015b, Sciacovelli et al., 2017b, Sciacovelli et al., 2017a) and are detailed in section 5.2. The availability of steam from the nuclear power plant provides opportunities to improve the power yield during discharge but requires significant modification of the Highview design, as discussed in section 5.2.6.

2.5.3. Financial studies

Cost analysis of LAES systems is not as readily available as that for engineering analyses, but there are still some papers available on the subject, particularly in recent years. (Morgan et al., 2015a) provides the earliest example of a cost analysis of a standalone system. It calculates equipment costs scaled from pieces of equipment of a known cost. This is an approach discussed in section 2.7 and one that would ultimately become part of the methodology of this thesis. The study concludes that the levelized cost of a mature LAES plant is comparable to that of PHES. It should be noted, however, that this study appears somewhat superficial when compared to more recent work, due to the fact that it does not simulate in-market plant performance and does not consider the influence of uncertainty on its cost analysis.

A paper co-authored by members of the University of Birmingham group (Xie et al., 2018) is associated with many of the engineering studies discussed in section 2.5.2. It provides a detailed assessment of the market viability of an LAES plant in the UK electricity market, focusing on revenues from two sources: electricity arbitrage and ancillary service payments from STOR services. The capital cost of the CES plant is estimated using Highview Power's cost estimator (Highview Power), which assesses cost based on three parameters; the storage and discharge rates, and the storage capacity. The use of this estimator is surprising; given the group's access to detailed engineering modelling, not performing a more detailed capital cost analysis seems like a missed opportunity.

The study (Xie et al., 2018) itself consists of a financial optimisation model with minimisation of system NPV as the objective of the optimisation algorithm. It uses a variety of metrics of economic performance including NPV, internal rate of return and payback period. Perhaps unusually, payback period is not based on discounted values, meaning it is unaffected by discount rate and may result in some misleading results. Electricity prices are simulated by resampling of the 2015 UK spot market prices. As sections 4.4.2 and 4.4.3 will show, this is not an overly optimistic approach; of the dataset used, represents a year of fairly low volatility in daily average electricity prices and an average year in terms of the price swing seen in daily profiles. Whilst the engineering analysis is not detailed, its assumptions are reasonable and presumably derived from the group's previous engineering-focused studies. The study does, however, assume that external heat is used as a by-product of another process and that it is obtained free of charge. This assumption is important and will be discussed again below.

The model assumes two revenue streams; one from electricity price arbitrage and one from the provision of STOR services to the UK grid. It speculates that additional revenue might be possible from frequency response services, but concedes that the very short response time required would necessitate additional equipment and increase plant capital cost. With regard to STOR, the paper notes that LAES can both absorb and supply energy to such a service and that whilst this requires a larger tank storage capacity, this does not greatly affect the capital cost of the plant.

The model itself assumes that the plant receives both standby payments for provision of STOR services and payments for whenever this service is utilised by the grid. The utilisation from day to day is triggered by a probability distribution. Only a portion of the plant's capacity is contracted for STOR services and the model ensures that there is always sufficient air stored to meet this demand by charging the system, where required, whenever there is an impending contracted period. The study's conclusions are arguably unfavourable of provision of this service. Whilst prices for this service are well in excess of electricity prices for the resampled dataset, only 12.5% of the contracted STOR volume is actually utilised. The study also notes that STOR services windows typically coincide with periods where the electricity price peaks. This limits opportunities for arbitrage where the system receives a call for STOR services at inopportune moments. Despite these issues, however, the study asserts that NPV results for plants that provide the STOR service are always preferable to plants which operate on an arbitrage-only means of revenue generation. Aside from this, the study shows that plant discharge capacities of 100 MW or greater are required for positive NPVs.

There is, however, one potential issue with this study. That is the assumption that waste heat is provided free of charge. The temperature of this waste heat is an input parameter for the model and ranges from 50 to 250°C. At the upper end, these temperatures are well above the boiling point of water and are arguably in the range where revenue-generating services, such as district heating, are possible. These temperatures are not out of the realms of possibility for free waste heat (PWR secondary loops operate at temperatures of around 300°C, these being on the low end of steam power cycle peak temperatures) but at the higher end could arguably be revenue-generating. The study predicts a threshold temperature 150°C for waste heat as being sufficient for positive system NPV. In short, whether a plant would be able to attain heat at the required temperature and at the required rate is an assertion that requires more justification than that given in the study.

The Birmingham University group (Kim et al., 2018) also performed a financial study, this time based on the results of their engineering study of both CAES and LAES systems discussed in section 2.5.2. This study features one of the more detailed analyses discussed in this section, where plant capital investment is directly calculated by sizing system components. Their financial modelling is a LCOE analysis which is essentially a life-cycle cost calculation of the per MWh cost of producing electricity based primarily on the plant capital cost, the system energy performance, and the cost of electricity used to charge the system. Overall, this is a detailed and valuable study and one that has somewhat damning conclusions for both technologies with high LCOE values of $125/MWh or greater. Combined with the assumption that the electricity to charge the system is purchased for $30/MWh, the study demonstrates that either a significant price swing is required of the system or that some form of external subsidy would be required to ensure profitability. (Wu et al., 2020) presents a similar LCOE analysis of an LAES system, this time coupled with a thermochemical ESS. Once again, this is a techno-economic analysis whose engineering study is discussed in section 2.5.2.

(Tafone et al., 2020) uses the parametric performance maps developed in (Tafone et al., 2019) in a financial model to determine the LCOS (levelized cost of storage) of a LAES plant. This is a relatively new metric that is, broadly, calculated by the discounted system cost divided by the discounted quantity of electricity generated over the lifetime of the plant. This is a valuable piece of information to have; it essentially represents the average price that electricity must be sold at for the plant to break even. The study determines a LCOS of €385/MWh; an extremely high electricity price compared to the UK's electricity spot market prices over the period from 2008 to 2015 (Smith and Halliday, 2016). The authors argue that this is within the realms of economic viability whilst conceding that it is reliant on opportune pricing. Despite this perhaps optimistic conclusion, the paper does represent a novel study of a nascent metric for examining

energy storage systems, although it does not attempt to model the day-to-day operation of the plant.

By contrast, (Lin et al., 2019) seeks to directly model the day-to-day operation of an LAES plant. Using Highview Power's cost estimation, and the UK electricity prices for 2015, the study aims to simulate how a plant would operate in the real world, depending on plant capacity. The model keeps a track of the amount of air stored and uses electricity prices (either past or future from the model's perspective) to set thresholds for when to charge or discharge the LAES system. Three different operating scenarios were tested: two where both past and future prices were used to set thresholds, and one where thresholds were set only by past prices. The study concludes that larger discharge power output plants perform better selling into the spot market, but that some sort of external waste heat is required for the plant to be profitable. This paper presents an ambitious modelling strategy that uses resampled electricity price data to determine the economic viability of an LAES plant and its conclusions are significantly less damning than those in (Tafone et al., 2020).

2.6. Engineering modelling

The core of the project that this thesis discusses is an engineering process simulation model. Given the time constraints of a PhD project and the availability of engineering software packages, the chosen path for the construction of this model is to use modelling software, rather than to code the model from scratch. At its most fundamental level, this software comprises a means to define sets of known parameters, unknown variables, and the sets of simultaneous equations that govern them, along with a means to solve those equations and calculate the unknowns. There are several options for process modelling software, some of which are detailed below.

MATLAB (MathWorks) is a multipurpose environment that facilitates data analysis and model creation. It is ubiquitous in both academia and industry for good reason; it offers a highly flexible numerical computing environment with the ability to call on functions written in other programming languages. It allows the development of proprietary simulations run within the MATLAB solver, as used in (Li et al., 2014). Additional packages, such as Simulink (MathWorks) assist with modelling engineering systems by allowing the construction of models in a modular sense and provide some pre-built models of process system components.

Aspen HYSYS (aspentech) is a process simulator geared primarily towards chemical engineering and focuses on the optimisation of engineering processes. It has been used in a

number of the papers discussed in section 2.5.2 (Antonelli et al., 2017, Morgan et al., 2015b). The broader family of Aspen software products (aspentech) offers packages for the optimisation of everything from top-level process design to detailed analysis of individual chemical processes or heat exchanger design. These software packages allow construction of models from a diverse set of prebuilt components. Whilst this software is expensive, the availability of prebuilt components is advantageous in that it dramatically reduces the work required for systems modelling. There are, however, two major drawbacks. Firstly, these components are something of a black box; there is little user control over the equations that govern the relationship between input parameters and outputs. Secondly, the software is proprietary, and any independent verification of results requires access to the Aspen software.

EES (F-Chart Software) is an equation-solving program that shares some similarities with MATLAB's solver. As discussed in section 2.5.2, the University of Birmingham group used this as their process modelling environment (Sciacovelli et al., 2017b, Sciacovelli et al., 2017a). It allows the definition and soloution of large arrays of equations and is entirely user-programmable, offering a distinct advantage over the Aspen family of programs. EES's solver allows the input of equations in any order and unlike MATLAB does not rely on user-defined algorithmic solving of complex systems.

Dymola (Dassault Systemes) is a simulation environment software package that is based on the open-source Modelica language (Mattsson and Elmqvist, 1997). Its use of Modelica makes it extremely versatile; Dymola is able to use the diverse open-source libraries of Modelica whilst allowing commercial entities to develop proprietary code that can be run within the simulation program. Dymola allows proprietary code to be protected and in this way straddles the gap between the transparency of MATLAB and the black box nature of Aspen.

Modelica itself is a modelling language. Unlike programming languages such as C++, Modelica code must be translated and executed within an external simulation environment. Like EES, Modelica code need not be algorithmic; the equations can be supplied to the environment in any order and supported simulation environments are required to be able to parse, rearrange and solve equations written in Modelica to produce results. There are many programs that implement Modelica; some, such as Dymola, are commercial whereas others, such as OpenModelica (Open Source Modelica Consortium), are entirely open-source. Modelica has a large userbase and an online community that continues to actively develop and publish a diverse set of open-source libraries.

The list of software packages summarised in this section is by no means exhaustive but does represent a good cross section of the options available. The programs discussed cover a spectrum from the work-intensive, but highly flexible MATLAB, to the prebuilt models Aspen. Software like Dymola and EES operate somewhere between these extremes, offering the powerful preprogramed solving abilities of Aspen but retaining the coding flexibility and transparency of MATLAB.

The requirements for the engineering model discussed in this project are reasonably simple. The model needs to be capable of both steady-state and dynamic process modelling. The latter is important; the cold store part of LAES in particular is a dynamic system whose properties change over the course of a simulation. The model also needs to be able to treat heat exchange in sufficient detail to allow phase changes to be modelled. This is particularly important for the NPP secondary loop and the liquefaction cycle modelling, both of which feature fluid phase changes. For its ability to facilitate the modelling of these aspects, as well as its open-source and transparent nature, Dymola was selected as the software package to be used in this project. Not only does this allow independent verification and follow-up of this work by others, it also allows development of a niche library of components for modelling liquefaction systems that may be of use to the wider Modelica community.

At the time this project was being developed, Modelica had not been used directly to simulate air liquefaction processes. That being said, many of the tools required had already been coded. The ThermoPower library (Casella and Leva, 2009, Casella and Leva, 2003) is a library that was developed for the modelling of thermodynamic systems within Modelica. It includes a variety of component models including fluid flows, heat exchangers and turbomachinery. The ExternalMedia library (Casella and Richter, Casella and Richter, 2008) provides a means of incorporating external code for calculation of thermophysical properties into a model.

The calculation of thermophysical fluid properties is an important part of any process model. In Modelica, thermophysical properties can be defined in two ways; either using a medium package within a Modelica library or looking up properties externally via the ExternalMedia library. The Modelica standard library contains two dry air models, however the lowest operating temperature of these is 200 K; not low enough to calculate properties in the liquid phase. The ExternalMedia library allows integration of a multitude of external thermophysical property codes. In the spirit of the transparent nature of this work, the open-source library CoolProp (Bell et al., 2014) was selected for integration. Its implementation is discussed in section 3.1.3.

One major limitation of the use of ExternalMedia is its treatment of multi-component fluid mixtures. At the time of writing, the library is incapable of implementing fluid models that constitute more than one component. Fortunately, CoolProp includes a pseudo-pure fluid model of air that treats air as a single fluid. For this reason, the return flow from the air liquefier must be treated with some caution. Many of the liquefaction cycles discussed in section 2.5 blend the return vapour stream with make-up air from the atmosphere following the expansion and separation process in the liquefier. This stream will be nitrogen-rich and will change the properties of the resulting air mixture at cryogenic temperatures by reducing its saturation temperature; essentially making it more difficult to liquefy. It is important that, in this model, this stream not be mixed with make-up air before being returned the liquefaction cycle and instead be exhausted to the atmosphere.

Definition of parameters is a central part of the engineering modelling process. NPP fluid flow and thermodynamic properties can be sourced directly from the system designers; regulatory application documents are particularly useful for this purpose. Heat exchange parameters, particularly heat transfer coefficients are more difficult, especially with the relatively diverse set of fluids and operating pressures that will be used in the engineering model. The standard approach to heat exchanger design is the use of so-called U-values as heat transfer coefficients. ESDU (formerly Engineering Sciences Data Unit) (IHS Markit, 2019) provides standards documents containing U-values for heat exchanger design, however access to this data was not available to this project. (Couper, 2012, Kuppan, 2013, Smith, 2005) provide a detailed list of heat transfer coefficient ranges for a variety of heat exchanger designs and working fluids. Given the resolution required by the model, and the lack of access to EDSU datasets, the decision was made to use these ranges in the final engineering model. The ensure the model would be conservative, the low end of the heat transfer ranges would be used resulting in a tendency for the model to overestimate heat exchanger size and thus cost.

2.7. Financial modelling

An early decision in this project was made to perform any financial modelling with some consideration of uncertainty. The fundamental requirements of such an analysis are an ability to define probability distributions, use these to predict model input parameters for successive iterations of the simulation, and to capture and collate the output variables. As with engineering modelling discussed in section 2.6, there are a variety of software packages and programming languages that are available for this purpose.

R (The R Foundation) is an open-source programming language that includes data analysis and modelling tools that would be ideal for financial modelling in the face of uncertainty. It offers tools for both probability distribution and time series fitting, both of which would prove vital to the model described in 0. The fact that it is a second programming language which was entirely unknown to this author prior to this project presents a significant issue, however. It was felt that learning a second language in addition to Modelica would be impossible within the time constraints of this project.

Microsoft Excel (Microsoft) is a spreadsheet program that is used within multiple industries for a variety of purposes. Its vast array of formulae and powerful macro automation means it is potentially a powerful financial modelling tool in its own right. Whilst Excel's RNG (random number generator) function would allow a means of predicting values from probability distributions, and is formulae would allow a means of defining the distributions themselves, Excel has no in-built means to capture results from multiple iterations of the same simulation and would require significant automation with VBA (Visual Basic for Applications) in order to facilitate this. This presents the same issue as R in that learning a second programming language in addition to Modelica would simply be too time consuming for this project.

Several plug-ins for Excel are designed specifically to perform financial modelling in the face of uncertainty. Of these, XLSim (Analycorp) and @RISK (Palisade) were considered for this project. The two are broadly similar in terms of their functionality; both offer an array of probability distributions, time series, data fitting algorithms and both automatically capture and collate simulation data and results. Both are implementations of VBA within Excel. An important difference lies in the probability distributions offered. @RISK offers some additional distributions, most notably PERT (project evaluation and review technique), which is used extensively in this project for the reasons discussed in 0. Another difference is @RISK's implementation of copulas, powerful tools that allow the definition of correlations between input probability distributions, something that would also prove to be important to the financial model in this project. As a result, @RISK was the software chosen for this project.

Financial modelling in the face of uncertainty requires a means of defining model probability distribution or time series parameters. Some parameters can be defined by distribution fitting. Given a sufficiently large dataset, distributions or time series can be defined according to the fitting algorithms offered in @RISK. This thesis had the benefit of access to a detailed historical dataset of UK electricity prices for the years 2008 to 2015 (Smith and Halliday, 2016), which facilitated the definition of the electricity price model parameters as discussed in detail in section 4.4. Other parameters, such as NPP cost or construction time, are much harder to

accurately define given the lack of a large historical dataset, the largely opaque nature of commercial costs of recently constructed plants and considerable contention over the actual cost of new nuclear plants (Kessides, 2010). In defining these parameters, then, a degree of user judgment is required. The approach to defining such parameters is discussed in section 4.2. The risk of error associated with such an approach can be reduced by a combination of testing different scenarios and sensitivity testing of the final result.

Some parameters can be defined based on detailed engineering analyses. An engineering process model can be used to estimate sizes of system components, allowing estimation of capital cost for those components and in turn an estimation of capital cost for the plant as a whole. A team at WPI (Worcester Polytechnic Institute) used such an approach to publish a number of papers on the economic performance of IGCC (integrated gasification combined cycle) plants in the US electricity market (Koc et al., 2012, Koc et al., 2013). The first of these papers (Koc et al., 2012) discusses a performance assessment of an IGCC plant and its use in estimating the asset cost of key components. The paper details the estimation of these components from differently-sized but similar components of known cost using the six-tenths rule (Peters et al., 1968):

$$C(A) = C(B)\left(\frac{S(A)}{S(B)}\right)^{0.6} \qquad (2\text{-}13)$$

where $C(A)$ is the unknown cost of piece of equipment A, $C(B)$ is the known cost of piece of equipment B, and $S(A)$ and $S(B)$ are the sizes of pieces of equipment A and B respectively. A slightly more detailed estimation can be obtained using the alternative formula (Peters et al., 1968):

$$C(A) = C(B)\left(\frac{S(A)}{S(B)}\right)^{X} \qquad (2\text{-}14)$$

This is very similar to equation (2-13) but includes the term X, a cost exponent specific to the given type of equipment, and in a plant with a variety of system components can provide a more accurate assessment of system components.

Given the investment costs of the key pieces of equipment, the WPI team (Koc et al., 2012) used the process described in (Peters et al., 1968) to estimate the overall plant capital investment. An Excel model with XLSim was then used to determine the NPV of the plant in question via a DCF (discounted cash flow) analysis in the presence of uncertainty. Uncertain

model inputs were defined using a combination of triangular probability distributions (defined using minimum, most likely, and maximum values) and resampling of historical data, where sufficient data was available. Revenue is assessed based on electricity price sales given the values of electricity price and plant capacity factor calculated via the defined probability distributions for each simulation iteration. Whilst not explicitly stated in the paper, the model seems to assume an equal capacity factor for each year of the simulation. This is not necessarily the case, particularly as the plant in question contains a reactor whose catalyst bed must be periodically replaced, potentially leading to significant variability in plant capacity factor from one year to the next. Such variation has an impact on NPV, given the importance of time-dependent value of revenue in DCF analyses. Despite this, however, the analysis in the paper provides a detailed and insightful account of the relative risk of plant investment given a detailed engineering analysis with which to estimate cost.

An interesting part of (Koc et al., 2012) is its consideration of the effect an accident at the plant on system NPV. The chance of an accident occurring in any given model year is defined by probability distribution and the cost of an accident incorporated into the NPV calculation. The relative risk of investment, or reduction thereof, in preventative safety measures is assessed as part of the study. A follow-up paper (Koc et al., 2013) provides a more detailed study of investment in preventative safety measures by assessing competing options for safety systems. Ultimately, the cost and likelihood of accidents, especially in nuclear plants, has historically been very difficult to quantify and the decision was made to omit consideration of accidents from the modelling in this project.

A cornerstone of the financial modelling process will be the estimation of plant cost. (Peters et al., 1968) describes a methodology for doing so by first estimating the costs of key pieces of equipment using equation (2-13), then by using a series of factors to estimate the overall plant cost. The factors are detailed in section 4.3.2. In addition to estimating equipment costs from equipment, it is also important to be able to adjust historical costs to present-day equivalents. This is done using the CEPCI (Chemical Engineering Plant Cost Index) in the following formula:

$$C(Y_1) = C(Y_2)\left(\frac{I(Y_1)}{I(Y_2)}\right) \qquad (2\text{-}15)$$

where $C(Y_1)$ and $C(Y_2)$ are the costs of a given piece of equipment in years Y_1 and Y_2 respectively and $I(Y_1)$ and $I(Y_2)$ are the indexes for those years. The values of CEPCI are published by the magazine Chemical Engineering and indices from the years 1990 to 2018 were used in this study (Jenkins, 2018, 2015, 2010, 2008). These are shown in Figure 2-9.

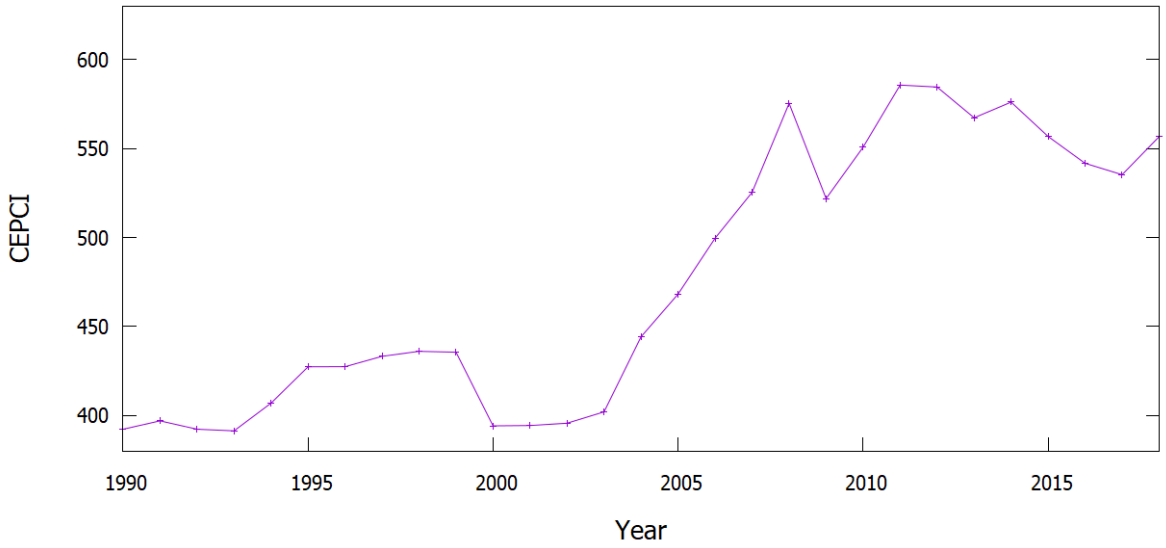

Figure 2-9: Values of CEPCI for 1990-2018

The use of equation (2-13) is reliant on scaling costs for pieces of equipment of known size but unknown cost from pieces of equipment of a known size and cost. It is then paramount that these base costs be as accurate as possible. Whilst (Peters et al., 1968) provides base costs for many of the required pieces of equipment, the original text is some six decades old at the time of writing and even the most recent edition contains costs that are nearly 30 years old. Alternative base costs to use for estimation were thus sought from literature and used where they were available.

Compressors and turbines are vital components for the charge and discharge cycles of LAES plants. (Couper, 2012) provides formulae for estimating the cost of both in 2009 US$ prices. Here, compressor costs are estimated using:

$$C_{\mathrm{COMP}} = 7{,}022\left(\frac{\dot{W}}{0.746}\right)^{0.62} \qquad (2\text{-}16)$$

where $\dot{W}$ is the rated power of the compressor in kW and the formula from the literature has been converted to 2018 GB£. Similarly, turbine costs are estimated using:

$$C_{\mathrm{TURB}} = 978\left(\frac{\dot{W}}{0.746}\right)^{0.81} \quad (2\text{-}17)$$

where $\dot{W}$ is the rated power of the turbine in kW and the formula has once again been converted to GB£. Cryoturbines are as having the same cost, in line with (Wu et al., 2020).

(Wu et al., 2020) provides an equation for estimating the cost of cryogenic pumps:

$$C_{\mathrm{PUMP}} = 0.483\,\dot{W} \quad (2\text{-}18)$$

where $\dot{W}$ is the rated power of the pump in kW.

The industry standard method for estimating heat exchanger cost is the use of C-values (Hewitt and Pugh, 2007), which calculate heat exchanger cost as a function of its type and surface area (or volume in the case of multi-stream exchangers). As with heat transfer coefficients, ESDU (IHS Markit, 2019) provides lists of C-values for this purpose, however this data was not available to this project. Other literature (Smith, 2005, Couper, 2012) provides means of estimating heat exchanger costs that are more detailed than the aforementioned textbook estimates (Peters et al., 1968), and provides examples that are more up to date. This literature (Couper, 2012, Smith, 2005) highlights the importance of consideration of operating pressure, material selection and heat exchanger type on capital cost. One (Smith, 2005), however, is reliant on cost law coefficients which are specific to heat exchanger design but not provided in the text. An alternative study (Wu et al., 2020) provides an equation for calculating heat exchanger capital costs , derived from the aforementioned (Smith, 2005). Converted to 2018 GB£ prices, this is:

$$C_{\mathrm{HX}} = 32{,}500\left(\frac{A}{80}\right)^{0.68} \quad (2\text{-}19)$$

where A is the heat exchanger area in m^2. This equation does not account for differences in cost associated with increasing pressure ratings of heat exchangers and assumes a parity in cost between heat exchangers of the same size regardless of their pressure rating. Since the LAES system in particular has multiple pressure stages each with separate heat exchange, the decision was made to use the data provided by (Peters et al., 1968) to calculate heat exchanger costs. This yielded five equations for different pressure ratings between 2 and 20 MPa in 2018 GB£ prices:

$$C_{\text{HX, 2 MPa}} = 151{,}879\left(\frac{A}{140}\right)^{0.44} \quad (2\text{-}20)$$

$$C_{\text{HX, 3 MPa}} = 190{,}203\left(\frac{A}{140}\right)^{0.44} \quad (2\text{-}21)$$

$$C_{\text{HX, 7 MPa}} = 227{,}109\left(\frac{A}{140}\right)^{0.44} \quad (2\text{-}22)$$

$$C_{\text{HX, 10 MPa}} = 287{,}434\left(\frac{A}{140}\right)^{0.44} \quad (2\text{-}23)$$

$$C_{\text{HX, 20 MPa}} = 359{,}399\left(\frac{A}{140}\right)^{0.44} \quad (2\text{-}24)$$

As Figure 2-10 shows, despite their smaller exponent, equations (2-20) to (2-24) provide significantly higher cost estimates than equation (2-19). Despite the discrepancy, it was deemed sufficiently important that cost differences between heat exchange units of different pressure ratings be properly captured to allow the model to err on the side of caution in this way. This also ensures that the model estimates cost conservatively.

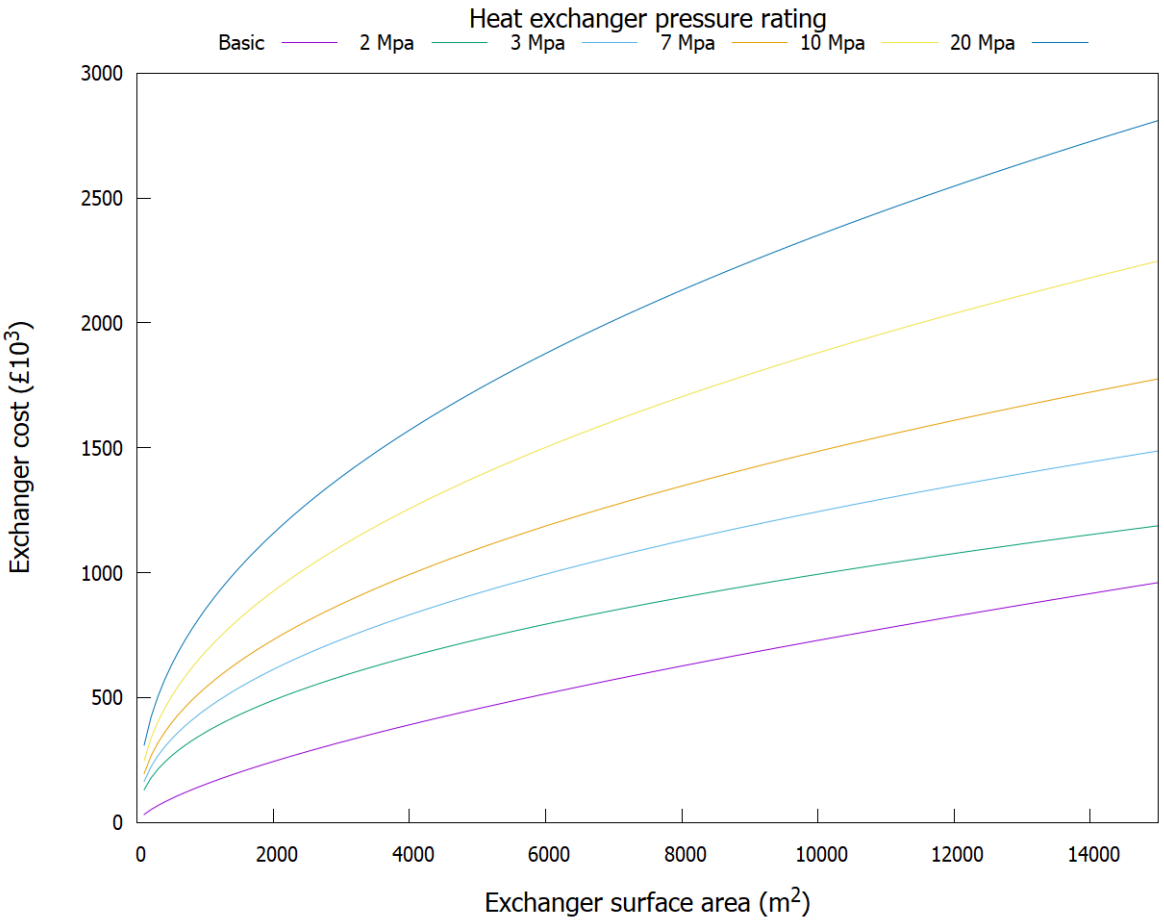

Figure 2-10: Heat exchanger cost model comparison

Storage vessels are also an important piece of equipment for this study. The storage tank for cryogenic air is ubiquitous to all LAES designs. It is, however, a complicated piece of equipment to assess the cost of, because there is limited cost data against which to assess the various cost models available in the literature.

(Peters et al., 1968) provides a starting point with which to assess storage tank costs. Assuming, for the moment, a stainless-steel tank, the cost can be obtained in 2018 GB£ prices using:

$$C_{\mathrm{TANK}} = 118{,}500\left(\frac{V}{450}\right)^{0.57} \qquad (2\text{-}25)$$

where V is the volume of the tank in m^3.

It is important to note, however that storage of cryogens requires more than simply a tank. Due to environmental heating, it is important that the tank be properly insulated. For industrial cryogenic gas plants, this means using a vacuum walled storage tank (Kerry, 2007), so the actual cost can reasonably be expected to be significantly higher than that given by equation (2-25).

(Hu et al., 2013) provides a base cost of US$ 800,000 for a 2,500 m^3 liquid oxygen storage tank in 2013 US$. With this base cost as a reference, and using the same cost exponent as equation (2-25), the cost can be obtained in 2018 GB£ using:

$$C_{\mathrm{TANK}} = 654{,}210\left(\frac{V}{2{,}500}\right)^{0.57} \qquad (2\text{-}26)$$

where V is the volume of the tank in m^3.

An alternative relation is proposed by (Wu et al., 2020). This linear relationship is based on the same base cost given in (Hu et al., 2013) and is given by:

$$C_{\mathrm{TANK}} = 262V \qquad (2\text{-}27)$$

where V is the volume of the tank in m^3.

Clearly, these two relationships are bound to differ significantly in their prediction of cost. It would be useful to compare these to actual cost data from real-world pieces of equipment to assess the relative merits of the two relationships. Whilst costs for different sizes of cryogenic tank were sparse in the literature reviewed, (Shi, 2012) provides actual cost data for LNG storage tanks against which these relationships might be compared. It is important to first assess the merits of such a comparison. Liquefied air and natural gas are both stored at or around atmospheric pressure. Their storage temperatures differ significantly though; LNG's saturation temperature at 101 kPa is 111.15 K whilst nitrogen's is 77.3 K at the same pressure. This means that the difference between the temperatures of the tank's contents and the environment, and hence the amount of insulation required, will be greater for storing air than for storing LNG. It is reasonable, then to expect that the costs for an air storage tank will be higher than for an LNG storage tank.

At this stage, it is also important to point out that an upper limit for storage tank size will be required. This project chooses to focus on systems that can be delivered with off-the-shelf system components. Searches for LNG storage tank manufacturers, for example (Chart Industries, 2018, Corban Energy Group, 2018) , suggest an upper limit of around 1,500 m^3 for manufactured tanks. Whilst larger tanks ranging into the hundreds of thousands of m^3 are possible (Corban Energy Group, 2018, Osaka Gas, 2017), these are specialist products built on-site. Furthermore, assuming a storage temperature of 77 K at 101 kPa, and a specific energy of liquefaction of 0.3 kWh/kg (towards the upper limit for the papers discussed in section 2.5.2), a tank size of 1,500 m^3 is sufficient to store approximately 400 MWh of electricity. A few such

tanks could thus provide storage in the gigawatt range and are thus sufficient for an LAES plant of those envisaged by the literature.

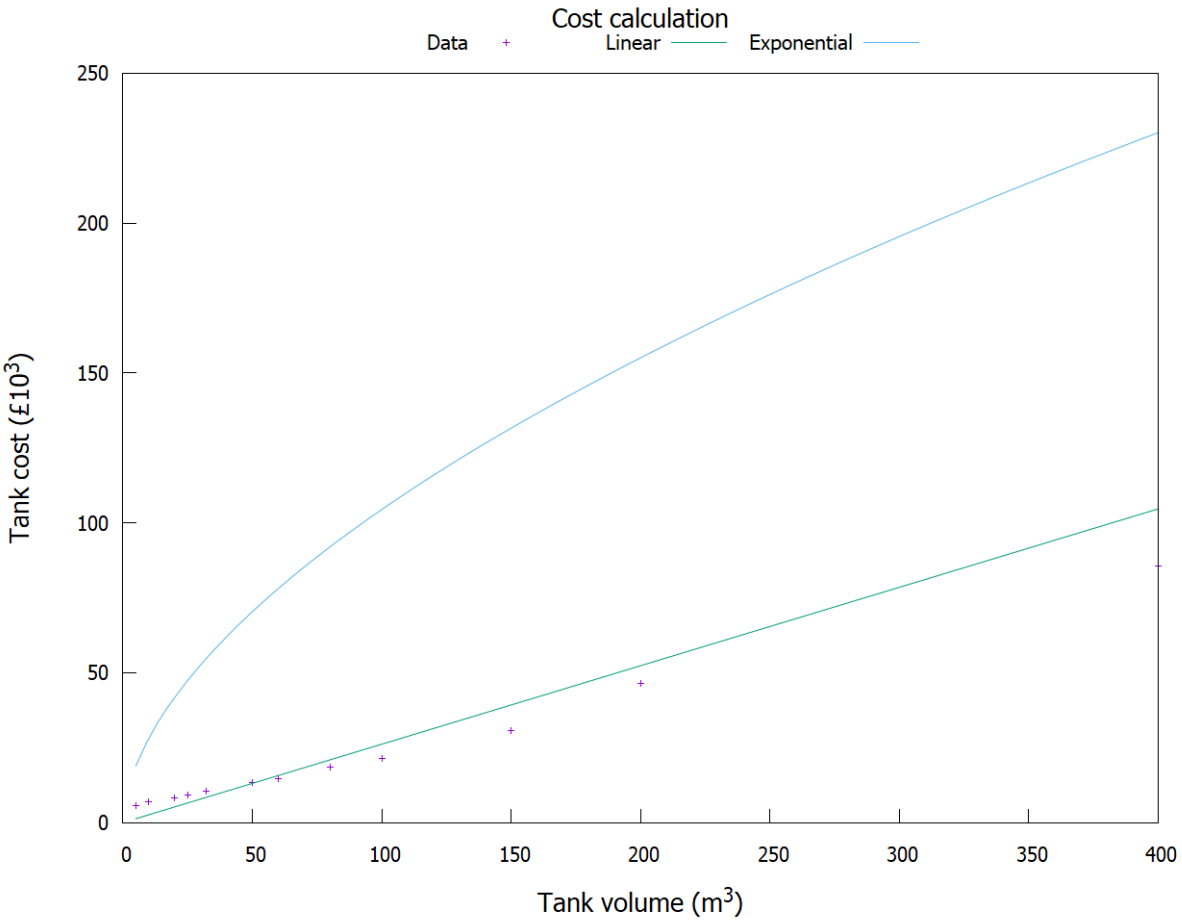

Figure 2-11: Storage tank cost estimation comparison with real-world data for LNG storage tanks

Figure 2-11 shows the comparison between the two cost estimation models equations (2-26) and (2-27) and the real-world data from (Shi, 2012). Clearly, the exponential cost model in equation (2-26) provides the highest cost estimation up to a tank volume of 2,500 m^3, where the exponential and linear equations intersect (as a result of both being based on the same base cost). From the real-world data, it would appear that both cost estimation models provide a higher liquid air tank cost than for an equivalent size of LNG tank, however the exponential model estimates costs well over double, whereas the linear model estimates costs at around 20% over the real-world data at tank sizes of 100 m^3 or above. Ultimately, the decision was taken to use the exponential model to once again ensure the model errs on the side of caution. The maximum tank size will be taken as 1,500 m^3, in line with the concept of taking all equipment off-the-shelf.

The values used for equation (2-14), the associated exponents, the CEPCI indices used and the equations used for the estimation of plant costs are listed in section 4.3.

2.8. Interim remarks

The discussions of section 2.5 of the literature review highlight that there is a significant body of work on LAES, both from an engineering perspective, and to a lesser extent, from an economic perspective. Nevertheless, there are some niches which have not been studied in the available literature, and the question of whether LAES plants can be successfully coupled with nuclear plants to allow them to fulfil a load following capacity remains almost entirely absent from the body of study on the subject. This is an interesting question in and of itself and represents a significant part of the focus of this thesis.

The core of this thesis, however, aims to answer a far broader, and potentially more practically valuable question. That is, whether engineering and financial modelling can be combined in such a way that an engineering system for energy storage can be optimised from a market-led perspective. This thesis will discuss the development of a modelling and methodological approach that will attempt to achieve exactly that. This, whilst applied specifically to the problem of a couple LAES and NPP design, has potentially far broader reaching applications.

The nature of many of the ESSs described in the literature means that they are asymmetrical, in that their charge and discharge power ratings are largely independent of one another. This is especially true of LAES. This presents a significant opportunity in that the power ratings of such systems might be tailored for the given market in which they are to operate. However, the effect of such engineering design is not trivial and, as 0 will discuss, has a significant impact on a system's cost. It is then not difficult to imagine a trade-off between optimising a system from an engineering design perspective for its chosen market and maximising its economic performance. This is an important consideration and one that is not explored in studies that perform either economic or engineering analyses in isolation. Indeed, there remain significant gaps in literature that attempts to combine the two approaches that are discussed in the following paragraphs.

Detailed cost and financial performance analyses are a feature lacking from the studies discussed in section 2.5.3. Despite many of those authors having an association with detailed engineering studies, many use Highview Power's cost estimator rather than directly estimating plant costs from engineering model data. Of the studies cited, there are only two exceptions to this (Kim et al., 2018, Wu et al., 2020), and not one of the works cited seek to directly simulate

the electricity spot market and its effect on the profitability, or otherwise, of the systems presented.

The detailed simulation of the electricity market is also a potentially important feature absent from the literature discussed. Studies that consider electricity prices tend to use a method known as resampling (Koc et al., 2012, Koc et al., 2013, Xie et al., 2018). This involves the use of historical electricity price data as a means of simulating the electricity price market. One major disadvantage of such a method is that it assumes that the past will accurately represent the future. As the discussions in section 4.4 will show, this is very rarely the case with electricity prices, which tend to exhibit significant variation in their patterns from one year to the next.

An alternative approach is the use of time series which are used to simulate stochastic data such a stock prices and have even been used in the simulation of electricity prices (Weron, 2014). Time series significant advantages over data resampling. Their parameters can be user-defined. This means that different hypothetical electricity markets can be simulated and the economic performance of system designs within them considered. Their parameters can also set by fitting them to existing data, which provides significant insight into how different market characteristics should be simulated. Such an approach is a middle ground between the fixed series provided by resampling and the more subjective simulated series provided by user-defined time series. Electricity market simulation by time series is an approach entirely absent from the literature on ESSs economic performance discussed in this thesis.

It is worth restating the thesis objectives from section 1.4 at this point and discussing which gaps in the literature they fill. As discussed in the previous paragraphs, detailed cost analyses of a variety of engineering configurations for LAES plants are absent from the majority of the literature with many authors preferring to utilise Highview Power's cost estimator for LAES designs. The sole study on a coupled LAES and NPP design (Li et al., 2014) is also mentioned as having significant shortcomings and a more detailed engineering analysis would provide a valuable contribution to the field. The completion of the following objectives will seek to fill these knowledge gaps:

- Develop an engineering model and library of components in the Modelica language for plant process modelling of the combined NPP and LAES system.
- Use the engineering model to determine operating parameters for a range of proposed plant configurations.
- Size components for the given plant configurations and use these to evaluate asset costs for the LAES plant.

Financial modelling of ESSs and of LAES plants in particular has often relied on deterministic modelling and resampling of electricity price data. In doing so, the conclusions regarding relative risk of differing plant configurations in uncertain conditions are impossible to make. The following objectives contribute to developing a methodology for economic analyses of such systems in the face of uncertainty, and applying it to the proposed hybrid plant:

- Develop a financial model for determining relative economic performance of the plant designs in the face of uncertain market conditions using Excel and the Palisade @RISK plugin.
- Use the financial model to determine the relative economic performance and investment risk of the plant design outputs from the engineering model.

The engineering and financial modelling approaches are discussed in Chapter 3 and 0 respectively. The simulation of a combined LAES and NPP system is discussed in Chapter 5 and the market-led design of said system is the subject of Chapter 6.

Chapter 3 - Engineering Modelling

3.1. Introduction

This chapter details the engineering model. Section 3.1.1 discusses the intended objectives of the model and 3.1.2 summarises the way Modelica code is implemented. This serves as a primer to section 3.2, which discusses the component models in depth. Chapter 5 details how the components were used to model the LAES system and the results obtained. Several of the component models have been written specifically for this study but are compatible with other user libraries based on the Modelica language and may be of use to the wider community. The model library is available via Open Research Data Online (Wilson, 2020b).

3.1.1. Objectives

As discussed in sections 2.5, 2.6 and 2.7, LAES is a promising candidate for coupling to an NPP for the purposes of load following. The reasons for this are discussed in these sections. Primarily, it is argued that this is a highly mature energy storage technology that could be built and indeed is being built, today. A secondary argument, but one that is more relevant to the engineering modelling that is to be described in this chapter is its low operating temperatures and opportunities for capturing and utilising low-grade waste heat. This latter point is worth discussing further here in as much as it relates to the core objectives of the modelling approach.

One of the core reasons for selecting LAES as the ESS for this thesis is its ability to capture very low-grade heat that might otherwise be considered waste. As is discussed in greater detail in section 5.2.1, the steam for an NPP's is heated in a steam generator before being expanded to a pressure well below atmospheric. At this point, it is condensed via heat exchange with a coolant water stream (hereafter denoted the tertiary coolant) that is itself cooled by air in a cooling tower before being discharged from the plant. The temperature profiles in the condenser mean that this tertiary coolant does not exceed 300 K (NuScale Power LLC, 2018b). The flow rates of tertiary coolant, however, are very high – in excess of 10,000 kg/s, as section 5.2.1 shows. This means that a significant amount of heat is ultimately rejected from the NPP.

This rejected heat is in a very low temperature form and is thus not particularly useful for industrial or domestic heating purposes. The LAES system presents an opportunity in this regard. During system discharge, the air remains at a low temperature following the vaporisation stage. The exact temperature varies in the literature but it typically in the region of 250 K. This presents an opportunity for coupling the system to an NPP. The temperature difference between the LAES plant's discharge air stream and the NPP's primary coolant is

sufficient for heat exchange to take place between the two, allowing the NPP's waste heat to be captured, utilised, and ultimately sold in the form of electricity. Quantifying the exact value of this opportunity is a significant gap in the literature and thus a key objective of modelling.

One final point discussed in section 2.5.2 relates to the cold recycle part of LAES plants. As is emphasised in those discussions, the capture of cold during system discharge and its utilisation when charging the system is paramount to the overall round-trip efficiency of the system. Two options are discussed in the literature: the use of hydrocarbon fluid media and the use of packed gravel bed thermal stores. Of these options, the latter was deemed most appropriate for study in this thesis, due to its demonstrable use in pilot plants and safety concerns associated with hydrocarbon fluids. Both points are discussed in detail in section 2.5.2.

The engineering model is intended to determine how a coupled NPP and LAES system could be built and to enable the sizing of components to facilitate plant cost estimation. In order to do this, it is required to fulfil the following objectives:

- Determine the rate and temperature at which the NPP side can supply steam to the LAES plant,
- determine the optimal LAES configuration given the constraints on the supply of power by the NPP side,
- develop flowsheets for the chosen plant designs and determine required component sizes.

3.1.2. Background

Modelica is an object-orientated modelling language. It is loosely based on C but has a number of additional commands to facilitate engineering systems modelling. Whilst it would be onerous and unnecessary to define the Modelica syntax in detail within this thesis, it is sensible to define the key terms and the way models are constructed in order for readers to fully understand the discussions that follow.

Dymola is the simulation environment used in this study for running Modelica code. It checks and compiles the code and operates the solvers required for integrating the models. Dymola will always check that a model has the same number of variables and equations prior to simulation. This is the reason that unused equations are required to balance some of the models discussed below.

3.1.3. Terminology

Packages are collections of models. For most purposes, these can be thought of simply as folders containing related models. There is, however, one important special case; the use of packages in fluid medium models. The set of models that define the relationships between fluid properties is defined within a package for that fluid. Defining these as packages allows component models to quickly replace one fluid with another. In this study, the ExternalMedia library (Casella and Richter, 2008) is used to define packages that reference the third party software CoolProp (Bell et al., 2014) for fluid thermophysical properties. The key fluid properties used are those for air and water, which are taken from (Lemmon et al., 2000) and (Wagner and Pruß, 2002) respectively.

Individual models interact via *flanges*, connected by *connectors*. Flanges and their associated connectors allow properties to be carried from on model to another. There are three types of variable associated with flanges and connectors available in Modelica:

- '*across*' variables which equate to the same value on both sides of the connector,
- '*flow*' variables which sum to zero on both sides of the connector,
- '*stream*' variables which are associated with material properties and are taken to be carried by the flange's flow variable.

Due to the relationship between flow and stream variables, each flange may only have a single flow variable, but may have any number of stream variables. In thermodynamic modelling, the change in a stream variable, such as enthalpy, through a component may be different depending on the direction of the flow. For this reason, Modelica requires that equations are used to define stream variable changes for both directions through a component. The *inStream* command facilitates this; where it is used, the stream variable in question is taken to be that entering a component and where it is absent, the variable is taken to be that leaving a component. Across variables are entirely independent and there is again no limit on the number that can be present in a single flange.

Related to flanges are *interfaces*. In this model, interfaces are used to transfer single variables via connectors. These are dimensionless real numbers and can be considered analogous to across variables, being equal on both sides of the connector.

Models are the sections of Modelica code that actually do calculations. Models open with the *definitions* section which defines *parameters*, initial values that are user-defined within the user interface and do not change over time, *constants*, fixed values that are user-defined within the

Modelica code itself, *variables* that the model uses to calculate values that change over time, and *outputs* which are variables that are made easier to access during post-processing. In addition, this section defines *fluid states*, which are essentially variables defining the thermodynamic state of a fluid. Variable and parameter definitions are associated with a either a base unit, a real number or an integer definition which is defined in the same line of code. All of these definitions may take the form of matrix vectors, which are represented by $Var[n]$ for a matrix variable Var of size n.

Fluid states are important for any models that used defined thermodynamic properties of fluids. To define a fluid state, two unique properties must be provided, for example enthalpy and pressure, or entropy and pressure. A combination of temperature and pressure is also acceptable under certain conditions. However, if the temperature and pressure provided specifies a thermodynamic state where the fluid is under a phase transition, the model will return an error. This is because a temperature and pressure can define a thermodynamic state at any point along that phase boundary, meaning that a unique state point cannot be defined.

The definitions section also defines other models, flanges or connectors that are used as sub-components of the model being defined. Such models would be expected to have the values of their parameters defined, either explicitly, or in terms of the parameters of is overarching model.

The *equation* section follows the definitions section and consists of the equations that calculate the change in variables over time. The modelling environment, which compiles and runs the Modelica code will typically decide in which order equations are calculated. This can be overridden by using an optional *algorithm* section which forces the environment to run equations in the order that they appear in the code and can appear either in conjunction or in place of the equation section. Finally, another optional section, the *initialisation* section allows the inclusion of equations that the model must satisfy at the start of each simulation run.

3.2. Component modelling

The following subsections detail the component models used in the engineering model. As discussed, Modelica and Dymola facilitate the construction of models in a modular fashion. The foundation of these models is the individual models of components. Many of the models used are based on the models available in the ThermoPower library for Modelica (Casella and Leva, 2009), but have been modified for use in this system. Wherever this is the case, the ThermoPower library is credited and the changes summarised.

Two types of flange are used in this study, both taken from ThermoPower. The first is a 2PF (two-phase fluid flow) flange, which transmits the following fluid properties from one component to another:

- A flow variable, $\dot{M}$, defining the mass flow rate of the fluid stream. Flow into a component is taken as positive and out of a component is taken as negative.
- An across variable, p, defining the absolute pressure of the fluid stream.
- A stream variable, h, defining the specific enthalpy of the fluid stream.
- A matrix stream variable, $X_i[m]$, defining the mass fraction of each component in the fluid flow, where m is the number of components. It should be noted that only single-component medium models are used for fluids in this study, such that this variable is redundant.

The second flange is a DHT (distributed heat transfer) flange for finite volumes, which transmits a matrix of material properties, where n is the number of volumes. This transmits the following material properties:

- A matrix across variable, $T[n]$, defining the absolute temperature of the materials.
- A matrix flow variable, $\dot{Q}[n]$, defining the heat flow rate at the volumes. Flow into a component is taken as positive and out of a component is taken as negative.

The component models used in the engineering model will now be discussed in detail. Following an opening paragraph for each model, a table will outline the details of each parameter, variable and fluid states used in the model. This table will include the symbol used for the item in this text, the name used in the Modelica code, the units for the item and a brief description. Following the table, the text will detail and discuss each equation used in the model.

3.2.1. One-dimensional finite volume flow model

The 1DFV (one-dimensional finite volume) flow model is the fundamental component for fluid flows in the engineering model and is primarily used as a sub-component in heat exchangers. An FV (finite volume) model approximates a system, such as a fluid flow, by dividing it into a set of volumes and dividing the relationships between these volumes and at the interfaces, regions hereafter referred to as nodes. This concept is shown in Figure 3-1.

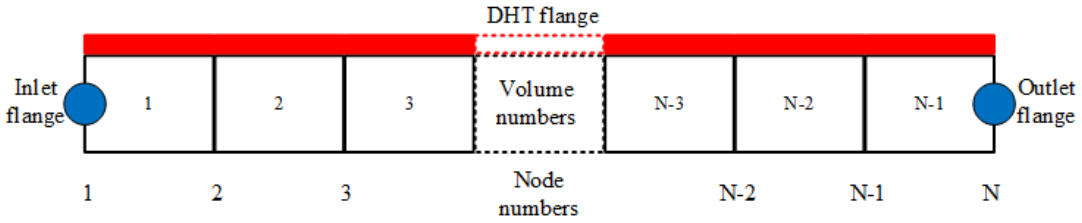

Figure 3-1: One-dimensional finite volume flow model diagram showing the role of the distributed heat transfer flange

ThermoPower (Casella, 2014) provides a basis for this model with a model that provides simulation of both thermodynamic and fluid dynamic properties in a flow. Whilst the thermodynamic considerations are vital for this engineering model, the fluid dynamic properties are less so. Indeed, detailed geometric design of heat exchangers is not considered within the scope of this study and the 1DFV flow model was simplified accordingly. The equations associated with friction factors were replaced with a single equation relating flow pressure drop to the inlet pressure. An additional initialisation equation was added to ensure steady-state mass in each volume during model initialisation.

Item	Code	Units	Description
			Parameters
	Medium		Replaceable medium package for fluid flow
N	N		Number of wall nodes for thermal variables
N_V	Nw		Number of volumes for thermal variables (defaults to $N-1$)
L	L	m	Length of fluid flow
H	H	m	Elevation of outlet over inlet
A	A	m^2	Flow cross-sectional area
ω	omega	m	Perimeter of heat-transfer surface
$\dot{M}_{\text{nom}}$	wnom	kg/s	Nominal mass flow rate
p_{drop}	PressureDrop		Pressure drop as a fraction of inlet pressure
γ	gamma	W/m^2kg	Heat transfer coefficient
			Initial parameters
p_{start}	pstart	Pa	Expected pressure start value
$h_{\text{start,inlet}}$	hstartin	J/kg	Expected starting fluid specific enthalpy at inlet
$h_{\text{start,outlet}}$	hstartout	J/kg	Expected starting fluid specific enthalpy at outlet
$h_{\text{start}}[N]$	hstart	J/kg	Expected starting fluid enthalpy vector
	SSinit		Boolean parameter for steady-state initialisation
			Variables
$\Delta p_{\text{friction}}$	Dpfric	Pa	Pressure drop due to friction
Δp_{static}	Dpstat	Pa	Pressure drop due to static head
p	p	Pa	Pressure for initial state calculations
$\Delta p_{\text{fric}}[N_V]$	dpf[N-1]	Pa	Pressure drop due to friction between nodes
$\dot{M}$	w	kg/s	Mass flow rate
$\bar{\dot{M}}[N_V$	wbar[N-1]	kg/s	Average mass flow rate for a volume
$\dot{Q}[N_V]$	Q[N-1]	W	Heat flow rate into a volume
$u[N]$	u[N]	m/s	Fluid velocity at a node

$T[N]$	T[N]	K	Fluid temperature at a node
$\bar{T}[N_V]$	Tbar[N-1]	K	Average temperature of each volume
$\bar{T}_{\text{wall}}[N_V]$	wall.T[N-1]	K	Average temperature of each DHT flange
$h[N]$	h[N]	J/kg	Fluid specific enthalpy at a node
$\tilde{h}[N_V]$	htilde[N-1]	J/kg	Fluid specific enthalpy for a volume
h_{liquid}	hl	J/kg	Saturated liquid specific enthalpy
h_{vapour}	hv	J/kg	Saturated vapour specific enthalpy
$\chi[N]$	x[N]		Fluid steam quality at a node
$\rho[N]$	rho[N]	kg/m^3	Fluid density at a node
ρ_{liquid}	rhol	kg/m^3	Saturated liquid density
ρ_{vapour}	rhov	kg/m^3	Saturated vapour density
$\bar{\rho}[N_V]$	rhobar[N-1]	kg/m^3	Average fluid density for a volume
M	M	kg	Mass of fluid in flow
		Fluid states	
$\tilde{S}[N]$	fluidState[N]		Thermodynamic state of fluid at a node
$\tilde{S}_{\text{sat}}$	sat		Properties of a saturated fluid
		Constants	
g	g	m/s^2	Acceleration due to gravity

Table 3-1: Properties for one-dimensional finite volume flow model

Three flanges are used in the 1DFV flow model. Firstly, an inlet 2PF flange is used with properties $\dot{M}_{\text{inlet}}$, p_{inlet} and h_{inlet} for the mass flow rate, pressure and enthalpy respectively at the inlet. Secondly, an outlet 2PF flange with properties $\dot{M}_{\text{outlet}}$, p_{outlet} and h_{outlet} for the mass flow rate, pressure and enthalpy respectively at the outlet. Finally, a DHT flange is used with properties $\bar{T}_{\text{wall}}[N_V]$ and $Q[N_V]$ for the temperature at and the heat transfer through the wall of the flow. The 2PF flanges are shown in blue and the DHT flange shown in red in Figure 3-1. A replaceable medium package defines the variables for the possible thermodynamic states.

Since the model will be run in steady-state, the mass balance for the model is expressed by equating mass flow in to mass flow out:

$$\dot{M}_{\text{inlet}} + \dot{M}_{\text{outlet}} = 0 \qquad (3\text{-}1)$$

The pressure drop for each volume j is calculated using:

$$\Delta p_{\text{fric}}[j] = \frac{p_{\text{drop}}\, p_{\text{inlet}}}{N-1} \qquad (3\text{-}2)$$

The total pressure drop for the flow is then calculated using:

$$\Delta p_{\text{friction}} = \sum_{j=1}^{N-1} \Delta p_{\text{fric}}[j] \qquad (3\text{-}3)$$

The total static pressure drop is calculated using:

$$\Delta p_{\text{static}} = \frac{gH}{(N-1)} \sum_{j=1}^{N-1} \bar{\rho}[j] \qquad (3\text{-}4)$$

Momentum balance for the system thus allows calculation of the outlet pressure:

$$p_{\text{outlet}} = p_{\text{inlet}} - \Delta p_{\text{friction}} - \Delta p_{\text{static}} \qquad (3\text{-}5)$$

Energy balance for each volume j is expressed:

$$\dot{Q}[j] = \frac{AL}{(N-1)} \bar{\rho}[j] \dot{\tilde{h}}[j] + \dot{\bar{M}}[j](h[j+1] - h[j]) - \frac{AL}{(N-1)} \dot{p} \qquad (3\text{-}6)$$

where $\dot{p}$ and $\dot{\tilde{h}}[j]$ are the respective derivatives of pressure and volume specific enthalpy with respect to time, t. In words, this equates the flow of heat into a volume to the energy stored in the fluid within the volume (first term), the net energy flowing into the volume (second term, noting that flow out of a volume is negative) and the energy stored when pressurising the fluid (third term).

The saturation state for the fluid, $\tilde{S}_{\text{sat}}$, is defined within the medium model as the saturation state at pressure p, taken to be the pressure at the flow inlet:

$$p = p_{\text{inlet}} \qquad (3\text{-}7)$$

From this definition, values for the saturated liquid and vapour specific enthalpies, h_{liquid} and h_{vapour} respectively, and the saturated liquid and vapour densities, ρ_{liquid} and ρ_{vapour} respectively, are set by reference to the medium model at $\tilde{S}_{\text{sat}}$.

The average density for each volume j is calculated depending on the state of the fluid within that volume, using if statements comparing the enthalpy entering the volume, $h[j]$, and the enthalpy leaving the volume, $h[j+1]$, hereafter referred to as the nodal enthalpies, to the

saturated liquid and vapour specific enthalpies, h_{liquid} and h_{vapour} respectively. Where both nodal enthalpies are smaller than the liquid enthalpy or both are greater than the vapour enthalpy, the fluid in the volume is taken to be single-phase and:

$$\bar{\rho}[j] = \frac{\rho[j] + \rho[j+1]}{2} \qquad (3\text{-}8)$$

If both nodal enthalpies are between the liquid enthalpy and the vapour enthalpy, the fluid in the volume is taken to be entirely two-phase and:

$$\bar{\rho}[j] = \frac{h_{\text{vapour}} - h_{\text{liquid}}}{\left(\frac{1}{\rho_{\text{vapour}}} - \frac{1}{\rho_{\text{liquid}}}\right)} \left(\frac{\ln\left(\rho[j] \middle/ \rho[j+1]\right)}{h[j+1] - h[j]} \right) \qquad (3\text{-}9)$$

If the enthalpy entering the volume is smaller than the liquid enthalpy and the enthalpy leaving the volume is between the liquid and vapour enthalpies, the fluid in the volume is taken to be transitioning from liquid to two-phase and:

$$\bar{\rho}[j] = \frac{\frac{1}{2}\left(\rho[j] + \rho_{\text{liquid}}\right)\left(h_{\text{liquid}} - h[j]\right) + \frac{h_{\text{vapour}} - h_{\text{liquid}}}{\left(\frac{1}{\rho_{\text{vapour}}} - \frac{1}{\rho_{\text{liquid}}}\right)} \ln\left(\frac{\rho_{\text{liquid}}}{\rho[j+1]}\right)}{h[j+1] - h[j]} \qquad (3\text{-}10)$$

If the enthalpy entering the volume is between the liquid and vapour enthalpies and the enthalpy leaving the volume is greater than the vapour enthalpy, the fluid in the volume is taken to be transitioning from two-phase to vapour and:

$$\bar{\rho}[j] = \frac{\frac{h_{\text{vapour}} - h_{\text{liquid}}}{\left(\frac{1}{\rho_{\text{vapour}}} - \frac{1}{\rho_{\text{liquid}}}\right)} \ln\left(\frac{\rho[j]}{\rho_{\text{vapour}}}\right) + \frac{1}{2}\left(\rho_{\text{vapour}} + \rho[j+1]\right)\left(h[j+1] - h_{\text{vapour}}\right)}{h[j+1] - h[j]} \qquad (3\text{-}11)$$

If the enthalpy entering the volume is less than the liquid enthalpy and the enthalpy leaving the volume is greater than the vapour enthalpy, the fluid in the volume is taken to be transitioning from liquid to two-phase to vapour and:

$$\bar{\rho}[j] = \frac{1}{(h[j+1] - h[j])}\left(\frac{1}{2}\left(\rho[j] + \rho_{\text{liquid}}\right)\left(h_{\text{liquid}} - h[j]\right)\right.$$
$$+ \frac{h_{\text{vapour}} - h_{\text{liquid}}}{\left(\frac{1}{\rho_{\text{vapour}}} - \frac{1}{\rho_{\text{liquid}}}\right)} \ln\left(\frac{\rho_{\text{liquid}}}{\rho_{\text{vapour}}}\right) \qquad (3\text{-}12)$$
$$\left. + \frac{1}{2}\left(\rho_{\text{vapour}} + \rho[j+1]\right)\left(h[j+1] - h_{\text{vapour}}\right)\right)$$

If the enthalpy entering the volume is between the liquid and vapour enthalpies and the enthalpy leaving the volume is less than the liquid enthalpy, the fluid in the volume is taken to be transitioning from two-phase to liquid and:

$$\bar{\rho}[j] = \frac{\frac{h_{\text{vapour}} - h_{\text{liquid}}}{\left(\frac{1}{\rho_{\text{vapour}}} - \frac{1}{\rho_{\text{liquid}}}\right)} \ln\left(\frac{\rho[j]}{\rho_{\text{liquid}}}\right) + \frac{1}{2}\left(\rho_{\text{liquid}} + \rho[j+1]\right)\left(h[j+1] - h_{\text{liquid}}\right)}{h[j+1] - h[j]} \qquad (3\text{-}13)$$

If the enthalpy entering the volume is greater than the vapour enthalpy and the enthalpy leaving the volume is less than the liquid enthalpy, the fluid in the volume is taken to be transitioning from vapour to two-phase to liquid and:

$$\bar{\rho}[j] = \frac{1}{(h[j+1] - h[j])}\left(\frac{1}{2}\left(\rho[j] + \rho_{\text{vapour}}\right)\left(h_{\text{vapour}} - h[j]\right)\right.$$
$$+ \frac{h_{\text{vapour}} - h_{\text{liquid}}}{\left(\frac{1}{\rho_{\text{vapour}}} - \frac{1}{\rho_{\text{liquid}}}\right)} \ln\left(\frac{\rho_{\text{vapour}}}{\rho_{\text{liquid}}}\right) \qquad (3\text{-}14)$$
$$\left. + \frac{1}{2}\left(\rho_{\text{liquid}} + \rho[j+1]\right)\left(h[j+1] - h_{\text{liquid}}\right)\right)$$

Where none of the criteria for equations (3-8) to (3-14) hold true, the fluid in the volume is taken to be transitioning from vapour to two-phase and:

$$\bar{\rho}[j] = \frac{\frac{1}{2}\left(\rho[j] + \rho_{\text{vapour}}\right)\left(h_{\text{vapour}} + h[j]\right) + \frac{h_{\text{vapour}} - h_{\text{liquid}}}{\left(\frac{1}{\rho_{\text{vapour}}} - \frac{1}{\rho_{\text{liquid}}}\right)} \ln\left(\frac{\rho_{\text{vapour}}}{\rho[j+1]}\right)}{h[j+1] - h[j]} \quad (3\text{-}15)$$

For each volume j, the average flow rate is equated to the inlet flow rate:

$$\bar{\dot{M}}[j] = \dot{M}_{\text{inlet}} \quad (3\text{-}16)$$

The fluid state at each node i, $\tilde{S}[i]$, is defined in the medium model using the pressure, p, and the specific enthalpy at that volume, $h[i]$. From this definition, values for the temperature, $T[i]$ and the density, $\rho[i]$, are set via lookup in the medium model.

The fluid velocity at each node i is calculated:

$$u[i] = \frac{\dot{M}}{A\rho[i]} \quad (3\text{-}17)$$

The steam quality for each node i is calculated depending on the state of the fluid at node $h[i]$ to h_{liquid} and h_{vapour}. Where $h[i] > h_{\text{vapour}}$, the fluid is entirely vapour and $\chi[i] = 1$. Where $h[i] < h_{\text{liquid}}$, the fluid is entirely liquid and $\chi[i] = 0$. Otherwise, the steam quality is calculated:

$$\chi[i] = \frac{h[i] - h_{\text{liquid}}}{h_{\text{vapour}} - h_{\text{liquid}}} \quad (3\text{-}18)$$

As mentioned previously, the enthalpy flow at a flange is considered to be carried by the mass flow rate. The 1DFV flow model does not specify a direction of flow, so specific enthalpy within a volume must be approximated to the specific enthalpy at a node bounding that volume. Since models are expected to be built such that flow will be from inlet to outlet flange, the enthalpy for a node i is equated to the fluid specific enthalpy leaving the previous volume:

$$h[i] = \tilde{h}[i-1] \quad (3\text{-}19)$$

The boundary conditions are then defined. The specific enthalpy at the first node is equated to the specific enthalpy flow into the first volume from the inlet. The specific enthalpy of the final volume is equated to the specific enthalpy at the outlet:

$$h[1] = h_{\text{inlet}} \tag{3-20}$$

$$\tilde{h}[N-1] = h_{\text{outlet}} \tag{3-21}$$

The specific enthalpy leaving the first volume at the inlet is equated to the specific enthalpy of the first volume:

$$h_{\text{inlet}} = \tilde{h}[1] \tag{3-22}$$

Equations (3-20) and (3-22) together make the model appear over-constrained. Within the code, this is not the case. As mentioned in section 3.1, stream variables are related to a flow variable for a given flange model. Modelica uses the *inStream* command to denote a stream variable flowing into a model and otherwise considers any stream variables to be leaving a model via the flange in question. Thus, equation (3-20) uses the inStream command within the code to identify this as a flow into the model.

The average temperature of each volume j is calculated as the average of the temperatures at either node:

$$\bar{T}[j] = \frac{T[j] + T[j+1]}{2} \tag{3-23}$$

The heat flow rate into each volume j is then calculated:

$$\dot{Q}[j] = (\bar{T}_{\text{wall}}[j] - \bar{T}[j]) \frac{\omega \gamma L}{(N-1)} \tag{3-24}$$

Heat will flow into the volume when the wall temperature is higher than the fluid temperature for a given volume. Hence, by definition, a positive value for $Q[j]$ represents a flow into the fluid in that volume.

$\bar{T}_{\text{wall}}[j]$ represents the value of the temperature at the DHT flange. The DHT is the means by which the model transfers heat between adjacent flow models. The way multiple flows are connected into larger models like heat exchangers is discussed in section 3.2.4.

At the start of modelling, the initial parameters are used for the starting points of the model variables. The vector $h_{\text{start}}[N]$ is defined with N values linearly spaced between $h_{\text{inlet, start}}$ and $h_{\text{outlet, start}}$. Then, the initial nodal enthalpies and the initial pressure are defined:

$$h[N] = h_{\text{start}}[N] \qquad (3\text{-}25)$$

$$p = p_{\text{start}} \qquad (3\text{-}26)$$

Should the steady-state initialisation Boolean parameter be set to true, the initial parameters are varied until the following equations are satisfied:

$$\frac{d\tilde{h}[N-1]}{dt} = \mathbf{0} \qquad (3\text{-}27)$$

$$\frac{dp}{dt} = 0 \qquad (3\text{-}28)$$

$$\frac{d\rho[j]}{dt} = \mathbf{0} \qquad (3\text{-}29)$$

i.e. initial pressure and the initial volume enthalpies and densities must be fixed with respect to time. Once these conditions are satisfied, the model run commences.

3.2.2. Counter-current flow regime

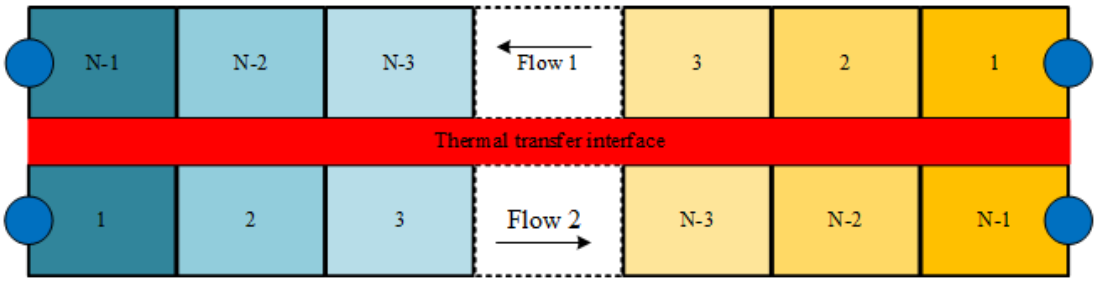

Figure 3-2: A counter-current flow regime

In plant design, a counter-current heat exchanger orients flows so that flows adjacent to a thermal transfer surface flow in opposite directions, as shown in Figure 3-2. Here, flow 1 enters the heat exchanger on the right at a high temperature and cools as it flows to the left. Conversely, flow 2 enters the heat exchanger on the left and warms as it flows to the right. This ensures that a temperature gradient between the flows is maintained all the way along the heat exchanger. In reality, the schematic shown in Figure 3-2 is a simplification, but this approach is sufficient for the purposes of the modelling approach described in this thesis.

The counter-current flow regime is required due to the fact that DHT flanges equate variables in volume j on one side of the flange with volume j on the opposite side, leading to a co-current flow regime. The ThermoPower model (Casella, 2014) was deemed sufficient for this study and was used without modification.

Item	Name in code	Units	Description
		Parameters	
N_V	Nw		Number of volumes for thermal variables
		Variables	
$\boldsymbol{C}[N_V]$	cVs[Nw]		Corresponding volumes matrix
$T_1[N_V]$	side1.T[Nw]	K	Temperature at flange 1
$T_2[N_V]$	side2.T[Nw]	K	Temperature at flange 2
$\dot{Q}_1[N_V]$	side1.Q[Nw]	W	Heat flow entering flange 1
$\dot{Q}_2[N_V]$	side2.Q[Nw]	W	Heat flow entering flange 2

Table 3-2: Properties for counter-current flow regime

This model consists of two DHT flanges, side 1 with properties $T_1[N_V]$ and $Q_1[N_V]$, and side 2 with properties $T_2[N_V]$ and $Q_2[N_V]$. The basis of the counter-current regime is the definition of a single-row matrix of size N_V whose first value is N_V and whose final value is 1:

$$\boldsymbol{C} = [N_V \quad N_V - 1 \quad \cdots \quad 2 \quad 1] \qquad (3\text{-}30)$$

Temperatures for corresponding volumes, j, are then equated:

$$T_1[j] = T_2[\boldsymbol{C}[j]] \quad (3\text{-}31)$$

Similarly, energy conservation is maintained across the regime:

$$\dot{Q}_1[j] = \dot{Q}_2[\boldsymbol{C}[j]] \quad (3\text{-}32)$$

This model achieves counter-current flow by the definition of matrix $\boldsymbol{C}$. For example, when $j = 1$, the value of $\boldsymbol{C}[1]$ returns N_V.

3.2.3. Metal tubes

The metal tubes model forms the final important part of heat exchanger models and simulates the flow of heat through and the accumulation of heat within metal tubes. The ThermoPower model (Casella, 2014) was again deemed sufficient for this study and was used without modification.

Item	Name in code	Units	Description
		Parameters	
N_V	Nw		Number of volumes for tube
L	L	m	Length of tube
r_{internal}	rint	m	Internal radius of tube
r_{external}	rext	m	External radius of tube
C_{vol}	rhomcm	J/m^{3}K	Volumetric heat capacity of tube metal
λ	lambda	W/mK	Thermal conductivity of tube metal
	WallRes		Boolean parameter for wall resistance
		Initial parameters	
$T_{\text{start,1}}$	Tstart1	K	Expected starting temperature of first volume
$T_{\text{start,N}}$	TstartN	K	Expected starting temperature of final volume
$T_{\text{start}}[N_V]$	Tstart[Nw]	K	Expected starting temperature of volumes
	SSinit	kg	Boolean parameter for steady-state initialisation
		Variables	
$T[N_V]$	Tvol[Nw]	K	Volume temperatures
A	Am	m^2	Area of metal tube cross-section
		Constants	
π	pi		Pi

Table 3-3: Properties for metal tube model

Two DHT flanges are used in the metal tube model. One for the internal surface with properties $T_{\text{internal}}[N_V]$ and $\dot{Q}_{\text{internal}}[N_V]$, and one for the external surface with properties $T_{\text{external}}[N_V]$ and $\dot{Q}_{\text{external}}[N_V]$.

The metal tube begins by asserting that the external radius of the metal tube is larger than the internal radius:

$$r_{\text{external}} > r_{\text{internal}} \quad (3\text{-}33)$$

If this is not true, the simulation is halted, and an error message returned.

The cross-sectional area of the tube is calculated:

$$A = \pi({r_{\text{external}}}^2 - {r_{\text{internal}}}^2) \quad (3\text{-}34)$$

Should the wall resistance Boolean parameter be set to true, the thermal resistance of the tube walls is accounted for. Heat conduction through the internal half-thickness of the tube is calculated for each volume j using:

$$\dot{Q}_{\text{internal}}[j] = \frac{2\lambda\pi \, {L}/{N_V} \, (T_{\text{internal}}[j] - T[j])}{\log\left(\frac{r_{\text{internal}} + r_{\text{external}}}{2r_{\text{internal}}}\right)} \quad (3\text{-}35)$$

Similarly, heat conduction through the external half-thickness of the tube is calculated for each volume j using:

$$\dot{Q}_{\text{external}}[j] = \frac{2\lambda\pi \, {L}/{N_V} \, (T_{\text{external}}[j] - T[j])}{\log\left(\frac{2r_{\text{external}}}{r_{\text{internal}} + r_{\text{external}}}\right)} \quad (3\text{-}36)$$

Where the wall resistance parameter is set to false, the simplification that there is no temperature gradient across the tube thickness is assumed and the temperatures for the internal and external surfaces are equated to the temperatures for the volumes j:

$$T_{\text{internal}}[j] = T[j] \quad (3\text{-}37)$$

$$T_{\text{external}}[j] = T[j] \quad (3\text{-}38)$$

Energy balance is defined for each volume j:

$${L}/{N_V} \, C_{\text{vol}} A \frac{dT[j]}{dt} = \dot{Q}_{\text{internal}}[j] + \dot{Q}_{\text{external}}[j] \quad (3\text{-}39)$$

At the start of modelling, initial temperatures vector $T_{\text{start}}[N_V]$ is defined with N_V values linearly spaced between $T_{\text{start},1}$ and $T_{\text{start, N}}$. The volume temperatures are then defined on these values:

$$T[N_V] = T_{\text{start}}[N_V] \qquad (3\text{-}40)$$

Should the steady-state initialisation parameter be set to true, the starting variables are varied until the following equation is satisfied:

$$\frac{dT[N_V]}{dt} = \mathbf{0} \qquad (3\text{-}41)$$

3.2.4. Heat exchangers

Heat exchangers are models built from the 1DFV flow, counter current regime and metal tube models in sections 3.2.1, 3.2.2 and 3.2.3 respectively. They are built in much the same way as in the ThermoPower library (Casella, 2014) however these have been built differently to reduce the number of parameters required for the model.

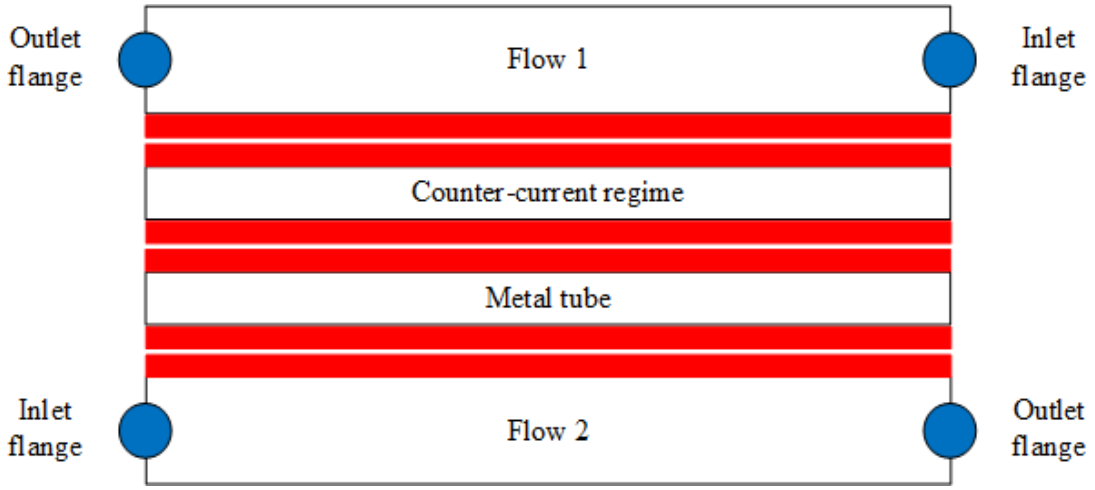

Figure 3-3: Heat exchanger schematic (red bars represent DHT flanges)

Figure 3-3 is a schematic diagram of a generic heat exchanger model. A heat exchanger consists of two 1DFV models, denoted flow 1 and flow 2, a counter-current flow regime and a metal tube model. Adjacent DHT nodes are connected, meaning that the across variable temperature is equal on both sides and the flow variable heat flows on connected sides sum to zero.

For brevity, only newly introduced parameters are discussed below. These parameters have been defined in order to limit the number of user-input parameters required where there is overlap in the components that constitute the heat exchanger model. Where sub-component parameters are omitted, these should be assumed as being defined in the top-level heat exchanger model and propagating through to the relevant components. For clarity, any component parameters are shown with a subscript in angle brackets, ⟨1⟩ for flow 1, ⟨2⟩ for flow

2, ⟨m⟩ for metal tube and ⟨c⟩ for counter-current flow regime. For example $L_{\langle 1 \rangle}$ references the length parameter for the flow 1 sub-component.

Item	Name in code	Units	Description
		Parameters	
	Flow1Medium		Medium package for flow 1 fluid
	Flow2Medium		Medium package for flow 2 fluid
N	Nodes		Number of wall nodes
A_1	Flow1ExchSurf	m^2	Exchange surface area for flow 1
V_1	Flow1Vol	m^3	Volume for flow 1
	RoundFlow2		Boolean parameter for perimeter of flow 2; true for circular, false for rectangular
a_2	Flow2SectLength	m	Length or diameter for flow 2 perimeter
b_2	Flow2SectWidth	m	Width for flow 2 perimeter (0 if circular)
d_{tube}	TubeThickness	m	Thickness of metal tube
γ	Gamma	W/m^2K	Minimum heat transfer coefficient

Table 3-4: Parameters for heat exchanger model

Parameters for the number of nodes and volumes are defined:

$$N_{\langle 1 \rangle} = N_{\langle 2 \rangle} = N \qquad (3\text{-}42)$$

$$N_{V,\langle 1 \rangle} = N_{V,\langle 2 \rangle} = N_{V,\langle \mathrm{m} \rangle} = N_{V,\langle \mathrm{c} \rangle} = N - 1 \qquad (3\text{-}43)$$

The length parameters for the flows and the metal tube are calculated as a function of the flow 1 surface area and volume:

$$L_{\langle 1 \rangle} = L_{\langle 2 \rangle} = L_{\langle \mathrm{m} \rangle} = \frac{{A_1}^2}{4\pi V_1} \qquad (3\text{-}44)$$

The cross-sectional area of flow 1 is calculated as a function of its heat exchange surface area and volume:

$$A_{\langle 1 \rangle} = \frac{\pi}{4}\left(\frac{4V_1}{A_1}\right)^2 \qquad (3\text{-}45)$$

The cross-sectional area of flow 2 is calculated depending on the perimeter shape Boolean parameter of flow 2. If this is true, then the flow is annular, and its cross-sectional area is calculated:

$$A_{\langle 2 \rangle} = \frac{\pi}{4}{a_1}^2 - \frac{\pi}{4}\left(\frac{4V_1}{A_1}\right)^2 \qquad (3\text{-}46)$$

Otherwise, if the perimeter of flow 2 is taken to be rectangular and its cross-sectional area is calculated:

$$A_{\langle 2 \rangle} = a_1 a_2 - \frac{\pi}{4}\left(\frac{4V_1}{A_1}\right)^2 \quad (3\text{-}47)$$

The perimeter of the heat transfer surface for both flows is taken as the perimeter of the internal flows, since this is the smaller heat exchange surface and the limit on the overall power of the heat exchanger:

$$\omega_{\langle 1 \rangle} = \omega_{\langle 2 \rangle} = \frac{4\pi V_1}{A_1} \quad (3\text{-}48)$$

The heat transfer coefficient for both flows is defined as the minimum heat transfer coefficient between the flows, since this will again be the limiting factor on heat exchanger power:

$$\gamma_{\langle 1 \rangle} = \gamma_{\langle 2 \rangle} = \gamma \quad (3\text{-}49)$$

The internal and external radii of the metal tubes are defined:

$$r_{\text{internal},\langle \text{m} \rangle} = \frac{2V_1}{A_1} \quad (3\text{-}50)$$

$$r_{\text{external},\langle \text{m} \rangle} = \frac{2V_1}{A_1} + d_{\text{tube}} \quad (3\text{-}51)$$

3.2.5. Intercoolers

The use of finite volume methods in the heat exchangers described in section 3.2.4 is a computationally intensive process, particularly during the initialisation stage of simulation. This is compounded when multiple heat exchangers are used in concert. It is, however, necessary when the minimum approach temperature in the heat exchanger is expected to occur along its length, rather than at the inlet or outlet. This is likely where fluid on one side of the heat exchanger is expected to undergo a phase change while the fluid on the other side is not.

There are instances in this plant design this is not necessary. One such instance occurs during the charge process of the LAES plant. Air heats up when it is compressed, which reduces the efficiency of the compression process. This effect can be mitigated by intercooling, that is

splitting the compression into stages and cooling the air in between these stages. This is done by intercooling.

Because there is little change in temperature on one side of an intercooler, compared to a large change in temperature on the other, finite volume modelling is unnecessary and computational load can be reduced by using a simpler approach to process modelling, discussed in this section. Component sizing can be performed using the LMTD (log mean temperature difference) method discussed in section 6.1.3.

The intercooler component is purpose-built for this model.

Item	Name in code	Units	Description
		Parameters	
	AirMedium		Medium package for air
	WaterMedium		Medium package for water
$T_{\text{outlet,air}}$	AirTargetTemp	K	Target temperature of air flow at outlet
$p_{\text{drop,air}}$	AirPressureDrop		Air pressure drop as a fraction of inlet pressure
$T_{\text{supply,water}}$	WaterTempIn	K	Temperature of water supply
$T_{\text{discharge,water}}$	WaterTempOut	K	Temperature of discharge water
p_{water}	WaterPressure	Pa	Pressure of water supply
$p_{\text{drop,water}}$	WaterPresssureDrop		Water pressure drop as a fraction of inlet pressure
η_{pump}	EtaPump		Efficiency of the pump as a decimal
		Variables	
$\dot{Q}$	Qdot	W	Heat removal rate
ρ	Rho	kg/m^3	Water density
$h_{\text{in,air}}$	hin	J/kg	Specific enthalpy of air at inlet
$h_{\text{out,air}}$	hout	J/kg	Specific enthalpy of air at outlet
$h_{\text{supply,water}}$	hsupply	J/kg	Specific enthalpy of water at supply
$h_{\text{discharge,water}}$	hdischarge	J/kg	Specific enthalpy of water at discharge
$\dot{W}$	Power	W	Pumping power required
$\dot{M}_{\text{water}}$	mdot	kg/s	Water mass flow flow rate

Table 3-5: Properties for intercooler model

Two flanges are used in the intercooler model. Firstly, an inlet 2PF flange is used with properties $\dot{M}_{\text{inlet,air}}$, $p_{\text{inlet,air}}$ and $h_{\text{inlet,air}}$ for the air mass flow rate, pressure and enthalpy respectively at the inlet. Secondly, an outlet 2PF flange with properties $\dot{M}_{\text{outlet,air}}$, $p_{\text{outlet,air}}$ and $h_{\text{outlet,air}}$ for the air mass flow rate, pressure and enthalpy respectively at the outlet.

Since flow reversal cannot be allowed in the intercooler for the modelling assumptions to hold, the model asserts that the inlet mass flow rate is positive:

$$\dot{M}_{\text{inlet,air}} > 0 \qquad (3\text{-}52)$$

Where this is not the case, the model is halted, and an error message posted.

Mass balance is defined:

$$\dot{M}_{\text{inlet,air}} + \dot{M}_{\text{outlet,air}} = 0 \qquad (3\text{-}53)$$

The pressure drop in the air flow is calculated:

$$p_{\text{outlet,air}} = \left(1 - p_{\text{drop,air}}\right) p_{\text{inlet,air}} \qquad (3\text{-}54)$$

The boundary conditions for the flow are defined:

$$h_{\text{in,air}} = h_{\text{inlet,air}} \qquad (3\text{-}55)$$

$$h_{\text{out,air}} = h_{\text{outlet,air}} \qquad (3\text{-}56)$$

Equation (3-55) uses the inStream command (see section 3.1.3) for $h_{\text{inlet,air}}$ to signify enthalpy entering the model. The outlet enthalpy, $h_{\text{out,air}}$, is defined based on $T_{\text{outlet,air}}$ and $p_{\text{outlet,air}}$ using the air medium model. A final unused balancing equation (see section 3.1.2) is supplied:

$$h_{\text{outlet,air}} = h_{\text{inlet,air}} \qquad (3\text{-}57)$$

This uses the inStream command for $h_{\text{outlet,air}}$ to calculate enthalpy at the inlet for reverse flows.

The total required rate of heat extraction is calculated:

$$\dot{Q} = \dot{M}_{\text{inlet,air}}\left(h_{\text{in,air}} - h_{\text{out,air}}\right) \qquad (3\text{-}58)$$

The water supply enthalpy, $h_{\text{supply,water}}$, is defined based on $T_{\text{supply,water}}$ and p_{water} using the water medium model. The water discharge enthalpy is defined using the water medium model based on $T_{\text{discharge,water}}$ and the calculated discharge pressure:

$$p_{\text{discharge,water}} = \left(1 - p_{\text{drop,water}}\right) p_{\text{supply,water}} \qquad (3\text{-}59)$$

The required water mass flow rate is defined:

$$\dot{Q} = \dot{M}_{\text{water}}\left(h_{\text{discharge,water}} - h_{\text{supply,water}}\right) \quad (3\text{-}60)$$

The pumping power required for the intercooler is calculated:

$$\dot{W} = \frac{\dot{M}_{\text{water}}}{\rho\eta_{\text{pump}}}\left(p_{\text{drop,water}}p_{\text{supply,water}}\right) \quad (3\text{-}61)$$

3.2.6. Compressors

Compressors are used to increase the pressure of gaseous flows. These are vital components for the air liquefier model. The compressor model is purpose-built for this study.

Item	Name in code	Units	Description
	Parameters		
	Medium		Medium package for fluid
$\dot{M}_{\text{design}}$	m_flow_des	kg/s	Design mass flow rate
PR	PR		Pressure ratio of compressor
$\eta[x, 2]$	tableEta		Table with x rows defining the compressor isentropic efficiency at different mass flow rates
	Initial parameters		
$p_{\text{start,inlet}}$	pstart_in	Pa	Start pressure at compressor inlet
$p_{\text{start,outlet}}$	pstart_out	Pa	Start pressure at compressor outlet
$T_{\text{start,inlet}}$	Tstart_in	K	Start temperature at compressor inlet
$T_{\text{start,outlet}}$	Tstart_out	K	Start temperature at compressor outlet
$\dot{M}_{\text{start}}$	m_flow_start	kg/s	Start mass flow rate through compressor
	Variables		
s_{inlet}	sin	J/kgK	Inlet specific entropy
$h_{\text{out,iso}}$	hout_iso	J/kg	Outlet specific enthalpy, assuming isentropic compression
h_{out}	hout	J/kg	Actual outlet specific enthalpy
p_{out}	pout	Pa	Outlet pressure
$\dot{M}$	w	kg/s	Mass flow rate through compressor
$\dot{W}$	Power	W	Compressor power consumption
η	eta		Compressor isentropic efficiency
$\dot{M}_{\text{factor}}$	m_flow_factor		Instantaneous mass flow rate as a fraction of design flow rate
	Fluid states		
$\tilde{S}_{\text{inlet}}$	state_in		Fluid state at inlet
$\tilde{S}_{\text{iso}}$	state_iso		Fluid state at outlet, assuming isentropic compression

Table 3-6: Properties for compressor model

Two flanges are used in the compressor model. Firstly, an inlet 2PF flange is used with properties $\dot{M}_{\text{inlet}}$, p_{inlet} and h_{inlet} for the air mass flow rate, pressure and enthalpy respectively

at the inlet. Secondly, an outlet 2PF flange with properties $\dot{M}_{\text{outlet}}$, p_{outlet} and h_{outlet} for the air mass flow rate, pressure and enthalpy respectively at the outlet.

Since flow reversal cannot be allowed in the intercooler for the modelling assumptions to hold, the model asserts that the inlet mass flow rate is positive:

$$\dot{M}_{\text{inlet}} > 0 \qquad (3\text{-}62)$$

Where this is not the case, the model is halted, and an error message posted.

Mass balance is defined:

$$\dot{M}_{\text{inlet}} + \dot{M}_{\text{outlet}} = 0 \qquad (3\text{-}63)$$

The instantaneous mass flow rate is defined:

$$\dot{M} = \dot{M}_{\text{inlet}} \qquad (3\text{-}64)$$

The mass flow rate factor is calculated:

$$\dot{M}_{\text{factor}} = \frac{\dot{M}}{\dot{M}_{\text{design}}} \qquad (3\text{-}65)$$

From this, a value for η is determined from the matrix $\eta[x, 2]$. The first column of this matrix contains the lookup values for $\dot{M}_{\text{factor}}$ while the second column contains the resulting efficiency for the compressor. The model interpolates values, resulting in a continuous relationship between $\dot{M}_{\text{factor}}$ and η. This is to capture the fact that compressor efficiency will fall when the compressor runs at less than its design capacity.

The inlet state, $\tilde{S}_{\text{inlet}}$, is defined using the medium model and the inlet properties p_{inlet} and h_{inlet}, with the inStream command used for the latter. The outlet pressure is defined:

$$PR = \frac{p_{\text{out}}}{p_{\text{inlet}}} \qquad (3\text{-}66)$$

The isentropic transformation is then applied. The specific entropy at the inlet, s_{inlet}, is determined from the state $\tilde{S}_{\text{inlet}}$. Assuming isentropic expansion, this entropy is the same at the

outlet and the isentropic outlet state, $\tilde{S}_{\text{iso}}$, is defined using the medium model and s_{inlet} and p_{out}. The isentropic outlet specific enthalpy,$h_{\text{out,iso}}$, is then determined from $\tilde{S}_{\text{iso}}$.

The actual outlet specific enthalpy can then be calculated using the definition of isentropic efficiency:

$$h_{\text{out}} = \frac{h_{\text{out,iso}} - h_{\text{inlet}}}{\eta} + h_{\text{inlet}} \qquad (3\text{-}67)$$

Finally, energy balance is used to calculate the compressor power consumption:

$$\dot{W} = \dot{M}(h_{\text{out}} - h_{\text{inlet}}) \qquad (3\text{-}68)$$

3.2.7. Turbines

Turbines are used to extract energy from expanding fluid flows. These are vital components for the air power model. The turbine model is purpose-built for this study and is very similar to the compressor model.

Item	Name in code	Units	Description
	Parameters		
	Medium		Medium package for fluid
$\dot{M}_{\text{design}}$	m_flow_des	kg/s	Design mass flow rate
PR	PR		Pressure ratio of turbine
$\eta[x, 2]$	tableEta		Table with x rows defining the turbine isentropic efficiency at different mass flow rates
	Initial parameters		
$p_{\text{start,inlet}}$	pstart_in	Pa	Start pressure at turbine inlet
$p_{\text{start,outlet}}$	pstart_out	Pa	Start pressure at turbine outlet
$T_{\text{start,inlet}}$	Tstart_in	K	Start temperature at turbine inlet
$T_{\text{start,outlet}}$	Tstart_out	K	Start temperature at turbine outlet
$\dot{M}_{\text{start}}$	m_flow_start	kg/s	Start mass flow rate through turbine
	Variables		
s_{inlet}	sin	J/kgK	Inlet specific entropy
$h_{\text{out,iso}}$	hout_iso	J/kg	Outlet specific enthalpy, assuming isentropic compression
h_{out}	hout	J/kg	Actual outlet specific enthalpy
p_{out}	pout	Pa	Outlet pressure
$\dot{M}$	w	kg/s	Mass flow rate through turbine
$\dot{W}$	Power	W	Turbine power consumption
η	eta		Turbine isentropic efficiency

$\dot{M}_{\text{factor}}$	m_flow_factor	Instantaneous mass flow rate as a fraction of design flow rate
Fluid states		
$\tilde{S}_{\text{inlet}}$	state_in	Fluid state at inlet
$\tilde{S}_{\text{iso}}$	state_iso	Fluid state at outlet, assuming isentropic compression

Table 3-7: Properties for turbine model

Two flanges are used in the turbine model. Firstly, an inlet 2PF flange is used with properties $\dot{M}_{\text{inlet}}$, p_{inlet} and h_{inlet} for the air mass flow rate, pressure and enthalpy respectively at the inlet. Secondly, an outlet 2PF flange with properties $\dot{M}_{\text{outlet}}$, p_{outlet} and h_{outlet} for the air mass flow rate, pressure and enthalpy respectively at the outlet.

Since flow reversal cannot be allowed in the turbine for the modelling assumptions to hold, the model asserts that the inlet mass flow rate is positive:

$$\dot{M}_{\text{inlet}} > 0 \qquad (3\text{-}69)$$

Where this is not the case, the model is halted, and an error message posted.

Mass balance is defined:

$$\dot{M}_{\text{inlet}} + \dot{M}_{\text{outlet}} = 0 \qquad (3\text{-}70)$$

The instantaneous mass flow rate is defined:

$$\dot{M} = \dot{M}_{\text{inlet}} \qquad (3\text{-}71)$$

The mass flow rate factor is calculated:

$$\dot{M}_{\text{factor}} = \frac{\dot{M}}{\dot{M}_{\text{design}}} \qquad (3\text{-}72)$$

From this, a value for η is determined from the matrix $\eta[x, 2]$. The first column of this matrix contains the lookup values for $\dot{M}_{\text{factor}}$ while the second column contains the resulting efficiency for the turbine. The model interpolates values, resulting in a continuous relationship between $\dot{M}_{\text{factor}}$ and η. As before, this is to capture the fact that turbine efficiency will fall when the turbine runs at less than its design capacity (Karakurt and Gunes, 2017).

The inlet state, $\tilde{S}_{\text{inlet}}$, is defined using the medium model and the inlet properties p_{inlet} and h_{inlet}, with the inStream command used for the latter. The outlet pressure is defined:

$$PR = \frac{p_{\text{out}}}{p_{\text{inlet}}} \qquad (3\text{-}73)$$

The isentropic transformation is then applied. The specific entropy at the inlet, s_{inlet}, is determined from the state $\tilde{S}_{\text{inlet}}$. Assuming isentropic expansion, this entropy is the same at the outlet and the isentropic outlet state, $\tilde{S}_{\text{iso}}$, is defined using the medium model and s_{inlet} and p_{out}. The isentropic outlet specific enthalpy, $h_{\text{out,iso}}$, is then determined from $\tilde{S}_{\text{iso}}$.

The actual outlet specific enthalpy can then be calculated using the definition of isentropic efficiency:

$$h_{\text{out}} = \eta\left(h_{\text{out,iso}} - h_{\text{inlet}}\right) + h_{\text{inlet}} \qquad (3\text{-}74)$$

Finally, energy balance is used to calculate the turbine power output:

$$\dot{W} = \dot{M}(h_{\text{inlet}} - h_{\text{out}}) \qquad (3\text{-}75)$$

It should be noted that equations (3-74) and (3-75) are the only differences from the compressor model.

3.2.8. Gravel bed

A gravel bed is an important part of the LAES system and provides a means of passively cooling air being liquefied using gravel that has been cooled by air that has previously been vaporised. This model has been purpose-built.

Item	Name in code	Units	Description
		Parameters	
N_{V}	Nw		Number of model volumes
M	M	kg	Total mass of gravel material
C_{m}	cm	J/kgK	Heat capacity of the gravel
κ	k	W/mK	Thermal conductivity of the gravel
A_{eff}	A_eff	m^2	Effective area for conduction
x_{vol}	VolDist	m	Distance between volume centres
		Initial parameters	
$T_{\text{start}}[N_V]$	Tvolstart[Nw]	K	Start temperature of all volumes
		Variables	
$T[N_V]$	Tvol[Nw]	K	Instantaneous volume temperature
$\dot{Q}_{\text{cond}}[N_V - 1]$	Q_Cond[Nw-1]	W	Volume heat transfer rates by conduction

Table 3-8: Properties for gravel bed model

A DHT flange is used in the gravel bed model for heat exchange with an associated fluid flow. This has properties $T_{\text{surf}}[N_V]$ and $\dot{Q}_{\text{surf}}[N_V]$ for the gravel bed surface temperature and the surface heat flow respectively.

Equations are defined for the heat flow between volumes for each volume j:

$$\dot{Q}_{\text{cond}}[j] = \frac{\kappa A_{\text{eff}}}{x_{\text{vol}}}(T[j+1] - T[j]) \qquad (3\text{-}76)$$

By definition, a positive value for $\dot{Q}_{\text{cond}}[j]$ represents a heat flow into that volume. The number of equations here is one less than the number of volumes, since they are concerned with the flow of heat between volumes.

With the inclusion of conduction, three energy balance equations are required. Firstly, two for the first volume, 1, and for the final volume, N_V:

$$\frac{MC_{\text{m}}}{N_V}\frac{dT[1]}{dt} = \dot{Q}_{\text{surf}}[1] + \dot{Q}_{\text{cond}}[1] \qquad (3\text{-}77)$$

$$\frac{MC_{\text{m}}}{N_V}\frac{dT[N_V]}{dt} = \dot{Q}_{\text{surf}}[N_V] - \dot{Q}_{\text{cond}}[N_V - 1] \qquad (3\text{-}78)$$

Finally, an equation for each other volume j where $j = 2, \dots, N_V - 1$:

$$\frac{MC_{\text{m}}}{N_V}\frac{dT[j]}{dt} = \dot{Q}_{\text{surf}}[j] + \dot{Q}_{\text{cond}}[j] - \dot{Q}_{\text{cond}}[j-1] \qquad (3\text{-}79)$$

The surface temperature is equated to the temperature of that volume for each volume j:

$$T_{\text{surf}}[j] = T[j] \qquad (3\text{-}80)$$

3.2.9. Cold storage

The gravel bed model discussed in section 3.2.8 needs to be combined with a fluid flow model, described in section 3.2.1, to be useful. As discussed in section 3.2.4, this allows parameters that are shared by both models to be defined at the top level, thus limiting the number of user-input parameters required.

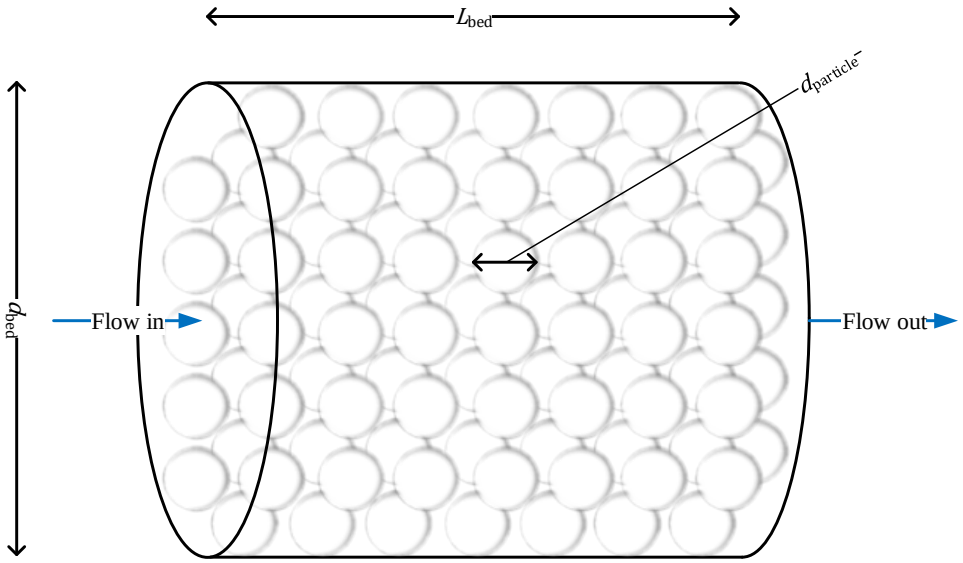

Figure 3-4: Gravel bed diagram showing key dimensions

Figure 3-4 is a diagram of the cold store. In reality, it is taken to be a cylindrical metal tank containing the gravel bed. The fluid, in this case air, enters the cold store at one end, exchanges heat with the surface of the particles comprising the gravel bed, and flows out of the opposite end. In the model, the same effect is achieved by connecting a 1DFV flow model with the gravel bed model via a DHT flange.

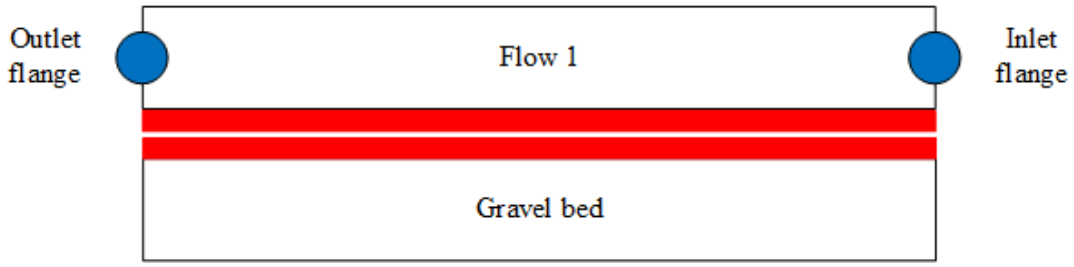

Figure 3-5: Gravel bed schematic (red bars represent DHT flanges)

Figure 3-5 shows a schematic of the gravel bed model and once again, adjacent DHT nodes are connected. As before, only newly introduced parameters are discussed below. Where sub-component parameters are omitted, these should be assumed as being defined in the top-level heat exchanger model and propagating through to the relevant components. For clarity, any component parameters are shown with a subscript in angle brackets, ⟨f⟩ for the 1DFV flow model and ⟨g⟩ for the gravel bed. For example $L_{\langle f \rangle}$ references the length parameter for the flow.

Item	Name in code	Units	Description
		Parameters	
	Medium		Medium package for flow fluid
N	Nodes		Number of wall nodes
d_{bed}	FlowDiameter	m	Internal diameter of the gravel bed
L_{bed}	FlowLength	m	Length of the gravel bed
ρ_{particle}	ParticleDensity	m	Density of the gravel bed particles
d_{particle}	ParticleDiameter	m	Diameter of the gravel bed particles
$\dot{M}$	NomMassFlowRate	kg/s	Nominal mass flow rate

Table 3-9: Parameters for cold storage model

Parameters for the number of nodes and volumes are defined:

$$N_{\langle \text{f} \rangle} = N \qquad (3\text{-}81)$$

$$N_{V,\langle \text{f} \rangle} = N_{V,\langle \text{g} \rangle} = N - 1 \qquad (3\text{-}82)$$

The flow length and area are defined:

$$L_{\langle \text{f} \rangle} = L_{\text{bed}} \qquad (3\text{-}83)$$

$$A_{\langle \text{f} \rangle} = \frac{\pi}{4} {d_{\text{bed}}}^2 \qquad (3\text{-}84)$$

The void fraction (the amount of empty space) of a gravel bed is an important factor to a number of other parameters. To simplify the following equations, it is hereafter denoted ε and is estimated using the empirical relationship (Sciacovelli et al., 2017b):

$$\varepsilon = 0.375 + 0.17 \frac{d_{\text{particle}}}{d_{\text{bed}}} + 0.39 \left(\frac{d_{\text{particle}}}{d_{\text{bed}}} \right)^2 \qquad (3\text{-}85)$$

As discussed in section 2.6, the perimeter of the heat transfer surface is defined:

$$\omega_{\langle \text{f} \rangle} = \frac{3\pi}{2} (1 - \varepsilon) d_{\text{bed}} \qquad (3\text{-}86)$$

As discussed in the same section, the heat transfer coefficient is defined using the empirical relationship:

$$\gamma_{\langle \text{f} \rangle} = \frac{700}{6(1-\varepsilon)} \left(\frac{4\dot{M}}{\pi {d_{\text{bed}}}^2} \right)^{0.76} {d_{\text{particle}}}^{0.24} \qquad (3\text{-}87)$$

The total mass of storage media is defined by multiplying the occupied volume fraction by the particle density:

$$M_{\langle g \rangle} = \frac{(1-\varepsilon)\pi}{4} d_{\text{bed}} L_{\text{bed}} \rho_{\text{particle}} \quad (3\text{-}88)$$

3.2.10. Vapour-liquid separator

Another important part of the liquefaction plant is the vapour-liquid separator. Following the expansion stage, the air will be in a two-phase state. The separator calculates the fluid properties and flow rates of the separated liquid and vapour fractions.

Item	Name in code	Units	Description
		Parameters	
	Medium		Medium package for flow fluid
		Variables	
χ_{mix}	x		Vapour quality of mix
$\dot{H}_{\text{mix}}$	HMixIn	W	Enthalpy flow rate of mix into separator
$\dot{H}_{\text{liquid}}$	HLiquidOut	W	Enthalpy flow rate of liquid out of separator
$\dot{H}_{\text{vapour}}$	HVapourOut	W	Enthalpy flow rate of vapour out of separator
p	p	Pa	System pressure
		Fluid states	
$\tilde{S}_{\text{mix}}$	InletState		Fluid state at the inlet
$\tilde{S}_{\text{mix,sat}}$	InletSat		Fluid saturation state at the inlet pressure

Table 3-10: Parameters for vapour-liquid separator model

Three 2PF flanges are used in the vapour-liquid separator model. An inlet flange is used with properties $\dot{M}_{\text{mix}}$, p_{mix} and h_{mix} for the mass flow rate, pressure and enthalpy respectively at the inlet. Two outlet 2PF flanges are used. The first with properties $\dot{M}_{\text{liquid}}$, p_{liquid} and h_{liquid} for the mass flow rate, pressure and enthalpy respectively at the liquid outlet. The second with properties $\dot{M}_{\text{vapour}}$, p_{vapour} and h_{vapour} for the mass flow rate, pressure and enthalpy respectively at the vapour outlet.

Since flow reversal cannot be allowed in the separator for the modelling assumptions to hold, the model asserts that the inlet mass flow rate is positive:

$$\dot{M}_{\text{mix}} > 0 \quad (3\text{-}89)$$

Where this is not the case, the model is halted, and an error message posted.

The inlet fluid state, $\tilde{S}_{\text{mix}}$, is defined on the inlet pressure p_{mix} and enthalpy h_{mix}. The vapour quality at the inlet, χ_{mix}, is defined by reference to this state. Mass balance can then be defined:

$$\dot{M}_{\text{liquid}} = (1 - \chi)\dot{M}_{\text{mix}} \quad (3\text{-}90)$$

$$\dot{M}_{\text{vapour}} = \chi\dot{M}_{\text{mix}} \quad (3\text{-}91)$$

The separator pressure is defined on the inlet pressure:

$$p = p_{\text{mix}} \quad (3\text{-}92)$$

Pressure is taken to be equal throughout the separator:

$$p_{\text{liquid}} = p_{\text{vapour}} \quad (3\text{-}93)$$

The inlet saturation state, $\tilde{S}_{\text{mix,sat}}$, is defined on the pressure p. The liquid enthalpy, h_{liquid}, is defined as the enthalpy at the bubble point with reference to $\tilde{S}_{\text{mix,sat}}$.

The enthalpy flow rates are defined:

$$\dot{H}_{\text{mix}} = \dot{M}_{\text{mix}} h_{\text{mix}} \quad (3\text{-}94)$$

$$\dot{H}_{\text{liquid}} = -\dot{M}_{\text{liquid}} h_{\text{liquid}} \quad (3\text{-}95)$$

$$\dot{H}_{\text{vapour}} = -\dot{M}_{\text{vapour}} h_{\text{vapour}} \quad (3\text{-}96)$$

Once again, the inStream command is for equation (3-94) to specify enthalpy flowing into the separator. Energy balance is thus defined:

$$\dot{H}_{\text{mix}} = \dot{H}_{\text{liquid}} + \dot{H}_{\text{vapour}} \quad (3\text{-}97)$$

A single unused balancing equation is defined:

$$\dot{M}_{\text{mix}} h_{\text{mix}} + \dot{M}_{\text{liquid}} h_{\text{liquid}} + \dot{M}_{\text{vapour}} h_{\text{vapour}} = 0 \quad (3\text{-}98)$$

In contrast to equations (3-94) to (3-96), the inStream command is used for h_{liquid} and h_{vapour} for reverse flow. This equation remains unused due to the assertion of equation (3-89) but its presence is required to balance the model.

3.2.11. Storage tank

Some means of fluid storage is required for the LAES plant. In this case, it is a fixed pressure tank. This model has been purpose-built.

Item	Name in code	Units	Description
		Parameters	
	Medium		Medium package for fluid
p	p	Pa	Tank design pressure
		Initial parameters	
M_{start}	Mstart	kg	Initial stored fluid mass
h_{start}	hstart	J/kg	Initial fluid specific enthalpy
	SSinit		Boolean parameter for steady-state initialisation
		Variables	
V	V	m^3	Volume of fluid stored
M	M	kg	Mass of fluid stored
H	H	J	Total enthalpy of fluid in tank
h	h	J/kg	Specific enthalpy of fluid in tank
ρ	rho	kg/m^3	Density of fluid in tank
h_{in}	hin	J/kg	Specific enthalpy at inlet
h_{out}	hout	J/kg	Specific enthalpy at outlet
		Fluid states	
$\tilde{S}$	state		Fluid state inside tank

Table 3-11: Parameters for storage tank model

Two flanges are used in the tank model. Firstly, an inlet 2PF flange is used with properties $\dot{M}_{\text{inlet}}$, p_{inlet} and h_{inlet} for the mass flow rate, pressure and enthalpy respectively at the inlet. Secondly, an outlet 2PF flange with properties $\dot{M}_{\text{outlet}}$, p_{outlet} and h_{outlet} for the mass flow rate, pressure and enthalpy respectively at the outlet.

An assertion is made that flow at the inlet let must be into the tank and flow at the outlet must be out of the tank:

$$\dot{M}_{\text{inlet}} > 0 \qquad (3\text{-}99)$$

$$\dot{M}_{\text{outlet}} < 0 \qquad (3\text{-}100)$$

The inlet and outlet specific enthalpies are then equated to the flange specific enthalpies:

$$h_{\text{inlet}} = h_{\text{in}} \qquad (3\text{-}101)$$

$$h_{\text{outlet}} = h_{\text{out}} \qquad (3\text{-}102)$$

The inStream command is used for equation (3-101) to denote enthalpy entering the tank. The flange specific enthalpies are equated to the specific enthalpy of the fluid in the tank:

$$h_{\text{inlet}} = h_{\text{outlet}} \qquad (3\text{-}103)$$

The flange pressure are equated to the tank pressures:

$$p_{\text{inlet}} = p_{\text{outlet}} \qquad (3\text{-}104)$$

Energy balance for the tank is defined:

$$\frac{dH}{dt} = \dot{M}_{\text{inlet}} h_{\text{in}} + \dot{M}_{\text{outlet}} h_{\text{out}} \qquad (3\text{-}105)$$

Mass balance is defined:

$$\frac{dM}{dt} = \dot{M}_{\text{inlet}} + \dot{M}_{\text{outlet}} \qquad (3\text{-}106)$$

The fluid specific enthalpy is defined:

$$H = Mh \qquad (3\text{-}107)$$

The fluid state within the tank, $\tilde{S}$, is defined using the pressure p and the specific enthalpy h. The fluid density, ρ is defined by reference to the fluid state. The volume of fluid within the tank is then calculated:

$$V = \frac{M}{\rho} \qquad (3\text{-}108)$$

3.2.12. Mass flow source

The mass flow source provides a supply of a fluid at a given flow rate. This flow rate can be set either by a parameter or by using an external real number source. The latter allows the user to vary the flow rate, rather than having it fixed throughout the simulation. This component determines the mass flow rate for all components connected to it. The ThermoPower model (Casella, 2014) was deemed sufficient for this study and was used with some small modifications.

Item	Name in code	Units	Description
			Parameters
	Medium		Medium package for fluid
$\dot{M}_{\text{nom}}$	w0	kg/s	Nominal mass flow rate
h	h0	J/kg	Nominal specific enthalpy
	use_in_w0		Boolean operator activating mass flow rate input
	use_in_h		Boolean operator activating specific enthalpy input
			Variables
$\dot{M}$	w	kg/s	Instantaneous mass flow rate

Table 3-12: Parameters for storage tank model

A single outlet 2PF flange with properties $\dot{M}_{\text{outlet}}$, p_{outlet} and h_{outlet} for the mass flow rate, pressure and enthalpy respectively at the outlet. Where the mass flow input Boolean is set to true, an interface is used to provide a mass flow input $\dot{M}_{\text{input}}$. Where the enthalpy input Boolean is set to true, an interface is used to provide a specific enthalpy input h_{input}.

The mass flow rate at the flange is defined:

$$\dot{M}_{\text{outlet}} = -\dot{M} \qquad (3\text{-}109)$$

The instantaneous mass flow rate is defined:

$$\dot{M} = \dot{M}_{\text{input}} \qquad (3\text{-}110)$$

Where the mass flow input Boolean is set to false, the input mass flow rate is defined using the fixed parameter:

$$\dot{M}_{\text{input}} = \dot{M}_{\text{nom}} \qquad (3\text{-}111)$$

The specific enthalpy is defined:

$$h_{\text{outlet}} = h_{\text{input}} \qquad (3\text{-}112)$$

Where the specific enthalpy input Boolean is set to false, the specific enthalpy is defined using the fixed parameter:

$$h_{\text{input}} = h_{\text{nom}} \qquad (3\text{-}113)$$

3.2.13. Mass flow sink

The mass flow sink provides a sink for a fluid at a given flow rate. This flow rate can be set either by a parameter or by using an external real number source. The latter allows the user to vary the flow rate, rather than having it fixed throughout the simulation. This component determines the mass flow rate for all components connected to it. The ThermoPower model (Casella, 2014) was again deemed sufficient for this study and was used with some small modifications.

Item	Name in code	Units	Description
			Parameters
	Medium		Medium package for fluid
$\dot{M}_{\text{nom}}$	w0	kg/s	Nominal mass flow rate
h	h0	J/kg	Nominal specific enthalpy
	use_in_w0		Boolean operator activating mass flow rate input
	use_in_h		Boolean operator activating specific enthalpy input
			Variables
$\dot{M}$	w	kg/s	Instantaneous mass flow rate

Table 3-13: Parameters for storage tank model

A single inlet 2PF flange with properties $\dot{M}_{\text{inlet}}$, p_{inlet} and h_{inlet} for the mass flow rate, pressure and enthalpy respectively at the inlet. Where the mass flow input Boolean is set to true, an interface is used to provide a mass flow input $\dot{M}_{\text{input}}$. Where the enthalpy input Boolean is set to true, an interface is used to provide a specific enthalpy input h_{input}.

The mass flow rate at the flange is defined:

$$\dot{M}_{\text{inlet}} = -\dot{M} \qquad (3\text{-}114)$$

The instantaneous mass flow rate is defined:

$$\dot{M} = \dot{M}_{\text{input}} \qquad (3\text{-}115)$$

Where the mass flow input Boolean is set to false, the input mass flow rate is defined using the fixed parameter:

$$\dot{M}_{\text{input}} = \dot{M}_{\text{nom}} \qquad (3\text{-}116)$$

The specific enthalpy is defined:

$$h_{\text{inlet}} = h_{\text{input}} \quad (3\text{-}117)$$

Where the specific enthalpy input Boolean is set to false, the specific enthalpy is defined using the fixed parameter:

$$h_{\text{input}} = h_{\text{nom}} \quad (3\text{-}118)$$

3.2.14. Pump (simple)

Two pump models were developed. This one is designed for use in conjunction with the flow controllers discussed in sections 3.2.12 and 3.2.13 in open power cycles and simply calculates the power required for a defined pressure increase based mass flow provided by a mass flow source or sink. A second pump model will be described in section 3.2.15 and acts as a flow controller. Both pump models were purpose-build for this model.

Item	Name in code	Units	Description
	Parameters		
	Medium		Medium package for fluid
Δp	dp	Pa	Pressure increase in pump
η	Eta		Pump efficiency
	Variables		
$\dot{M}$	w	kg/s	Mass flow rate
$\dot{V}$	q	m^3/s	Volumetric flow rate
h	h	J/kg	Fluid specific enthalpy
h_{in}	hin	J/kg	Specific enthalpy of fluid at inlet
h_{out}	hout	J/kg	Specific enthalpy of fluid at outlet
ρ	rho	kg/m^3	Fluid density
$\dot{W}$	Power	W	Power consumption
	Fluid states		
$\tilde{S}_{\text{inlet}}$	state_in		Fluid state at inlet

Table 3-14: Properties for pump (simple) model

Two flanges are used in the pump (simple) model. Firstly, an inlet 2PF flange is used with properties $\dot{M}_{\text{inlet}}$, p_{inlet} and h_{inlet} for the air mass flow rate, pressure and enthalpy respectively at the inlet. Secondly, an outlet 2PF flange with properties $\dot{M}_{\text{outlet}}$, p_{outlet} and h_{outlet} for the air mass flow rate, pressure and enthalpy respectively at the outlet.

Flow reversal is not allowed in the pump, so the model asserts that the inlet mass flow rate is positive:

$$\dot{M}_{\text{inlet}} > 0 \quad (3\text{-}119)$$

Where this is not the case, the model is halted, and an error message posted.

The mass flow rate is defined:

$$\dot{M} = \dot{M}_{\text{inlet}} \qquad (3\text{-}120)$$

The fluid state at the inlet, $\tilde{S}_{\text{inlet}}$, is defined based on the inlet specific enthalpy, h_{inlet}, and the inlet pressure, p_{inlet}. The fluid density, ρ, is defined by reference to this state. The volumetric flow rate is calculated:

$$\dot{V} = \frac{\dot{M}}{\rho} \qquad (3\text{-}121)$$

The power consumed by the pump is defined:

$$\dot{W} = \frac{\Delta p \dot{V}}{\eta} \qquad (3\text{-}122)$$

The outlet pressure is calculated:

$$\Delta p = p_{\text{outlet}} - p_{\text{inlet}} \qquad (3\text{-}123)$$

The inlet and outlet pressures are equated to the model variables:

$$h_{\text{in}} = h_{\text{inlet}} \qquad (3\text{-}124)$$

$$h_{\text{out}} = h_{\text{outlet}} \qquad (3\text{-}125)$$

Here, equation (3-124) uses the inStream command to specify specific enthalpy entering the pump. An additional balancing equation for reverse flow is defined but remains unused due to the assertion in equation (3-119).

$$h_{\text{out}} = h_{\text{inlet}} \qquad (3\text{-}126)$$

Mass balance is defined:

$$\dot{M}_{\text{inlet}} + \dot{M}_{\text{outlet}} = 0 \qquad (3\text{-}127)$$

Energy balance is defined:

$$\dot{M}_{\text{inlet}} h_{\text{in}} + \dot{M}_{\text{outlet}} h_{\text{out}} + \dot{W} = 0 \qquad (3\text{-}128)$$

3.2.15. Pump (controller)

This second pump model defines mass flow as a parameter and is used itself as a flow controller for closed cycles where there is no source or terminus for the flow. To facilitate this role, this pump also defines initialisation fluid properties at either the inlet or the outlet, allowing it to replace the role of a source in a closed power cycle. As with the pump (simple) model, this was purpose-built for this model.

Item	Name in code	Units	Description
		Parameters	
	Medium		Medium package for fluid
p_{outlet}	poutlet	Pa	Fluid pressure at outlet
η	Eta		Pump efficiency
		Initial parameters	
$\dot{M}_{\text{start}}$	wstart	kg/s	Initial mass flow rate
$T_{\text{outlet,start}}$	Toutlet	K	Initial fluid temperature
		Variables	
Δp	dp	Pa	Pressure increase in pump
$\dot{M}$	w	kg/s	Mass flow rate
$\dot{V}$	q	m^3/s	Volumetric flow rate
h_{in}	hin	J/kg	Specific enthalpy of fluid at inlet
h_{out}	hout	J/kg	Specific enthalpy of fluid at outlet
ρ	rho	kg/m^3	Fluid density
$\dot{W}$	Power	W	Power consumption
		Fluid states	
$\tilde{S}_{\text{inlet}}$	state_in		Fluid state at inlet
$\tilde{S}_{\text{outlet,start}}$	state_out		Initial fluid state at outlet

Table 3-15: Properties for pump (controller) model

As before, two flanges are used in the pump (controller) model. Firstly, an inlet 2PF flange is used with properties $\dot{M}_{\text{inlet}}$, p_{inlet} and h_{inlet} for the air mass flow rate, pressure and enthalpy respectively at the inlet. Secondly, an outlet 2PF flange with properties $\dot{M}_{\text{outlet}}$, p_{outlet} and h_{outlet} for the air mass flow rate, pressure and enthalpy respectively at the outlet.

Again, flow reversal is not allowed in the pump, so the model asserts that the inlet mass flow rate is non-negative:

$$\dot{M}_{\text{inlet}} \geq 0 \qquad (3\text{-}129)$$

In this model, the starting mass flow rate is defined during initialisation:

$$\dot{M} = \dot{M}_{\text{start}} \qquad (3\text{-}130)$$

The initial fluid state, $\tilde{S}_{\text{start}}$, is defined according to T_{start} and p_{start}. The initial specific enthalpy is defined based on this initial fluid state. Where the startInlet Boolean is set to true, this specific enthalpy is used to define the start value for h_{in}. Otherwise, it is used to define the starting value for h_{out}.

Finally, the starting pressures are defined:

$$p_{\text{inlet}} = p_{\text{start}} \qquad (3\text{-}131)$$

$$p_{\text{outlet}} = p_{\text{start}} \qquad (3\text{-}132)$$

Equation (3-131) is used where the startInlet Boolean is set to true and equation (3-132) is used where the Boolean is set to false.

3.2.16. A note on flow controllers

The storage tank in section 3.2.11, the mass flow controller in sections 3.2.12 and 3.2.13, and the pump (controller) in section 3.2.15 provide all of the means of control required for the open cycle models. The storage tank and the pressure sink allow pressure to be defined at either the origin or the terminus of the flow, with the pressures throughout the remainder of the model calculated either via flow pressure drops or by turbomachinery pressure ratios. The latter allows mass flow rate to be defined at either a source or sink (containing an infinite amount of the fluid in question) and the mass flow rates throughout the remainder of the model being calculated by the respective components' mass balance equations. It is important to note that only one pressure definition and one mass flow rate definition should be used for each model to prevent the model from becoming over constrained.

3.2.17. Flow joiner

ThermoPower (Casella, 2014) provides a basis for this model, however the original model allows flow reversal through the component. Due to the construction of the flow splitter discussed in section 3.2.18 , reverse flow is not necessary and the ThermoPower model was simplified to prevent reverse flow through the joiner.

Three 2PF flanges are used in the joiner model. Two inlet flanges are used with properties $\dot{M}_{\text{inlet,1}}$, $p_{\text{inlet,1}}$ and $h_{\text{inlet,1}}$, and $\dot{M}_{\text{inlet,2}}$, $p_{\text{inlet,2}}$ and $h_{\text{inlet,2}}$ for the mass flow rate, pressure and

enthalpy at the inlets 1 and 2 respectively. One outlet 2PF flange is used with properties $\dot{M}_{\text{outlet}}$, p_{outlet} and h_{outlet} for the mass flow rate, pressure and enthalpy respectively at the outlet. No user-defined parameters are required.

Assertions are made concerning the inlet mass flow rates:

$$\dot{M}_{\text{inlet},1} > 0 \qquad (3\text{-}133)$$

$$\dot{M}_{\text{inlet},2} > 0 \qquad (3\text{-}134)$$

Where these are not true, the model is halted, and an error message posted.

Mass balance is defined:

$$\dot{M}_{\text{inlet},1} + \dot{M}_{\text{inlet},2} + \dot{M}_{\text{outlet}} = 0 \qquad (3\text{-}135)$$

Pressure is defined on the outlet flow:

$$p_{\text{inlet},1} = p_{\text{outlet}} \qquad (3\text{-}136)$$

$$p_{\text{inlet},2} = p_{\text{outlet}} \qquad (3\text{-}137)$$

Energy balance is defined:

$$\dot{M}_{\text{inlet},1} h_{\text{inlet},1} + \dot{M}_{\text{inlet},2} h_{\text{inlet},2} + \dot{M}_{\text{outlet}} h_{\text{outlet}} = 0 \qquad (3\text{-}138)$$

Once again, the inStream command is used for the inlet specific enthalpy terms to specify these properties entering the joiner. Additional balancing equations are defined but remain unused due to the assertions made by equations (3-133) and (3-134):

$$h_{\text{inlet},1} = h_{\text{outlet}} \qquad (3\text{-}139)$$

$$h_{\text{inlet},2} = h_{\text{outlet}} \qquad (3\text{-}140)$$

Here, the inStream command is used for the outlet specific enthalpies to specify reverse flow properties.

3.2.18. Flow splitter

ThermoPower (Casella, 2014) provides a basis for this model, however the original model was modified to prevent reverse flow through the joiner.

Item	Name in code	Units	Description
		Parameters	
SR	SplitRatio		Proportion of inlet flow sent to outlet 1

Table 3-16: Properties for flow splitter model

Three 2PF flanges are used in the splitter model. One inlet 2PF flange is used with properties $\dot{M}_{\text{inlet}}$, p_{inlet} and h_{inlet} for the mass flow rate, pressure and enthalpy respectively at the inlet. Two outlet flanges are used with properties $\dot{M}_{\text{outlet,1}}$, $p_{\text{outlet,1}}$ and $h_{\text{outlet,1}}$, and $\dot{M}_{\text{outlet,2}}$, $p_{\text{outlet,2}}$ and $h_{\text{outlet,2}}$ for the mass flow rate, pressure and enthalpy at the outlets 1 and 2 respectively.

Assertions are made on the inlet mass flow rate:

$$\dot{M}_{\text{inlet}} > 0 \qquad (3\text{-}141)$$

Where this is not true, the model is halted, and an error message posted.

Outlet mass flow rates are defined:

$$\dot{M}_{\text{outlet,1}} = -\dot{M}_{\text{inlet}} SR \qquad (3\text{-}142)$$

$$\dot{M}_{\text{outlet,2}} = -\dot{M}_{\text{inlet}} (1 - SR) \qquad (3\text{-}143)$$

Pressure is defined on the inlet flow:

$$p_{\text{inlet}} = p_{\text{outlet,1}} \qquad (3\text{-}144)$$

$$p_{\text{inlet}} = p_{\text{outlet,2}} \qquad (3\text{-}145)$$

Outlet specific enthalpies are defined:

$$h_{\text{inlet}} = h_{\text{outlet,1}} \qquad (3\text{-}146)$$

$$h_{\text{inlet}} = h_{\text{outlet,2}} \qquad (3\text{-}147)$$

Once again, the inStream command is used for the inlet specific enthalpy terms to specify these properties entering the splitter. An additional balancing equation is defined but remains unused due to the assertions made by equation (3-141).

$$h_{\text{inlet}} = h_{\text{outlet},1} \qquad (3\text{-}148)$$

Here, the inStream command is used for the outlet specific enthalpy to specify reverse flow properties.

3.3. Model validation

Validation is an important part of any modelling regimen, especially when a combination of existing and novel code is being used to simulate a complex engineering system, as is the case in this thesis. A major hurdle to validation of the model is that there is only one instance in the literature of a coupled NPP and LAES plant design (Li et al., 2014). The shortcomings of this work are discussed in detail in section 2.5.2 and their implications are explored in the results of Chapter 5. The lack of a comparable plant thus makes holistic model validation impossible.

That said, the modular nature of the model described in this chapter and the way in which components can be tested in isolation allows validation of individual components to be performed against available data, which provides assurances that the novel code is fit for purpose and performing as intended. For this purpose, the Birmingham University and Highview Power literature discussed in section 2.5.2 was used primarily due to the rigour and transparency in its engineering approach, and those groups' access to the pilot plant and their resulting ability to compare their modelling results with experimental data. For some parts of the NPP, NuScale regulatory applications were used.

The basic machinery components (turbines, compressors, and pumps) were compared against the work of the Birmingham University group using their modelling parameters and flow thermophysical properties. All provided identical results the given conditions. This is perhaps unsurprising given the relatively straightforward nature of the modelling of such components and the highly mature state of modelling in this area.

Heat exchangers present something of a greater issue to validation. There are a variety of approaches to heat exchanger modelling, of which the finite volume approach described herein is one of the more complex. The simplifying assumption has been made of a continuous heat transfer coefficient throughout each flow of a given heat exchanger further complicates comparison. The approach taken to ensuring that heat exchanger results would be as accurate

as possible was to set heat transfer coefficients such that thermal power loads on a given heat exchanger of a given size would match those from the literature. For water-water heat exchangers, the NuScale regulatory application (NuScale Power LLC, 2018a) provides the flow stream, heat exchanger area and thermal load data required to make these comparisons. For air-air and air-water heat exchangers, an article from Highview Power (Morgan et al., 2015a) provides the necessary data.

The gravel bed model is perhaps the most difficult component to compare to available data. Whilst the Birmingham University group provide a thorough and detailed treatment of the gravel bed (Sciacovelli et al., 2017b), the assumption of a linear pressure drop along the cold store, as described in section 3.2.9, represents a significant departure from this work. Nevertheless, comparisons can still be made; not least in the quantity of heat transferred between the working fluid and the gravel bed during comparable charge and discharge cycles for a given mass of thermal storage medium. These comparisons show that the quantity of heat transfer was within 1% for a comparable charge or discharge cycle. Whilst this was deemed sufficient for the modelling work discussed in this thesis, the simplifying assumption of a linear pressure drop is an important one that is discussed in greater detail in section 7.3.1.

Ultimately, the comparisons made provide considerable assurance that the engineering modelling approach will provide results sufficiently accurate for the purposes of this thesis: the evaluation of LAES plant output power ratings and the sizing of the components required to achieve these. Whenever a plant design model was built from components, of the kind described in Chapter 5, all flow variables into and out of components were compared to ensure that flanges and connectors were operating as expected.

In light of this, this author would assert that the results of the engineering modelling approach are as accurate as possible in light of the simplifying assumptions that have been made. In a more philosophical sense, the simplifying nature of any modelling approach is non-trivial, and it is important that the developer of any engineering model be aware of the limitations of such assumptions and be as transparent as possible of their implications. This is the purpose of section 7.3.1.

Chapter 4 - Financial modelling

4.1. Introduction

This chapter details the financial model. Section 4.1.1 summarises the objectives of the financial model while section 4.1.2 goes into greater detail of the minutiae of financial modelling under uncertain conditions. Section 4.2 details the basis for, and definition of, the probability distributions for the initial model parameters. Section 4.3 details the way that plant capital costs have been estimated from equipment costs. Section 4.4 details the basis for, and definition of the time series functions used to simulate SPOT market prices. Section 0 details the way the model has been built from its components and summarises the key parameters and their values. The model library is available via Open Research Data Online (Wilson, 2020a)

Model parameters and calculated variables are defined using symbols; either Latin-script alphabet letters or Greek letters. The symbols used, their definitions, and the sections in which parameters or variables are introduced are summarised in Table 4-1. Where variable values vary depending on the values of other variables, the time period symbol is given in brackets, e.g. $A(D)$ defines the daily average price, A, for a given day, D. Where the same parameter is defined independently for different models, the differentiation is made using a subscript, e.g. $\mu_{A(D)}$ described the mean parameter for the daily average price model, whereas $\mu_{\varepsilon(P)}$ denotes the mean parameters for the half-hourly period error value.

Symbol	Description
	Parameters and variables
$\dot{M}$	Mass flow rate
$\dot{W}$	Power
A	Daily average price
C	Cost
I	Chemical engineering plant cost index
N	Random number
R	Revenue (cash flow)
S	Electricity sale price
a	Autoregressive coefficient
b	Moving average coefficient
i	Percentage rate
s	Equipment size
y	Time series value for descriptions
α	Amplitude
β	BetaGeneral distribution parameters
δ	Price difference
ε	Error value (for electricity price model)
ϵ	Error value (for time series model definitions)
θ	Clayton copula parameter
μ	Mean

σ	Volatility (standard deviation)
φ	Ratio
Time periods	
Y	Year
Q	Quarter
D	Day
P	Period (half-hour)
t	Arbitrary time period for descriptions
Identifying subscripts	
CHG	Charge
CONST	Construction
CPI	Consumer prices index
CfD	Contract for difference
DIS	Discharge
DISC	Discount rate
FUEL	Fuel
NPP	Nuclear power plant
O&M	Operation and maintenance
REFUEL	Refuel

Table 4-1: Parameter, variable and other subscript symbol definitions

4.1.1. Objectives

The financial model is intended to determine hybrid plant economics when selling into real-world markets. In order to do this, it is required to fulfil the following objectives:

- determine uncertain initial parameters such as plant capital cost and construction times using probability distributions,
- simulate spot market electricity prices over an extended period using time series,
- estimate NPV distributions under first-of-a-kind (FOAK) and nth-of-a-kind (NOAK) scenarios for different plant outputs.

4.1.2. Background

Financial modelling of power plants is fraught with uncertainty. This is especially true of nuclear power given the complexities of construction, the high capital cost and the frequent overruns in construction time. This study adds further complexity by including energy storage and sale of power into multiple markets; some power is sold on a CfD basis while the variable power output is sold into the SPOT market, where prices are most volatile.

Monte Carlo modelling offers a means of incorporating uncertainty into financial modelling. In an entirely deterministic model, input parameters such as plant cost and construction time are given discrete values and yield a single output, often an NPV value from a DCF analysis. DCF is a means of considering the time-dependent value of money. This is done by estimating future

cash flows and then discounting them based on the cost of capital. This is captured in the following equation:

$$NPV = \sum_{Y=0}^{N} \frac{R(Y)}{(1 + i_{DISC})^{Y}} \qquad (4\text{-}1)$$

where N is the total number of periods, in this case years, $R(Y)$ is the cash flow for a given year, Y is that year and i_{DISC} is the discount rate, dependent on the cost of the capital used to fund the project. Discount rates are determined by the potential appreciation in the value of capital were it not used in a project, typically the interest or growth garnered from more conventional and predictable investments.

In Monte Carlo modelling, each initial parameter is given defined by a probability distribution rather than a static value. The model is then run for a large number of iterations and with each iteration, parameter values are using an RNG and the corresponding probability distribution. Running the model tens of thousands or even hundreds of thousands of times yields a probability distribution for the NPV, rather than a single static value, which provides the relative likelihood of different NPV values.

The model described below also requires the prediction of stochastic variables, chiefly the electricity price and the CPI. In reality, these variables are not simply random. Their values form series where one value is dependent on previous values in the series to a greater or lesser degree. This is in contrast to probability distributions where a value selected for a given iteration has no dependence on the previous values selected and imposes no preference on any future values selected. Time series have long been used in financial modelling, for example in the prediction of share prices.

Obviously, a key consideration in the construction of a model is the definition of the probability distributions used for initial parameters and the definition of time series models used to predict stochastic variables. This chapter describes the decision-making process used in defining these distributions and time series. Section 4.2 describes the definition of distributions for initial parameters, section 4.3 those for the LAES plant capital cost, and section 4.4 describes the definition of time series models.

4.2. Monte Carlo modelling – Initial parameters

This section details the decision-making process in the definition of probability distributions for the Monte Carlo financial model. These definitions are based on historical data as much as possible. It should be noted, however, that their definition remains a largely subjective process and, as a result, not everyone will agree with the justifications to follow. This highlights the importance of sensitivity analysis in the final decision as to whether a plant will be built. As similar plants are built, the distributions should move closer to certainty, allowing a more informed decision to be made by prospective plant operators. Sensitivity analysis will highlight the most important considerations for this process. The parameters used in the final model are summarised in Table 4-5 in section 0.

4.2.1. Nuclear power plant spending factor

The determination of NPP capital cost is a complex problem beyond the scope of this project. The manufacturer's system price will be used for the model, but it is important to consider that overspend is likely on a large NPP construction project. This will be incorporated into the model by a capital cost factor by which the base plant price will be multiplied, with a factor of 1 representing a project that is delivered on-budget. The shape of the probability distribution that defines this factor is an important consideration as the capital investment for the project is an early-stage cost and, as a consequence of DCF likely to be a major driver in the overall NPV of the project. Given that this study considers a novel SMR-based power plant, there is no historical data that this can be directly based on. As a result, the decision was made to use PERT (project evaluation and review technique) distributions. This has the benefit of using a small number of easily defined parameters (minimum, most likely and maximum).

Detailed accountings of costs for recently built nuclear plants are elusive at best, and at worst entirely hidden from the public (Kessides, 2010). As a result, much of the discussion in this section is based upon news articles and the scant financial details that have been made publicly available. Complex engineering projects in the UK and overseas commonly come in over budget, often significantly (MacLeod, 2014, Staff Writer, 2014). The examples shown are all large-scale construction projects, so clearly the capital dedicated to plant construction can be overspent substantially – some of these projects overspend by 100% or more.

Within the nuclear industry, there are also significant overspends. The EPR (European Pressurised Reactor) is the most recent and high-profile example of this. Finland's Olkiluoto EPR was estimated to cost EUR 3.7bn for a 1.6 GWe plant when its construction was first

agreed. Costs were estimated in 2012 to have risen to EUR 8bn (Landauro, 2012) – an overspend of well over 100%. It's important to note that EDF have not updated their cost estimates since the 2012 estimate (Rosendahl and Forsell, 2017), so this is almost certainly out-of-date information. France's Flamanville EPR is even worse – the most recent cost estimate is EUR 10.9bn (World Nuclear News, 2018), up from the starting estimate of EUR 3.3bn – an increase of 230% in 6 years.

The cost rise described in the preceding discussion would seem extreme, and indeed it is. The fact that these significant rises have occurred so soon after the commitment to build has been agreed is further questionable. Whilst it is not the place of this thesis to speculate the reactor designer's potential foreknowledge of overspend, this does raise an important point in the context of financial modelling undertaken herein. Clearly, this kind of overspend is a likely consequence of being the first to build a particular plant, that is, building a FOAK plant. Whilst subsequent NOAK plants are not guaranteed to provide more accurate cost assessments, the assumption that they will is one that is made in this thesis.

That being said, the proposed system considered in this study utilises an SMR, of significantly smaller capacity than the EPR. SMRs are intended to avoid many of the potential pitfalls of conventional nuclear power due to their small, modular nature. The benefits of SMRs are in economies of volume as opposed to economies of scale (Roulstone, 2015). Simply put, being able to build more SMRs could reduce costs as components can be mass produced. We can consider this in a qualitative sense as follows:

The EPRs mentioned are 1.65 GW (electric) plants, which, assuming each has a final commissioned cost of EUR 11bn, or say £10bn (an approximately similar cost of each of the UK's two intended EPRs at the Hinckley Point site (Farrell and Macalister, 2015). This provides a commissioned cost of £6,061 per kW. The original estimate for the Finnish and French plants was £2,037 per kW. The current estimate for the NuScale SMR is $4,200 or £3,500 per kW.

Comparing the EPR and SMR initial plant estimates first, this is perhaps what could be expected - the cost per unit power of the NuScale SMR is around 1.5 times the cost of the EPR - which could represent the increase of per unit costs associated with economies of scale. This is perhaps to be expected; nuclear plants have long suffered from higher costs due to a lack of learning and there is every reason to think that the same would be the case for SMRs until they begin to be built in large numbers (Roulstone, 2015). Even the French nuclear programme, arguably one of the most successful worldwide, saw considerable cost increases, although as (Lévêque, 2015)

notes, this was largely due to redesigns associated with increases in plant size. Similarly, the early SMRs will not benefit from the promised economies of volume.

Whether SMRs can indeed benefit from serialised construction at all is a matter of no small debate. Detailed design and costing of the NPP part of the proposed plant is beyond the scope of this thesis, however the benefits of smaller and serialised construction can be contextualised by considering the pressure vessel of a PWR, a part making up a significant portion of equipment costs (Mizia, 2008). The EPR features the largest pressure vessel, with the fewest separate parts of any reactor build to date, and a range of problems related to both supply chain and material defects have plagued the early EPRs and contributed considerably to delays and cost rises. It is not unreasonable to argue that smaller pressure vessels for SMRs will reduce both equipment costs and supply chain issues, potentially helping to deliver on the promised cost savings associated with SMRs (Power Technology, 2013, Boldon et al., 2014).

This historical insight can be used to define the minimum and maximum ends of the probability distribution for the spending factor. The minimum factor should be the expected production cost for the plant, a factor of 1. The maximum factor should be the maximum historical overspend in the UK – double the budget, or a factor of 2. This is, of course, less than the comparative Flamanville overspend of 3, but it is a core assumption of this thesis that SMR cost savings are achieved. A further benefit of a statistical modelling approach is that conclusions are not static and can be re-evaluated as new data becomes available. The main point of contention is the location of the most likely value between these points.

Since this study intends to explore both FOAK and NOAK scenarios for the nuclear plant, two distributions are required. For a FOAK plant, the most likely value can reasonably be expected to be at the upper end of the probability distribution. In an alternative NOAK scenario, where several such plants have been constructed, the actual project spend can be reasonably expected to be much closer to the expected value, with a reduced maximum spend. The defined distributions for this factor are shown in Figure 4-1.

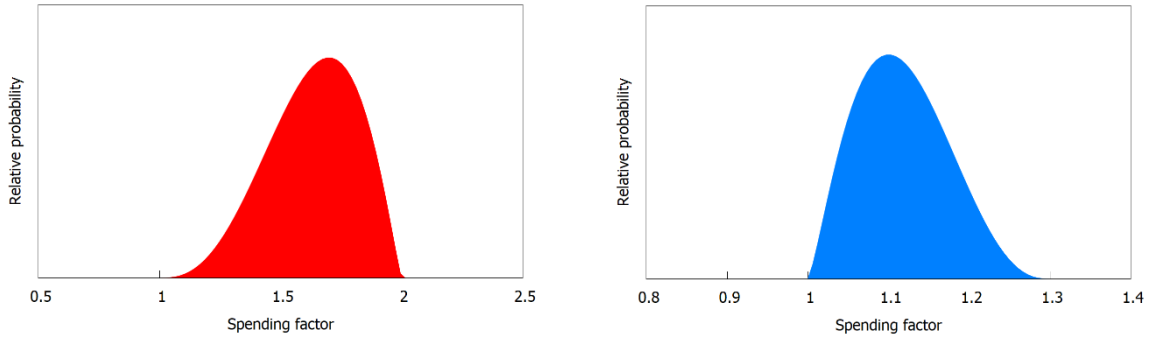

Figure 4-1: Spending factor probability distributions - FOAK on left, NOAK on right

4.2.2. Nuclear power plant construction time

The construction time for the plant is of major practical significance. Whilst nuclear plants run for in excess of sixty years, the fact that plant profitability is considered on an NPV (net present value) basis in this model means that discounted cash flows for years far into the future become almost negligible. Consider the NPV formula:

$$NPV = \sum_{Y=0}^{N} \frac{R(Y)}{(1 + i_{DISC})^{Y}} \qquad (4\text{-}1)$$

where N is the total number of periods, in this case years, $R(Y)$ is the revenue for a given year, t is the current year and i_{DISC} is the discount rate.

In the case of a nuclear power plant that takes 5 years to build and runs for 60, even at modest discount rates of say 8%, the denominator of this formula increases by a factor of 10 over a 30-year period. After the 5 years of construction, the nature of the NPV formula means that the cash flow is discounted by a factor of 1.47 and after 30 years of operation it is discounted by 14.8. Indeed, at 60 years, cash flow is discounted by a factor of nearly 150. This massively outweighs the effect of inflation, which is historically between 2 and 3%. This illustrates the importance of build time. Longevity of nuclear power plants cannot make up for the revenue lost during construction when project value is assessed in this way.

NuScale state a period of 5 years construction time including mobilisation, with a critical path of 3 years (NuScale). The model assumes that costs may be spread over the initial construction period but that funds must be reserved and allocated to the project prior to committing to the 3 year critical path, meaning that these final years of construction can be considered to contribute to loss of revenue. How this is done in model is discussed in section 0.

The way this is expressed within the financial model depends on the limitations of the model. Construction time is analysed by year, and part years cannot be considered due to the use of an annual discount rate. As a result, construction time is not defined by a factor but by a whole number of years. This means that the continuous PERT distribution cannot be used and a binomial distribution is used instead, providing only integer values to the model. This distribution uses 3 parameters; n describing the number of possible values to be taken, p defining how the probabilities of each is weighted and a shift value providing the first of the possible values.

In the model, construction is split into two phases; mobilisation where initial costs are spread over the years and critical path where all capital is considered to be invested in the project and is applied to costs in the first year of critical path construction. Construction projects in the UK have typically seen delays of between 10 and 30% of the expected construction time for the project. This contrasts with the EPR, which has seen construction times double at its Finnish and French plants.

With this information in mind, two potential routes are considered for the construction time values. Firstly, an early scenario where the considered plant is one of the first of its kind and secondly an experienced scenario where several of these plants have been built. Again, the FOAK scenario will weight probabilities towards the higher end, while the NOAK scenario will weight probabilities towards the time expected by the plant designer. The construction times for mobilisation are shown in Figure 4-2 and those for the critical path are shown in Figure 4-3.

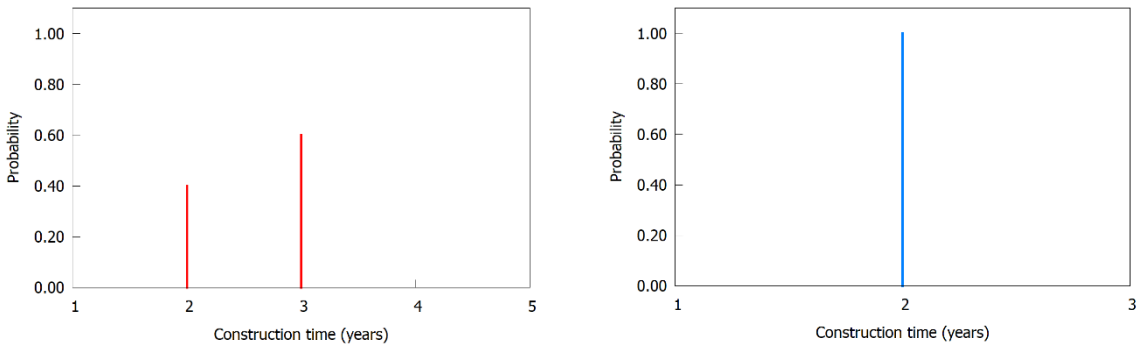

Figure 4-2: Mobilisation construction time probability distributions - FOAK on left, NOAK on right

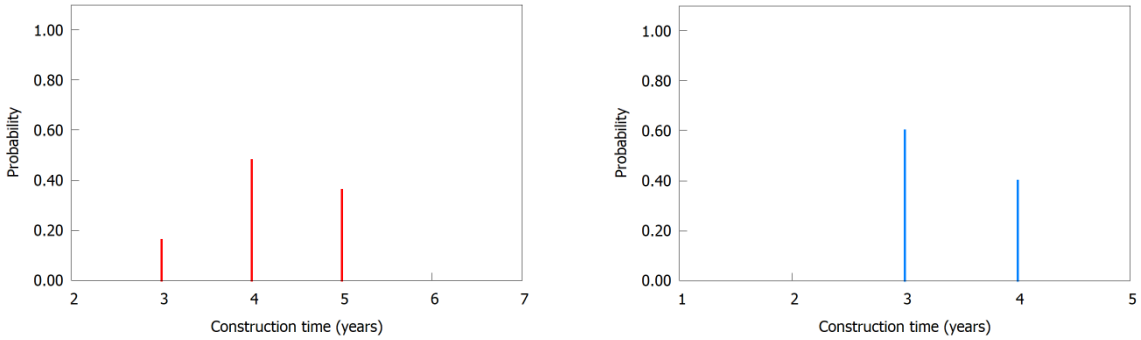

Figure 4-3: Critical path construction time probability distributions - FOAK on left, NOAK on right

Of course, in reality, the construction time and the overspend are closely linked – delays in construction mean workers are on site and paid for longer. As a result, the capital cost and construction time are linked using a copula. A copula correlates two probability distributions and in this model ensures that a high construction cost is correlated to a longer construction time. A three-dimensional Clayton copula is used to correlate the modelled values of NPP spending factor, mobilisation and critical path construction times possible in @RISK. The degree of correlation is defined using a parameter, θ.

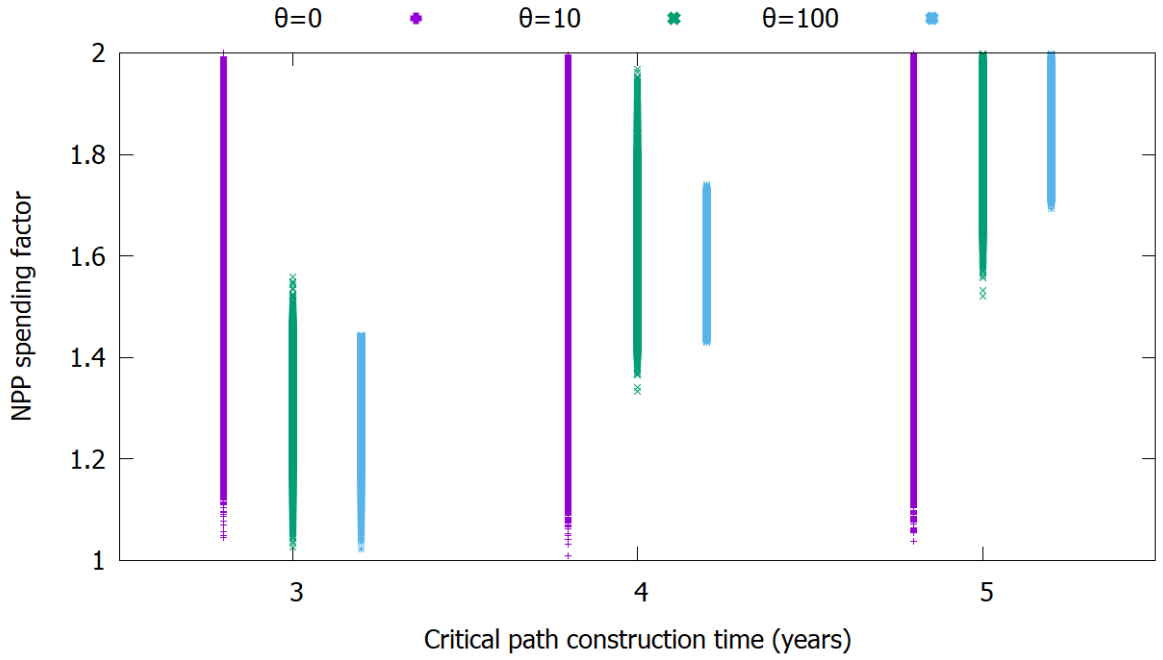

Figure 4-4: Copula parameter comparison using FOAK parameters

The effect of a copula on the modelled values of critical path construction times is shown in Figure 4-4. There are 100,000 points for each value of θ. The effect is clear; the larger the value of θ, the greater the correlation between spending factor and construction time. With $\theta = 0$, there is no forced correlation and the values of NPP spending factor for the different construction times overlap entirely. As θ increases in value, correlation increases and the overlap in NPP spending factor values lessens. For modelling purposes, it was assumed that correlation was high but that there would be some degree of overlap, so a value of $\theta = 25$ was used.

4.2.3. LAES plant construction time

As with the nuclear power plant, the construction time for the LAES plant is also defined by a binomial distribution. The key difference here is that LAES uses existing technology with an established supply chain and fewer safety-critical components (Highview Power, 2015). Plants

can thus be constructed over much shorter time frames. Mobilisation is taken to be 1 year, and critical path timescales are considered to be 1-2 years. Critical path times are weighted towards longer duration for the FOAK scenario and shorter for the NOAK scenario.

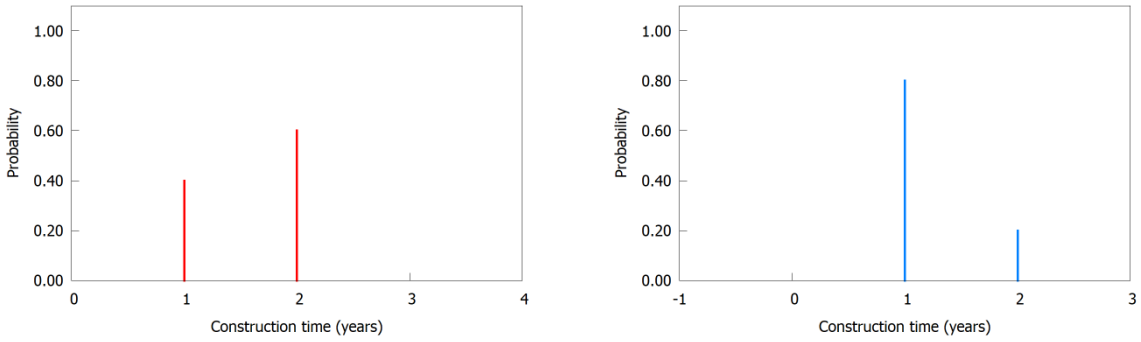

Figure 4-5: LAES mobilisation construction time probability distributions - FOAK on left, NOAK on right

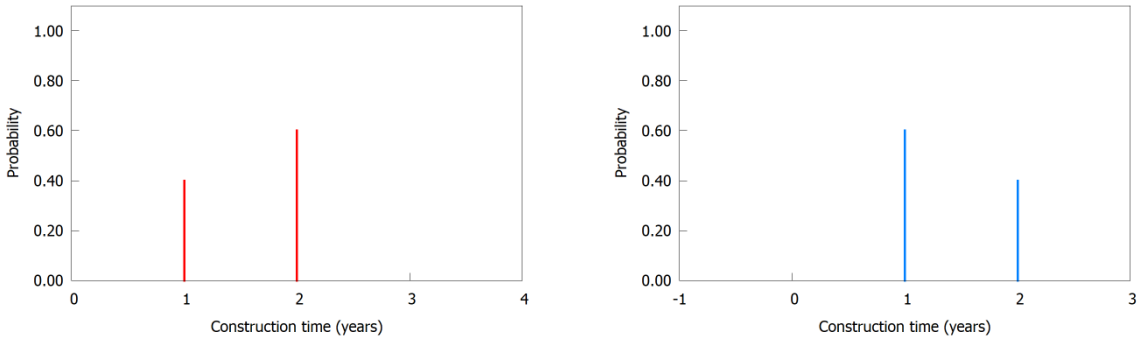

Figure 4-6: LAES critical path construction time probability distributions - FOAK on left, NOAK on right

4.3. Detailed cost estimation – LAES plant

4.3.1. Equipment capital cost estimation

The costs for the LAES system are the focus of this project and have been dealt with in more detail than the NPP costs since the engineering model allows the plant to be simulated and its equipment accurately sized. The approach taken to obtaining base costs for pieces of equipment is discussed in section 2.7. Broadly, equipment costs are estimated using the following formula (Peters et al., 1968):

$$C(s_1) = C(s_2)\left(\frac{s_1}{s_2}\right)^X \qquad (4\text{-}2)$$

where $C(s_1)$ is the unknown cost of piece of equipment of size s_1, $C(s_2)$ is the known cost of piece of equipment of size s_2, and X is a cost exponent for the type of equipment. This is detailed further in section 2.6.

The price data obtained has been retrieved from several sources spanning the previous 3 decades. As a result, the price for each piece of equipment must be adjusted for a 2018 equivalent price. This is done using the CEPCI (Chemical Engineering Plant Cost Index) in the following formula:

$$C(Y_1) = C(Y_2)\left(\frac{I(Y_1)}{I(Y_2)}\right) \qquad (4\text{-}3)$$

where $C(Y_1)$ and $C(Y_2)$ are the costs of a given piece of equipment in years Y_1 and Y_2 respectively and $I(Y_1)$ and $I(Y_2)$ are the indexes for those years. The CPI data has been collated from (Vatavuk, 2015, 2010, 2008) and is shown in Figure 4-7.

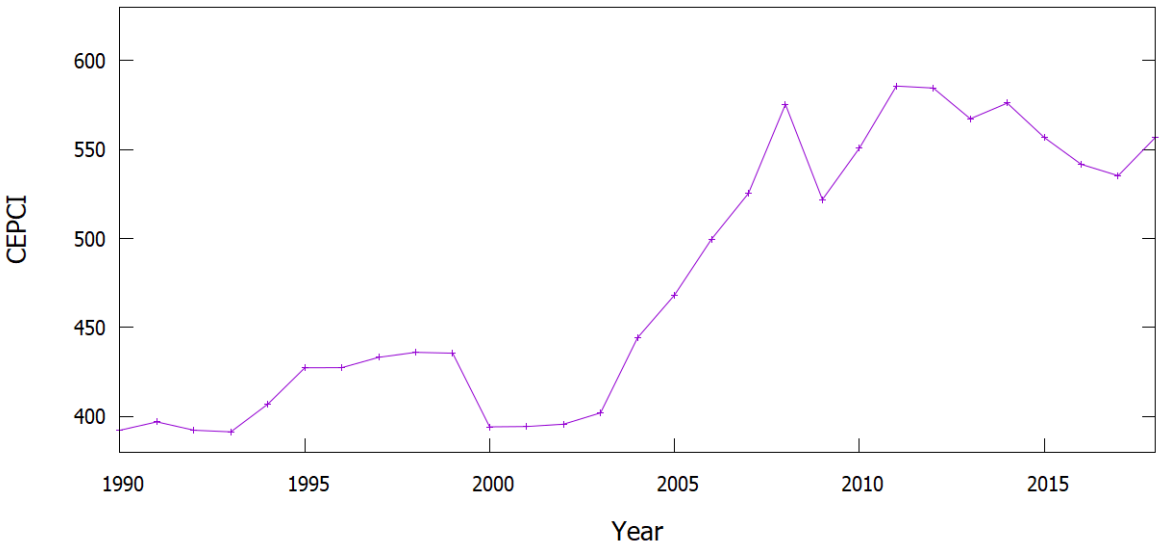

Figure 4-7: Values of CEPCI for 1990-2018

The origin of the base costs used, along with their adjusted 2018 GB£ values and their exponents are detailed in section 2.7 and summarised in Table 4-2.

Equipment	$C(s_2)$	s_2	X	Size units
Compressor	7,022	0.746	0.62	kW
Turbine	978	0.746	0.81	kW
Pump	0.483	1	1	kW
Heat exchanger (rated to 2 MPa)	151,879	140	0.44	m^2
Heat exchanger (rated to 3 MPa)	190,203	140	0.44	m^2
Heat exchanger (rated to 7 MPa)	227,109	140	0.44	m^2
Heat exchanger (rated to 10 MPa)	287,434	140	0.44	m^2
Heat exchanger (rated to 20 MPa)	359,399	140	0.44	m^2
Storage tank	654,210	2,500	0.57	m^3
Cold store	834,211	2,500	0.57	m^3

Table 4-2: Equipment 2018 cost data, sizes and exponents for cost estimation

These costs form the basis of an Excel spreadsheet that acts as a cost estimator for the total capital cost of these key pieces of equipment and produces a probability distribution for the LAES plant capital investment. The weighting factors for the cost estimator are shown in section 4.3.2 and the plant capital costs produced discussed in Chapter 6.

4.3.2. Plant capital investment estimation

A capital cost investment amount was then estimated using the estimation of the major pieces of equipment according to the method in (Peters et al., 1968). An alternative would have been to use the Lang factors, which provide a more rudimentary means to estimate total plant cost using a single factor. Despite these factors being over 70 years old, they remain accurate today for order-of-magnitude capital estimates for process plants (Wolf, 2015). However, given the detailed engineering analysis that has been used to size the major pieces of equipment, it makes sense to perform a more detailed cost estimation based on the factors available in the literature. Given that these factors are provided in terms of a minimum, maximum and typical value, this approach lends itself to the use of PERT distributions, using these factors for the minimum, maximum and most likely value respectively. The parameters used are shown in Table 4-3.

Item	Minimum	Most likely	Maximum
Yard Improvement			
Site clearing	0.4%	0.8%	1.2%
Roads and walks	0.2%	0.6%	1.2%
Rail	0.3%	0.6%	0.9%
Fencing	0.1%	0.2%	0.3%
Yard and fence lighting	0.1%	0.2%	0.3%
Parking areas	0.1%	0.2%	0.3%
Landscaping	0.1%	0.1%	0.2%
Other improvements	0.2%	0.3%	0.6%
Service facilities			
Steam distribution	0.2%	1.0%	2.0%
Water supply, cooling, pumping	0.4%	1.8%	3.7%
Water treatment	0.5%	1.3%	2.1%
Water distribution	0.1%	0.8%	2.0%
Electric substation	0.9%	1.3%	2.6%
Electric distribution	0.4%	1.0%	2.1%
Sanitary waste disposal	0.2%	0.4%	0.6%
Communications	0.1%	0.2%	0.3%
Fire protection	0.3%	0.5%	1.0%
Safety installations	0.2%	0.4%	0.6%
Engineering and services			
Engineering	1.5%	2.2%	6.0%
Drafting	2.0%	4.8%	12.0%
Purchasing	0.2%	0.3%	0.5%
Accounting	0.2%	0.3%	1.0%
Travel and living	0.1%	0.3%	1.0%
Reproductions and communication	0.2%	0.2%	0.5%
Construction			
Temporary construction and operations	1.0%	1.7%	3.0%
Construction tools and rental	1.0%	1.5%	3.0%
Home office personnel	0.2%	0.4%	2.0%
Field payroll	0.4%	1.0%	4.0%
Travel and living	0.1%	0.3%	0.8%
Taxes and insurance	1.0%	1.2%	2.0%
Startup materials and labour	0.2%	0.4%	1.0%

Table 4-3: PERT distribution parameters for LAES plant cost estimation (Peters et al., 1968)

The probability distributions based on these factors have been used in an @RISK model to estimate the probability distribution for the overall capital investment for the plant in question. Of course, whilst detailed study of the equipment and estimation of its cost has been performed, this remains only an estimate and potential inaccuracy must be considered. It was however decided that the conservative selection of possible cost comparisons in section 2.7 meant that addition hedging of costs was neither necessary nor appropriate.

Once the model has been run for the capital investment distribution, these results are fit to the library of available distributions in @RISK, which are then rated using the AIC (Akaike Information Criterion). The most accurate fit was shown to be the BetaGeneral function for all plant configurations. This is a Beta distribution that has been scaled to fit to maximum and minimum values, rather than general values between 0 and 1. This is the distribution upon which the PERT distribution is based. It requires two shape parameters, β_1 and β_2 as well as a maximum and minimum for the distribution.

4.4. Time series parameters

Time series are used in the model to predict two key factors: the electricity price for each half-hourly period and the evolution of the CPI over years. Definition of these series is made easier by the availability of large datasets to which the models can be fitted. A dataset of the SSP over the years 2008-2015 (Smith and Halliday, 2016) was used to parametrise the electricity price model. The analysis of this data is discussed in detail in this section. A dataset of CPI over the years 2002-2018 (Gooding, 2018) was used to parametrise the CPI model.

4.4.1. Electricity price modelling

As will be discussed in this section, the electricity price data is extremely complex and exhibits patterns in its hourly, daily and seasonal variation. Early attempts were made to fit a single time series model to the electricity price data to predict the evolution of the electricity price over time. This presented two problems.

Firstly, predicting electricity prices for half-hour periods over a period of 30 years results in over a half million discrete values. Time series models use a combination of the overall trend and the most recent values to predict each subsequent value. Because of this, using a single time series tended to allow the values to increase or decrease to ridiculous values towards the later stages of the model.

Secondly, time series models are very much stochastic models based on an RNG. As such, there is no way to define repeating patterns within these time series. This means that daily peaks and troughs are not properly captured by a time series model. Given that daily price profiles are societally driven (e.g. an evening peak occurs between 17:00 and 18:00 as people return home but schools and offices remain lit), it was felt important to properly capture these features.

In order to properly capture these patterns, the data was split into components prior to time series fitting. First, the mean average system sell price, $A(D)$, for each day, D, was calculated.

Then, ratio, $\varphi(P)$ of the system sell price, $S(P)$, for each period, P, to that day's average price was calculated. The average of these prices was then found for each month of the year and used to define a daily price profile curve. Finally, the absolute difference, $\varepsilon(P)$, between the price predicted by the profile curve and the daily average and the actual price was calculated.

This process provided two series to which time series models were then fitted: a daily average price series and an error value series, described in sections 4.4.2, and 4.4.4 respectively. In addition, the study yielded daily price profile curves, described in section 4.4.3. The model could then calculate a system sell price, $S(P)$, for a given half-hour period using:

$$S(P) = [\varepsilon(P) + \varphi(P)] \times A(D) \qquad (4\text{-}4)$$

An important feature for the dataset used was that it included years where the daily average was highly volatile and years where it was more stable. Similarly, some years exhibited substantial daily variance with large differences between periods of high price and low price, while others had much less variation in the half-hourly prices, with prices remaining fairly stable over the course of a day. This provided an understanding of what different markets look like and allowed the testing of a variety of scenarios for electricity prices.

4.4.2. Daily average price

As discussed in section 4.4, the first analysis performed on (Smith and Halliday, 2016) was to calculate the daily mean for the system sell price, with the intention of determining whether there was any evidence of seasonal or annual cyclic variation. The evolution of this average price over the years of the dataset is shown over the following pages, along with a 30-day

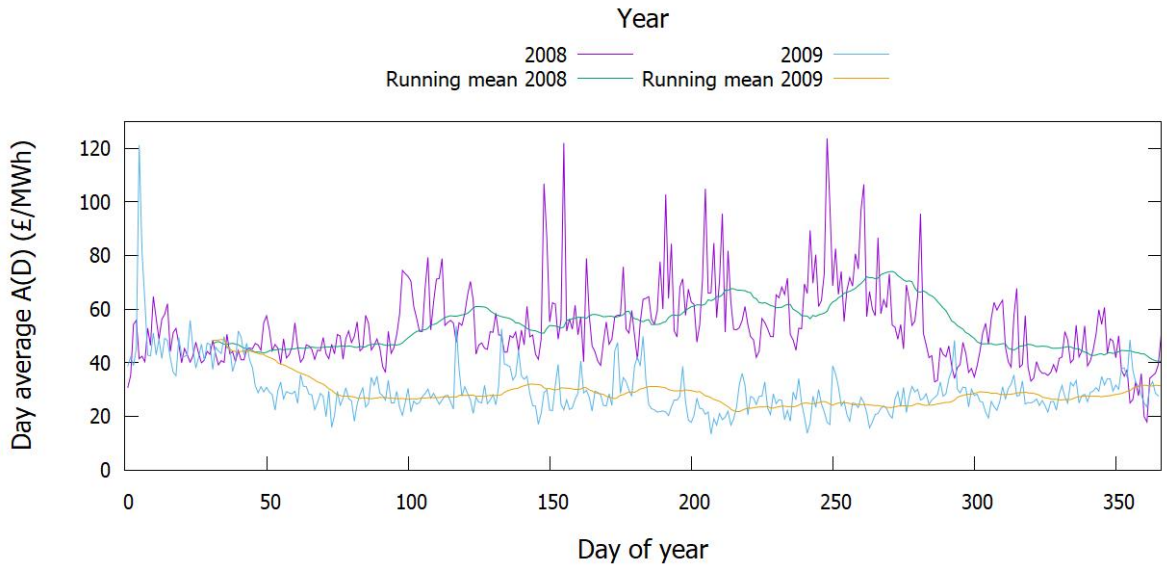

Figure 4-8: A(D) data for 2008/2009

running mean average. Charts are limited to displaying two years in order to maintain visual clarity, and to allow particularly interesting years to be isolated.

The data for 2008 and 2009 is shown in Figure 4-8. For 2008, the data appears to show some seasonal variation, specifically in the significantly higher volatility in daily average price in the middle of the year. Whilst 2009 exhibits a similar pattern, the effect is lessened. The running mean for the data is also shown for the 30th day of each year onwards. From this, it can be seen that average prices in 2008 increase in the middle of the year and fall again towards the end of the year. Perhaps most importantly, there is a marked increase in running average following price shocks, indicating that the effect of price shocks lasts for some time. In 2009, prices fall steadily during the first quarter and exhibit a modest rise towards the end of the year. The ongoing effect of price shocks is still visible but lessened compared to 2008.

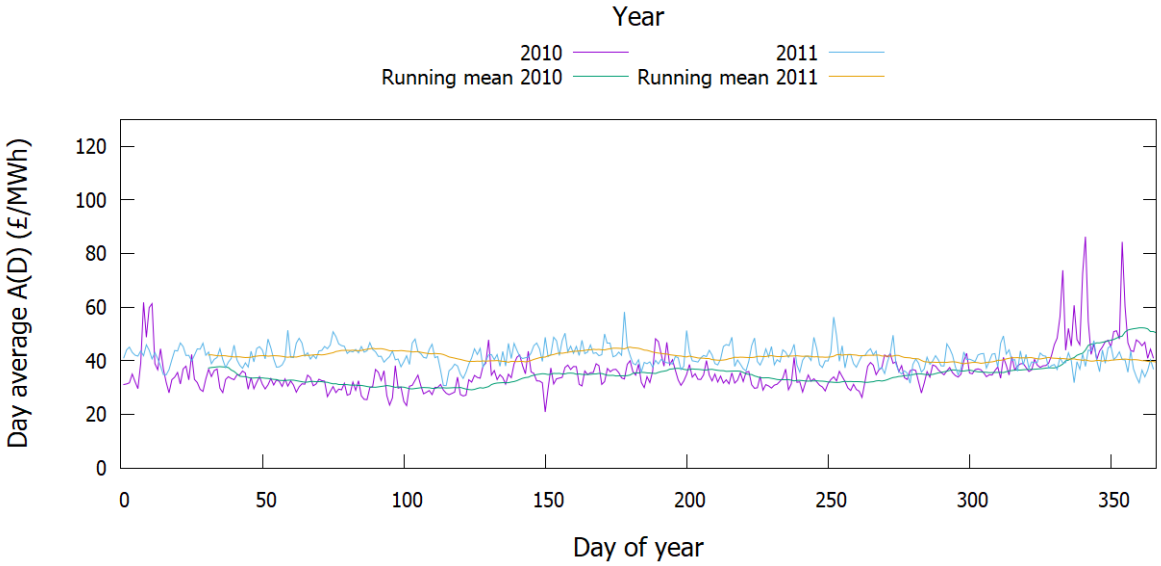

Figure 4-9: A(D) data for 2010/2011

The data for 2010 and 2011 is shown in Figure 4-9. Other than high volatility at the beginning and end of 2010, the prices typically show low volatility throughout both years. Interestingly, this high volatility at the end of 2010 does not continue into the beginning of 2011. The running means show that other than the periods of high volatility in 2010, prices are largely consistent throughout both years. The ongoing effect of shocks remains present in 2010 but is largely absent in 2011.

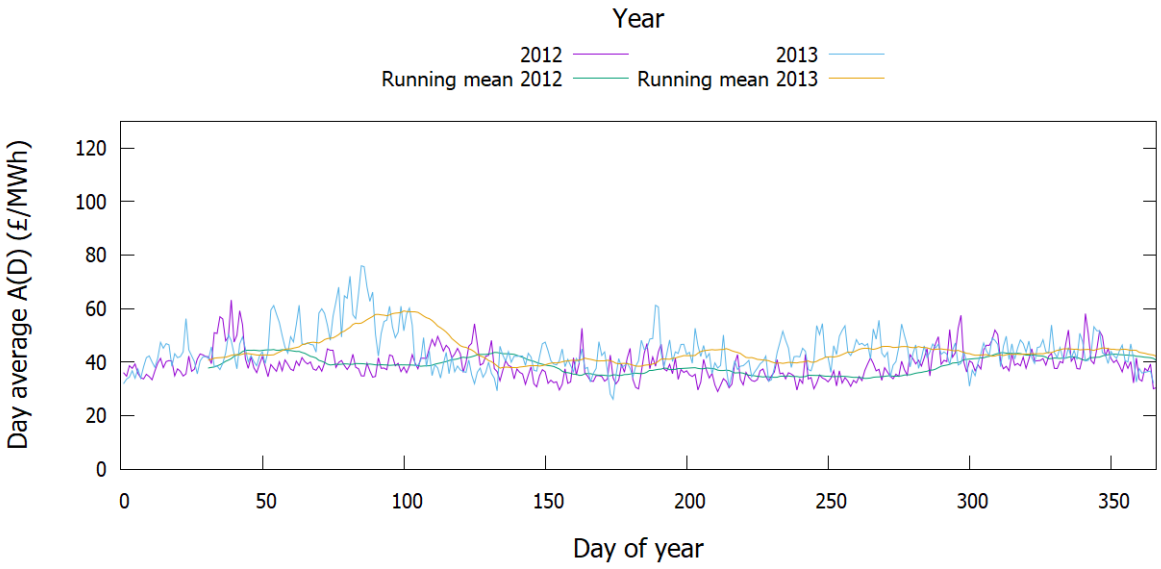

Figure 4-10: A(D) data for 2012/2013

The data for 2012 and 2013 is shown in Figure 4-10. Once again, other than short-lived periods of high volatility, volatility is low, and the running mean shows that prices are largely consistent throughout the year. Both years show some ongoing effect of price shocks.

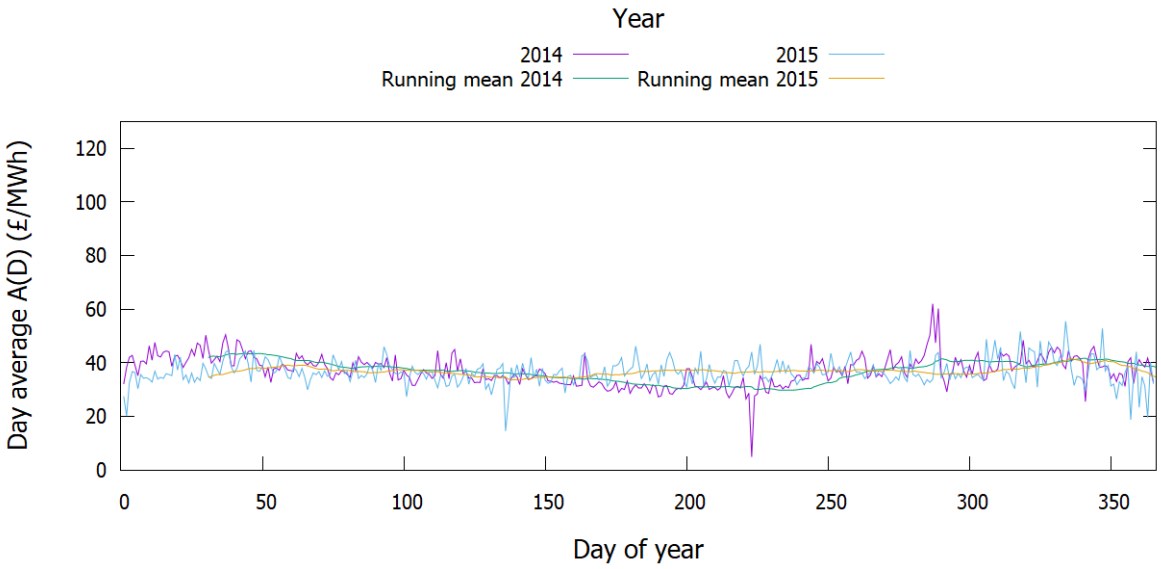

Figure 4-11: A(D) data for 2014/2015

The data for 2014 and 2015 is shown in Figure 4-11. 2014 exhibits some short-lived price shocks and shows some seasonally cyclic behaviour. 2015 is broadly similar to 2012 and 2013 in its behaviour. In both years, the ongoing effect of price shocks is almost entirely absent.

As the discussion in this section shows, there is some evidence of seasonal variation in the daily average electricity prices for some years and evidence of stability throughout the year for others.

As discussed in section 2.5.2, however, the importance of cold recycle to LAES means that it is unsuitable for seasonal-duration storage. Thus, as long as the diurnally cyclic behaviour of electricity price and its seasonal dependence is properly captured, as is discussed in section 4.4.3, and as long as the daily average price model accurately captures volatility, it is reasonable to assume that the seasonally cyclic behaviour will not affect the performance of LAES within the modelled market. The effect of shocks is more contentious, but there is considerable evidence that price shocks can have a medium-term effect on pricing that can last for up to two months. It is important that the model be capable of capturing this behaviour and the user have adequate control over this phenomenon in order to explore different scenarios.

Given the assumption that seasonally cyclic behaviour need not be captured, but that the effect of shocks is important, the decision was made to use a time series model to predict values of $A(D)$. There are several time series models available to the @RISK software. These are:

- AR (autoregressive) first and second order
- MA (moving average) first and second order
- ARMA (autoregressive moving average) first order
- ARCH (autoregressive conditional heteroskedasticity) first order
- GARCH (generalised ARCH) first order
- BMMR (Brownian motion mean reversion) first order

These all have some history of use in electricity price modelling (Weron, 2014). With a substantial dataset available, it made the most sense to use the fitting algorithms built into the software to define the time series models. As discussed in section 2.7, the software provides a variety of time series models. As a starting point, the daily average data was used to fit all time series models available.

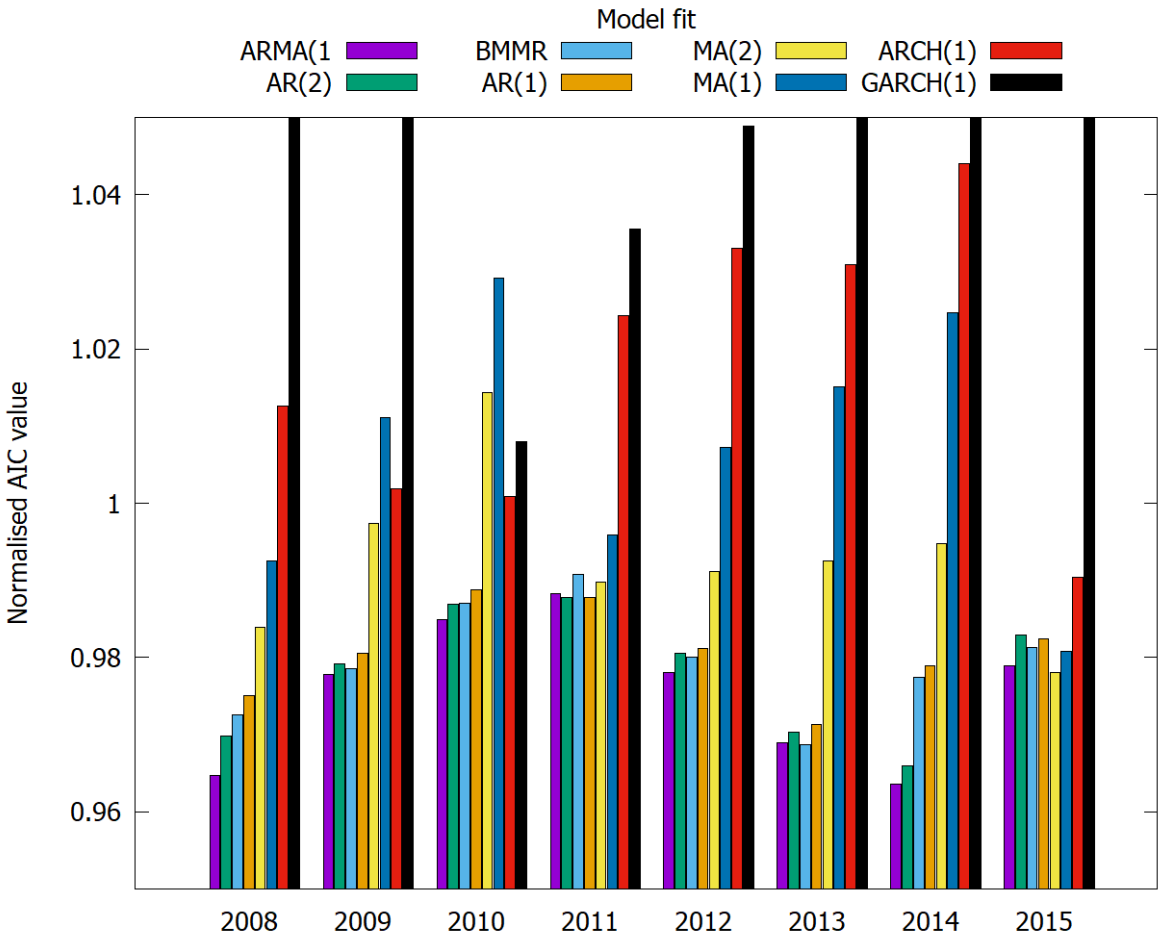

Figure 4-12: Time series model fit comparison (lower AIC value represents a better fit)

Figure 4-12 shows a comparison of the time series models for the years of data available; a lower value represents a better fit. Since the AIC values are generally quite close together, and the values from one year to another can vary significantly, the values have been normalised for the sake of comparison. This was done by dividing each AIC value by the average AIC value for that year. The comparison shows that the first-order ARMA time series provides the best fit in the majority of cases, and close to in the remainder. Thus, this series was chosen as the basis of the daily average price model.

An ARMA model is a combination of AR and MA models. Its parameters are average, μ, volatility, σ, autoregressive coefficient, a with magnitude less than 1, moving average coefficient, b, initial value $y(0)$, and initial error $\epsilon(0)$. Whilst @RISK's series fitting algorithms will assist with parameter definition, it's worth considering how values are calculated and in order to understand which of these parameters should be user-defined. Each consecutive value is based on an RN, $N(t)$, taken from a normal distribution with mean 0 and standard deviation 1. For the t^{th} series value, an error term is calculated:

$$\epsilon(t) = \sigma N(t) \qquad (4\text{-}5)$$

Then, the time series value, $y(t)$, is calculated using:

$$(y(t) - \mu) = a(y(t-1) - \mu) + b\epsilon(t-1) + \epsilon(t) \qquad (4\text{-}6)$$

Examining equation (4-6) shows the importance of the values of a and b. Considering the equation without the b term yields the equation for a first-order AR model:

$$y(t) = \mu + a(y(t-1) - \mu) + \epsilon(t) \qquad (4\text{-}7)$$

Considering the first term following on the right of the equation, if the previous value $y(t-1)$ is far from the mean, this term will be large in magnitude. Since the mean of $\epsilon(t)$ is zero and its standard deviation is small, the average result of this will be that the term before the equals will be large and of the same sign. Hence, if one value of the time series is far from the mean, the next will, on average, tend to get further from the mean – in the same direction, hence the description of this model as autoregressive. The larger the value of a, the greater this effect.

Now, considering equation (4-6) without the a term yields the equation for a first-order MA model. Rearranging:

$$y(t) = \mu + b\epsilon(t-1) + \epsilon(t) \qquad (4\text{-}8)$$

In contrast to the AR model, the previous error value, $\epsilon(t-1)$, has a direct effect on the current term but the actual previous value, $Y(t-1)$, has no effect. Consideration of equations (4-7) and (4-8) has thus showed the key difference between these two models; shocks (i.e. large values of $\epsilon(t)$) have a significant effect on an MA model but only for a finite number of values. The immediate effect of shocks is lessened in an AR model, but the because each value $y(t)$ is strongly dependent on its previous value, and ultimately on all previous values, shocks affect series values until the end of the series.

With this understanding of model behaviour, the fitting shown in Figure 4-12 can be put into the context of the qualitative discussion of the analysis of dataset (Smith and Halliday, 2016). ARMA models represent a middle ground between AR and MA models where shocks have a modest medium-term effect, less significant than MA models and for a shorter time than AR models. It is for this reason that MA and AR models fit similarly well to one another, and to the ARMA model, in years where the effect of shocks is almost entirely absent, such as 2011 and 2015. In 2008, where the effect of shocks is most obvious in the data, but remains short-term, the difference between the ARMA and AR model fits is greatest.

The values a and b act together to have a complex effect on the values taken by an ARMA time series. As a result, the decision was taken to define these by applying @RISK's fitting algorithms to the available data.

By definition, the time series models will ultimately take a mean of value μ, with the cumulative mean moving closer to μ as the value of t increases. The decision was taken to allow the model user to define μ since this would allow the examination of different electricity price scenarios. The volatility, σ, controls the size each error value, $\epsilon(t)$, amplifying the effect of the normal distribution that is used to define these values. Once again, the decision was taken to allow the user to define these values for the sake of testing different scenarios. Direction was taken from the values resulting from @RISK's fitting algorithms for different years from the data set for direction on what value this should take for more or less volatile years.

The initial value $y(0)$, and initial error $\epsilon(0)$ simply represent the start of the series. Since the daily average price time series will be extended for the 30 years over which modelling is performed, initial values will have a negligible effect. Thus, the decision was taken to define the value $y(0) = \mu$ and $\epsilon(0) = 0$ in year 0 for simplicity.

The time series was used to model an average price, $A(D)$ for a given day, D.

4.4.3. Daily profile

The daily profile data was analysed by calculating the ratio, $\varphi(P)$, of the price, $S(P)$ for a given period, P, to the average price for that day, $A(D)$:

$$\varphi(P) = \frac{S(P)}{A(D)} \qquad (4\text{-}9)$$

With the values of $\varphi(P)$ calculated for each period of the dataset (Smith and Halliday, 2016), mean averages of the resulting data for $\varphi(P)$ were calculated with the data split in the following ways:

- data split by quarter,
- data split by month,
- data split into weekend and weekday datasets by month.

This section will first discuss analysis of the data split by quarter, followed by analysis of the data split into weekends and weekdays by month. The focus will be on qualitative data analysis, identifying patterns and speculating on the reasons behind them.

A quantitative analysis of how well the ratio $\varphi(P)$ predicts prices for the given splits, and how best to model the errors in this prediction will be the focus of section 4.4.4.

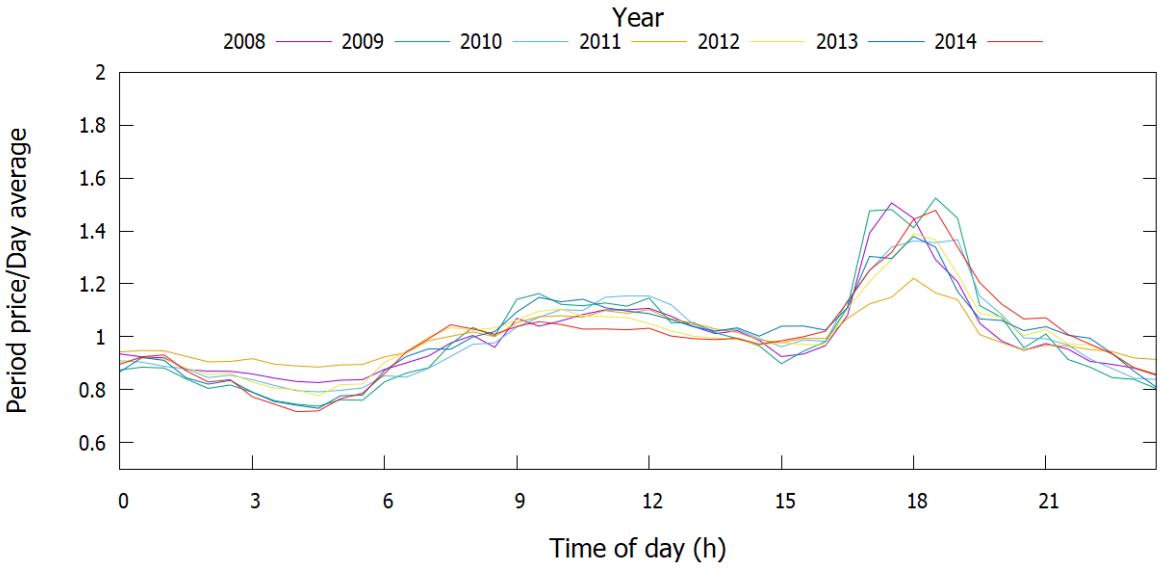

Figure 4-13: $\varphi(P)$ day profile for first quarters

The first quarter daily price profiles for each year are shown in Figure 4-13. For this winter period, the daily price profile is largely consistent for each year of the dataset. Each year shows a trough overnight from around midnight to around 06:00. Peaks also occur around similar times of 18:00 each day, presumably due to the fact that people are returning home and workplaces remain lit and heated. For the most part, years with shallow troughs have correspondingly short peaks; 2011 is a good example of this with a relatively flat daily profile compared to the other years.

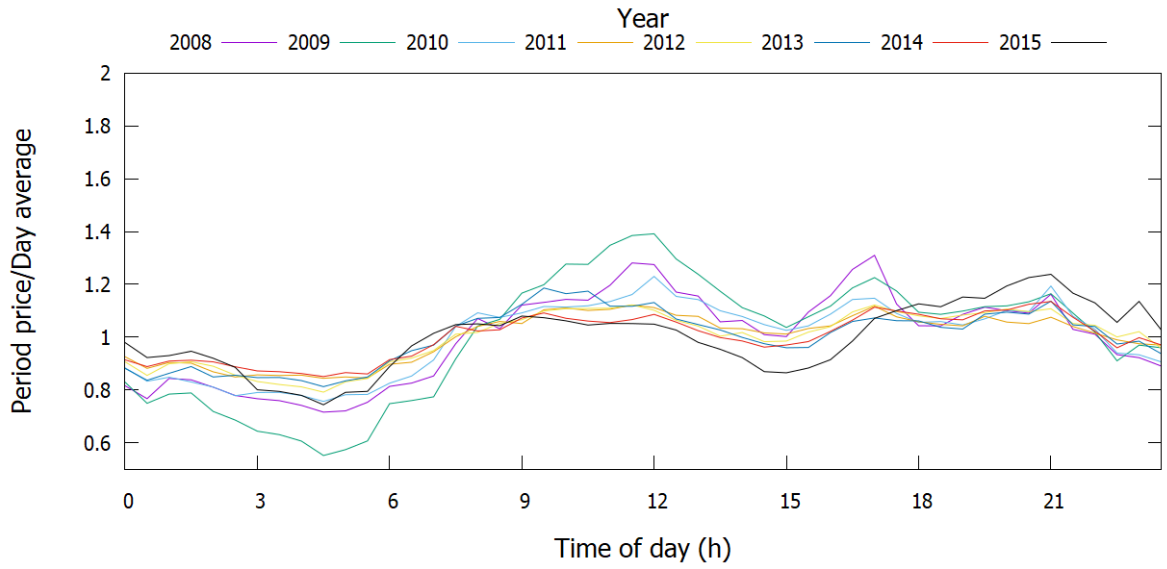

Figure 4-14: $\varphi(P)$ day profile for second quarters

The second quarter daily price profiles for each year are shown in Figure 4-14. For this spring period, trough times occur at a similar time of day to the first quarter data. The peak is far less pronounced and occurs at midday, most likely due to workplace air conditioning. Once again, shallow troughs correspond to short peaks.

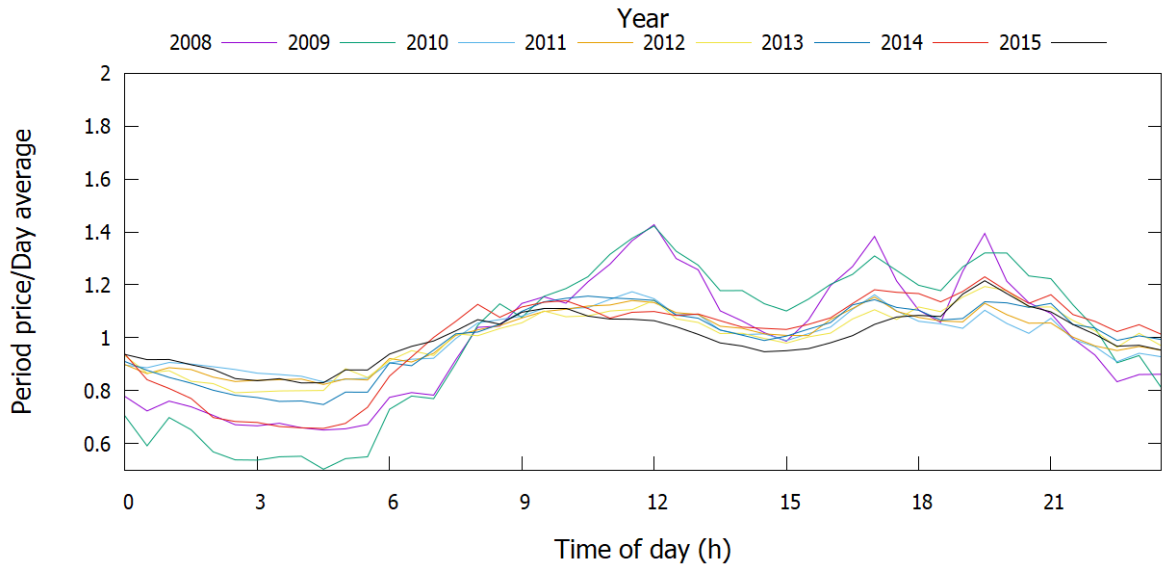

Figure 4-15: $\varphi(P)$ day profile for third quarters

The third quarter daily price profiles for each year are shown in Figure 4-15. This summer data exhibits a pattern broadly similar to the spring data. The afternoon profile is slightly flatter.

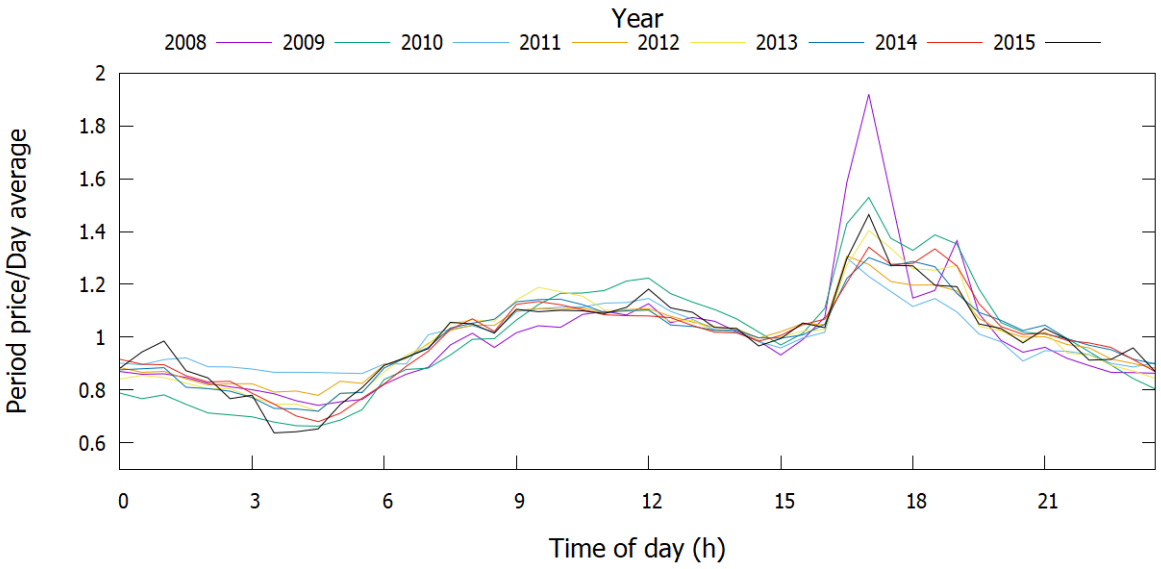

Figure 4-16: $\varphi(P)$ day profile for fourth quarters

The fourth quarter daily profiles for each year are shown in Figure 4-16. This autumn data exhibits a pattern broadly similar to the winter data.

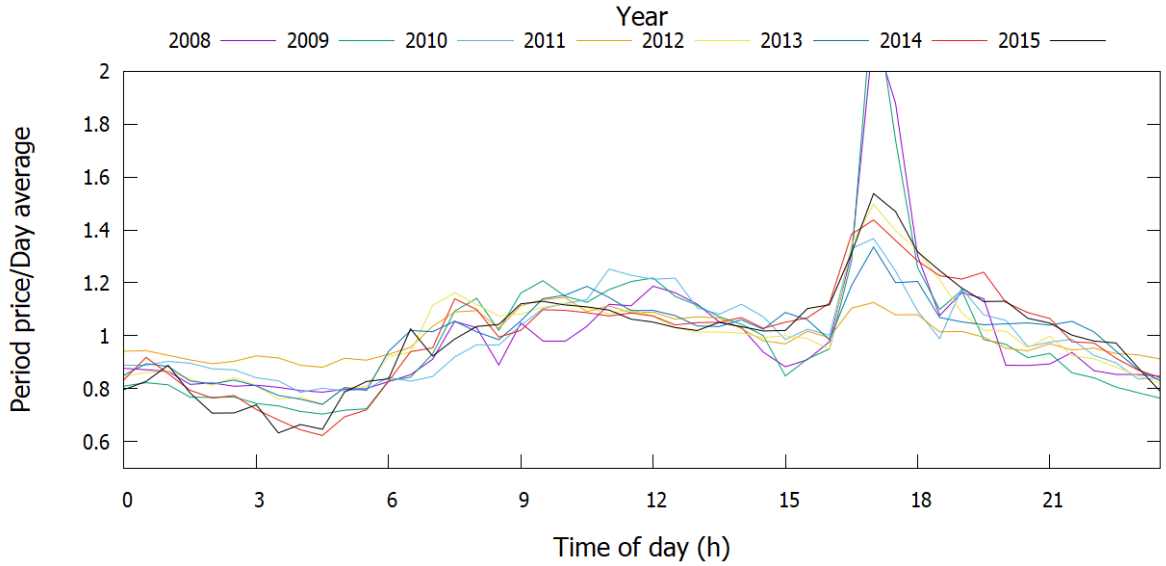

Figure 4-17: $\varphi(P)$ day profile for January weekdays

The daily profiles for January weekdays for each year are shown in Figure 4-17. The patterns are similar to the first quarter data shown in Figure 4-13, however the peaks are more pronounced and narrower, with a single-period peak around 17:30 for most years. Perhaps most interestingly, the shallowest troughs no longer occur in the same years as the shortest peaks.

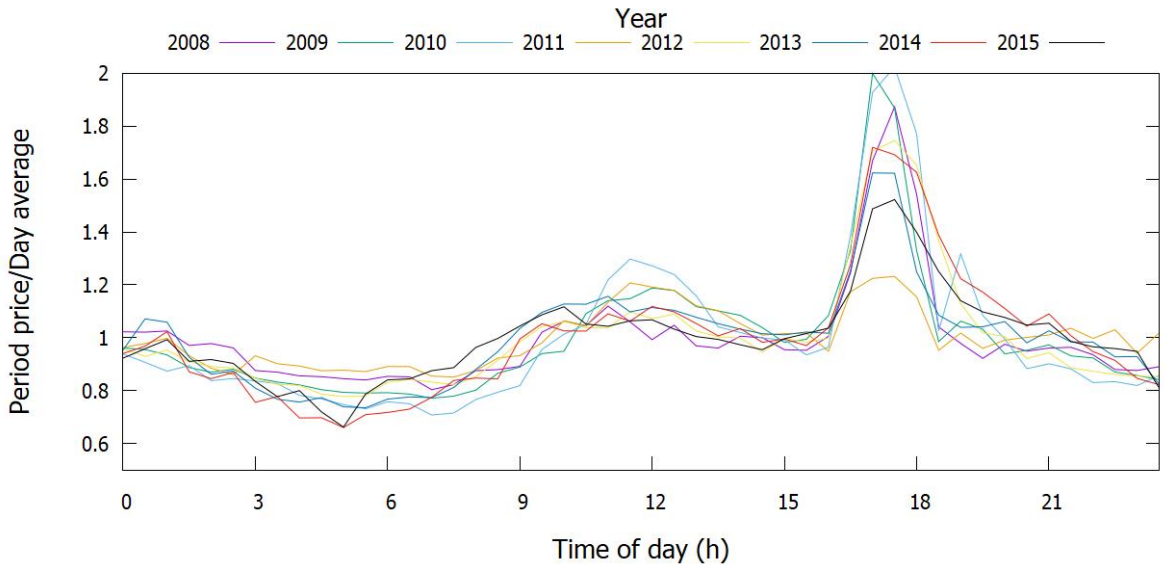

Figure 4-18: $\varphi(P)$ day profile for January weekends

The daily profiles for January weekends for each year are shown in Figure 4-18. Whilst similar to the weekday data, this data exhibits a broader trough at night, beginning slightly later around 01:00 and ending at around 10:00. Surprisingly, the 17:30 afternoon peak remains and would seem to indicate that this phenomenon is not confined to the working week. Indeed, the peak is more evident in later years at weekends than it is for weekdays.

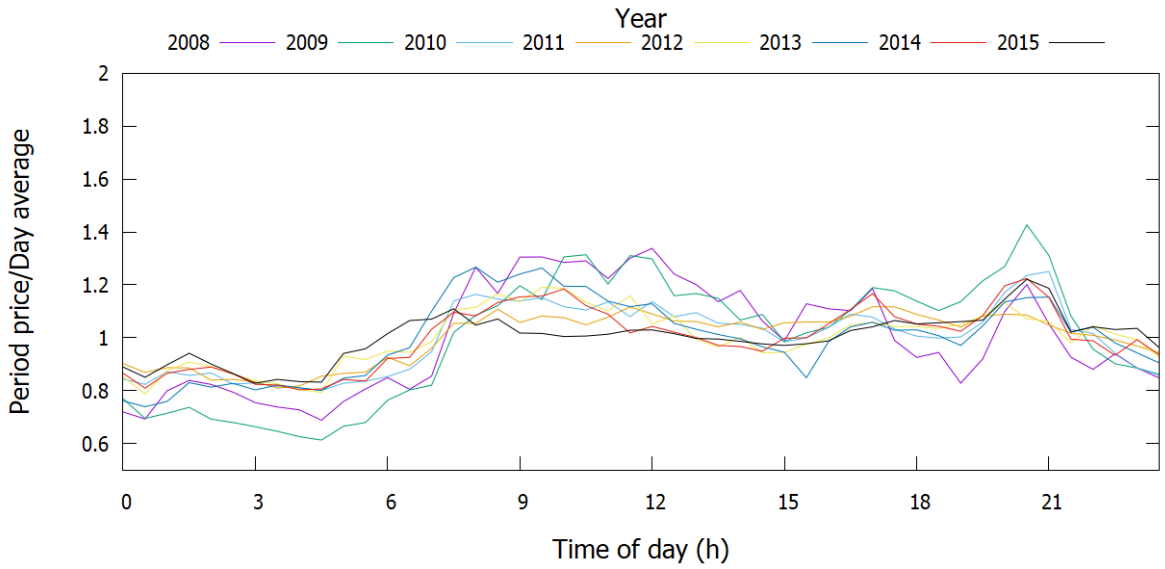

Figure 4-19: $\varphi(P)$ day profile for April weekdays

The daily profiles for April weekdays for each year are shown in Figure 4-19. This time, the patterns differ a little more from the second quarter patterns seen in Figure 4-14. The midday peak is now far broader and less pronounced. A more pronounced peak occurs around 21:00, presumably when lights start being switched on in homes. The trough is less broad than for

January weekdays, most likely because it is becoming lighter in the mornings and home lighting is not required. The characteristic deep troughs coinciding with high peaks is once again apparent in this data.

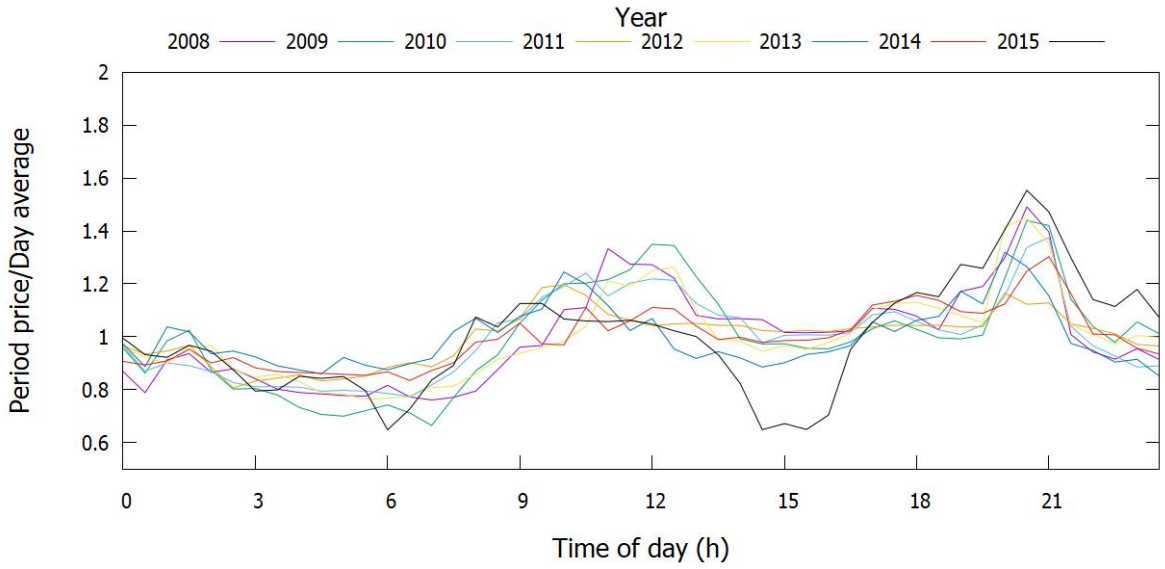

Figure 4-20: $\varphi(P)$ day profile for April weekends

The daily profiles for April weekends for each year are shown in Figure 4-20. As for January, the night-time trough starts later and lasts longer. This time, the midday peak is a little more pronounced and the 21:00 is much the same as for weekdays. There is an anomalous trough at 15:00 in 2015, most likely due to increasing installation of solar panels around that time.

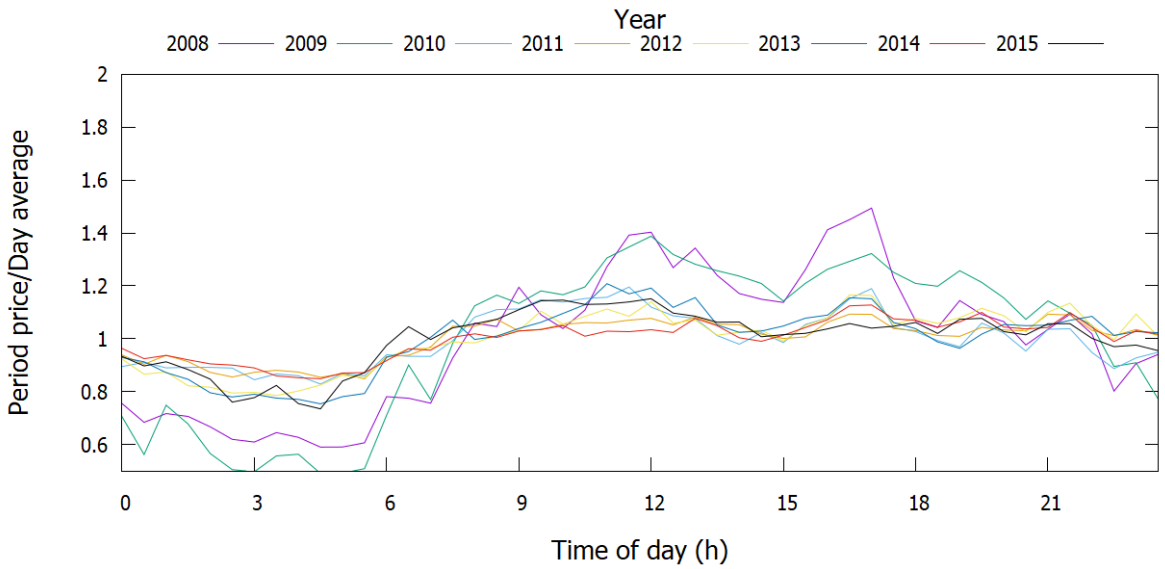

Figure 4-21: $\varphi(P)$ day profile for July weekdays

The daily profiles for July weekdays for each year are shown in Figure 4-21. Much like the third quarter data in Figure 4-15, the profile for the whole day is very flat for the later years of the dataset.

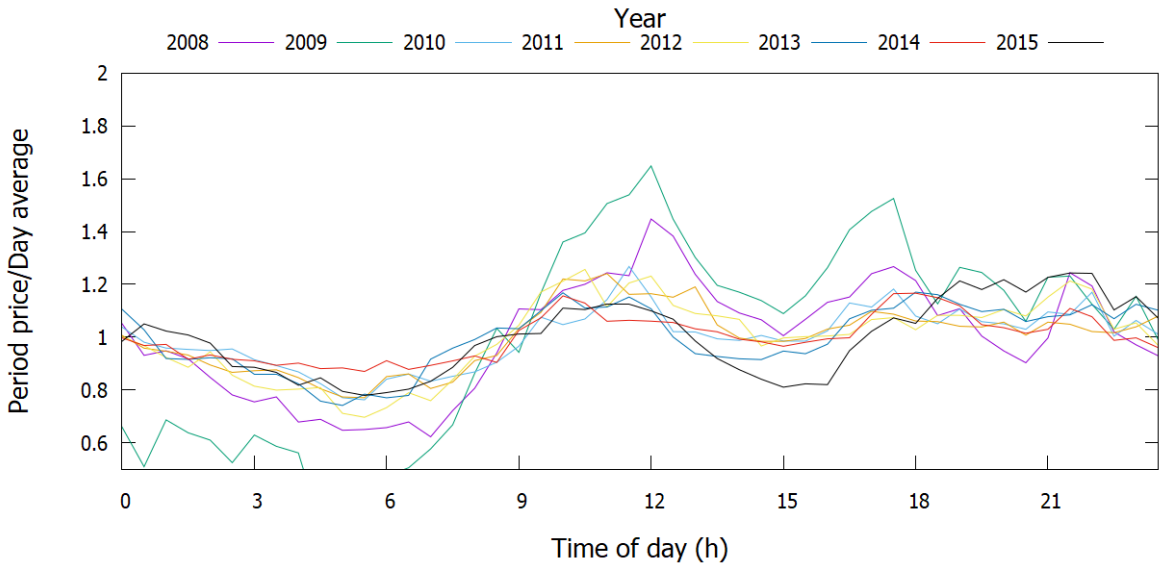

Figure 4-22: $\varphi(P)$ day profile for July weekends

The daily profiles for July weekends for each year are shown in Figure 4-22. These profiles are much the same as those for July weekdays. Once again, the profile is very flat throughout the day and peaks are almost entirely absent. Much as for the April data, 2015 shows a high degree of variability throughout the day.

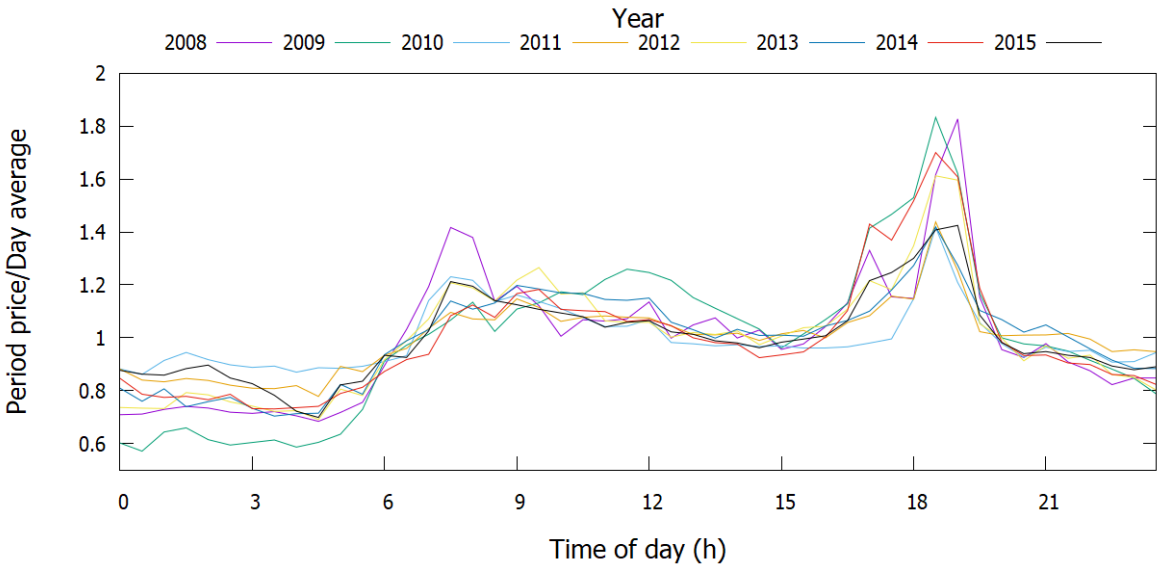

Figure 4-23: $\varphi(P)$ day profile for October weekdays

The daily profiles for October weekdays for each year are shown in Figure 4-23. As Autumn approaches, the evening peaks become more pronounced, although later than in January, as the days are longer.

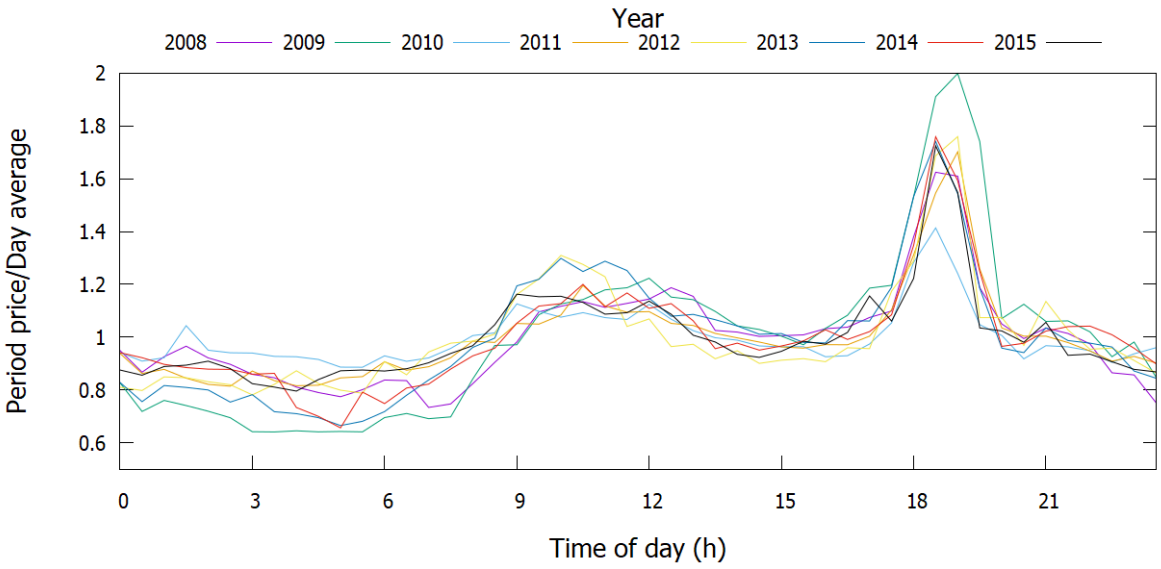

Figure 4-24: $\varphi(P)$ day profile for October weekends

The daily profiles for October weekends for each year are shown in Figure 4-24. Much as for January, the evening peak remains present at weekends and is more apparent at weekends than it is during the week.

The analysis of the electricity price daily profile data reveals some interesting patterns. Firstly, it would appear lighting is a key driver of electricity price throughout the day. The evening peaks are largest in the evenings in the autumn and winter months. As the UK moves out of winter, peaks become less pronounced and occur later into the evening as days get longer. Moving into autumn, peaks become more pronounced and start to occur earlier as days get shorter.

The troughs exhibit behaviour that differs more from weekdays to weekends than seasonally. Typically, prices begin to rise around 06:00 on weekdays as people awaken for work. At weekends, this rise is less steep and occurs later in the day, presumably as a result of more people sleeping late at weekends.

Importantly for this model, the overall shape of the profile appears broadly consistent. Aside from the anomalous profile of the April 2015 weekends, monthly profiles follow similar shapes year-on-year and for the most part, deeper troughs coincide with higher peaks. This adds credence to the assumption that daily profiles are behaviourally driven by electricity consumers. It is important to note, however that the April 2015 weekend result coincided with an increased presence of solar generators; capacity increased 70% on the previous year. As a result, there does seem to be some evidence of supplier-driven pricing. It is unfortunate that the dataset available (Smith and Halliday, 2016) did not continue beyond 2015.

In taking the assumption of consumer-driven pricing, it was decided that the financial model would use the available data to create curves that would define the daily evolution of electricity prices. Given the demonstrable differences between months and between weekdays and weekends in the latter part of this section, the decision was made to define curves on this basis. Each month has two daily profile curves defined within the model: one for weekdays and one for weekends. The curves were defined for half-hourly periods on the average of those periods for the relevant days over all 8 years of the dataset.

With the shapes of the profile curves defined, a method for user control of the amplitudes of the curves had to be devised. This was done by calculating the difference, $\delta(P)$, between the value of $\varphi(P)$ and 1, by definition the average value of the curve:

$$\delta(P) = \varphi(P) - 1 \qquad (4\text{-}10)$$

The controls for the model allow the user to define a multiplier for the value of $\delta(P)$ for specified periods. To limit the number of parameters under user control, one amplitude parameter is user-defined for each quarter of each year. This is defined as the amplitude, $\alpha(Q)$, for a given quarter Q. The model then applies this amplitude to the six profiles that fall within that quarter (two for each month representing weekdays and weekends) by multiplying it by the relevant values of $\delta(P)$. Thus, an amplitude of less than one would represent below-average daily volatility and an amplitude of greater than one would represent above-average daily volatility.

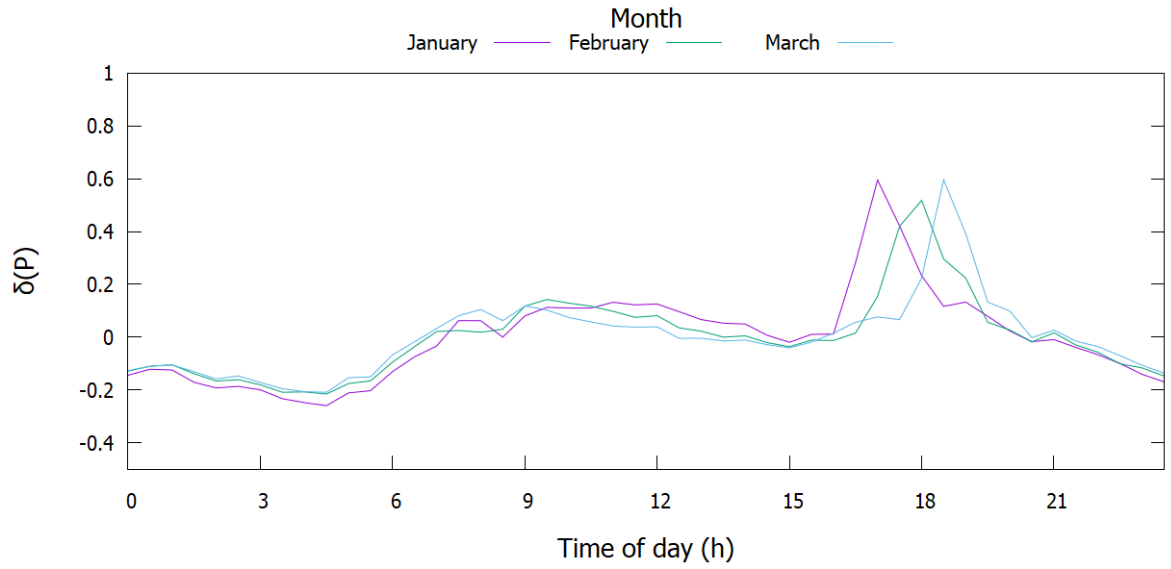

Figure 4-25: $\delta(P)$ model curve for first quarter weekdays

The values for $\delta(P)$ for weekdays in the first quarter of the model are shown in Figure 4-25. The effect of days getting longer and the peak becoming later is clearly evident here.

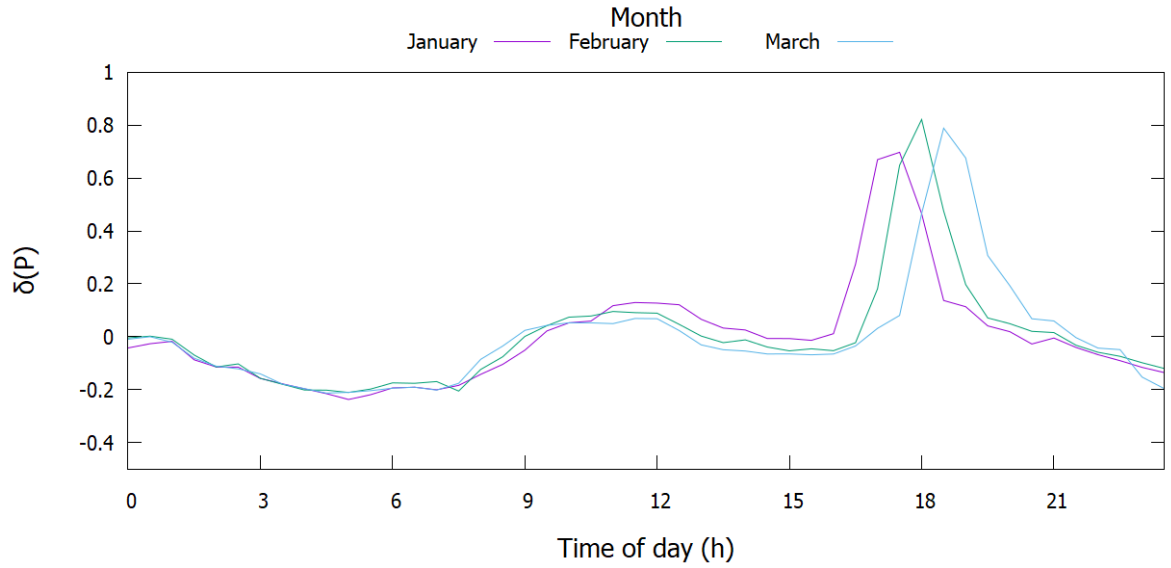

Figure 4-26: $\delta(P)$ model curve for first quarter weekends

The values for $\delta(P)$ for weekends in the first quarter of the model are shown in Figure 4-26. Weekends exhibit more pronounced peaks and an overnight trough that begins and ends later.

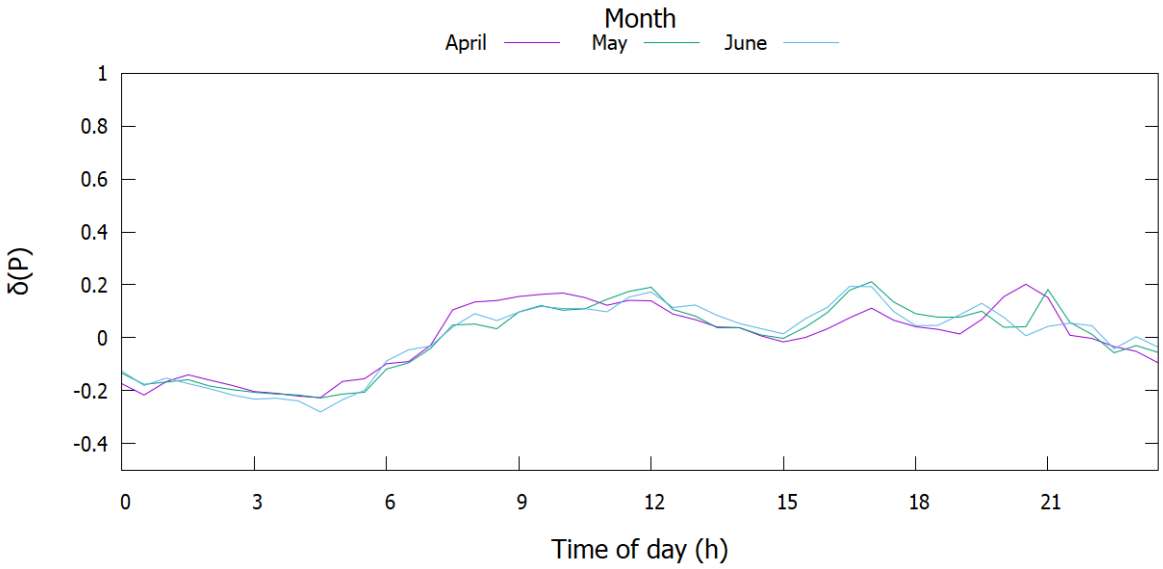

Figure 4-27: $\delta(P)$ model curve for second quarter weekdays

The values for $\delta(P)$ for weekdays in the second quarter of the model are shown in Figure 4-27. The effect of longer days is shown in the reduced evening peaks. A small midday peak is also becoming apparent moving into late spring.

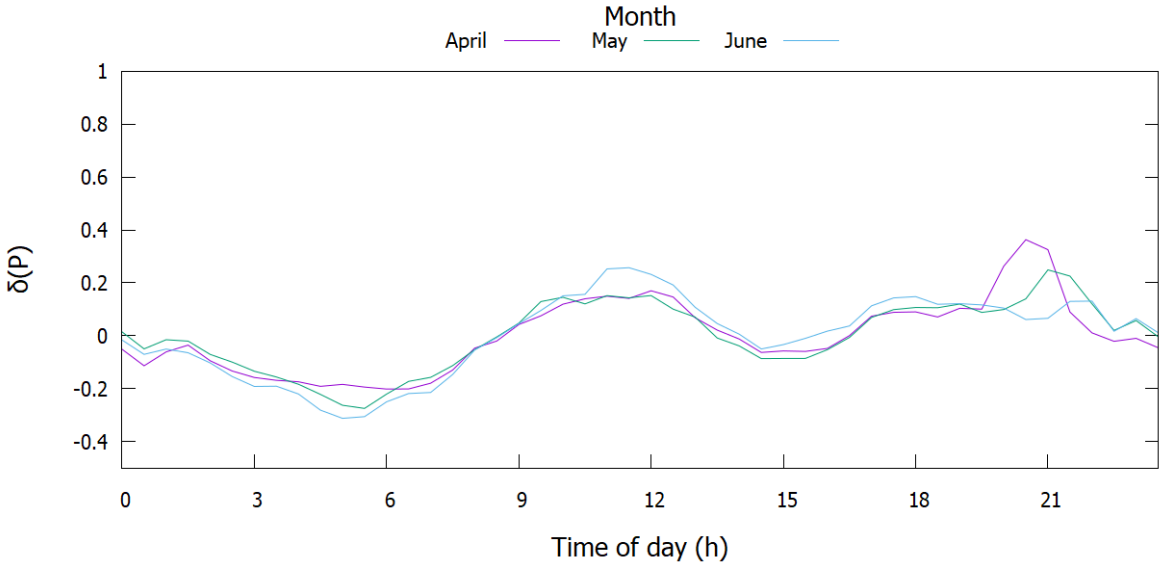

Figure 4-28: $\delta(P)$ model curve for second quarter weekends

The values for $\delta(P)$ for weekends in the second quarter of the model are shown in Figure 4-28. Once again weekends exhibit slightly more pronounced peaks and an overnight trough that begins and ends later. The effect of lengthening days on the evening peak is more apparent here, as is the effect of hotter days on the midday peak.

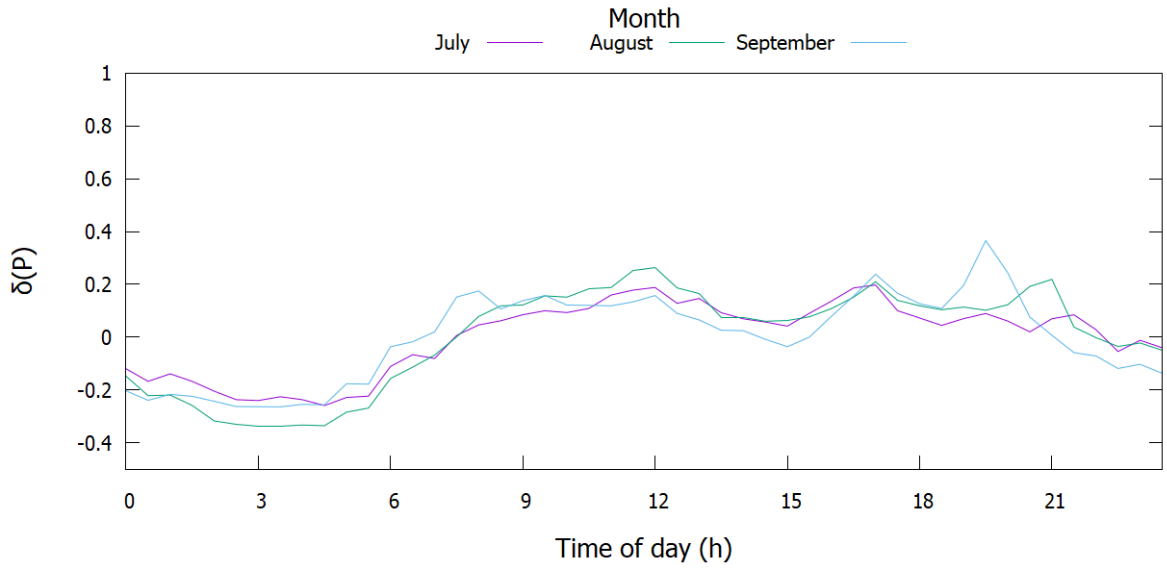

Figure 4-29: $\delta(P)$ model curve for third quarter weekdays

The values for $\delta(P)$ for weekdays in the third quarter of the model are shown in Figure 4-29. The evening peak is beginning to return and become more apparent as summer ends. The small midday peak also falls away later into the year.

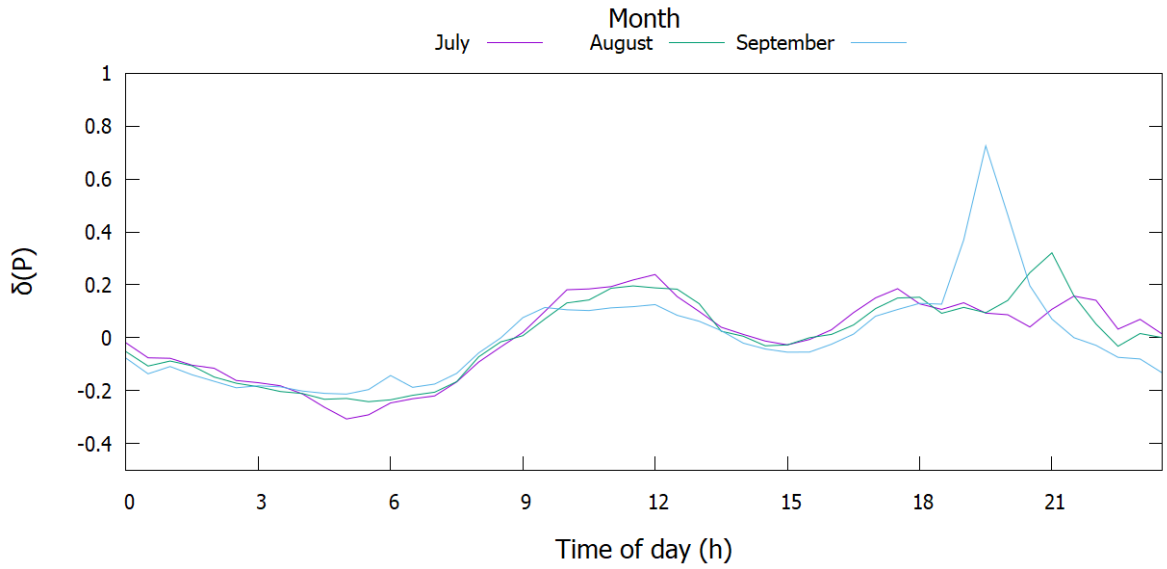

Figure 4-30: $\delta(P)$ model curve for third quarter weekends

The values of $\delta(P)$ for weekends is shown in Figure 4-30. The effect of the changing season is once again more apparent for the weekend curves.

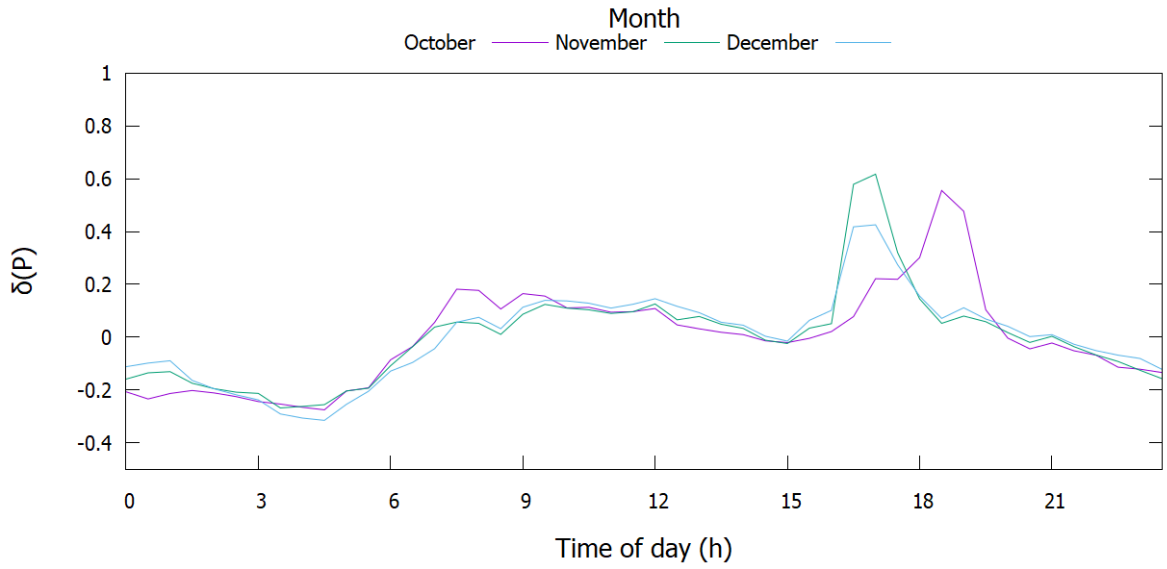

Figure 4-31: $\delta(P)$ model curve for fourth quarter weekdays

The values for $\delta(P)$ for weekdays in the fourth quarter of the model are shown in Figure 4-31. As days get shorter, the peaks occur earlier in the day. The midday peak is less apparent.

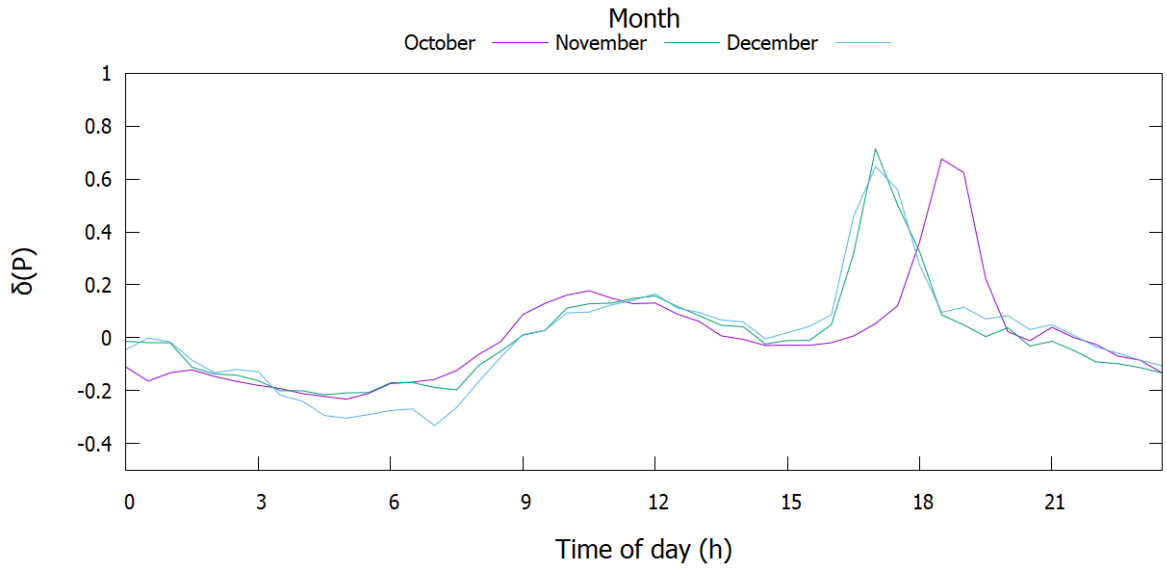

Figure 4-32: $\delta(P)$ model curve for fourth quarter weekends

The values for $\delta(P)$ for weekends in the fourth quarter of the model are shown in Figure 4-32. As with other times of year, the peaks are more apparent at weekends.

The values of $\delta(P)$ shown in Figure 4-25 to Figure 4-32 evidence the cyclic diurnal nature of the electricity prices. These values form an integral part of how the financial model in this study captures this behaviour. As mentioned above, the user can control the amplitude of this diurnal

cycle using an amplitude parameter, $\alpha(Q)$. The final values of $\varphi(P)$ are then calculated for each period using:

$$\varphi(P) = \alpha(Q)\delta(P) + 1 \qquad (4\text{-}11)$$

By calculating $\varphi(P)$ using the values of $\delta(P)$, the model ensures that the average value of $\varphi(P)$ is always 1, ensuring that the daily average, $A(D)$, always remains such, no matter how large the amplitude. It is important to note that the prediction of an electricity price, $S(P)$, for a half-hour period in this way will result in identical ratio $\varphi(P)$ for every day in a given quarter. Clearly, this is not representative of the actual behaviour of the electricity price relative to the day average. In order to properly capture this, a final stochastic variable, the error value $\varepsilon(P)$, for each period was introduced into the model to reintroduce unpredictability into the diurnal cycle. The modelling of this variable is discussed in section 4.4.4.

4.4.4. Half-hourly error value

Calculation of the half-hourly error value provides a measure of how well the values of $\varphi(P)$ predict the dataset (Smith and Halliday, 2016) values of $S(P)$. Section 4.4.3 discussed how the values of $\varphi(P)$ calculated for each period of the dataset split in the following ways:

- data split by quarter,
- data split by month,
- data split into weekend and weekday datasets by month.

As discussed, daily profile curves were calculated for each of these data subsets. The difference between the model predicted values of $\varphi(P)$ and the values calculated for the data were then calculated as an error value, $\varepsilon(P)$, for each period P:

$$\varepsilon(P) = \varphi_{\text{actual}}(P) - \varphi_{\text{model}}(P) \qquad (4\text{-}12)$$

where the actual and model subscripts denote values taken from the dataset calculations and the model respectively. These calculations provided three sets of error values showing how well each type of profile curve predicted its relevant data subset. In this section, the quality of the predicted values will be compared by studying the statistical spread of $\varepsilon(P)$ values. Where specific data splits result in particularly large or small improvements in prediction of $\varphi(P)$, the data will be studied and discussed in more detail.

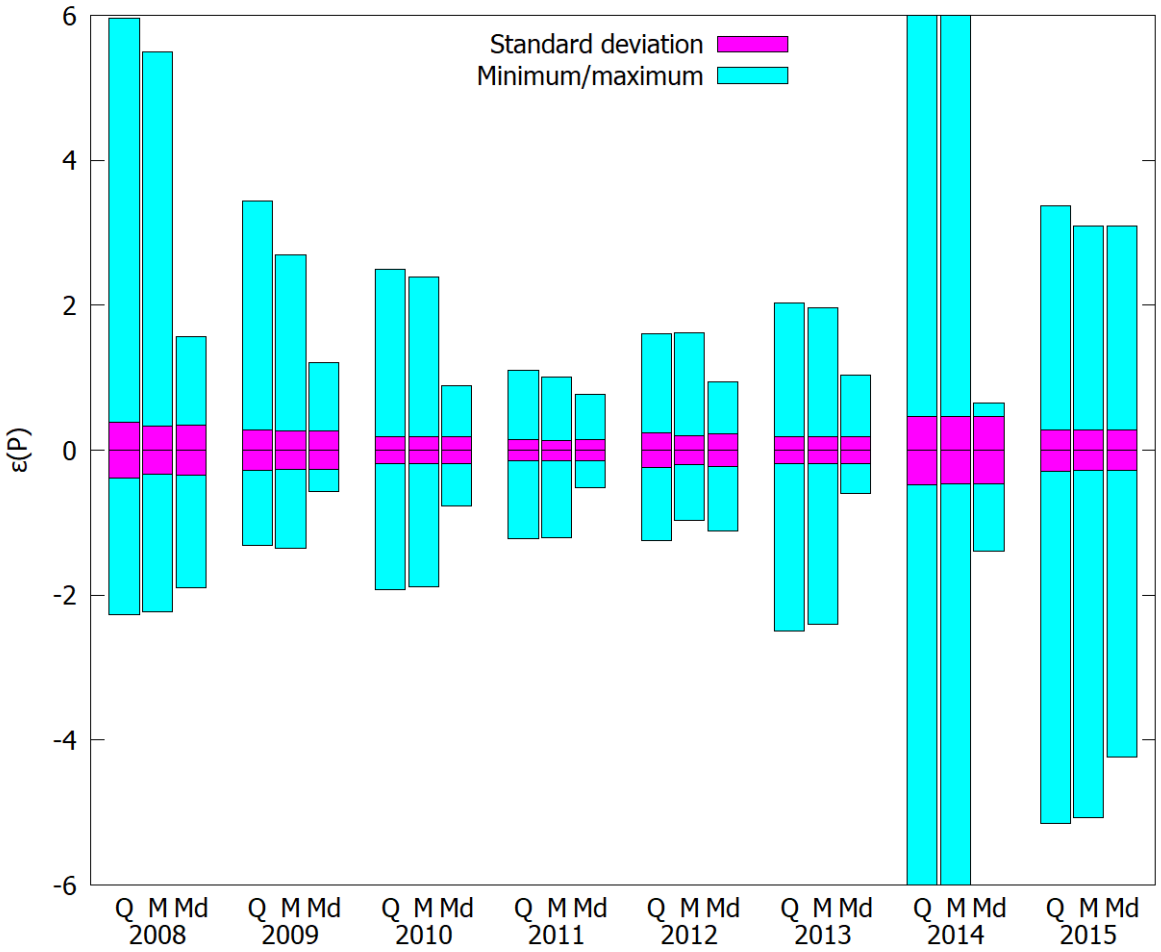

Figure 4-33: Prediction quality comparison for $R(P)$ models 'Q' shows quarterly split data, 'M' shows monthly split data and 'Md' shows data split monthly and into weekends and weekdays

Figure 4-33 compares the maximum and minimum values, as well as the standard deviation for $\varepsilon(P)$, depending on the method of splitting the dataset. From considering only the standard deviation, it would appear that defining models for $\varphi(P)$ based on monthly splits provides better prediction accuracy than additionally splitting the data by weekend and weekday. This is, however, not the whole story, as despite modest reductions in standard deviation, the maximum and minimum values for $\varepsilon(P)$ that result are significantly higher in all cases.

For the sake of brevity, only years of significant interest will be examined in more detail in this section. 2008 and 2014 show the most dramatic reduction in spread for $\varepsilon(P)$ when further splitting the dataset, whereas 2015 shows the most modest improvement. 2012 shows the largest difference between standard deviation values for the two approaches to monthly split, so this will also be looked at in greater detail.

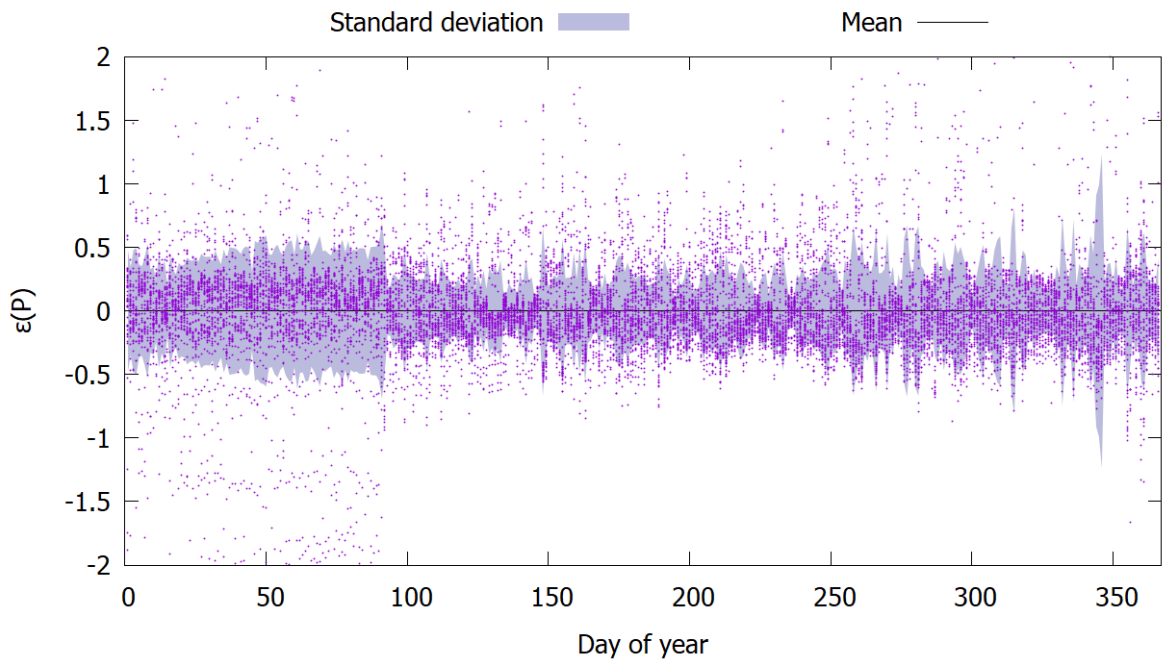

Figure 4-34: ε(P) values for 2008 for data split by quarter

The values of $\varepsilon(P)$ for the 2008 quarterly split are shown in Figure 4-34, along with the standard deviation and mean. The figure reveals some important information: primarily that the model for $\varphi(P)$ is a relatively poor predictor in the first quarter compared to the rest of the year. Additionally, the majority of values for the second and third quarters of the year that lie outside the standard deviation are positive. This means that when the model is predicting $\varphi(P)$

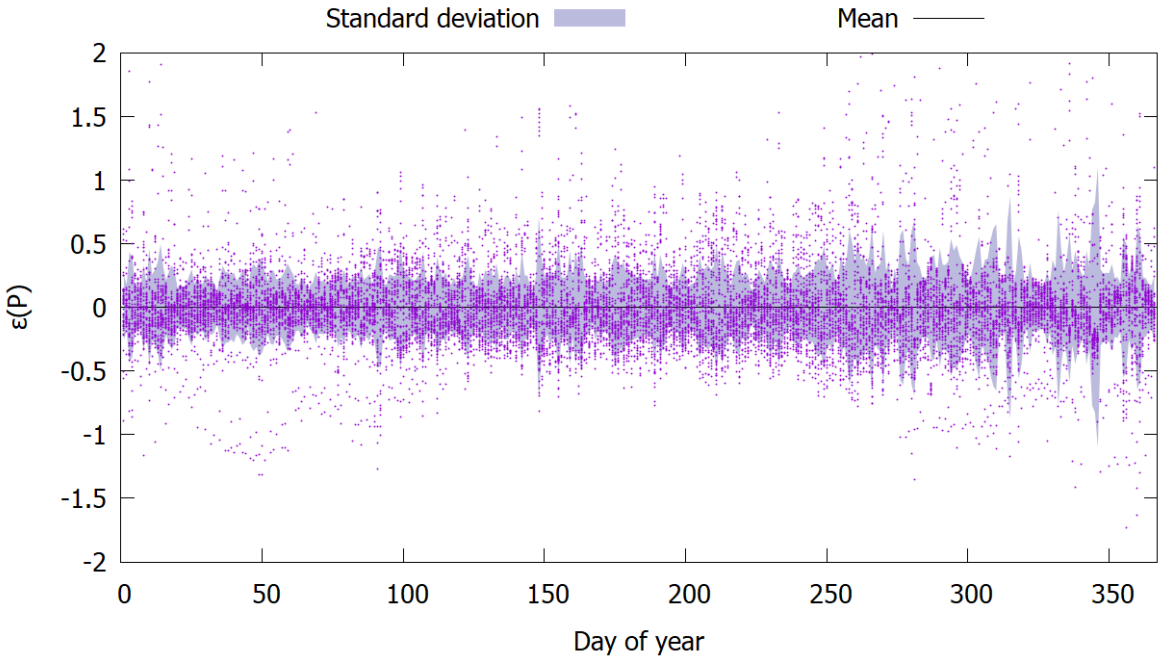

Figure 4-35: ε(P) values for 2008 for data split by month

comparatively poorly, it is underestimating its value. This is further exemplified by the higher density of points below the mean but within the standard deviation for this period.

The values of $\varepsilon(P)$ for the 2008 monthly split are shown in Figure 4-35. The improvement in prediction accuracy in the first quarter is readily apparent comparing this with Figure 4-34. There is more symmetry around the mean over the whole year, meaning that the model is not tending to favour underestimation as much compared to the quarterly split, however there is still some evidence of this.

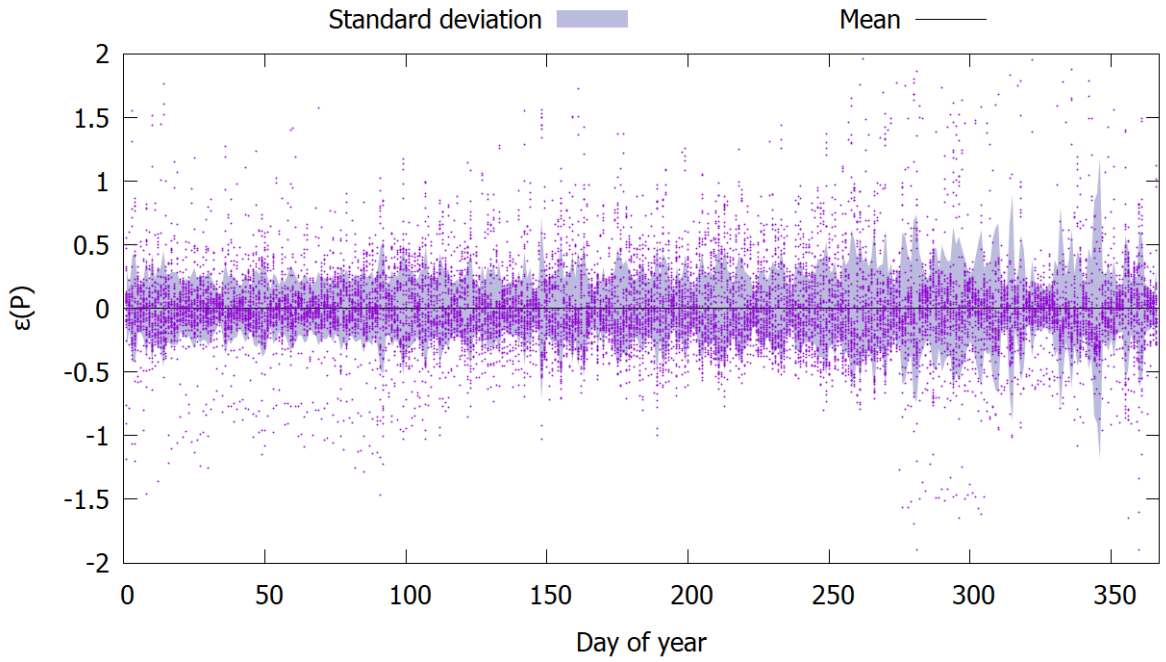

Figure 4-36: ε(P) values for 2008 for data split by month and weekend/weekday

The values of $\varepsilon(P)$ for the 2008 monthly split with weekday/weekend separation are shown in Figure 4-36. The datapoints show a similar distribution to those in Figure 4-35, but with greater error values in the first and at the beginning of the fourth quarter. Overall prediction quality is largely similar to the monthly split, if not a little worse.

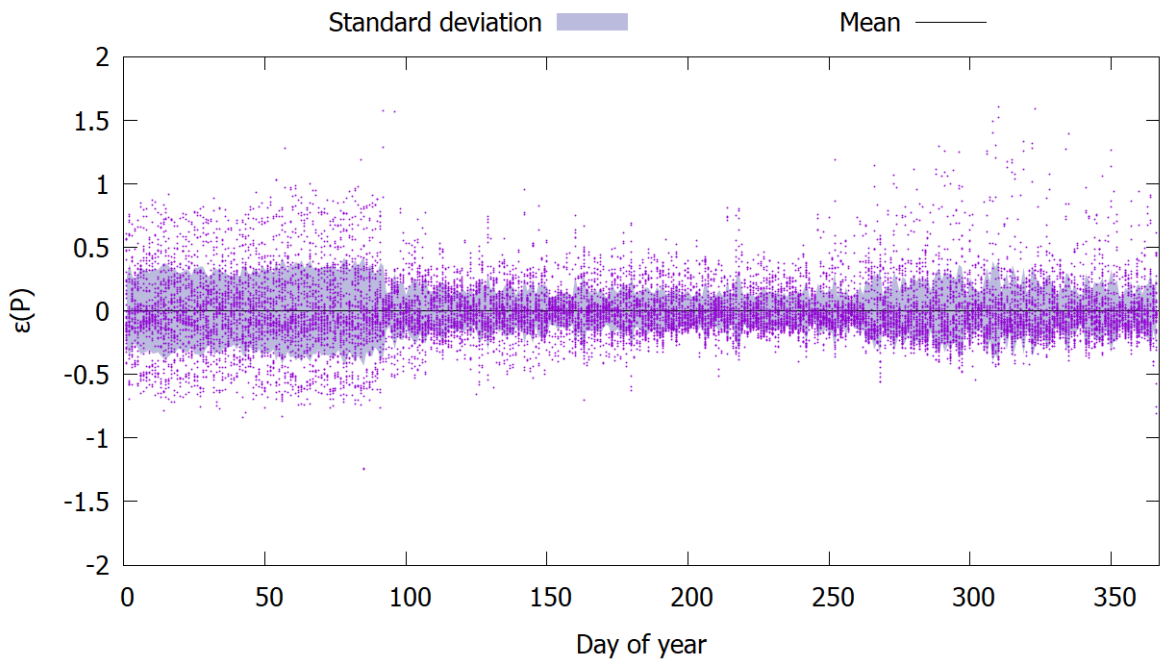

Figure 4-37: ε(P) values for 2012 for data split by quarter

The values for $\varepsilon(P)$ for the 2012 quarterly split are shown in Figure 4-37. As with the 2008 data, there is clear evidence of poor prediction in the first and last quarters compared with the rest of the year. The underestimation of $\varphi(P)$ values remains present in the final quarter but is far less noticeable during the rest of the year.

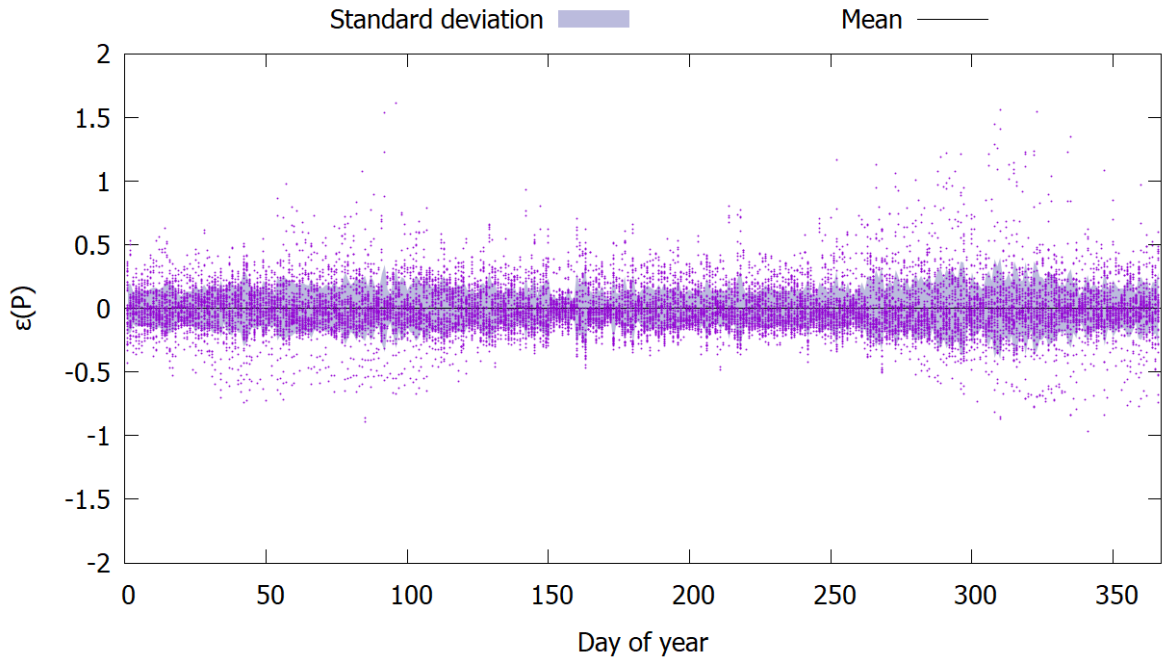

Figure 4-38: ε(P) values for 2012 for data split by month

The values for $\varepsilon(P)$ for the 2012 monthly split are shown in Figure 4-38. As with 2008, there is a significant improvement in prediction accuracy over the monthly split.

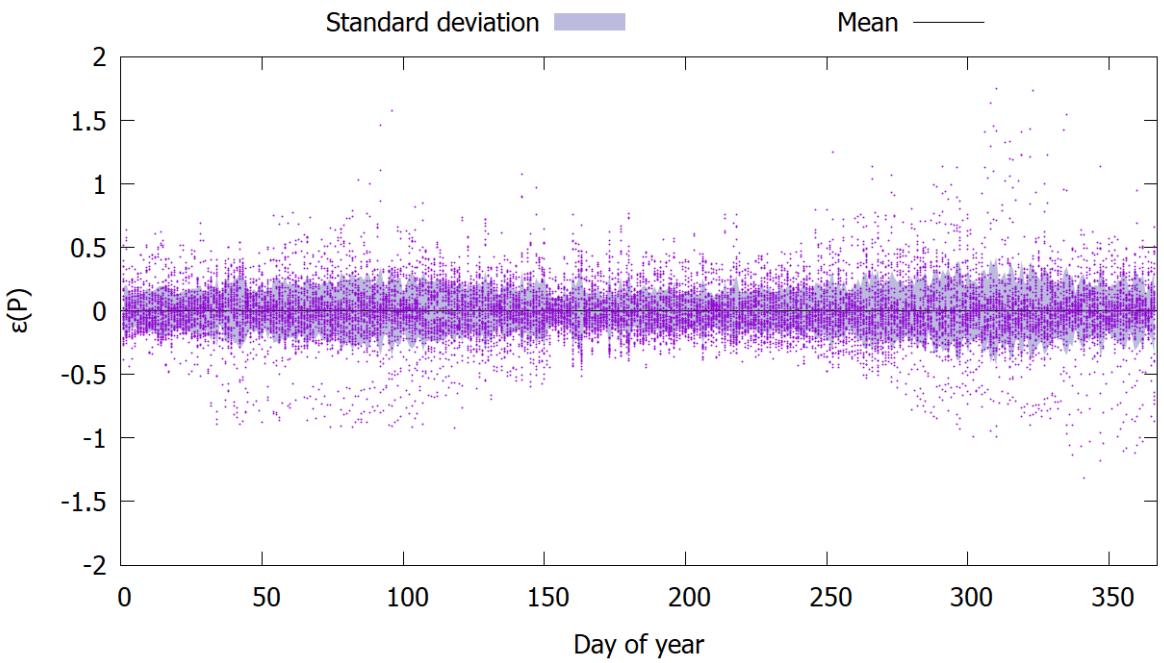

Figure 4-39: ε(P) values for 2012 for data split by month and weekend/weekday

The values of $\varepsilon(P)$ for the 2012 monthly split with weekday/weekend separation are shown in Figure 4-39. As might be expected from Figure 4-33, the prediction accuracy has worsened compared to the monthly split without day separation, especially in the first five months of the year. The effect is, however, only slight.

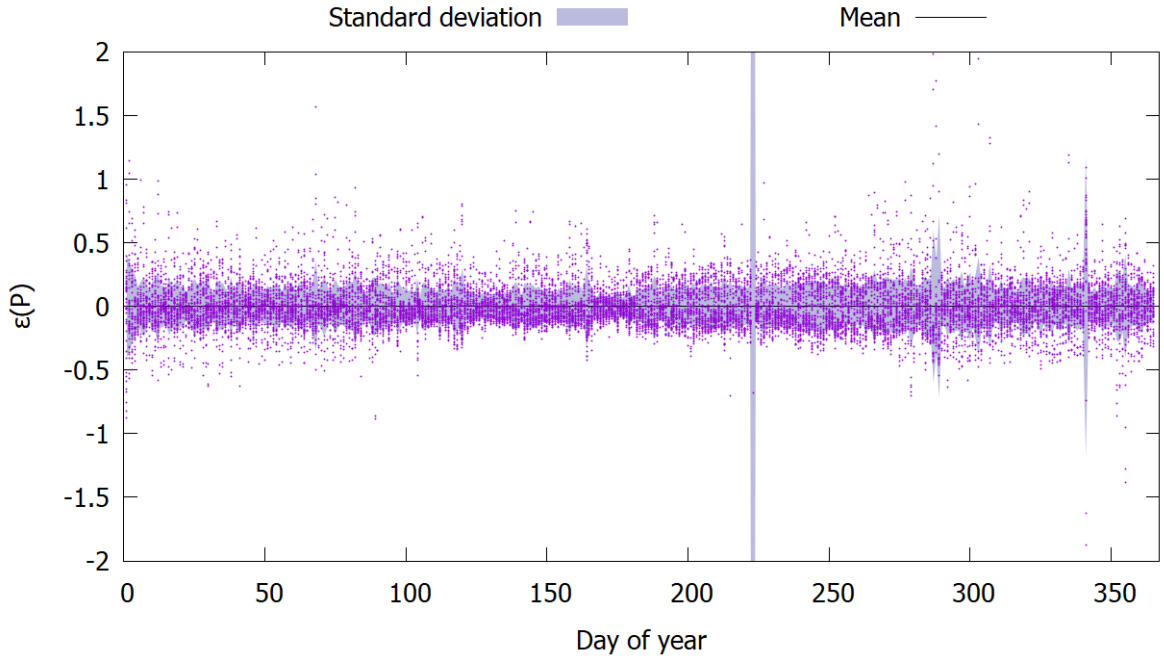

Figure 4-40: ε(P) values for 2014 for data split by quarter showing an anomalous day in August

The values for $\varepsilon(P)$ for the 2014 quarterly split are shown in Figure 4-40. Of all the quarterly splits so far, this is by far the best predictor of error values. As the caption notes, there is an

anomalous day on 11th August with an extremely high standard deviation and very few values within the range of the y-axis. Viewing the data, this is a consequence of large mismatches between supply and demand on that day, with supply being 100 MWh or more in excess of demand for several balancing periods on that day.

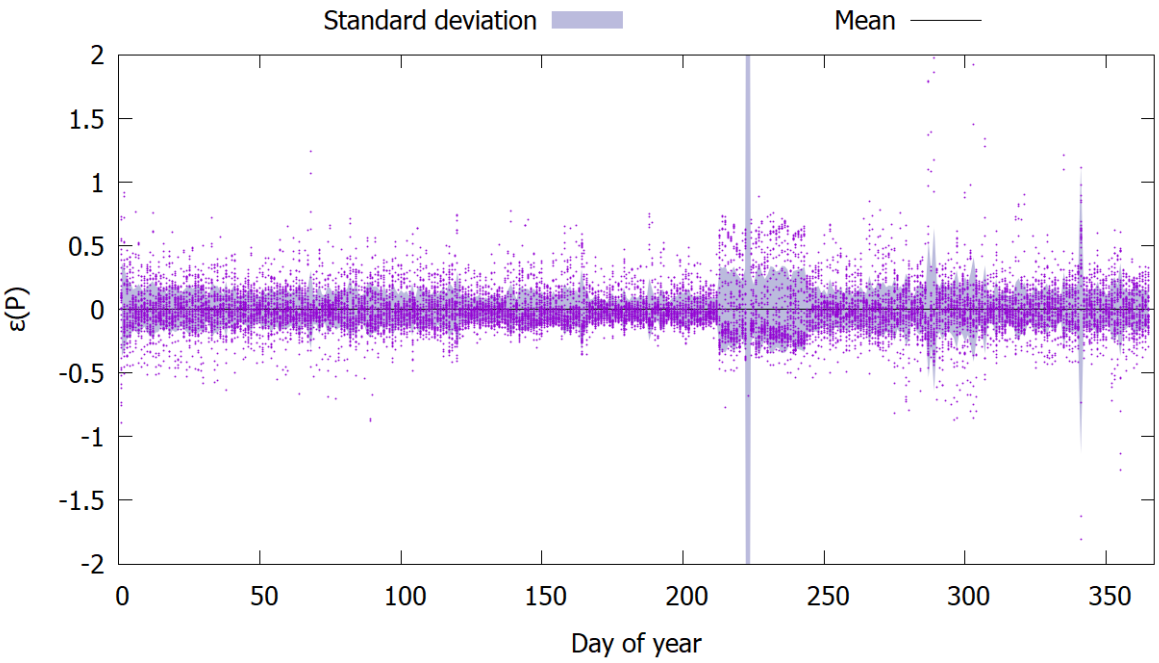

Figure 4-41: ε(P) values for 2014 for data split by month showing an anomalous August

The values for $\varepsilon(P)$ for the 2014 quarterly split are shown in Figure 4-41. This shows near-negligible improvement over the quarterly split and shows particularly poor prediction of values for the month of August. This is a consequence of the anomalous day on 11 August not having been omitted from calculation of the daily profile for that month. Overall, this the most marginal improvement seen in and of the monthly splits so far.

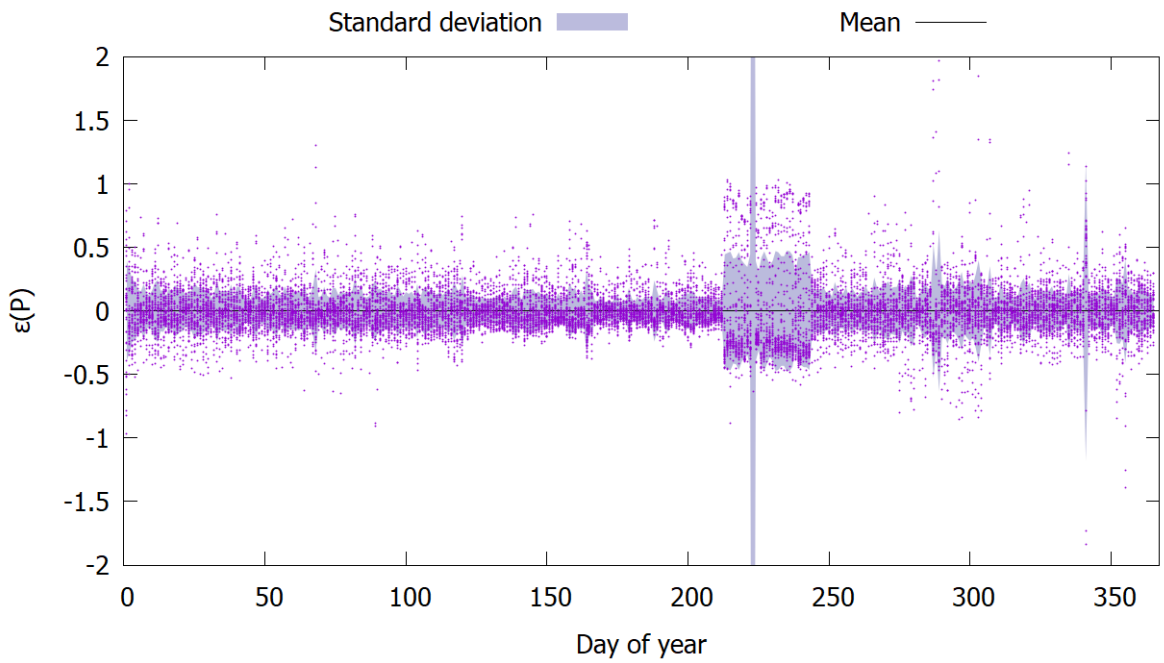

Figure 4-42: ε(P) values for 2014 for data split by month and weekend/weekday showing an anomalous August

The values of $\varepsilon(P)$ for the 2014 monthly split with weekday/weekend separation are shown in Figure 4-42. The majority of the year is very similar to the basic monthly split with a slightly narrower spread of values, however August prediction accuracy has again worsened significantly. The poor prediction in August is perhaps the reason for the modest improvement in $\varepsilon(P)$ standard deviation seen in Figure 4-33. This particularly volatile August might also be the key contributing factor to the significantly higher standard deviations for 2014 compared to the other years of the dataset.

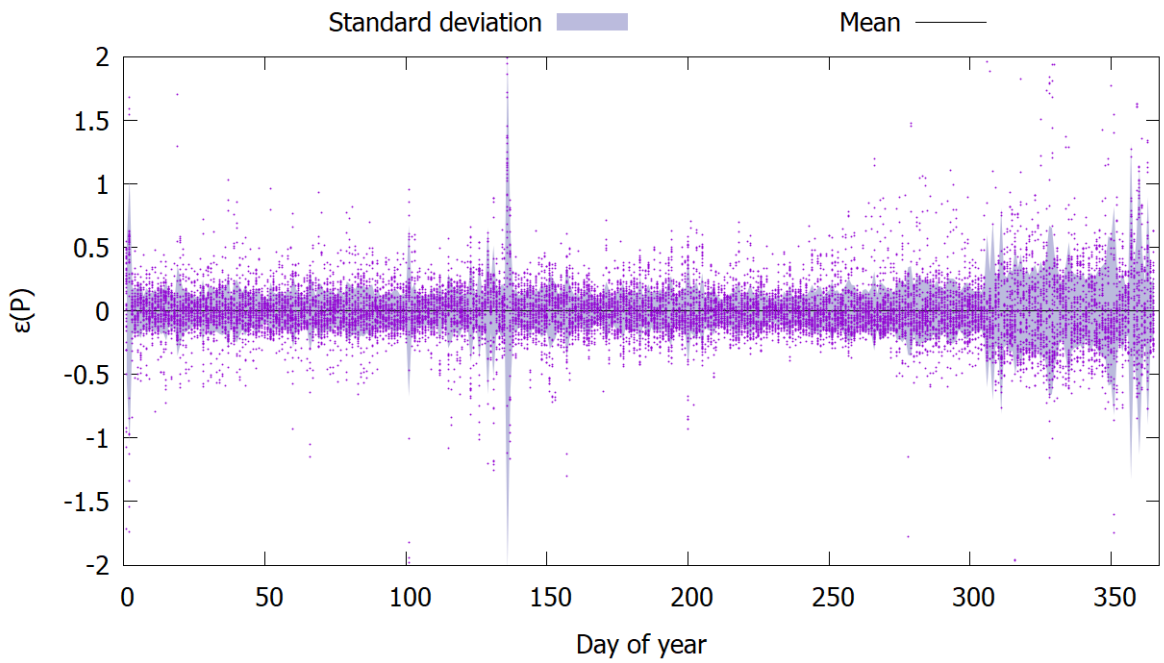

Figure 4-43: ε(P) values for 2015 for data split by quarter showing an anomalous day in May

The values of $\varepsilon(P)$ for the 2015 quarterly split are shown in Figure 4-43. Prediction accuracy is very good overall; by far the best of all the detailed examples in this section. Fourth quarter prediction accuracy is lower than the rest of the year but not particularly bad. Once again, there is an anomalous day on 16th May. Unlike 11th August 2014, there is no clear reason for this. Electricity prices seem particularly volatile on 16th May, but the mismatch between demand and supply is neither greater nor more sporadic than other days in May.

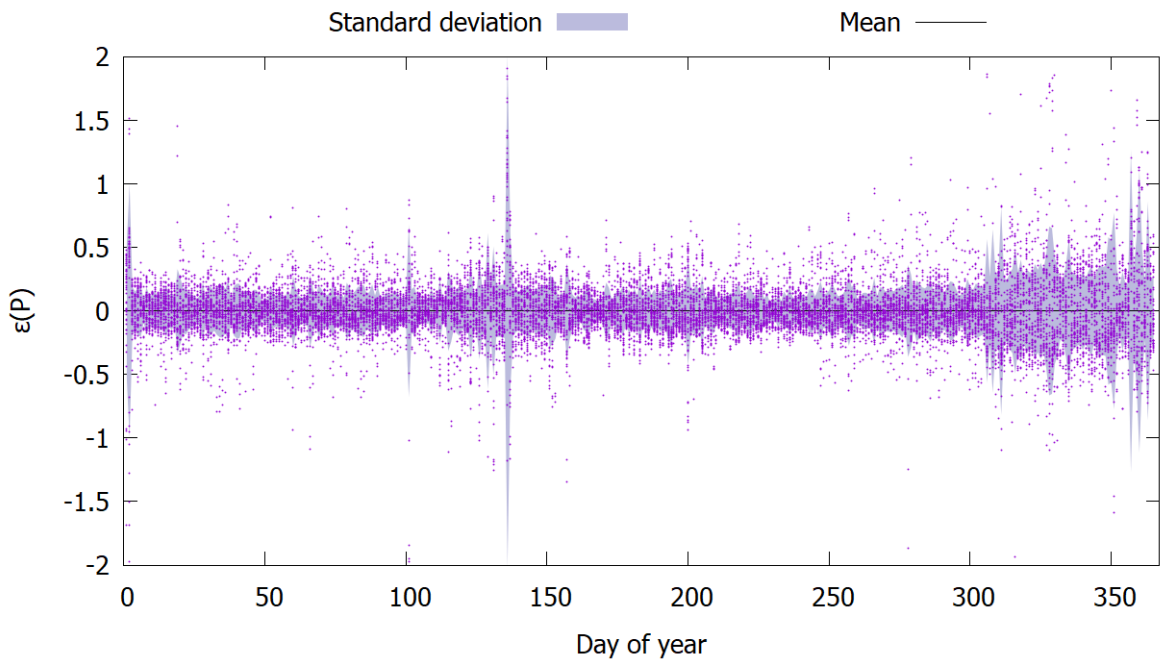

Figure 4-44: ε(P) values for 2015 for data split by month

The values of $\varepsilon(P)$ for the 2015 monthly split are shown in Figure 4-44. As might be expected from Figure 4-33, there is only a very modest improvement in prediction accuracy.

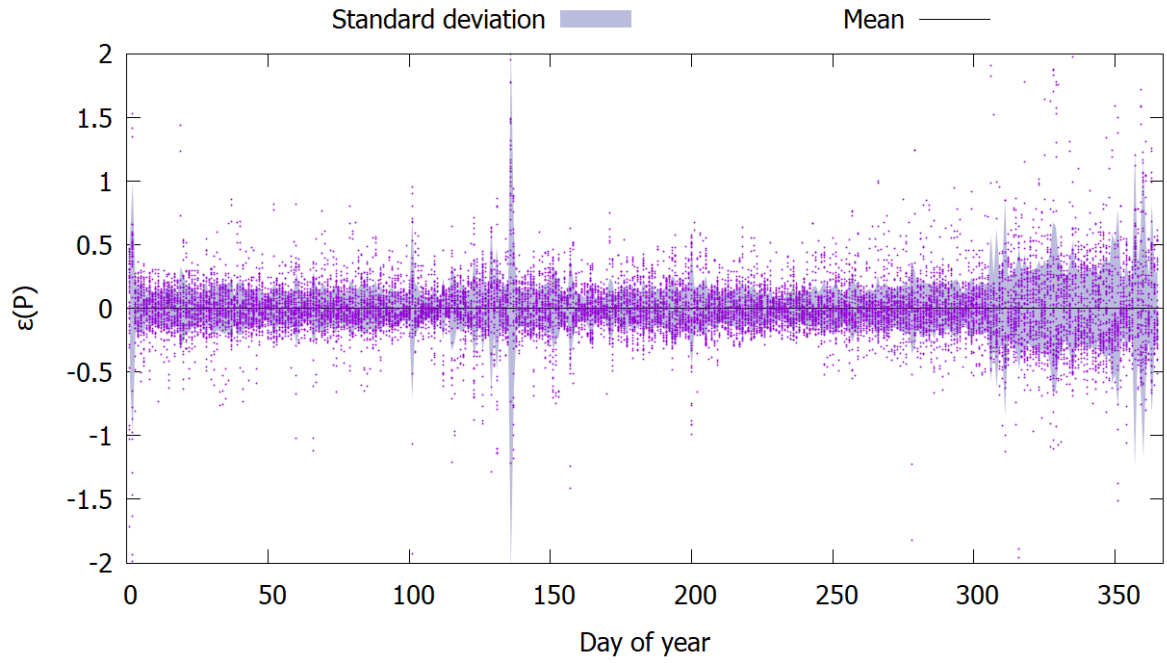

Figure 4-45: ε(P) values for 2014 for data split by month and weekend/weekday

The values of $\varepsilon(P)$ for the 2015 monthly split with weekday/weekend separation are shown in Figure 4-45. Once again, improvements are barely noticeable.

One of the most important pieces of information that can be gleaned from Figure 4-34 to Figure 4-45 is that there are several occasions where particularly large magnitude values of $\varepsilon(P)$ occur on the same day, as can be seen by the clustering of datapoints in vertical columns. This is perhaps explainable in terms of volatility; when a given day's $S(P)$ progression is unusually volatile, the modelled values of $\varphi(P)$ are likely to predict $S(P)$ poorly for the whole day. This has an important influence on the modelling approach to the $\varepsilon(P)$ values. Simple probability distributions could be fit to the data and used to predict $\varepsilon(P)$, however if the hypothesis that poor predictions are often caused by particularly volatile days holds true, time series models, particularly those that have an immediate and short-term response to shocks, might provide a better means of prediction.

It is also worth noting that the clustering of datapoints in this way has a tendency to occur on only one side of the mean; i.e. when the model underestimates the value of $\varphi(P)$, it tends to do so for the whole day, and so too when it overestimates. As discussed in section 4.4.2 this has an important effect on time series selection. MA time series tend to generate values that oscillate on either side of the mean, whereas AR time series tend to generate values that stay on one side of the mean for extended periods. In terms of shocks, in MA series, one shock is typically followed by another whereas in AR series, shocks tend to be followed by periods of relative calm. It is reasonable to expect, then, that AR series should model the behaviour discussed in the previous paragraph better than MA series. Alas, time series models are stochastic in nature and there is no way to directly define the length of calm periods in AR series in a way that would effectively capture the periodic nature of the prediction accuracy of $\varphi(P)$. Indirectly, it is conceivable that one could use a combination of probability distributions and time series to achieve this effect, with a distinct AR series being used for each day modelled and the parameters of these series defined individually via probability distribution. However, for the model described in this work, defining time series in this way would be onerous in the extreme requiring some 10,000 individually defined time series models to cover the 30-year period of the model.

Using time series has an unfortunate consequence; values produced by probability distributions are independent of one another whereas values produced by time series must be computed sequentially and thus place a far greater computational load on the model. This has a significant impact on model runtimes, especially in Monte Carlo modelling where simulations are run for thousands of iterations at a time. However, conversely to the discussions in section 4.4.2 regarding seasonal patterns, it is important that the model be capable of capturing this behaviour. With an LAES system being capable of charging and discharging in a single day, sudden short-lived periods of volatility in $\varepsilon(P)$ are likely to have a significant effect on spot

market pricing and thus on plant revenue. Given the considerations in this paragraph and the previous two, the decision was made to test data fits for both probability distributions and time series.

Initial testing showed that Laplace and logistic probability distributions offered the best fit in the majority of cases. Loglogistic offered a good fit for several years, but there were other years where @RISK was unable to determine a suitable fit. GARCH, ARMA, first order AR and first order MA time series offered the best fit in most cases. ARCH and GARCH series are particularly suited to capturing datasets that exhibit volatility clustering and may potentially offer a good means of capturing the short periods of high volatility seen in the $\varepsilon(P)$ data (signified by the short periods of high standard deviation).

ARCH and GARCH processes are used when the data's standard deviation varies over time, exactly as seen in the $\varepsilon(P)$ data. ARCH models assume that the standard deviation follows an AR model, whereas GARCH models assume that the standard deviation follows and ARMA model. ARCH parameters are average, μ, positive volatility, ω, positive autoregressive coefficient, a, initial value $y(0)$, and initial standard deviation $\sigma(0)$. Each consecutive value is based on an RN, $N(t)$, taken from a normal distribution with mean 0 and standard deviation 1. The t^{th} series value is calculated:

$$y(t) = \mu + \sigma(t)N(t) \qquad (4\text{-}13)$$

where the value of $\sigma(t)$ is modelled using:

$$\big(\sigma(t)\big)^2 = \omega + a(y(t-1) - \mu)^2 \qquad (4\text{-}14)$$

As with the discussion in section 4.4.2, it is worth considering these equations in detail to determine exactly how consecutive values are calculated. As shown in equation (4-14), the standard deviation for a given value of the series is driven by the volatility parameter, ω and a second term with the autoregressive coefficient, a. When the previous value of y is far from the mean, this second term will be large, meaning that the value of $\sigma(t)$ will also be large meaning that the value of y is more likely to be far from the mean. This behaviour is very much like that seen in the AR model. The value of a relative to ω defines how strong this autoregressive effect is.

As shown in equation (4-13), the value of $\sigma(t)$ drives the value of y. When, $\sigma(t)$ is large, more extreme values of $N(t)$ will drive y further from the mean. Because $N(t)$ is a standard

deviation, its mean value, and hence the mean value of the second term will be zero, meaning that the mean of y will be equal to μ for series with many values.

GARCH parameters are average, μ, positive volatility, ω, positive autoregressive coefficient, a, positive moving average coefficient, b, initial value $y(0)$, and initial standard deviation $\sigma(0)$. As with an ARCH model, the t[th] series value is calculated:

$$y(t) = \mu + \sigma(t)N(t) \qquad (4\text{-}15)$$

where the value of $\sigma(t)$ is modelled using:

$$\big(\sigma(t)\big)^2 = \omega + a(y(t-1) - \mu)^2 + b\big(\sigma(t-1)\big)^2 \qquad (4\text{-}16)$$

If b is taken to be zero, this yields equation (4-14) for an ARCH model. If a is taken to be zero, then equation (4-16) becomes:

$$\big(\sigma(t)\big)^2 = \omega + b\big(\sigma(t-1)\big)^2 \qquad (4\text{-}17)$$

As the equation shows, the standard deviation for a given value of the series is driven by the volatility parameter, ω and a second term with the moving average coefficient, b. This second term shows that a large value of standard deviation is expected when the value of the previous standard deviation is large. This behaviour is very similar that that seen in the moving average model discussed in section 4.4.2. The effect of this moving average behaviour on $\sigma(t)$ is governed by the size of b relative to ω.

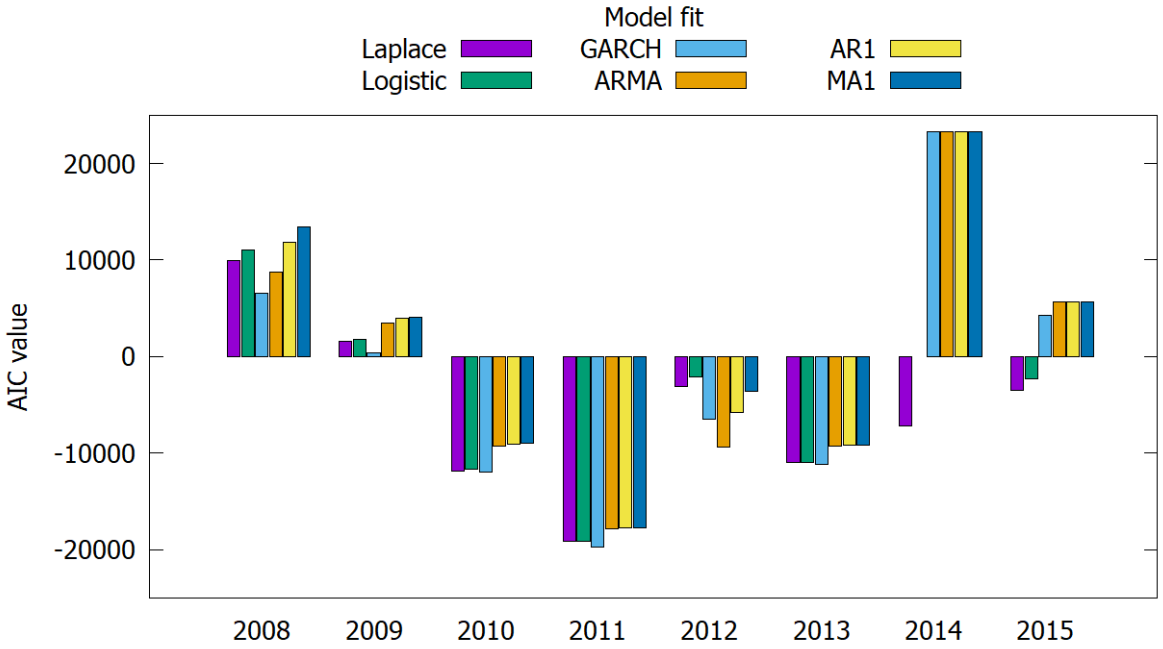

Figure 4-46: Model fit comparison for quarterly split data (lower AIC value represents a better fit, no fit was possible where bars are missing)

The model fit comparison for the quarterly split data is shown in Figure 4-46. This shows that in almost all cases, the probability distributions and GARCH time series provide a better fit than the ARMA, AR and MA time series.

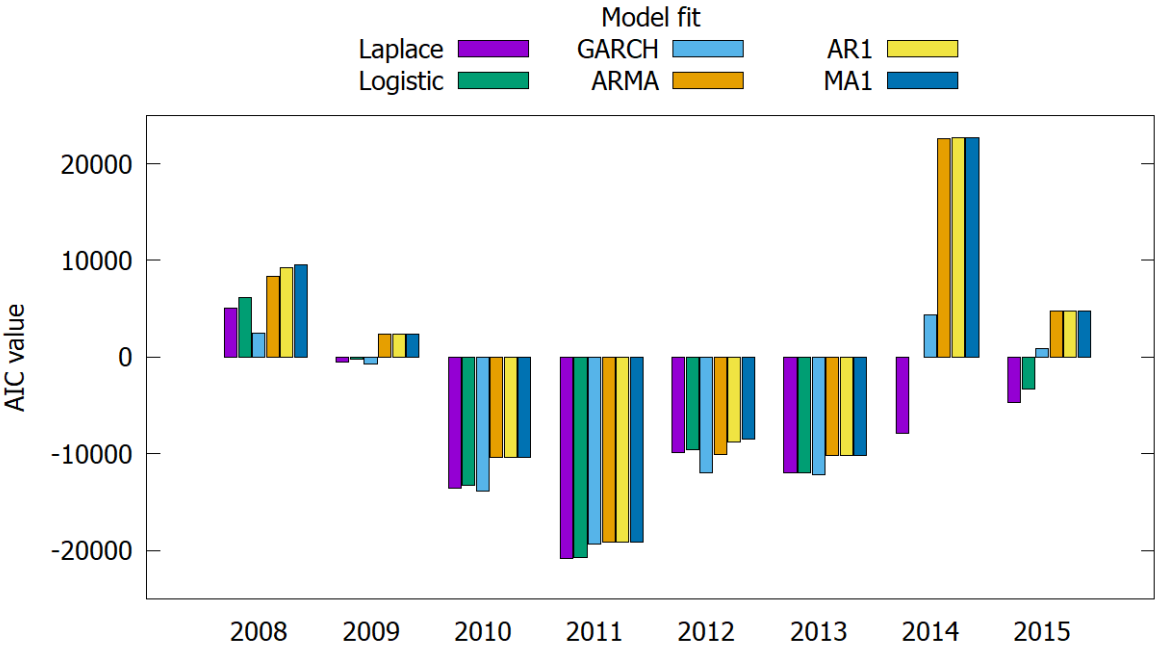

Figure 4-47: Model fit comparison for monthly split data (no fit was possible where bars are missing)

The model fit comparison for the monthly split is shown in Figure 4-47. As with the quarterly split, the GARCH and probability distributions exhibit a better fit in almost all cases and this preference is somewhat more apparent.

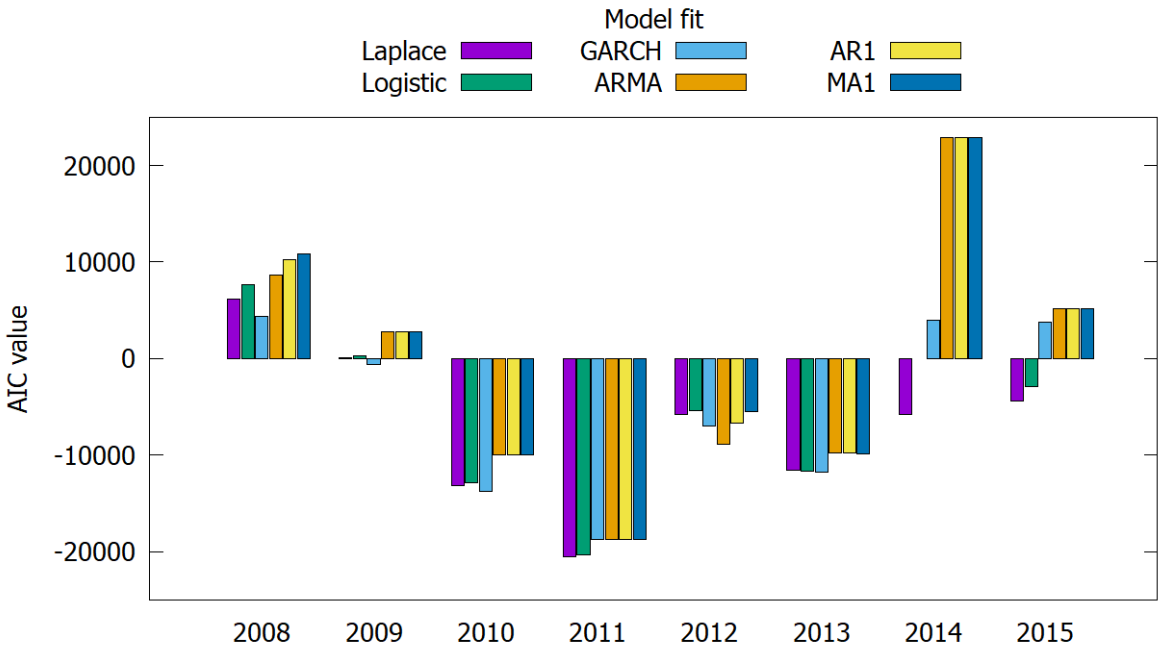

Figure 4-48: Model fit comparison for monthly and weekend/weekday split data (no fit was possible where bars are missing)

The model fit comparison for the monthly split with weekday/weekend separation is shown in Figure 4-48. There is little difference between this and Figure 4-47, except for 2012 and 2015 where the superiority of the GARCH fit to the other time series is less apparent.

From examination of Figure 4-46 to Figure 4-48, it would appear that probability distributions and GARCH models all offer better fits to the $\varepsilon(P)$ data than the ARMA, MA and AR models. It is however important to note that for all probability distributions tested, as well as the GARCH and MA time series, a given value being above or below the mean has no bearing on the likelihood of the following value being above or below the mean. As the discussion regarding Figure 4-34 to Figure 4-45 notes above, the data for $\varepsilon(P)$ generally exhibits strong directionality relative to the mean over the course of a day. AR time series, and to a lesser extent ARMA time series, are better suited to capturing this characteristic of the $\varepsilon(P)$ data and likely to be better suited to this aspect of the model.

Given that there is little difference in fit quality between these models, and that in all years except 2009, 2014 and 2015, there is little difference in fit quality between the GARCH and the other time series, the final decision was taken to use an AR time series to ensure that the directionality of the $\varepsilon(P)$ data was properly captured by the model.

4.4.5. Consumer Price Index

Plant costs, such as operation and maintenance and fuelling costs are subject to inflation. In addition, strike prices are adjusted each year according to CPI (Department of Energy and Climate Change, 2013). The decision was made to use this index in order to adjust plant costs and the strike price throughout the duration of the model. As a result, the model requires a means of simulating CPI rates for its duration. A time series was fit to the CPI annual rate data

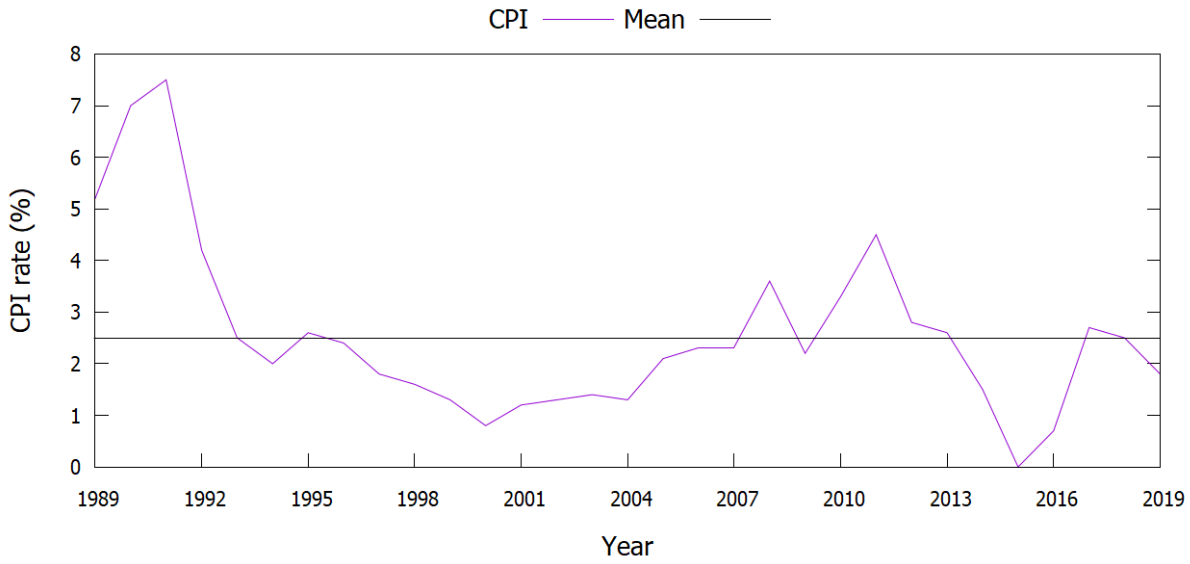

Figure 4-49: CPI annual rate data 1989-2019

(King, 2020), as shown in Figure 4-49.

The time series fit was performed with the available time series in @RISK and yielded a first-order MA process as the best fit. This series is introduced in section 4.4.2. It has four parameters; mean, μ, volatility, σ, moving average coefficient b and initial error term $\epsilon(0)$. As with AR and ARMA series, for the tth series value, an error term is calculated based on a random number generated by a normal distribution $N(t)$ with mean 0 and standard deviation 1:

$$\epsilon(t) = \sigma N(t) \qquad (4\text{-}18)$$

Then, the time series value, $y(t)$, is calculated using:

$$y(t) = \mu + b\epsilon(t-1) + \epsilon(t) \qquad (4\text{-}19)$$

As discussed in section 4.4.2, shocks have a substantial effect on subsequent values of $y(t)$, but only for a short period. Values are expected to oscillate on both sides of the mean and not to show preference for one side or another following shocks. Whilst the data in Figure 4-49 is

for a relatively limited period of 20 years, this is broadly what can be seen; the data appears to oscillate above and below the mean.

4.5. Model construction

The financial model is built in an Excel spreadsheet with a single front page for the entry of model parameters. The user-defined parameters and their nominal values are listed in Table 4-4. Parameters of interest whose effect will be explicitly explored during modelling are indicated, as are the LAES plant characteristics which are defined via the engineering model and the parameters either defined by or calculated from a probability distribution for each iteration. The symbol I in parentheses is used to indicate a parameter that changes each iteration.

Input parameters		
Symbol	**Value**	**Description**
$C_{\mathrm{NPP,BASE}}$	£1.05bn	Base asset cost of NPP
S_{CfD}	*1	Starting NPP CfD price
$\varphi_{\mathrm{COST,NPP}}(I)$	*3	NPP spending factor
$C_{\mathrm{NPP}}(I)$	*3	Iteration cost of NPP
$C_{\mathrm{LAES}}(I)$	*3	Iteration cost of LAES
$t_{\mathrm{MOB,NPP}}(I)$	*3	Iteration mobilisation construction time for the NPP (years)
$t_{\mathrm{CRIT,NPP}}(I)$	*3	Iteration critical path construction time for the NPP (years)
$t_{\mathrm{MOB,LAES}}(I)$	*3	Iteration mobilisation construction time for the LAES (years)
$t_{\mathrm{CRIT,LAES}}(I)$	*3	Iteration critical path construction time for the LAES (years)
$C_{\mathrm{NPP,MOB}}(I)$	*3	Iteration NPP mobilisation construction costs
$C_{\mathrm{NPP,CRIT}}(I)$	*3	Iteration NPP critical path construction costs
$C_{\mathrm{LAES,MOB}}(I)$	*3	Iteration LAES mobilisation construction costs
$C_{\mathrm{LAES,CRIT}}(I)$	*3	Iteration LAES critical path construction costs
φ_{CONST}	0.30	Proportion of cost spent during construction mobilisation
$C_{\mathrm{O\&M,NPP}}$	£30m	Fixed O&M costs for the NPP
C_{REFUEL}	£10m	Refuelling costs for the NPP
$\varphi_{\mathrm{O\&M,LAES}}$	1.5%	O&M costs for the LAES as a percentage of LAES plant cost
$C_{\mathrm{O\&M,LAES}}(I)$	*3	Iteration LAES O&M costs
$\dot{W}_{\mathrm{NPP}}$	300 MW	Electrical power of the NPP
$\dot{W}_{\mathrm{CHG}}$	*2	Electrical power consumption of LAES during charge
$\dot{W}_{\mathrm{DIS}}$	*2	Electrical power yield of LAES during discharge
$\dot{M}_{\mathrm{CHG}}$	*2	Air mass flow rate during charge
$\dot{M}_{\mathrm{DIS}}$	*2	Air mass flow rate during discharge
$M_{\mathrm{TANK,MAX}}$	*2	Maximum storage capacity of the liquid air tank
$t_{\mathrm{START,CHG}}$	*1	Start time for charging period
$t_{\mathrm{START,CHG}}$	*1	End time for charging period
$t_{\mathrm{START,DIS}}$	*1	Start time for discharging period
$t_{\mathrm{END,DIS}}$	*1	End time for discharging period
t_{FUEL}	500 d	Reactor uptime for a single fuel load
t_{REFUEL}	10 d	Reactor downtime for refuelling
Y_{START}	2020	Year in which plant construction begins
T_{CORP}	20%	Corporation tax on profits
i_{CPI}	*3	CPI rate
i_{DISC}	*1	Discount rate

*Table 4-4: Financial model fixed parameters (*1 represents a user-defined parameter of interest, *2 represents a parameter defined by the chosen plant configuration, *3 represents an initial parameter defined by, or calculated from, a probability distribution for each iteration)*

The front page also defines the probability distribution parameters and the time series parameters for the uncertain model inputs. The chosen parameters for the uncertain initial probability distributions are shown in Table 4-5.

PERT distribution parameters	FOAK scenario			NOAK scenario		
	Minimum	Most likely	Maximum	Minimum	Most likely	Maximum
NPP spending factor $\varphi_{\mathrm{COST,NPP}}$	1	1.7	2	1	1.1	1.3
Binomial distribution parameters	**FOAK scenario**			**NOAK scenario**		
	$\boldsymbol{n}$	$\boldsymbol{p}$	shift	$\boldsymbol{n}$	$\boldsymbol{p}$	shift
NPP construction time – mobilisation	1	0.6	2	0	0.4	2
NPP construction time – critical path	2	0.6	3	1	0.4	3
LAES construction time – mobilisation	1	0.6	1	1	0.2	1
LAES construction time – critical path	1	0.6	1	1	0.4	1

Table 4-5: Financial model initial uncertain probability distribution parameters

The chosen parameters for the time series are shown in Table 4-6. The parameters for mean and volatility for the $A(D)$ time series, as well as volatility for the $\varepsilon(P)$ time series, remain user-defined to allow exploration of different market price scenarios. Whilst not displayed in the table, amplitude factors are similarly defined for each quarter in the front page. All time series parameters are user-defined once every five years (for year 0, 5, 10, etc.) and are interpolated between these values for the 30 modelled years. The option remains to directly adjust the interpolated parameters if necessary, however this is not done in this study. Mean daily average electricity prices are defined in 2019 (year 0) prices and are adjusted by CPI for each subsequent year, as discussed in section 4.5.1.

ARMA time series parameters	**Mean**	**Volatility**	**Autoregressive coefficient**	**Moving average coefficient**
Daily average electricity price $A(D)$	$*^1$	$*^1$	0.8	-0.2
First-order AR parameters	**Mean**	**Volatility**	**Autoregressive coefficient**	**Initial value**
Half-hourly error value $\varepsilon(P)$	0	0.12	0.6	0
First-order MA parameters	**Mean**	**Volatility**	**Moving average coefficient**	**Initial error term**
Consumer price index, i_{CPI}	0.225	0.002	0.823	0

Table 4-6: Financial model time series parameters ($*^1$ represents a user-defined parameter of interest)

The front page defines the initial parameters from probability distributions for each iteration run of the model. The iteration value for the spending factor of the NPP, $\varphi_{\mathrm{COST,NPP}}(I)$, is used to calculate the iteration cost of the NPP from the NPP base cost, $C_{\mathrm{NPP,BASE}}$:

$$C_{\mathrm{NPP}}(I) = C_{\mathrm{NPP,BASE}} \times \varphi_{\mathrm{COST,NPP}}(I) \quad (4\text{-}20)$$

The construction time iteration parameters for the mobilisation and critical path construction times for both the NPP and the LAES plant, $t_{\mathrm{MOB,NPP}}(I)$, $t_{\mathrm{CRIT,NPP}}(I)$, $t_{\mathrm{MOB,LAES}}(I)$ and $t_{\mathrm{CRIT,LAES}}(I)$ are determined from their respective probability distributions. The iteration cost for LAES, $C_{\mathrm{LAES}}(I)$, is determined from its probability distribution and the annual O&M cost is calculated using the ratio $\varphi_{\mathrm{O\&M,LAES}}$:

$$C_{\mathrm{O\&M,LAES}}(I) = C_{\mathrm{LAES}}(I) \times \varphi_{\mathrm{O\&M,LAES}} \quad (4\text{-}21)$$

The NPP mobilisation and critical path construction costs, $C_{\mathrm{NPP,MOB}}(I)$ and $C_{\mathrm{NPP,CRIT}}(I)$ respectively are calculated using the construction cost ratio φ_{CONST}:

$$C_{\mathrm{NPP,MOB}}(I) = C_{\mathrm{NPP}}(I) \times \varphi_{\mathrm{CONST}} \quad (4\text{-}22)$$

$$C_{\mathrm{NPP,CRIT}}(I) = C_{\mathrm{NPP}}(I) \times (1 - \varphi_{\mathrm{CONST}}) \quad (4\text{-}23)$$

The LAES mobilisation and critical path construction costs are similarly calculated:

$$C_{\mathrm{LAES,MOB}}(I) = C_{\mathrm{LAES}}(I) \times \varphi_{\mathrm{CONST}} \quad (4\text{-}24)$$

$$C_{\mathrm{LAES,CRIT}}(I) = C_{\mathrm{LAES}}(I) \times (1 - \varphi_{\mathrm{CONST}}) \quad (4\text{-}25)$$

These calculated iteration values are then used to populate the columns of the annual accounts sheet that represent the project years during which the plant is under construction, as described in section 4.5.2.

4.5.1. Electricity price model sheets

The electricity price model consists of four sheets. The first three calculate the values of $A(D)$ for each day, the values of $\varepsilon(P)$ for each period and the values of $\varphi(P)$ for each period. The final sheet calculates the system sell price $S(P)$ based on the values in the other three sheets. The four sheets will now be discussed in turn, starting with the $A(D)$ sheet. As discussed in section 0, the mean parameter, $\mu_{A(D)}(Y)$, for year Y for each time series is taken from the user-

defined front page parameters and the resulting interpolations. Since all 31 values of $\mu_{A(D)}(Y)$ are defined in year $Y = 0$ prices, its values are adjusted according to CPI for all subsequent years according to the formula:

$$\mu_{A(D)}(Y) = \mu_{A(D)}(Y)\big((i_{CPI}(Y)+1)(i_{CPI}(Y-1)+1)\cdots(i_{CPI}(2)+1)(i_{CPI}(1)+1)\big) \quad (4\text{-}26)$$

Parameter values for $\sigma_{A(D)}$ over the modelled years are similarly taken from the front sheet but since these represent volatility, they do not need to be adjusted for CPI. The parameters for the autoregressive coefficient $a_{A(D)}$ and the moving average coefficient $b_{A(D)}$ are taken from the front sheet but remain fixed throughout the course of the model. One time series is then calculated for each year using the ARMA formula from section 4.4.2. This yields a value of $A(D)$ for each day, D, according to the series parameters and the following equation:

$$\big(A(D) - \mu_{A(D)}(Y)\big) = a_{A(D)}\big(A(D-1) - \mu_{A(D)}(Y)\big) + b_{A(D)}\epsilon(D-1) + \epsilon(D) \quad (4\text{-}27)$$

where $\epsilon(D)$ is an error term calculated with standard deviation defined by $\sigma_{A(D)}$ and a random number $N(D)$ from a normal distribution with mean 0 and standard deviation 1:

$$\epsilon(D) = \sigma_{A(D)}N(D) \quad (4\text{-}28)$$

For simplicity, the initial value for a given year is taken to be equal to the average value for that year, i.e. $A(0) = \mu_{A(D)}(Y)$, and the initial error term is taken to be zero, i.e. $\epsilon(0) = 0$. This process yields 31 separate series for the duration of the model each with 366 values. These time series are recalculated for each iteration of the simulation.

The second sheet calculates the day curves based on the values of $\delta(P)$ shown in Figure 4-25 to Figure 4-32 of section 4.4.3. The user-defined amplitude values, $\alpha(Q)$, are then used to calculate the final values of $\varphi(P)$ for each period using:

$$\varphi(P) = \alpha(Q)\delta(P) + 1 \quad (4\text{-}29)$$

This process yields 31 separate series for the duration of the model each with 17,568 values. Since these series are adjusted by the half-hourly error values, they are fixed for each iteration of the simulation.

The third sheet simulates the half-hourly error values, $\varepsilon(P)$, using an AR time series as discussed in section 4.4.4. This series uses a mean value $\mu_{\varepsilon(P)}(Y)$ and volatility $\sigma_{\varepsilon(P)}$ for each year, taken from the user-defined front sheet parameters and the resulting interpolations. The

autoregressive coefficient $a_{\varepsilon(P)}$ and the initial error term $\epsilon_{\varepsilon(P)}(0)$ remain fixed for each year of the model.

$$\varepsilon(P) = \mu_{\varepsilon(P)}(Y) + a_{\varepsilon(P)}\big(\epsilon(P-1) - \mu_{\varepsilon(P)}(Y)\big) + \epsilon(P) \qquad (4\text{-}30)$$

where $\epsilon(D)$ is an error term calculated with standard deviation defined by $\sigma_{A(D)}$ and a random number $N(D)$ from a normal distribution with mean 0 and standard deviation 1:

$$\epsilon(D) = \sigma_{\varepsilon(P)} N(D) \qquad (4\text{-}31)$$

This process yields 31 separate series for the duration of the model each with 17,568 values. These time series are recalculated for each iteration of the simulation.

The fourth sheet calculates the system sell price $S(P)$ for each period, based on the values in the other three sheets, according to:

$$S(P) = [\varepsilon(P) + \varphi(P)] \times A(D) \qquad (4\text{-}32)$$

This sheet provides the final absolute values of electricity price, already adjusted for CPI, that are then used to populate the yearly calculation sheets described in section 4.5.3.

4.5.2. Annual accounts sheet

This sheet represents the annual balance sheets for the plant. Each column represents one year. A single column contains one row for each of the variables shown in Table 4-7.

Annual accounts sheet variables	
Symbol	**Description**
$S_{\mathrm{CfD}}(Y)$	Strike price for a given year
$i_{\mathrm{CPI}}(Y)$	CPI rate for a given year
$C_{\mathrm{CONST}}(Y)$	Construction costs for a given year
$C_{\mathrm{O\&M,NPP}}(Y)$	NPP O&M costs for a given year
$C_{\mathrm{O\&M,LAES}}(Y)$	LAES O&M costs for a given year
$C_{\mathrm{REFUEL}}(Y)$	Refuelling costs for a given year
$C_{\mathrm{TOTAL}}(Y)$	Total costs for a given year
$R_{\mathrm{SALES}}(Y)$	Sales revenue for a given year
$P_{\mathrm{GROSS}}(Y)$	Gross profit for a given year
$T_{\mathrm{CORP}}(Y)$	Corporation tax for a given year
$P_{\mathrm{NET}}(Y)$	Net profit for a given year
$NPV(Y)$	NPV to date for a given year

Table 4-7: Annual accounts sheet variables

The first year of plant operation is denoted $Y = 1$. Construction years are filled backwards from this column, with the final year of construction being year $Y = 0$. NPP mobilisation

construction costs, $C_{\mathrm{NPP,MOB}}(I)$, are divided evenly between the years $Y = 0 - \left[t_{\mathrm{CRIT,NPP}}(I) + t_{\mathrm{MOB,NPP}}(I)\right]$ and $Y = 0 - \left[t_{\mathrm{CRIT,NPP}}(I) + 1\right]$. The critical path construction costs, $C_{\mathrm{NPP,CRIT}}(I)$ and assigned entirely to year $Y = 0 - t_{\mathrm{CRIT,NPP}}(I)$. LAES construction costs are similarly assigned to the relevant years.

All user-defined cost parameters are defined in 2020 prices, with this being the first year of construction in the model, i.e. year $Y = 0 - \left[t_{\mathrm{CRIT,NPP}}(I) + t_{\mathrm{MOB,NPP}}(I)\right]$. The year $Y = 1$ values for $S_{\mathrm{CfD}}(Y)$, $C_{\mathrm{CONST}}(Y)$, $C_{\mathrm{O\&M,NPP}}(Y)$, $C_{\mathrm{O\&M,LAES}}(Y)$ and $C_{\mathrm{REFUEL}}(Y)$ are all adjusted according to $i_{\mathrm{CPI}}(Y)$ for the intervening years in exactly the same fashion as the values of $\mu_{A(D)}(Y)$ in equation (4-26) and populated into the column for year $Y = 1$. The same method is used to populate their values for the remaining 29 years of the model. Values of $C_{\mathrm{REFUEL}}(Y)$ are set to zero unless the given year's calculation sheet shows that refuelling has taken place that year. Total costs, $C_{\mathrm{TOTAL}}(Y)$, are then calculated from the sum of all cost variables.

Values of $R_{\mathrm{SALES}}(Y)$ from each year are taken from the values of R_{TOTAL} from the given year's calculation sheet as discussed in section 4.5.3. Gross profit is the calculated using:

$$P_{\mathrm{GROSS}}(Y) = R_{\mathrm{SALES}}(Y) - C_{\mathrm{TOTAL}}(Y) \qquad (4\text{-}33)$$

Corporation tax is calculated based on gross profit (or taken to be zero where $P_{\mathrm{GROSS}}(Y)$ is negative), and the value of $P_{\mathrm{NET}}(Y)$ is thus calculated:

$$P_{\mathrm{NET}}(Y) = P_{\mathrm{GROSS}}(Y) \times [1 - T_{\mathrm{CORP}}] \qquad (4\text{-}34)$$

The NPV to date for the given year is calculated using:

$$NPV(Y) = \sum_{Y=0-\left[t_{\mathrm{CRIT,NPP}}(I)+t_{\mathrm{MOB,NPP}}(I)\right]}^{Y} \frac{R(Y)}{(1+i_{DISC})^{Y}} \qquad (4\text{-}35)$$

This calculation is important because it allows the discounted payback period to be calculated by counting the total number of years for which $NPV(Y) < 0$. Finally, the overall project NPV over the 30-year lifespan of the plant, plus its construction years, $NPV(I)$, for the given iteration, is calculated as:

$$NPV = \sum_{Y=0-[t_{\mathrm{CRIT,NPP}}(I)+t_{\mathrm{MOB,NPP}}(I)]}^{30} \frac{R(Y)}{(1+i_{DISC})^{Y}} \qquad (4\text{-}36)$$

The discounted payback period and the overall project NPV are taken as model iteration outputs and are recorded and collated for each iteration of the simulation by @RISK

4.5.3. Yearly calculation sheets

The 30 yearly calculation sheets are the workhorse of the financial model. These are arranged with each row representing a half-hour period of the model. Each column calculates a different variable or defines the operating state of the plant. The plant has five operating conditions:

- **Baseload**: the plant is operating as a baseload NPP.
- **Charge**: the plant is charging the LAES system.
- **Discharge**: the plant is discharging the LAES system.
- **Offline**: the plant is refuelling; neither the NPP nor the LAES system are operating.
- **Restart**: the plant is refuelled and ready to restart.

System variables	
Symbol	**Description**
$S_{\mathrm{CfD}}(Y)$	Strike price for a given year
$t(P)$	Time of day for a given period
$S(P)$	Spot market price for a given period
$\dot{W}_{\mathrm{FIX}}(P)$	Fixed power output for a given half-hour period
$\dot{W}_{\mathrm{VAR}}(P)$	Variable power output for a given half-hour period
$R_{\mathrm{TOTAL}}(P)$	Total revenue for a given half-hour period
$R_{\mathrm{NPP}}(P)$	NPP revenue for a given half-hour period
$R_{\mathrm{LAES}}(P)$	LAES revenue for a given half-hour period
$t_{\mathrm{UP}}(P)$	Length of time the plant has been up for during a given period
$t_{\mathrm{DOWN}}(P)$	Length of time the plant has been down for during a given period
$M_{\mathrm{TANK}}(P)$	Mass currently stored in the tank
ΔM_{TANK}	Change in mass in the tank
$\mu(P)$	Mean average cost to charge

Table 4-8: Yearly calculation sheet variables

The calculations used in each column will now be described in this section. The first column defines the current time of day, $t(P)$ for the given period. This simply cycles through 24 hours for every 48 rows of the spreadsheet.

The second set of columns define the plant's output power for the period in question. The first column calculated the plant's fixed power output for the period, $\dot{W}_{\mathrm{FIX}}(P)$. For any time the plant is online, this is simply taken from the parameter sheet value for $\dot{W}_{\mathrm{NPP}}$. When the period's

operating decision is '**Offline**', this is taken to be zero. The second column calculates the variable power output of the plant, $\dot{W}_{\mathrm{VAR}}(P)$. When the periods operating decision is 'charge', this is taken to be equal to $-\dot{W}_{\mathrm{CHG}}$ and when the period's operating decision is 'discharge', this is taken to be equal to $\dot{W}_{\mathrm{DIS}}$. At all other times, this is taken to be zero.

The next set of columns define the plant's stored air capacity, M_{TANK}. The second of these, the stored air change, ΔM_{TANK}, takes a value of $\dot{M}_{\mathrm{CHG}}$ when the period's operating decision is '**Charge**' and a value of $-\dot{M}_{\mathrm{DIS}}$ when the period's operating decision is '**Discharge**'. The first column calculates the current period's value of M_{TANK} as the sum of the previous period's value of M_{TANK} and the previous period's value of ΔM_{TANK}.

The next set of columns define the period's spot market electricity price and the resulting revenue from the plant. The first takes the value of $S(P)$ for the relevant period, as defined in section 4.4.3. The second column calculates the NPP revenue for the period, $R_{\mathrm{NPP}}(P)$, as the product of $\dot{W}_{\mathrm{FIX}}(P)$ and the strike price for the given year, $S_{\mathrm{CfD}}(Y)$. The third column calculates the LAES revenue for the period, $R_{\mathrm{LAES}}(P)$, as the product of $\dot{W}_{\mathrm{VAR}}(P)$ and $S(P)$. The fourth column calculates the total revenue for the period, $R_{\mathrm{TOTAL}}(P)$, as the sum of the previous two columns.

The next two columns keep a running tally of the length of time the plate has been running and the plant has been down for refuelling. The first, $t_{\mathrm{UP}}(P)$, is the running total of days the plant has been running. If the previous period's operating decision is '**Restart**', this is reset to zero, otherwise, $^{1}/_{48}$ is simply added to the previous period's value. The second column, $t_{\mathrm{DOWN}}(P)$, is the running total of days the plant has been refuelling. If the previous period's operating decision is '**Offline**', then $^{1}/_{48}$ is added to the previous period's value, otherwise this is reset to zero.

The penultimate column keeps a rolling average of the cost to charge the system, $\mu(P)$. Whenever the operating decision is '**Charge**', this takes the value of the current period's spot market price, $S(P)$. If the current operating decision is '**Baseload**' and the previous periods was '**Charge**', $\mu(P)$ takes the mean average of all of the non-zero values in this column in the previous 12 hours. If the current operating decision is '**Baseload**', this takes the value of the same variable in the previous period. Finally if the previous period's decision is '**Discharge**', this is reset to zero.

The final column defines the operating decision for each period of the model. This is done using IF formulae in accordance to the flowchart presented in Figure 4-50. The first two steps of the decision making determine whether the NPP requires refuelling or whether it is ready to restart. If the plant downtime, $t_{\mathrm{DOWN}}(P)$, is equal to the required time to refuel the NPP, t_{REFUEL}, the decision is set to '**Restart**'. If the plant's uptime, $t_{\mathrm{UP}}(P)$, is equal to the lifetime of the fuel load, t_{FUEL}, the decision is set to '**Offline**'.

The next steps determine whether the plant should charge or discharge. If the air storage tank is empty and the current time of day is within the charge window set by $t_{\mathrm{START,CHG}}$ and $t_{\mathrm{END,CHG}}$, the operating decision is set to '**Charge**'. If the tank is neither empty nor full, that decision is similarly set to '**Charge**'. Then, if the plant was discharging the previous period and the tank in not yet empty, the operating decision is set to '**Discharge**'. If the storage tank is full and the current spot market price, $S(P)$, is greater than the rolling average charge price, $\mu(P)$, the decision is similarly set to '**Discharge**'. If none of these criteria apply, the decision is set to '**Baseload**'.

Total values of R_{TOTAL} are calculated at the bottom of each yearly calculation sheet.

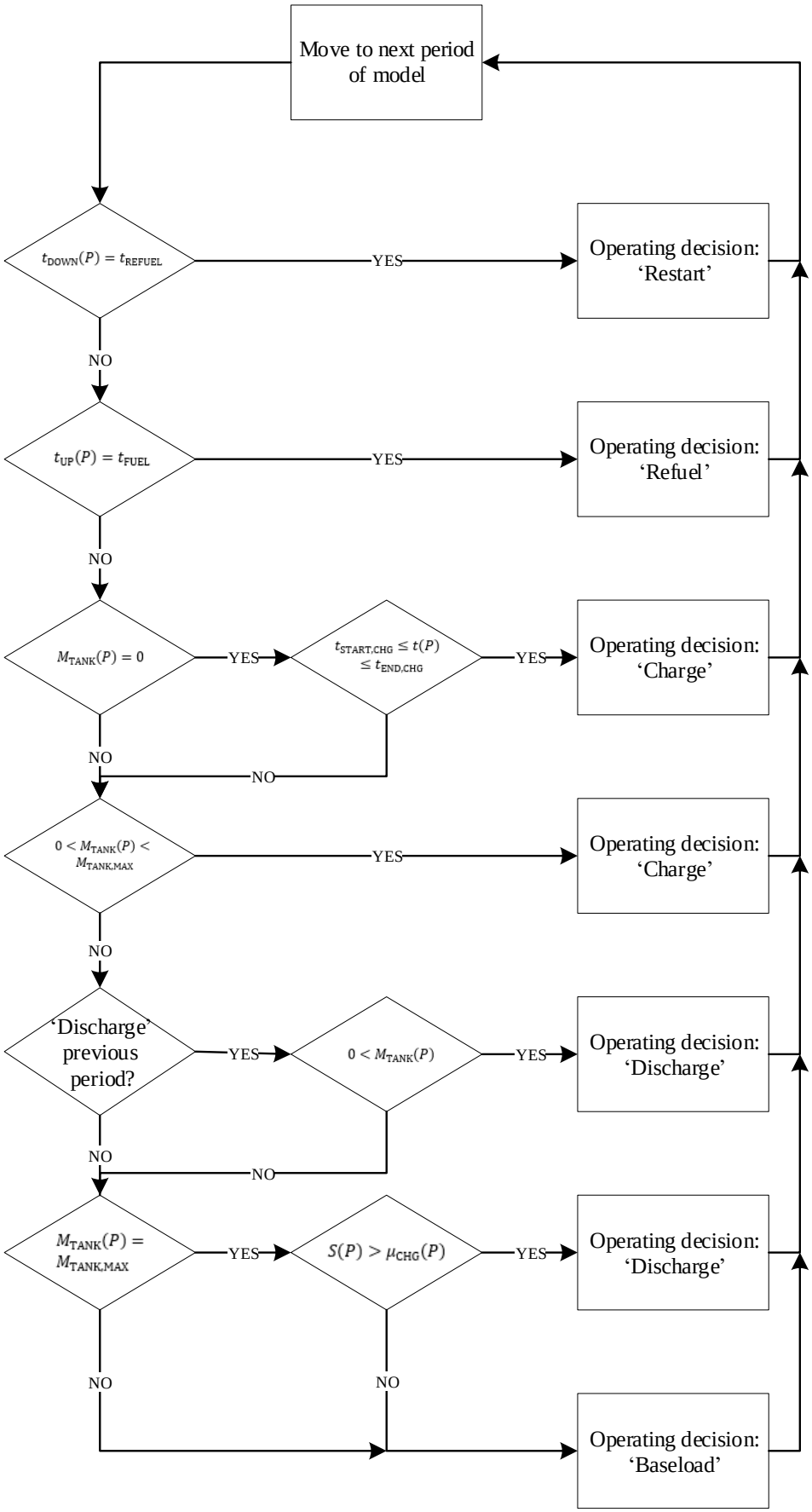

Figure 4-50: Plant operating decision

Chapter 5 - Configurational modelling

5.1. Introduction

There are multiple process configurations possible for the steam, air liquefier and air power cycles of the LAES plant. Sections 2.7 details how costs of key pieces of equipment are to be calculated and section 4.3 details how these drive the overall cost of the LAES plant. The differences in potential configurations are significant in terms of not only the size, but also the numbers of heat exchangers and power train components; components that make up the lion's share of the LAES system capital investment.

This thesis is less concerned with optimisation from a thermodynamic perspective than from a economic perspective. Ultimately, as this chapter and Chapter 6 will show, thermodynamic efficiency improvements come at a real financial cost. The initial investigative modelling in these chapters aims to answer the question of whether the additional revenue resulting from these improvements are worth their cost. It will compare system configurations and assess their relative NPVs to allow an optimal system configuration to be defined.

5.2. Initial engineering modelling

Following basic model testing and component model validation, engineering modelling was begun. The initial engineering model was built up from a basic system with a small number of isolated components eventually to a full system with all components. One of the advantages of the modular construction of the engineering model is the ability to test components or cycles in isolation. This reduces computing load and allows parameter sweeps to be performed much more quickly. It also facilitated diagnosing issues with the model as it was developed. The LAES system being explored has two cycles; the liquefier cycle and the power cycle. As a starting point, a symmetrical system was designed with a discharge mass flow rate of 100 kg/s, and a charge mass flow rate of 101 kg/s. This additional 1% is charge mass flow rate is to account for boil-off losses from the stored air tank since this is not explicitly considered by the model.

As a starting point, the availability of heat from the secondary loop of the NPP was determined using an isolated model of the steam cycle, as discussed in section 5.2.1. The LAES system was then studied. Starting in section 5.2.2, the cold store was investigated to determine the effect of charging and discharging on the temperatures and heat storage of the system. Following this, in section 5.2.3, the discharge system was studied to determine the effect of applying NPP heat to the LAES system. Then, in section 5.2.4 the power consumed by the charge cycle was studied.

Finally, in section 5.2.6, the different plant configurations were modelled. At this point, the cold store and other components were sized for the different system configurations.

5.2.1. Supply of nuclear steam

The starting point of engineering modelling was to determine how much heat could be made available from the NPP for supply to the air power cycle during discharge. Steam turbines are expanded to a vacuum and this provides the best possible efficiency for the steam cycle, as it allows a much larger amount of heat to be extracted from the steam than expanding to atmospheric pressure. This is because decreasing the turbine outlet pressure lowers the saturation temperature of water, allowing more energy to be extracted from the water before it condenses. Since steam turbines can tolerate a steam quality of no less than around 85%, this results in a lower outlet temperature and a greater energy yield from the turbine. It has a disadvantage when coupling to a LAES plant in that the lower saturation temperature of water reduces the peak temperature of the air in the discharge cycle as highlighted in section 2.6 in the context of (Li et al., 2014) and demonstrated via modelling in section 5.2.1. For brevity, the different configurational options in this section have been denoted S-*y* where *y* is the number designation of that configuration.

Several steam cycles were studied. The first two assumed providing heat to the discharge cycle air using only the condenser coolant from the NPP. In the first (configuration S1), steam was expanded to a vacuum and in the second (configuration S2, steam was expanded to atmospheric pressure. These have the advantage of ensuring that the NPP's power output does not change between times when the discharge cycle is running and times when the NPP is simply running in baseload. In the latter, however, this would increase condenser coolant temperature but reduce plant output power by 25%. Considering this is a design choice and that this would affect the NPP's power output even during baseload operation, this is a significant cost to power output to benefit a system that will only operate for a part of the day. Ultimately, the low-grade heat provided by both cycles, at less than 373 K, meant that the discharge cycle performed very

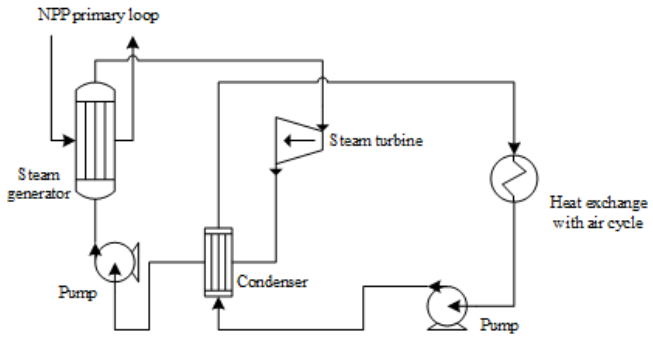

Figure 5-1: Steam cycle configuration S1/S2

poorly, limiting the round-trip efficiency of the LAES plant to less than 25%. With only marginal savings in equipment cost, these options were quickly discarded, however the steam cycle results remain recorded here for posterity.

Configurations S1 and S2 are shown in Figure 5-1. It is important to note at this stage that this is a simplified schematic. The NPP considered herein is the NuScale iSMR. A 300 MWe plant would consist of a total of 6 nuclear reactors each with its own secondary loop consisting of steam generator, turbine, condenser and pump.

The third steam cycle explored (configuration S3) considered diverting a portion of the secondary loop steam away from the steam turbines and directly to the air power cycle. This has some potential disadvantages in that running turbines at a flow rate lower than that of their design lowers their efficiency. This configuration is shown in Figure 5-2. As before, this diagram and the model have been simplified to treat the system of multiple SMR steam generators and multiple turbines as a single cycle. Table 5-1 shows the parameters used in the S3 model, but an additional parameter has been introduced to define the quantity of steam diverted away from the secondary loop.

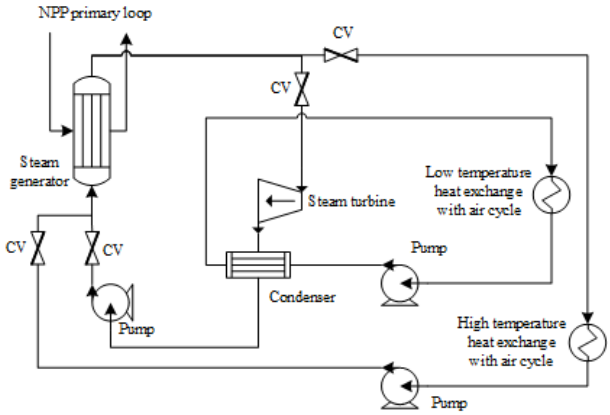

Figure 5-2: Steam cycle configuration S3

In light of the discussions in section 2.3, it is important to note that the secondary loop should not be shut down completely. In this study it is assumed that the steam turbines operate between 50 and 100% of their rated power. It is furthermore important to consider that running the turbines at anything other than their design flow rate results in a loss of efficiency. As discussed in section 3.2.7, the model defines this using a matrix parameter $\eta[x, 2]$ that defines x values of $\dot{M}_{\text{factor}}$ (the ratio of the actual mass flow rate to the design mass flow rate) against their resulting isentropic efficiencies, η. The values for $\eta[x, 2]$ are taken from (Karakurt and Gunes, 2017) and interpolated to provide the continuous relationship shown in Figure 5-3.

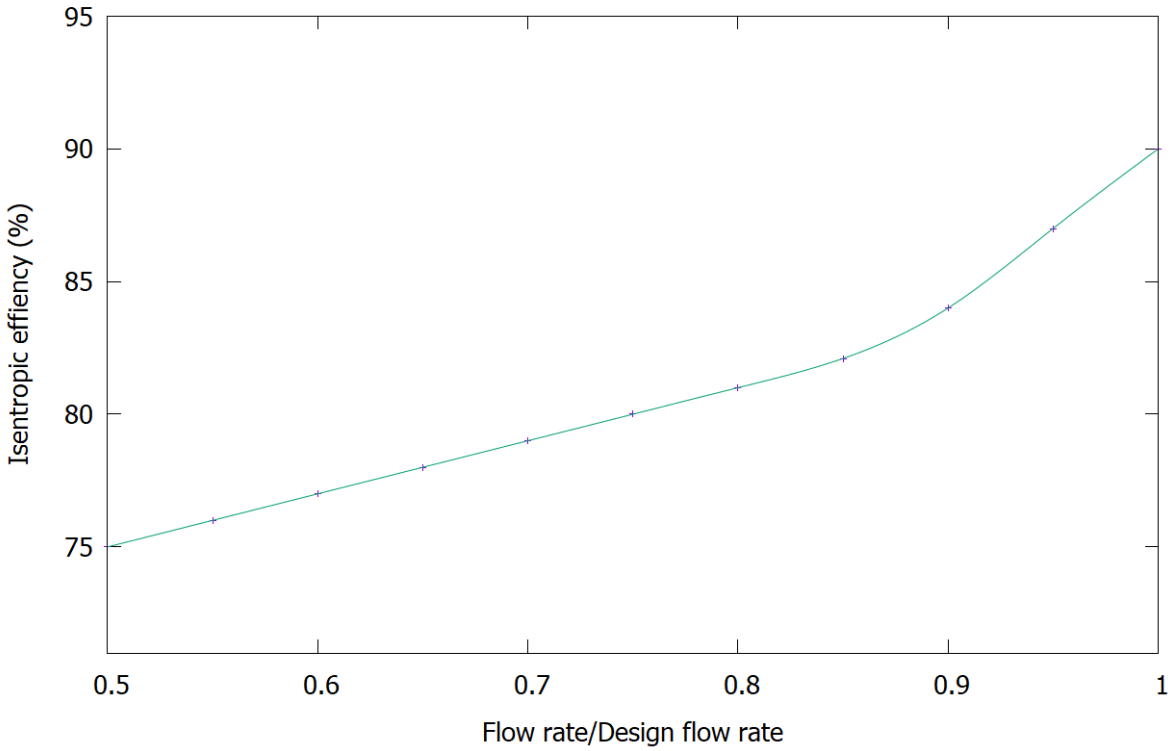

Figure 5-3: Values of steam turbine isentropic efficiency for the parameter $\eta[x, 2]$

All steam cycle configurations are optimised by performing a parameter sweep. The objective is to determine the required mass flow rate for the secondary loop to operate in a steady state. Additional equations are defined at the top level of the steam cycle model to assist with optimisation. The first of these calculates the rate of change of specific enthalpy, $\frac{dh_{\text{pump}}}{dt}$, in the flow stream following the pump. For this optimisation, the size of the condenser is set to very large to prevent it from being a limiting factor in the extraction of heat from the post-turbine water stream. The model is then run repeatedly over a range of mass flow rates. The mass flow rate for which $\frac{dh_{\text{pump}}}{dt} = 0$, is considered sufficient for the system. The size of the condenser is then reduced as much as possible without reducing the heat transfer rate.

The modelling parameters are shown in Table 5-1.

Parameter	**Value**	**Units**
Primary loop thermal power	960	MWth
Steam generator heat exchange surface area	1666	m^2
Steam generator heat transfer coefficient	875	$W/m^2 K$
Secondary loop peak temperature	580.0	K
Secondary loop minimum temperature	314.8	K
Secondary loop peak pressure	3,450	kPa
Secondary loop expansion pressure, configuration S1/S3	21.5	kPa
Secondary loop expansion pressure, configuration S2	101.3	kPa
Secondary loop mass flow rate	402	kg/s

Water pressure drops	0.01	
Tertiary coolant supply temperature	298.15	K
Tertiary coolant peak temperature	310	K
Tertiary coolant supply pressure	102.5	kPa
Condenser heat transfer surface area	Optimisation parameter	
Condenser heat transfer coefficient	1610	$W/m^2 K$
Steam turbine peak efficiency	90	%
Steam turbine off-design efficiency	Figure 5-3	
Pump efficiency	80	%

Table 5-1: Key parameters for steam cycle models – all configurations

The results for configuration S1 are shown in Figure 5-4. As might be expected, increasing the condenser outlet temperature reduces the required mass flow rate but increases the required exchanger surface area. The NPP power output is the design 300 MWe.

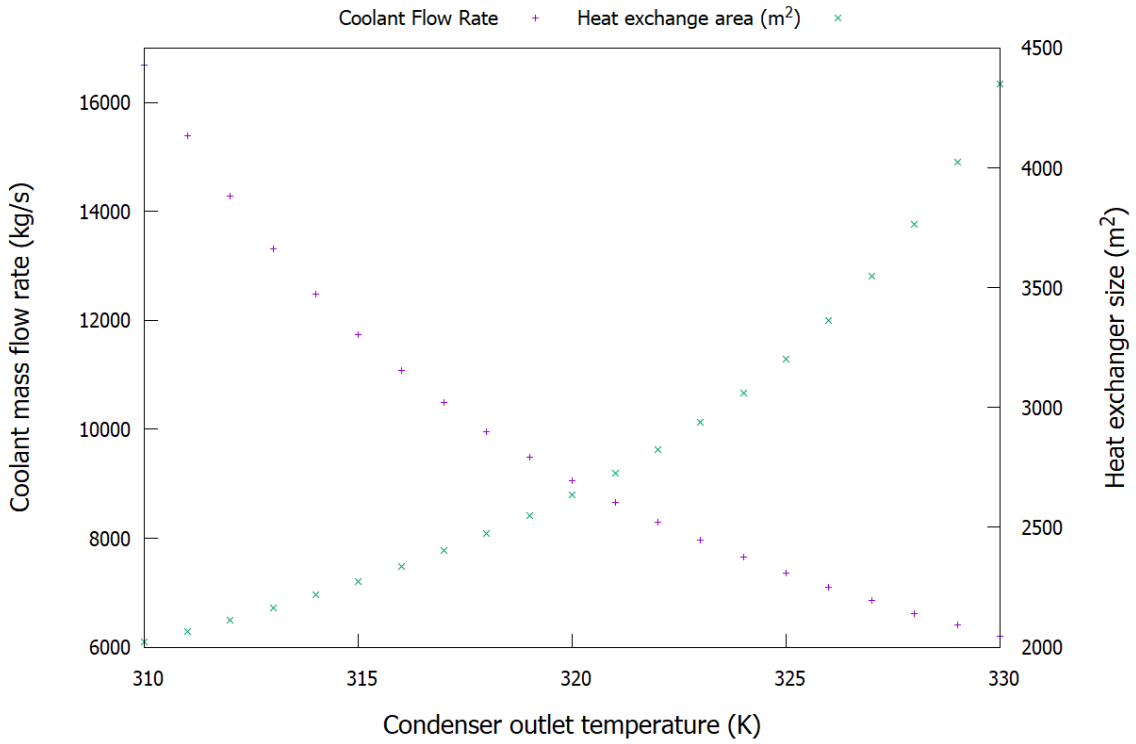

Figure 5-4: Configuration S1 results

The results for configuration S2 are shown in Figure 5-5. As before, these are much as expected. In this mode of operation, NPP power output is significantly reduced to 227 MWe. This is a significant power reduction and also requires significant design changes be made to the NPP. The operating pressure of a condenser is a design decision and cannot be changed during plant operation. As a result of this, the plant would have to run at this reduced power throughout its life, not just during the discharge cycle of the LAES plant. The loss of 25% of the NPP power was deemed too large to justify any potential benefits from increased LAES temperatures and hence this configuration was dismissed as a viable design.

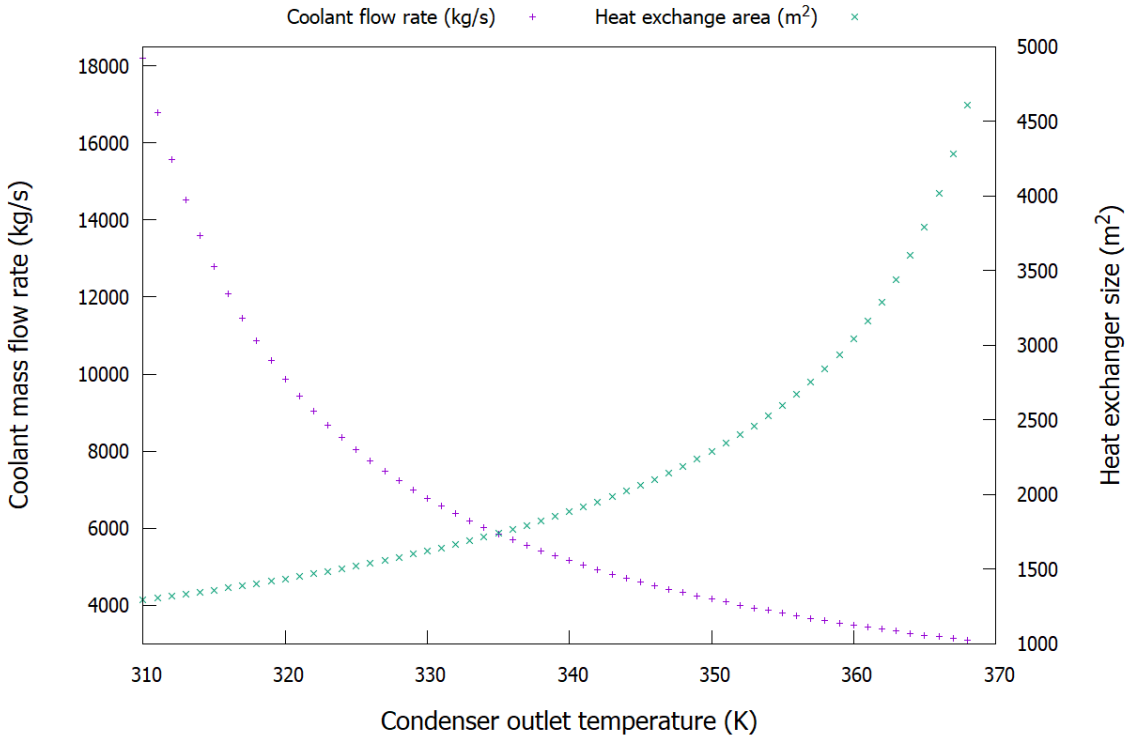

Figure 5-5: Configuration S2 results

Finally, the results for configuration S3 are shown in Figure 5-6 to Figure 5-8. Note that the x-axis now shows the ratio of secondary loop flow sent to the air power cycle.

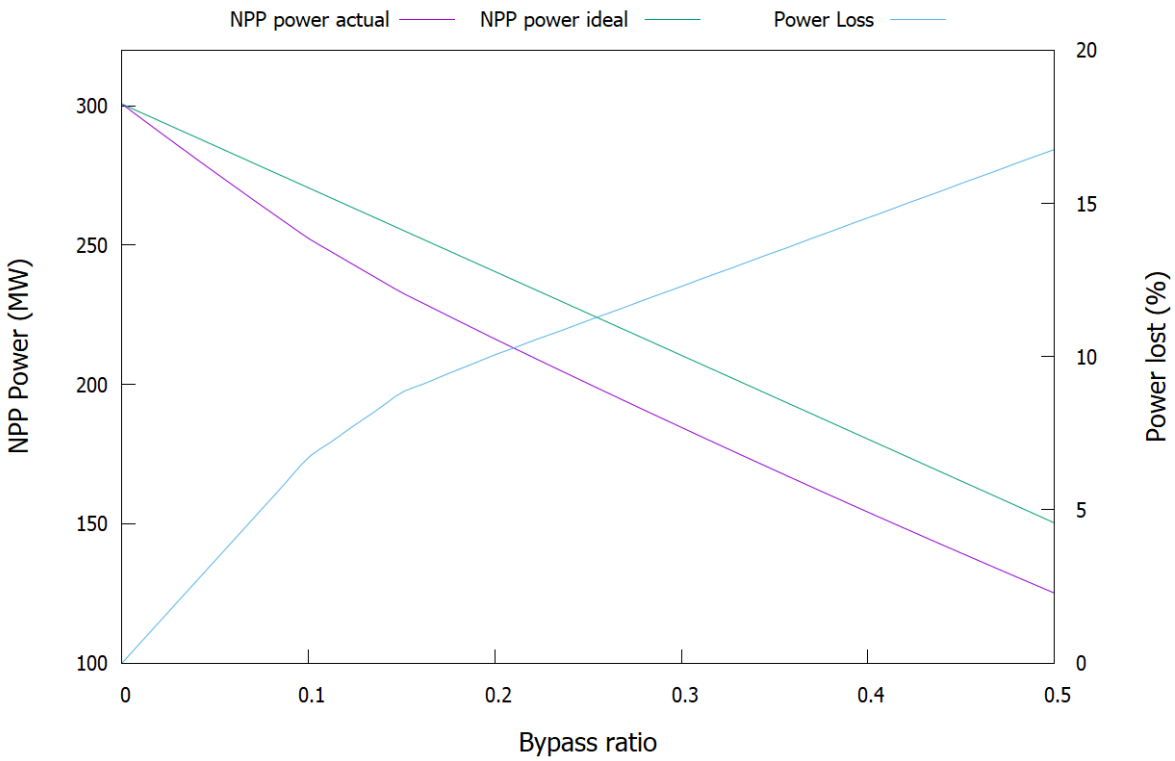

Figure 5-6: Configuration S3 NPP power output results

Figure 5-6 shows the power output of the NPP as a function of the amount of steam that bypasses the secondary loop. Whilst this figure only shows the power outputs for 310 K condenser outlet temperature, increasing the coolant-side condenser outlet temperature provides only small power improvements in the range of tens of kilowatts. These improvements are related to the savings in pumping power due to the reduced coolant flow rates. The 'ideal' line shows the power output that the plant would yield if the steam turbine's isentropic efficiency were continuous throughout the operating mass flow rate range. The 'actual' line shows the power output given the flow rate dependency of isentropic efficiency shown in Figure 5-3. The power lost line shows the percentage difference between the ideal and actual lines.

As might be expected, the most power is lost at the highest bypass ratios where the isentropic efficiency of the turbine is at its lowest. The percentage of power lost increases most steeply at low bypass ratios and almost linearly at higher bypass ratios. Figure 5-6 has important implications for the use of nuclear steam during discharge of the LAES plant. Using the higher-grade heat from the NPP comes at a significant power cost and could potentially outweigh the gains from improvement in LAES power output. The implications are discussed in more detail in section 5.2.3.

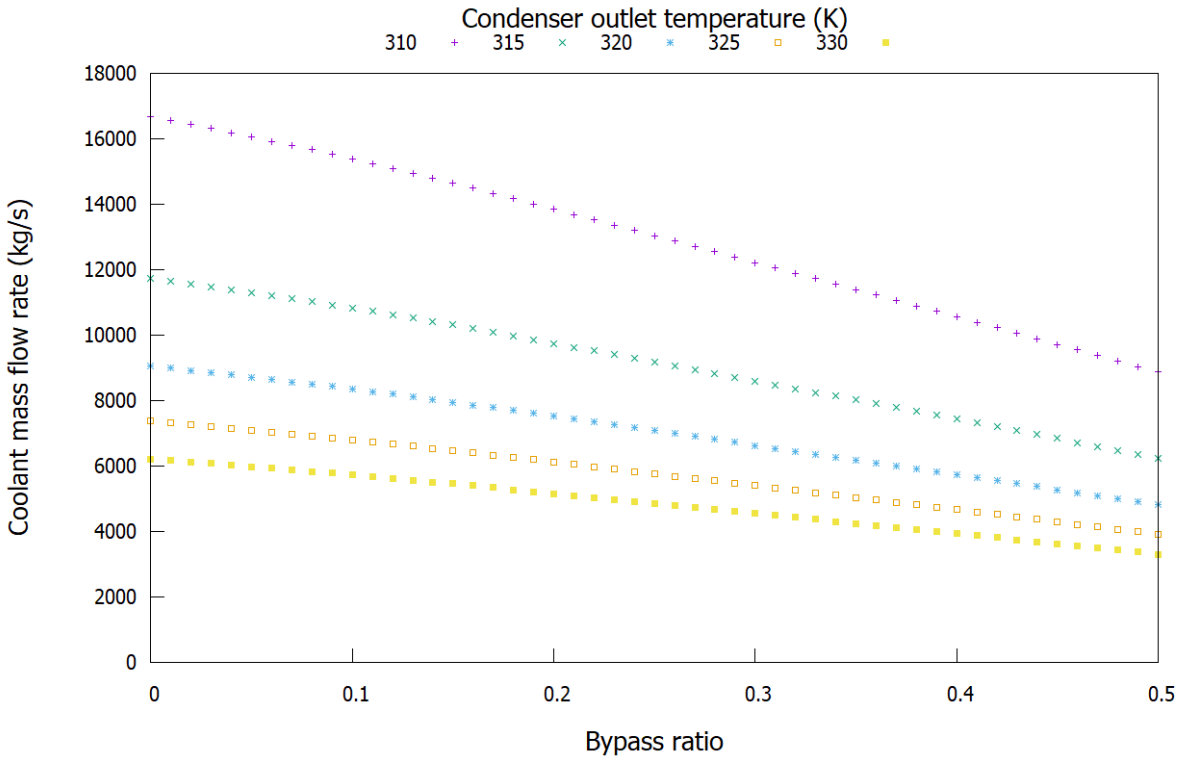

Figure 5-7: Configuration S3 coolant mass flow rate results

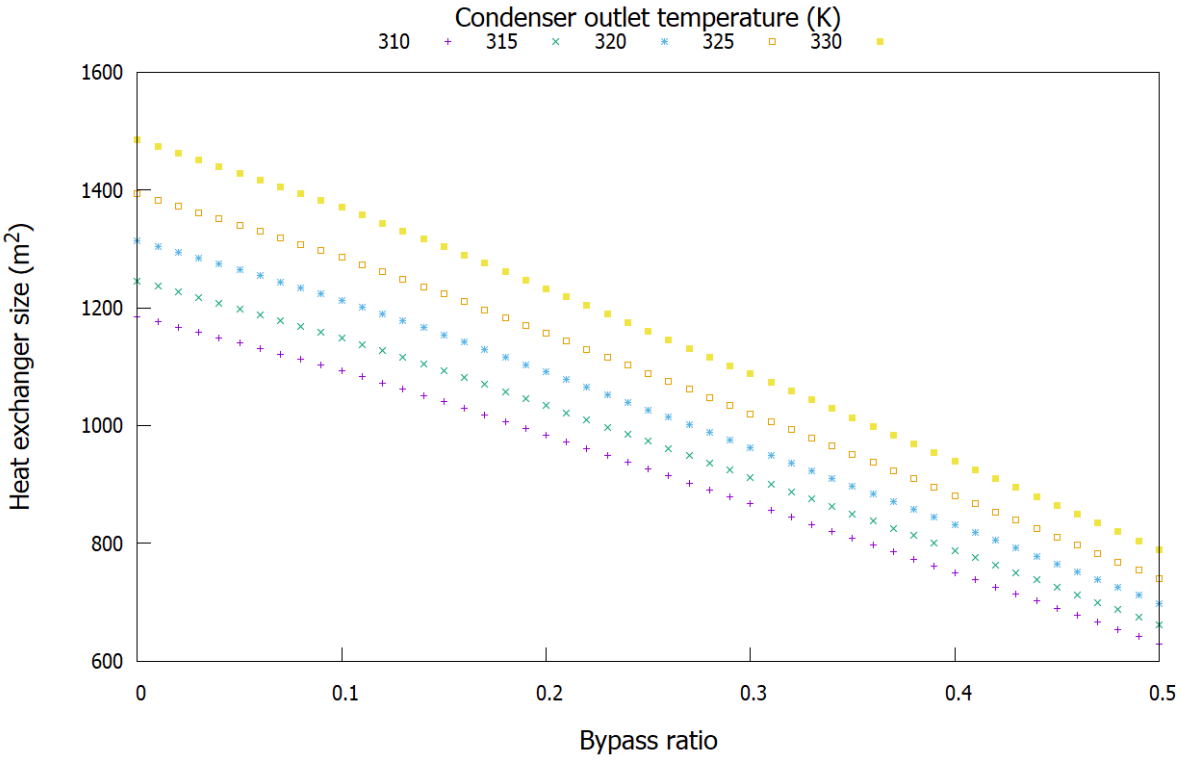

Figure 5-8: Configuration S3 condenser surface area results

Figure 5-7 shows the condenser coolant mass flow rate results, whilst Figure 5-8 shows the resulting required condenser sizes for configuration S3. The flow rate results are much as expected. Increasing the bypass ratio and thus decreasing the NPP secondary loop mass flow rate reduces the required coolant flow rate and the resulting heat exchanger size. Increasing the condenser coolant-side outlet temperature results in a reduced coolant flow rate but increases the condenser size requirement due to the smaller temperature difference between the secondary loop and coolant flows at the hot end of the condenser.

5.2.2. Cold store modelling

As discussed above, the charge and discharge thermodynamic cycles are almost entirely independent with the exception of one key component; the cold store.
The sizing of this component is of critical importance; the cold store will be heated by the incoming air during each charging phase and cooled by the liquefied air during each discharge phase. During charging, only the liquefied fraction is sent to the storage tank, and thus only this fraction is available to cool the bed again during discharge.

Testing was performed on isolated models to determine the effect of key model parameters and duty cycling on the performance of the cold store. In order to do this, the cold recycle system components were modelled in isolation using mass flow sources and sinks. Simulations were run for 1800 s to the evolution of temperatures in the gravel bed and in the air at the outlet of the cold store. Testing was first performed to understand the effect of cold store heating during a hypothetical charge cycle on the heat extraction rate, average bed temperatures and outlet temperatures using a range of supply pressures using the parameters in Table 5-2.

Parameter	Value
Inlet air temperature	298.15 K
Inlet air mass flow rate	150 kg/s
Inlet air pressure	101.325 kPa
Bed particle diameter	0.02 m
Bed particle density	2320 kg/m^3
Bed particle specific heat capacity	810 J/kg K
Initial bed temperature	88 K
Bed pressure drop	0.05
Bed diameter	3 m
Bed length	15.5 m

Table 5-2: Parameters used for testing the effect of charging on cold store temperatures

The implications of the importance of gravel bed size are most apparent when referring to Figure 5-9. The outlet air temperature begins to rise at a time of 500 s, shown by the vertical red line. At the same time, the bed heating rate begins to fall. This is an important point; once the outlet temperature begins to rise, less heat will be extracted from the charge air stream and the resulting mixture will have a lower liquid fraction once it has been expanded. Since the power consumption of the compression cycle will not change for a given configuration at a set flow rate and peak pressure, the energy input per unit mass of liquid air produced (i.e. the specific energy of liquefaction) will increase and the overall efficiency of the system will fall.

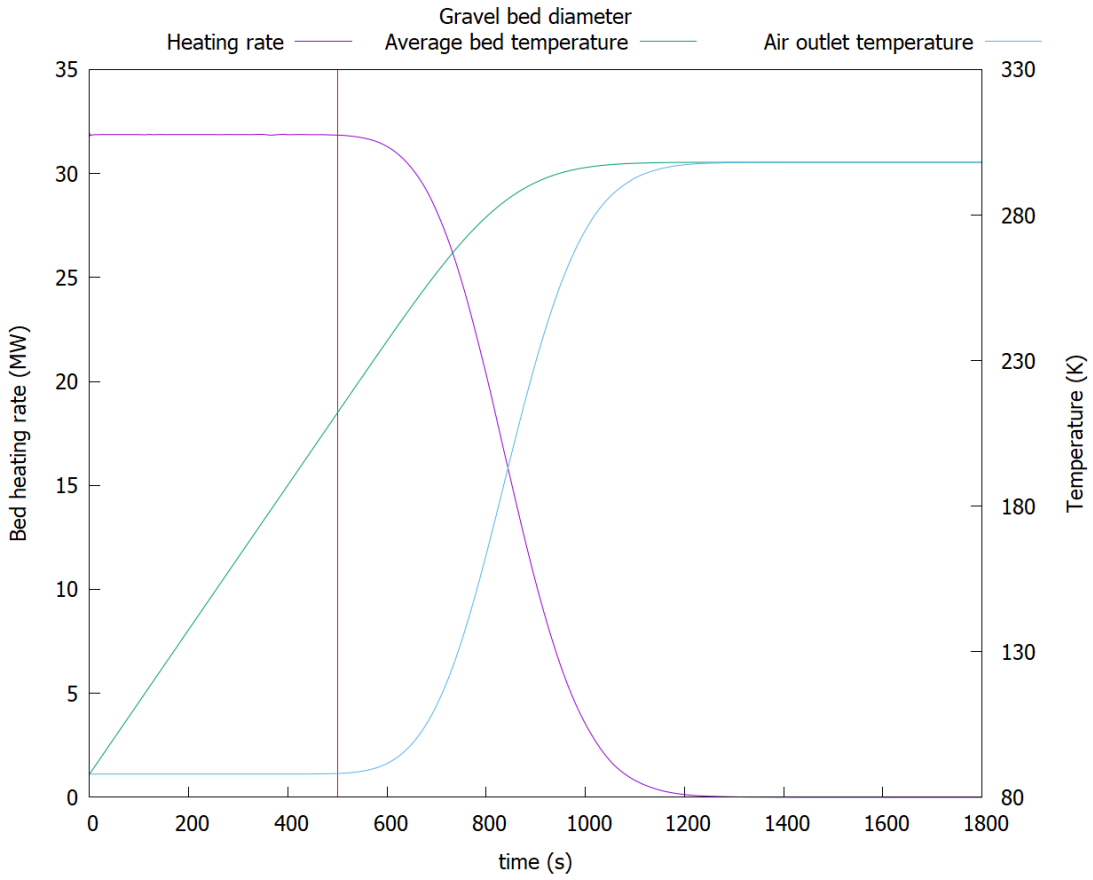

Figure 5-9: Heating rate, average bed temperature and air outlet temperature during a single charge cycle

The same model was run for a cold store during a hypothetical discharge cycle to understand the effect of cold store cooling. The parameters used for the model are shown in Table 5-3.

Parameter	Value
Inlet air temperature	88 K
Inlet air mass flow rate	150 kg/s
Inlet air pressure	101.325 kPa
Bed particle diameter	0.02 m
Bed particle density	2320 kg/m^3
Bed particle specific heat capacity	810 J/kg K
Initial bed temperature	298.15 K
Bed pressure drop	0.05
Bed diameter	3 m
Bed length	15.5 m

Table 5-3: Parameters used for testing the effect of discharging on cold store temperatures

The results for discharging are shown in Figure 5-10. These mirror those for charging. Note that here, the heating rate is still shown. That is, the rate of heat transfer into the gravel bed.

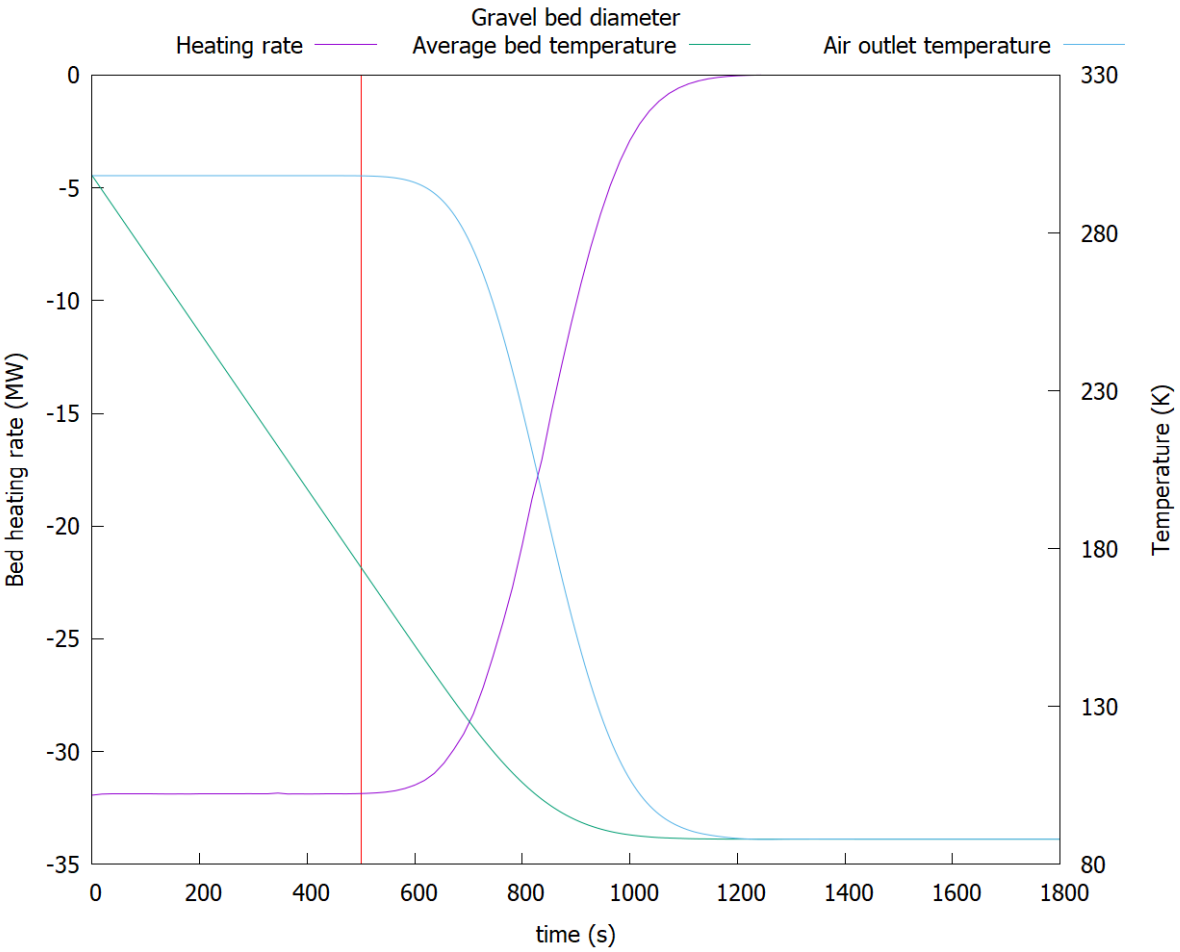

Figure 5-10: Cooling rate, average bed temperature and air outlet temperature during a single discharge cycle

Because the bed is being cooled during discharge, this is negative. In a corollary of what occurs during system charging, the outlet temperature of the bed begins to fall at around 500 s and the rate of heat extraction from the bed begins to fall. This implies equally important considerations for the cold store during system discharge. The cold store air stream exchanges heat with the discharge air via a heat exchanger. As the cold store temperature, and hence the air temperature

at the outlet, falls, the temperature difference across this heat exchanger will also fall. This reduces the amount of heat that can be imparted to the discharge air stream during discharge which in turn reduces the quantity of specific cold recycle that can be achieved. As noted in section 2.5.2, maximising cold recycle is paramount to achieving optimal liquefaction efficiency when charging the system.

5.2.3. Discharge cycle modelling

The third step in exploratory engineering modelling was demonstration of the air power cycle. This system is far simpler system to model than the air liquefier cycle and, as such, was modelled in its entirety for all configurations considered. For brevity, cycles considered in this section are denoted D-*y* where *y* is the number of turbine stages used.

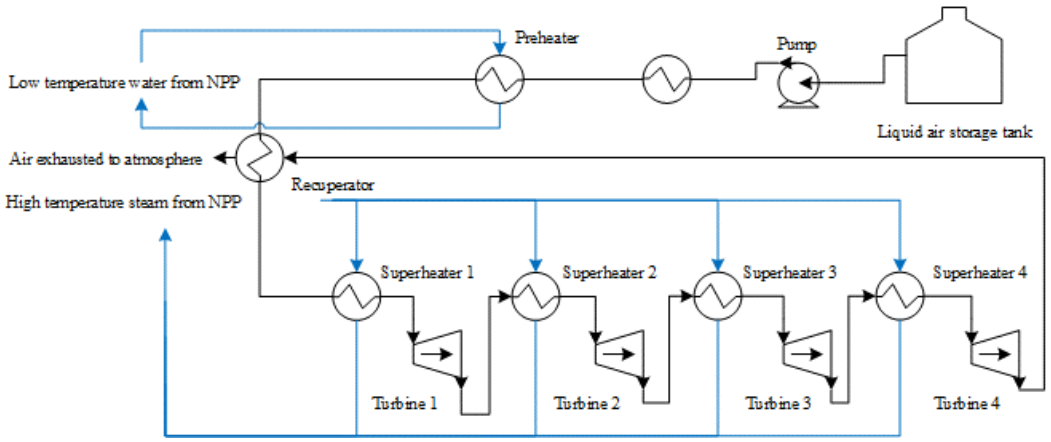

Figure 5-11: Air power cycle configuration D-4

The air power cycle first pumps the liquid air from the tank to the peak discharge temperature. The pressurised but still liquid air is then vaporised in a heat exchanger where it cools the air used in the cold recycle loop. It then travels through additional heat exchangers; the first a preheater which uses the condenser water from the NPP's tertiary loop to further heat the air stream and the second a recuperator used to recover residual heat from the exhaust air. The air then passes through the expansion sequence, each stage of which involves superheating the air using NPP secondary loop steam before expanding it in a turbine.

It was expected that the power train efficiency would improve with staged expansion. In the air power cycle, air is heated by steam or water from the NPP in the quantities and at the temperatures shown in section 5.2.1. Ultimately, the inlet temperature from a single turbine is limited by the saturation temperature of the NPP secondary loop, as this represents the pinch point in the air superheaters. As the temperature through the turbine falls, so too does the power it produces. By adding multiple turbine stages and reheating the air following each turbine stage, the power output can be increased. There are, of course, capital cost implications

associated with the additional turbines and heat exchangers required to achieve these improvements, as is discussed in Chapter 6.

One discharge configuration was considered; only the number of expansion stages was varied. Figure 5-11 shows the discharge configuration with 4 turbine stages. Initial modelling showed that the key parameter for system optimisation is the peak discharge pressure. The water stream flow rates were varied according to the results of section 5.2.1. Because all design options utilise multiple turbines, the proportion of the stream diverted to each turbine is also an important optimisation parameter. Optimising these parameters ensure that each expansion stage has the highest possible turbine inlet temperature whilst also ensuring that the quantity of steam diverted from the NPP secondary loop was kept to a minimum.

Parameter	**Value**	**Units**
Secondary loop peak temperature	580.0	K
Secondary loop minimum temperature	314.8	K
Secondary loop peak pressure	3,450	kPa
Secondary loop mass flow rate	402	kg/s
Water pressure drops	0.01	
Tertiary coolant peak temperature	310	K
Tertiary coolant return temperature	298.15	K
Air mass flow rate	Swept parameter	
Condenser heat transfer surface area	Optimisation parameter	
Superheater heat transfer coefficient	300	$W/m^2 K$
Air turbine peak efficiency	85	%
Pump efficiency	80	%

Table 5-4: Key parameters for discharge cycle models – all configurations

Parameter sweeps were performed on the total ratio of NPP steam sent to the discharge cycle, the ratios of steam sent to each turbine, the peak discharge pressure, and the discharge mass flow rate of the cycle. Top level model expressions calculate the specific energy yield:

$$\beta_{\text{discharge}} = \frac{\dot{W}_{\text{discharge}}}{\dot{M}_{\text{discharge}}} \qquad (5\text{-}1)$$

where $\beta_{\text{discharge}}$ is the discharge specific energy, $\dot{W}_{\text{discharge}}$ is the discharge power (net of both the power reduction in the NPP and the power consumed by the pump) and $\dot{M}_{\text{discharge}}$ is the discharge mass flow rate. This yields the amount of energy generated for each kilogram of discharged air. The result has been converted to kWh/kg rather than J/kg to achieve parity with the literature and ease comparison.

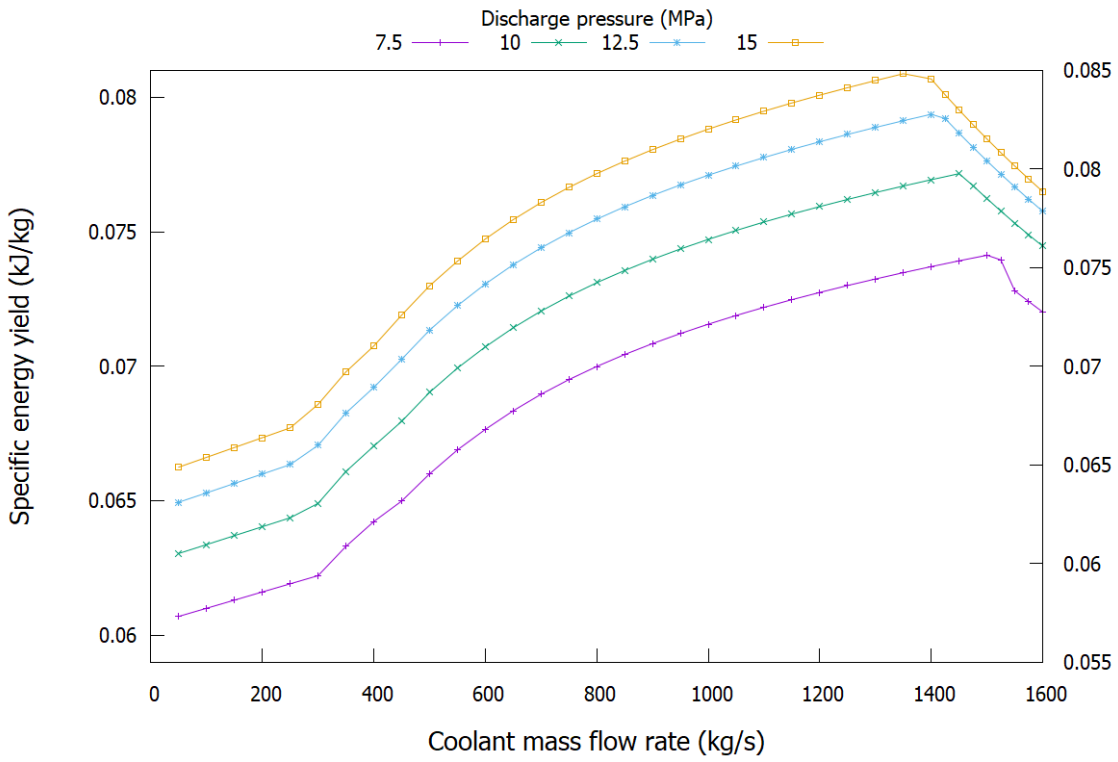

Figure 5-12: D-2 discharge specific energy yields

Figure 5-12 shows the effect of increasing the discharge mass flow rate of the system for a 2-turbine discharge cycle. For this, and indeed all discharge configurations, increasing mass flow rate increases the specific energy yield of the system (the net energy yielded at the turbines for each kg of liquid air sent through the cycle). This is due to the fact that that increasing mass flow rate requires drawing additional heat from the NPP secondary loop. As can be seen in Figure 5-3 and Figure 5-6, the NPP's steam turbine efficiency and hence NPP output power falls most steeply at small bypass ratios (and, by corollary, so too does the percentage of power lost to increasing inefficiency). As a result, each incremental increase in bypass ratio results in a smaller increment of NPP power lost to reduced steam turbine efficiency.

There is, of course, a limit to this improvement, set by the limit on steam diversion discussed in section 5.2.1. Once the ratio of steam diverted from the NPP secondary loop reaches 50%, increases to discharge mass flow rate cannot draw extra steam from the NPP secondary loop. This results in a fall in turbine inlet temperatures and a decline in specific energy, as seen by the downturn above mass flow rates of 1,400 kg/s. The effect occurs earlier at higher pressure due to air having a higher specific heat capacity and thus fully utilising available NPP heat at

lower mass flow rates. Despite this, increasing discharge pressure improves specific energy yield throughout the mass flow rate range.

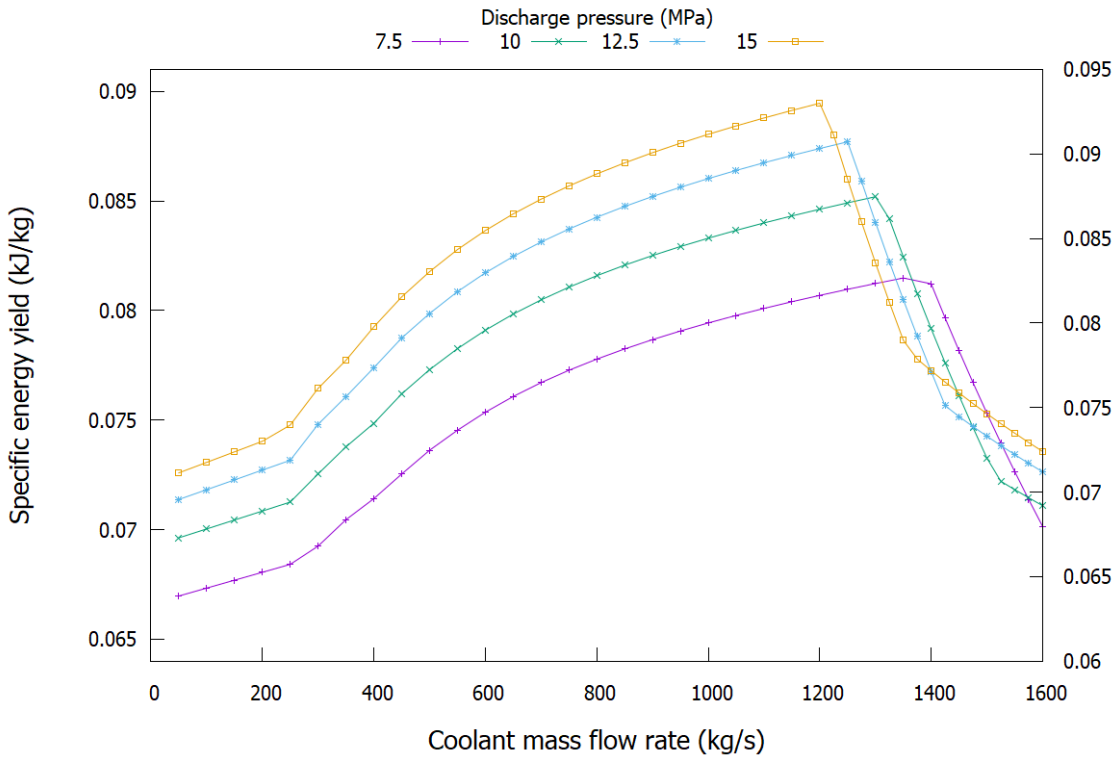

Figure 5-13: D-3 discharge specific energy yields

Figure 5-13 shows the effect of increasing the discharge mass flow rate of the system for a 3-turbine discharge cycle. These are largely similar to those for the D-2 discharge cycle, with specific energy yield increasing as mass flow rate rises and with improvements exhibited by increasing the peak cycle pressure. As expected, increasing the number of turbines has improved the specific energy yield. There is, however, one important feature of the results that warrants further discussion. Above the peak, the specific energy yield does not drop off linearly as seen in Figure 5-12. Instead, it shows an initially steep decline. The result of this is that there are points above the optimal flow rate where lower pressures actually achieve greater specific energy yields.

This is a result of the effectiveness of the recuperator. Recuperators are designed to capture exhaust heat from a power cycle by using it to heat the working fluid at an earlier stage of the cycle. In the recuperator, the exhaust air leaving the cycle (on the hot side of the recuperator) is at atmospheric pressure, whilst the air on the cold side is at just below the peak discharge pressure of the cycle. Increasing the peak discharge pressure increases the heat capacity of the air on the cold side whilst simultaneously lowering the outlet temperature of the turbine. These effects conspire to reduce recuperator heat loads for higher pressures, resulting in a lower inlet

temperature for the first stage turbine. This results in a reduced power output and the regions where specific energy yield is higher for lower pressures.

Incidentally, this phenomenon is not seen in configuration D-2. This is because the larger pressure ratios required for a 2-turbine system to achieve the same peak pressure extract more heat from each stage of the expansion cycle and result in a similarly lower turbine outlet temperature from each stage. Above discharge flow rates of around 300 kg/s, this turbine outlet temperature means that the exhaust is actually cooler than the incoming air, and the recuperator is undesirable. The recuperator was removed from the model for any simulations where this occurred to ensure that the system was not wasting energy by heating the exhaust air.

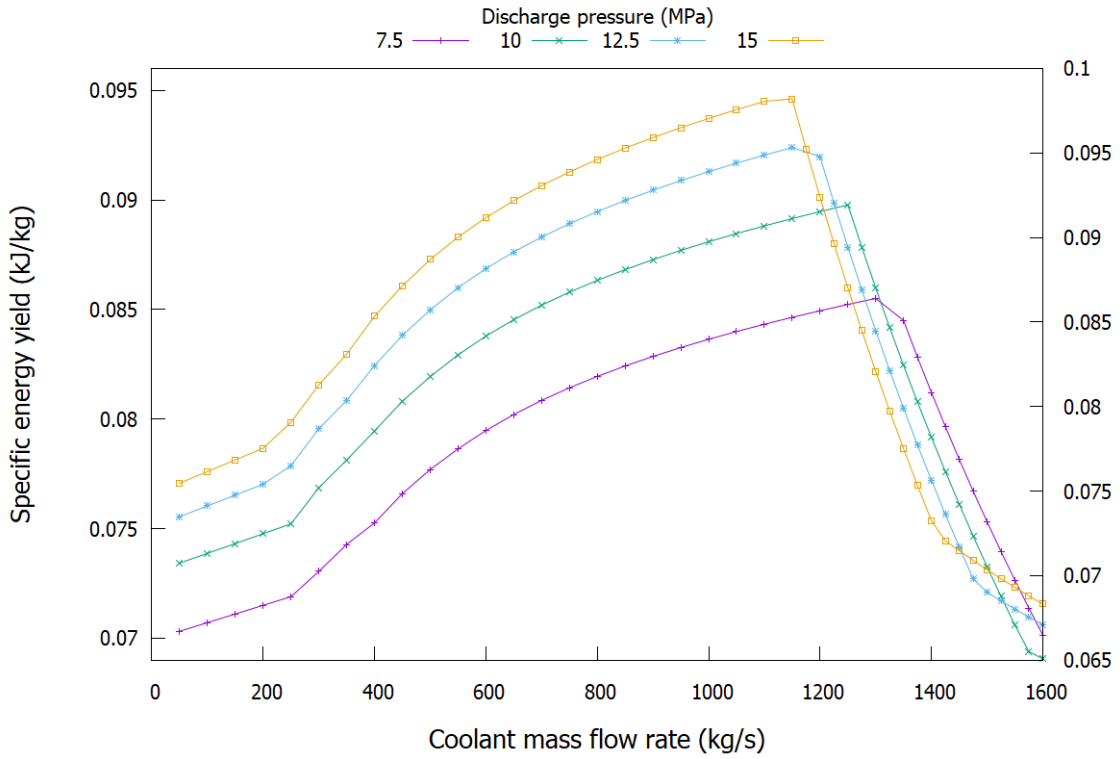

Figure 5-14: D-4 discharge specific energy yields

Figure 5-14 shows the effect of increasing the discharge mass flow rate of the system for a 4-turbine discharge cycle. The results are much the same as those in Figure 5-13 and exhibit the same phenomenon at high flow rates with lower pressures achieving higher specific energy yields in certain circumstances. Once again, the effect of increasing the number of turbines is pronounced; significantly more so than increasing from 2 to 3 turbines.

The ratios of secondary loop steam sent to each turbine stage are also important to discharge cycle efficiency. Whilst increasing discharge mass flow rate increases the required diversion ratio of steam from the NPP to each stage of the expansion process, the optimal ratios remain fixed independent of discharge mass flow rate. The ratios do, however, vary somewhat with the peak pressure of the discharge cycle, typically increasing slightly as pressure is increased (more heat is required as the air has a higher specific heat capacity), although this variance is very small. Figure 5-15 shows that for all optimal ratios, the most significant fraction of the NPP steam is diverted to the first turbine stage. This can be understood in terms of the turbine inlet temperatures. The discharge air stream leaves the recuperator at a temperature somewhat lower than it leaves each turbine stage, so the temperature increase between the superheater inlet and outlet is greater for this first stage and the required mass flow rate of NPP steam is greater.

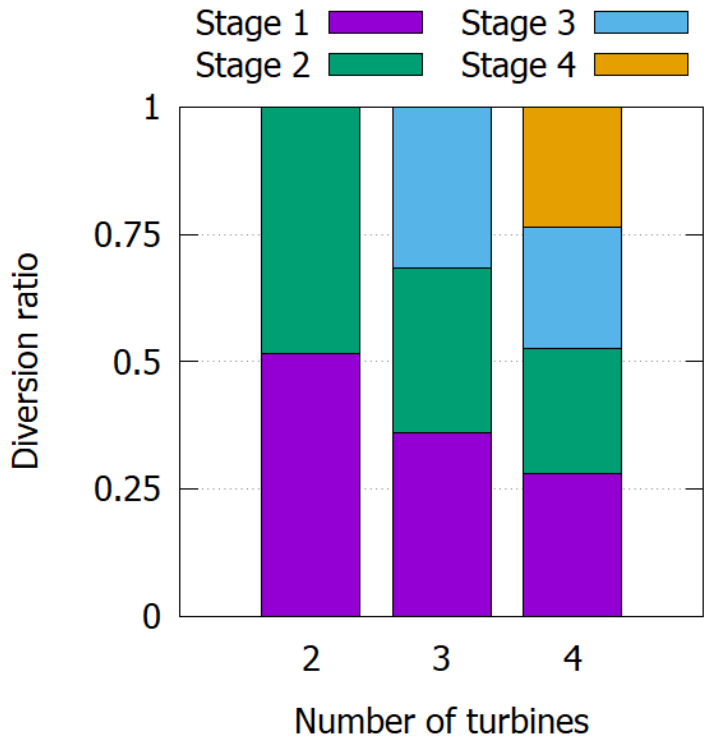

Figure 5-15: stage diversion ratios for 15 MPa discharge pressure

5.2.4. Cold store duty cycling

The next step was to determine the performance of the cold store in a coupled liquefier and power system over a number of duty cycles. The cold store is heated during the charging cycle and cooled during the discharging cycle, as discussed in section 5.2.2. Because of this temperature cycling, the cold store can be expected to eventually reach cyclic equilibrium, a point at which the amount of energy stored in, and the temperature profiles along the cold store do not vary from one cycle to the next. This section explores this effect and attempts to determine an optimal size for the cold store.

A further important consideration is ensuring sufficient temperature differences in the heat exchangers for sufficient heat flows. Figure 5-17 is a schematic diagram of the heat flows between the charge and discharge cycles and the cold store.

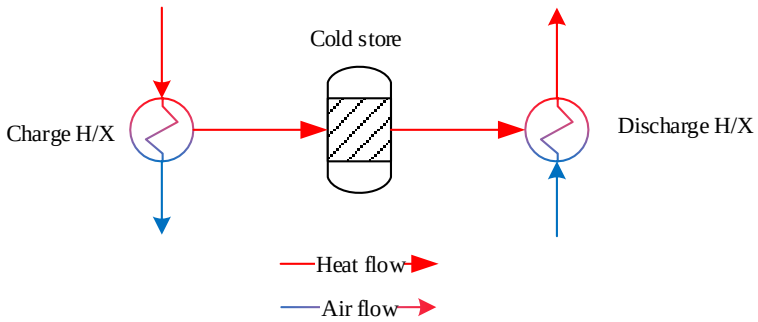

Figure 5-17: Schematic of heat flows between charge/discharge cycles and cold store

As shown, as the air flow is heated on discharge, the cold store is cooled. Conversely, as the air flow is cooled during system charging, the cold store is heated. Initial modelling demonstrates that the temperature swings in the gravel bed and the charge and discharge heat exchangers might be sufficient to create a phase change in the air streams. Thus, careful attention must be paid to the saturation points of air. The black line in Figure 5-16 shows the saturation point for

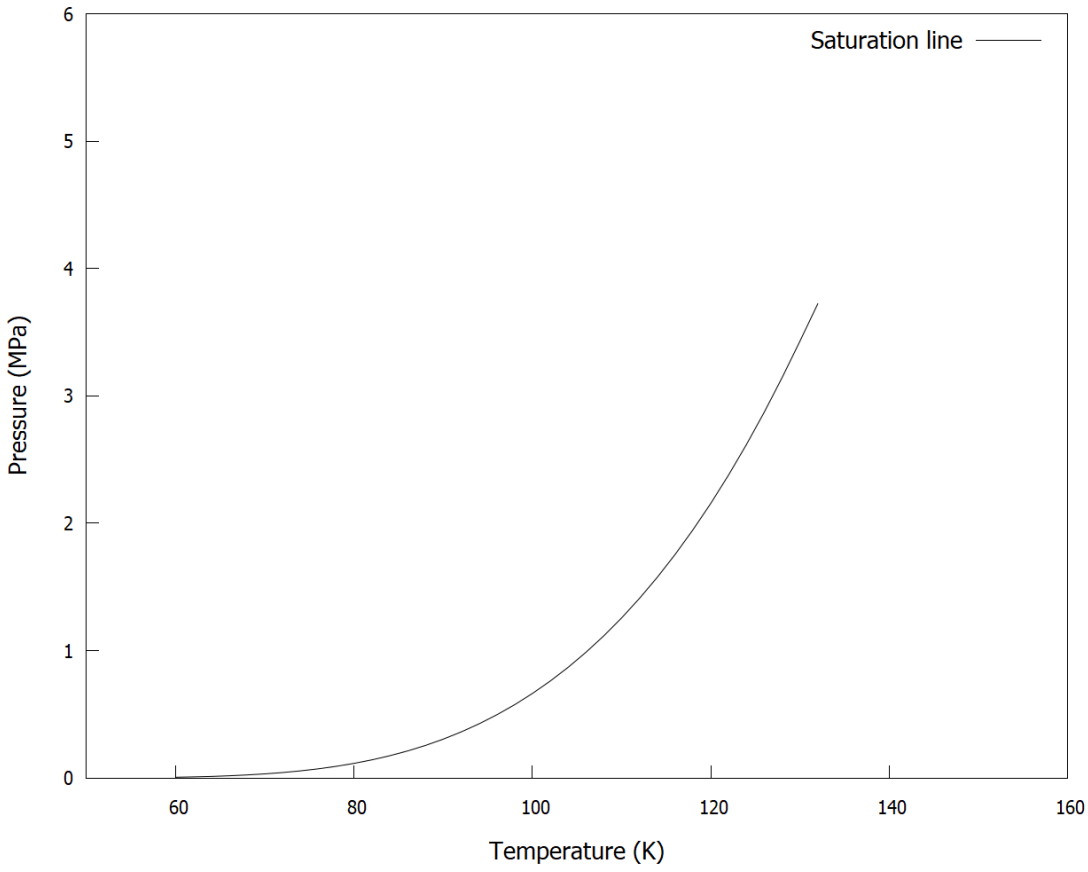

Figure 5-16: p-T diagram showing saturation points for air

air at a range of temperatures and pressures. Careful attention must be paid to heat exchanger pressures in this range to ensure that the saturation temperatures of the two streams provide a sufficiently large gradient to facilitate heat transfer between the streams.

The critical point for air occurs at a pressure of 3.7858 MPa and a temperature of 132.63 K (Lemmon et al., 2000). Above this point, in the top-right quadrant of the p-T diagram, air is a supercritical fluid and differences between phases are indistinguishable. Transitions from this quadrant to either the top-left (the compressible liquid region) or the bottom-right (the gaseous region) involve zero heat of vaporisation and were thought to potentially mitigate the issue of pinch points caused by phase transitions. Operating above the critical pressure was also expected to provide an advantage from an operational perspective in that the pumps used in the cold store loop would always operate at densities comparable to those of liquid air, preventing cavitation and limiting operating power consumption. As a result, the initial decision was made to use an operating pressure of 4 MPa for the cold recycle system.

However, this in itself did not mitigate the problems associated with the phase change in air. As can be seen in Figure 5-18, air experiences a spike in specific heat capacity at around 140 K. This is analogous to the latent heat of vaporisation and represents a temperature at which a pinch point will occur in the heat exchanger. This is a potentially significant issue for the air liquefaction cycle where it is important that the air reach the lowest temperature possible before expansion in order to maximise liquid yields. A pinch point at a higher temperature is a potentially significant hurdle to achieving this objective. It is similarly important to note that the cold recycle loops in the plant designs discussed in section 2.6 operate at temperatures well above the atmospheric pressure saturation point, such that phase transitions are not necessarily an issue.

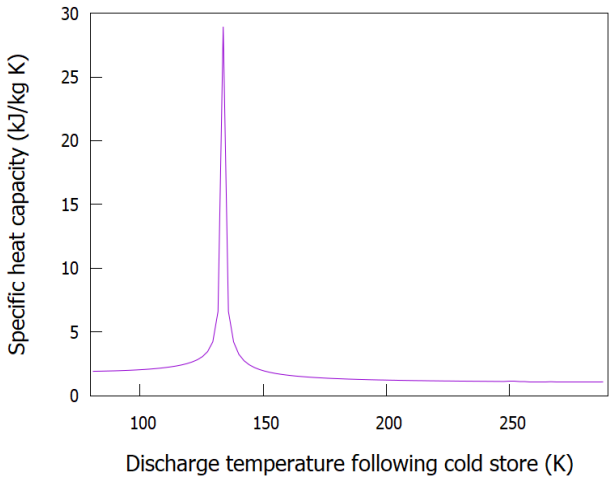

Figure 5-18: Air specific heat capacity at 4 MPa

Operating outside in the supercritical rather than the gaseous region will increase the power consumed by pumping air within the cold recycle loop. It is worth considering by exactly how much this will affect plant energy balance. In order to do so, it is important to understand how air density changes with pressure and temperature. This is shown in Figure 5-19. The sharp drops in density occur at phase transitions.

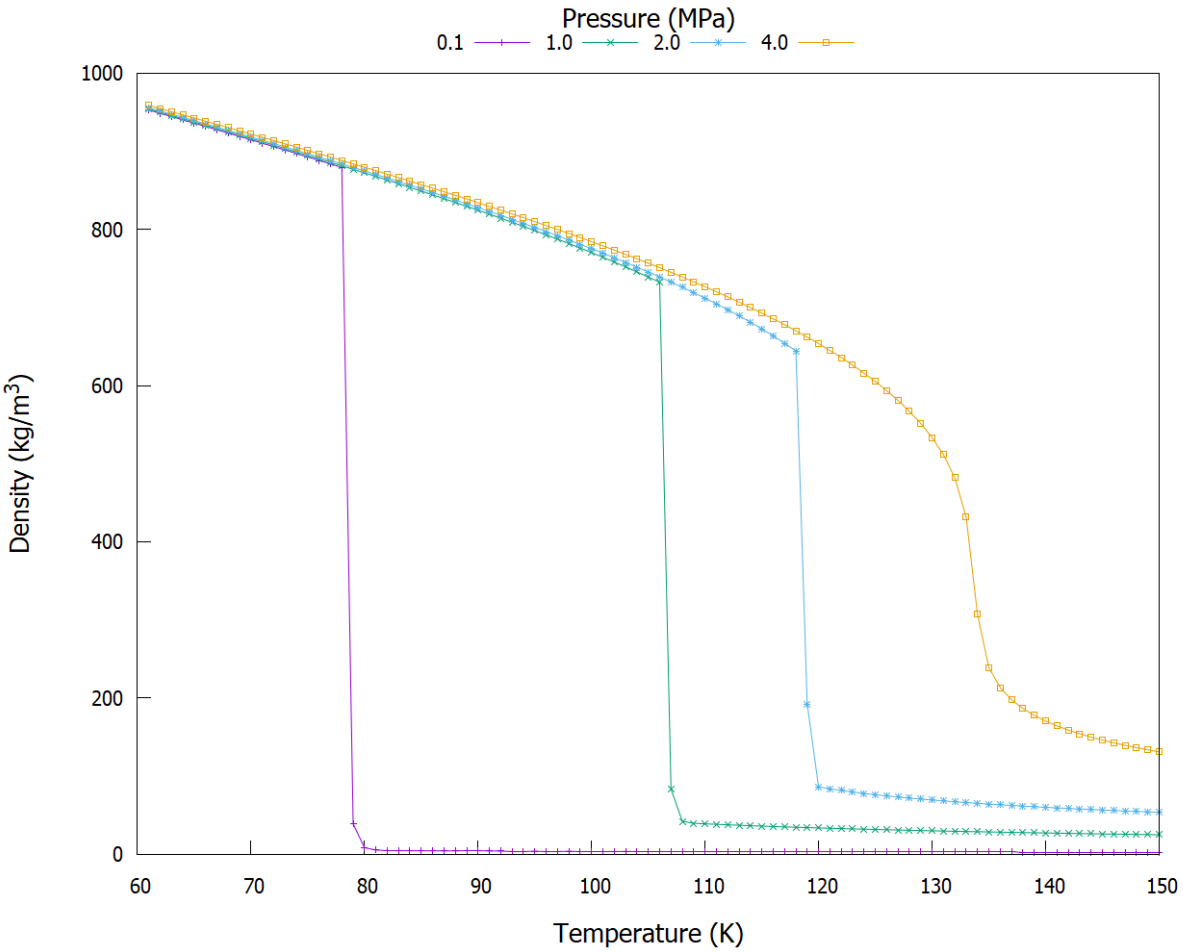

Figure 5-19: Density of air for different temperatures and pressures

As can be seen, as air temperature increases, its density falls. As discussed in section 3.2.14, the power required to pump a fluid through a given pressure increase, Δp, is given by:

$$\dot{W} = \frac{\Delta p \dot{M}}{\eta \rho} \qquad (5\text{-}2)$$

where $\dot{M}$ is the fluid's mass flow rate, ρ is its density and η is the pump's efficiency. As a result, a decrease in density results in a increase in pumping power. From equation Figure 5-19, it can be seen that liquid density falls by a factor of around 200, resulting in a likewise increase in pumping power. It is important to note, however, that for the modest mass flow rates and

pressure drops seen in the literature, the pumping power remains in the sub-megawatt and the decision was made to use a low-pressure cold store operating at atmospheric pressure, in line with the literature. This eases both engineering modelling, from the perspective of the aforementioned minimum approach temperatures, and financial modelling in maintaining operating pressure parity between air storage tanks and cold store tanks as discussed in section 2.7.

Considering the points discussed so far in this section points to how to build the model itself. At this stage in the project, the known parameters were limited. The temperature of liquefied air for a given storage pressure is known and can be used as a starting point for an air stream mass flow source. As discussed in section 2.5, and shown in section 5.2.3, the peak discharge pressure is an important parameter determining turbine performance. It will also affect the temperature of the air following pumping, and likewise the temperature difference in the cold store air streams, and thus the amount of cold that can actually be recycled to the charging cycle.

This information provides a means to estimate the size of the cold store prior to full modelling. This is important given the multi-parameter nature of the system and the parameter sweep approach to engineering modelling. Estimating component sizes serves to narrow the design space for the system and limit the required system modelling. Since air pumping is performed before the cold store inlet, and the model assumes a pressure drop proportional to the inlet pressure, the temperature delta across heat exchangers on the charge and discharge sides of the cold store loop will be equal. This delta will be approximately equal to the difference between the cold store temperatures following charge and following discharge, subject to the discussions at the beginning of this section.

Simple models were built to determine the likely cold store loop parameters. As a starting point, the theoretical maximum specific cold recycle available depending on the temperature difference across the heat exchanger between the discharge cycle and the cold recycle loop. The specific cold recycle, that is the amount of heat transferred to the discharge stream per kilogram of air discharged, is shown in Figure 5-20. As shown, the higher the peak discharge pressure (the further along the x-axis), the smaller the specific cold recycle. Conversely, the higher the intermediate discharge temperature, the greater the specific cold recycle, as a greater temperature difference is achievable across the discharge-side cold store heat exchanger and between the hot and cold states of the cold store.

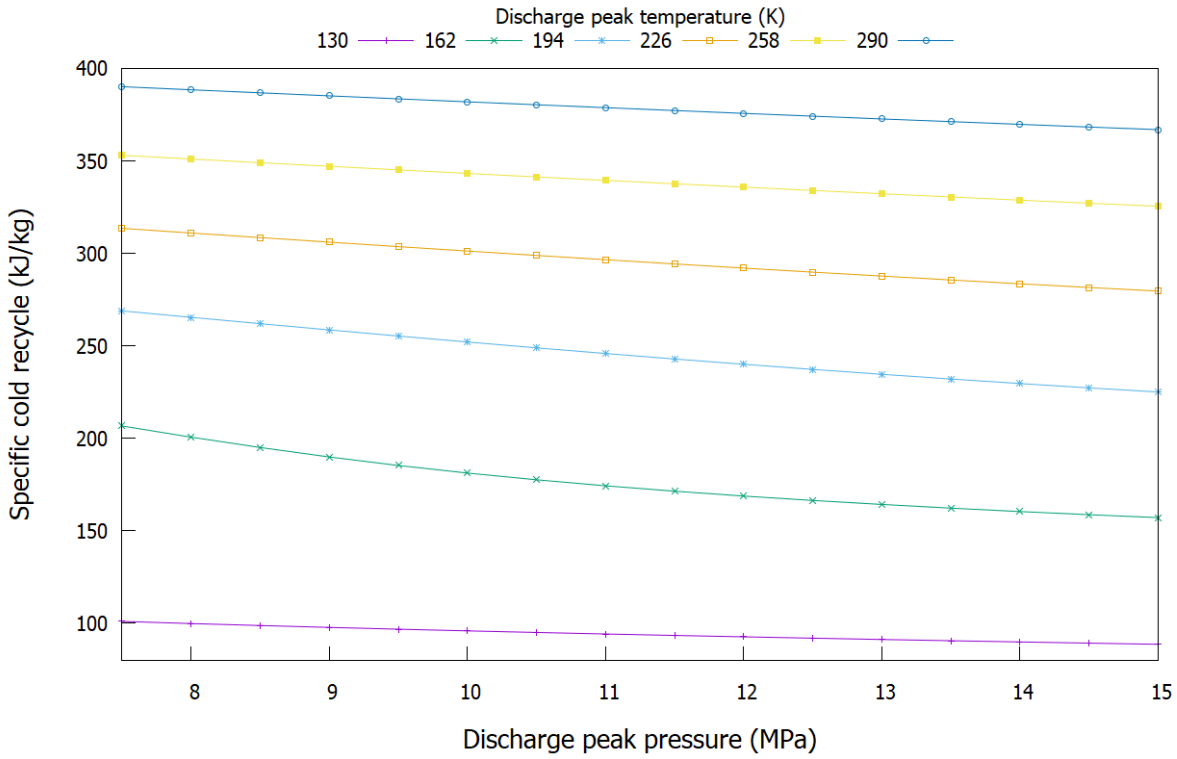

Figure 5-20: Theoretical specific cold available for isolated cold store modelling

These results have important implications for the system's overall round-trip efficiency. Higher peak discharge pressures will result in higher turbine power but will lessen the amount of cold recycle possible for a given temperature delta, increasing the temperature of the charge air stream prior to expansion, as discussed in section 5.2.5. Thus, a higher peak discharge pressure may ultimately reduce the round-trip efficiency by reducing the efficiency of the liquefier.

The results in this section have important implications for the cold store. As Figure 5-9, Figure 5-10 and the subsequent discussions show, the cold store heat transfer rate, the air temperature at the outlet and the temperature of the cold store itself all vary as the cold store is cooled. The amount of storage capacity can be controlled by varying the length of the cold store, but in turn will affect its heat transfer rates during both the charge and discharge cycles.

With this information in mind, duty cycle modelling of the cold store was begun. This was performed using the same model shown in Figure 5-21.

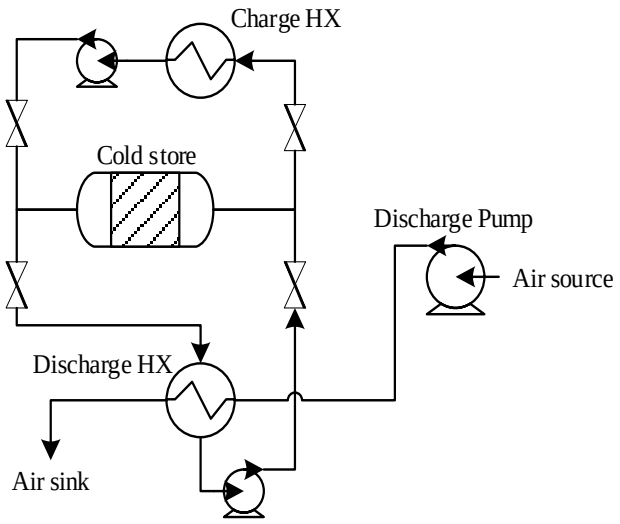

Figure 5-21: Isolated model for testing cold store parameters

The cold store was modelled in cycles to a point of cyclic equilibrium. That is, the point at which the heat transferred to the cold store during the charging phase was equal to the heat lost by the gravel bed during the discharging phase. Typically, this occurred after around 20 cycles. This modelling was performed using the parameters shown in Table 5-5. It was assumed that the charge cycle would operate at a significantly larger mass flow rate than the discharge cycle, since only some of the total air flow compressed will be liquefied. A high mass flow rate was used to ensure that the maximise heat transfer between the cold store and the charge air stream.

Parameter	**Value**	**Units**
Discharge mass flow rate	100	kg/s
Discharge source temperature	78.9	K
Discharge source pressure	101.325	kPa
Discharge peak pressure	12,500	kPa
Cold store loop mass flow rate	185	kg/s
Cold store loop peak pressure	101.325	kPa
Cold store starting temperature	150	K
Cold store diameter	3	m
Cold store length	Swept parameter	
Bed particle diameter	0.02	m
Bed particle density	2320	kg/m^3
Bed particle specific heat capacity	810	J/kg K
Charge mass flow rate	150	kg/s
Charge source temperature	293.15	K
Charge source pressure	18,000	kPa
Heat exchanger pressure drops	0.01	
Pump efficiency	90	%

Table 5-5: Cold store duty cycle model parameters

The cold store model discussed in sections 3.2.8 and 3.2.9 is capable of modelling axial conduction along the length of the cold store. At this stage, however, the length of the periods during which the system might be idle and the cold store temperatures would approach equilibrium was not known. As a result of this, the assumption was made that there would be no conduction through the cold store and the parameter for the thermal conductivity of the gravel bed, κ, was set to zero. The implications of this assumption are discussed in section 7.3.1.

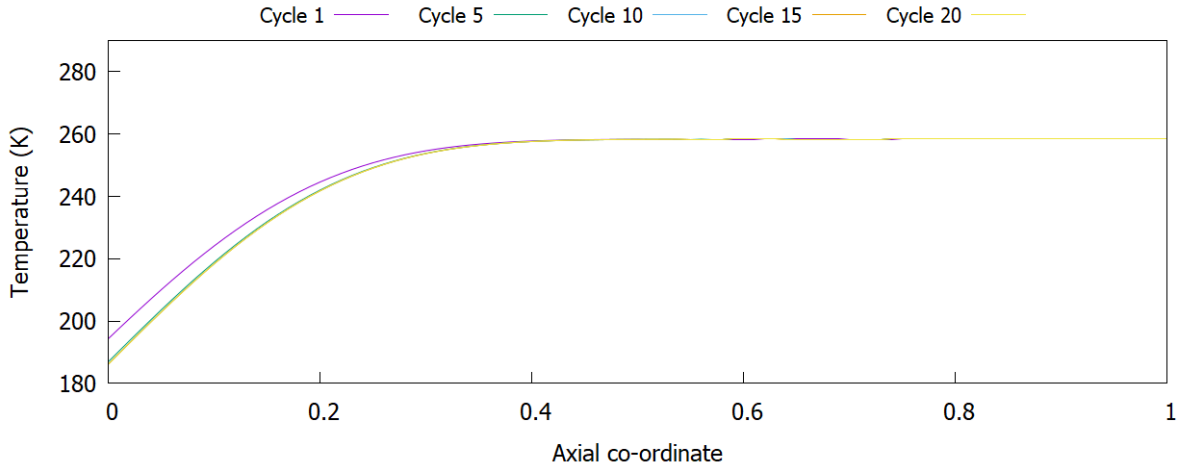

Figure 5-22: Axial temperature profile of the cold store following charge for a 16m cold store

As will be discussed below, the efficiency of the cold recycle system is dependent on maximising temperature differences across the cold store loop heat exchangers. In order to maximise efficiency of the cold recycle system, (Sciacovelli et al., 2017b) envisages an arrangement of parallel cold stores which are operated sequentially during a single duty cycle, allowing temperature differences to remain at nominal levels for as large a part of the duty cycle as possible. Essentially, this reduces the amount of time that they operate at points beyond the red line in Figure 5-9 and Figure 5-10. A similar system was assumed to operate for this project, and it was assumed that four cold store cells would serve a single half-hour duty cycle for the 100 kg/s symmetrical system being designed. Much like (Sciacovelli et al., 2017b), a single-

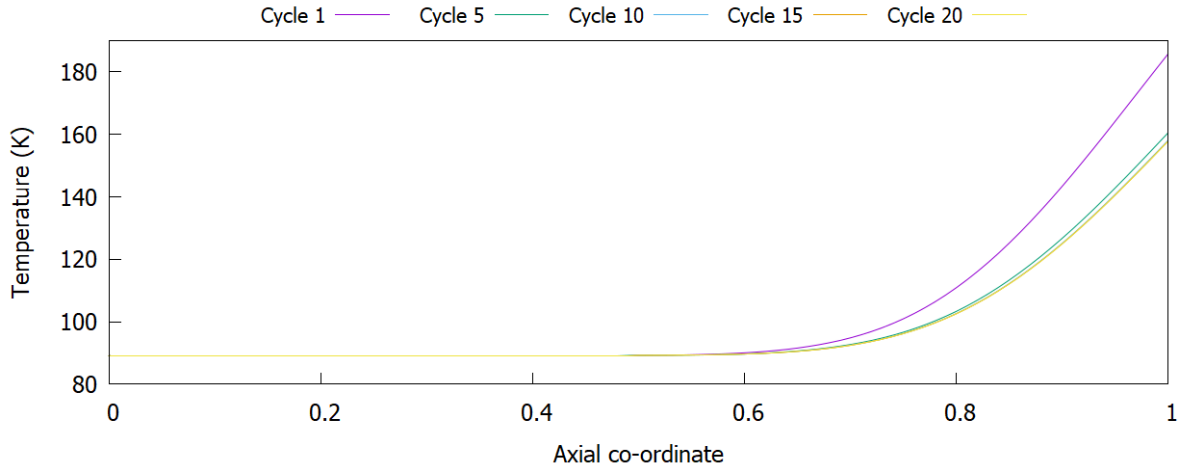

Figure 5-23: Axial temperature profile of the cold store following discharge for a 16m cold store

cell system was used to model the behaviour of a transient system, and as a result, the simulations were run for 450 s.

Figure 5-23 shows the temperature profile of the cold store following discharge cycles 1, 5, 10, 15 and 20 for the example of a 16 m cold store. The x-axis shows the axial co-ordinate; essentially the length along the cold store normalised to the length of the whole cold store. As the figure shows, the temperature profile has converged to a state of cyclic equilibrium by around cycle 10. Figure 5-22 shows temperature profiles following charge cycles, exhibiting the same convergence behaviour.

Figure 5-24 shows how the energy capacity of the cold store varies with its length. This is shown as both an amount in kWh, and a percentage of the theoretical energy available based on the enthalpy difference across the discharge heat exchanger at the start of the simulation, the discharge flow rate and the length of time for which the simulation was run (in this case, just below 4000 kWh).

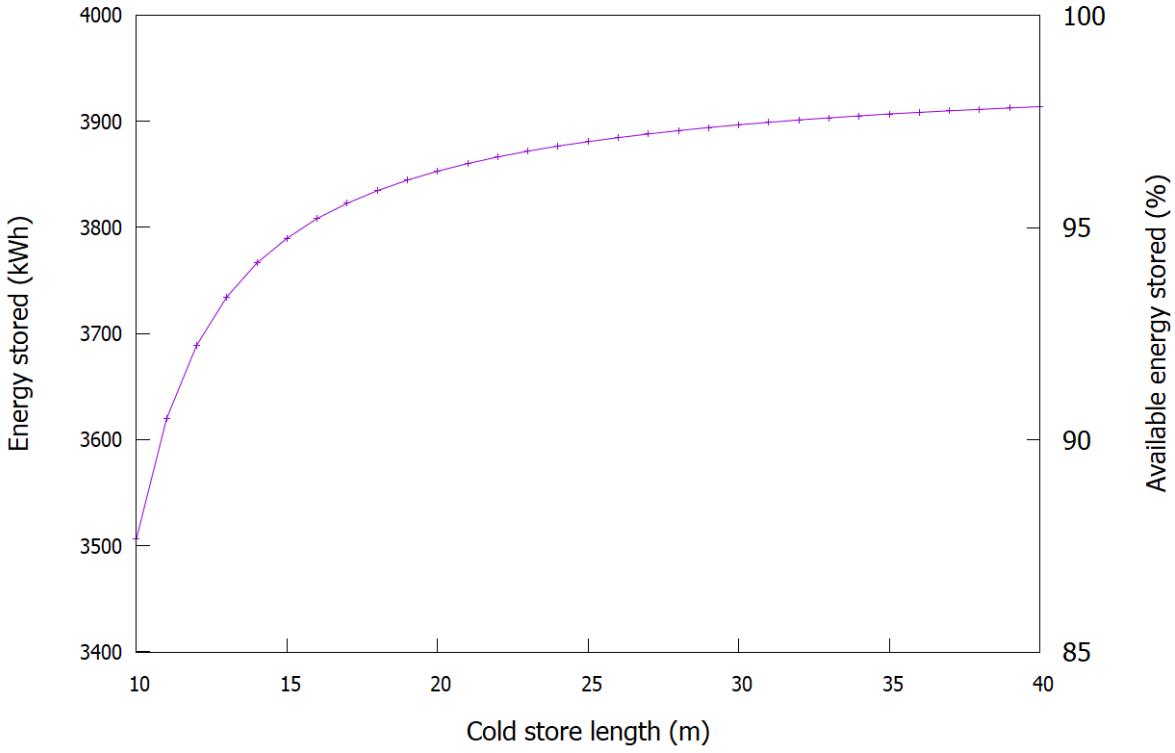

Figure 5-24: Cold store energy capacity dependency on cold store size

The percentage of available energy that is stored is an important metric. The cold store is a dynamic system and its temperature rises during the discharge cycle. As this occurs, the temperature difference of the air across the cold store loop side of the discharge heat exchanger will reduce, and the heat load of that heat exchanger will similarly fall. This can be seen in Figure 5-25. The line at the top is the temperature of the air in the cold store loops at the store's outlet. The falling line below this represents the average temperature of the gravel; as this falls, so too does the air temperature at the outlet. Two lines are shown increasing from bottom-left to top-right. The yellow line is the ideal cold that could be stored; essentially the initial storage rate extrapolated linearly. The blue line shows the actual cold stored and this falls as the outlet temperature falls due to the aforementioned reduction in heat load of the discharge-side heat exchanger.

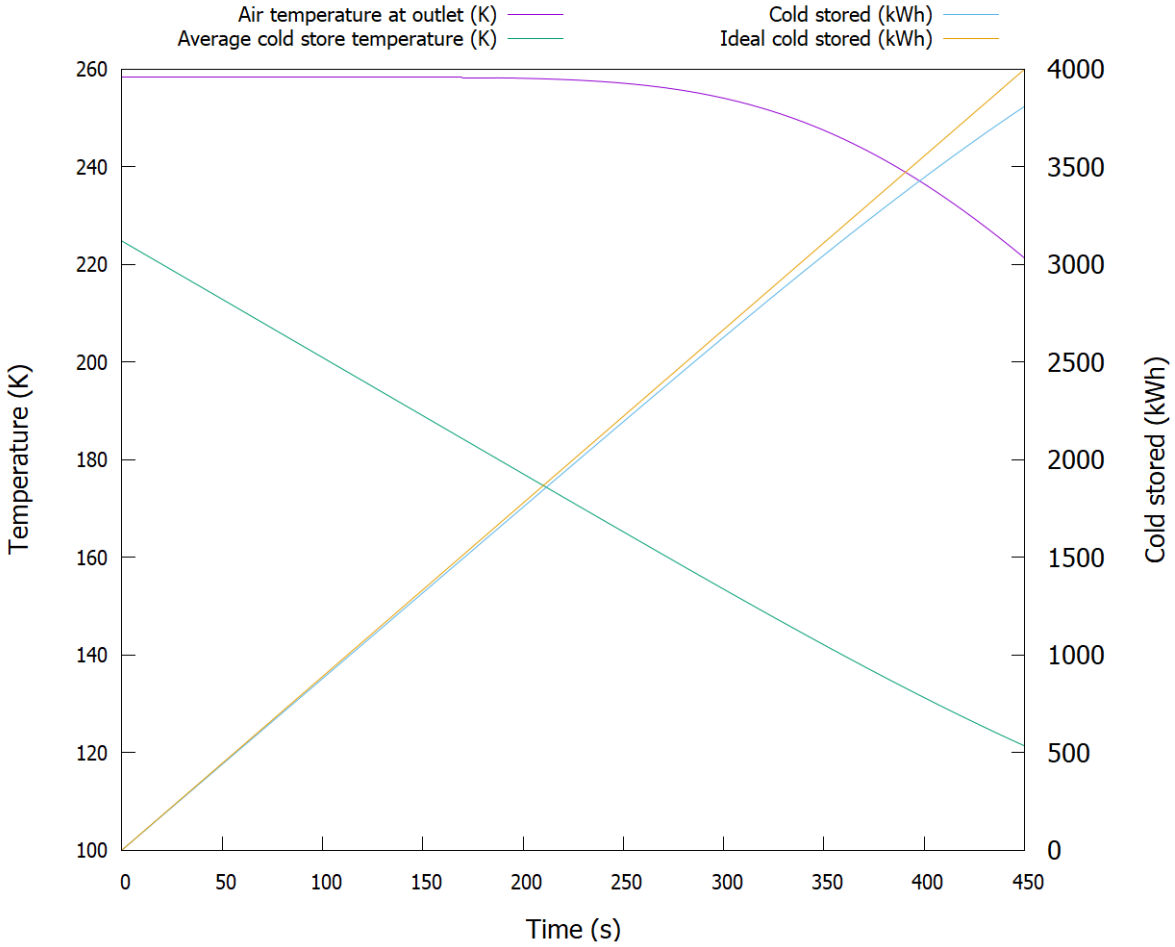

Figure 5-25: Cold store energy stored and temperature profiles over a single discharge cycle with a 16m cold store

This is an interesting consequence of the of the finite volume approach to modelling the cold store. Because the gravel bed part of the cold store is modelled as an array of finite volumes, the volumes will essentially cool down (or heat up) sequentially/ from the inlet to the outlet end as air enters the bed and equilibrates with the cold store volumes. Because of the fact that

conduction between the volumes is assumed to be zero for the purposes of this simulation, the finite volumes act almost as individual cold store cells, in the context discussed above. As a result, the volumes at the inlet end of the cold store are always fully heated or cooled during the charge or discharge phases, respectively. A consequence of this is that shown in Figure 5-24. Essentially it means that the cold stored will approach 100% of that theoretically available as the size of the cold store approaches infinity. Whilst this is an interesting quirk of the modelling approach, it does not necessarily mean that the model is poorly representative of real-life conditions; the same behaviour discussed in the previous paragraph as regards flow temperature transients and the resulting cold capture will manifest in a real system.

As a result of this, this system can never extract 100% of the theoretically available energy from the discharge air stream. This can be seen in Figure 5-24; whilst the graph has begun to level off and its behaviour at lengths larger than around 20 m is somewhat linear, it is still continuing to level off beyond this point. This presented a difficult design decision at this stage as there is no obvious choice for a cut off point for an optimal cold store size. Ultimately, a larger cold store will always be preferable from an efficiency perspective, but this must be offset against cost considerations. A capture of 95% of the available cold was deemed sufficient for this design and thus, a cold store size of 16m was taken as the size of the store for this quantity of cold stored.

Due to the complexity of optimising the cold store length, this process was only performed once. The amount of energy the cold store is capable of storing is defined by:

$$Q = MC_{\mathrm{m}}\Delta T \qquad (5\text{-}3)$$

where M is the mass of gravel in the cold store, C_{m} is its specific heat capacity and ΔT is the temperature difference between the charged state and the discharged state. This is, of course, a simplification, as the cold store does not have a uniform temperature along its axis at the end of either phase. It is, however, sufficient for these purposes. In order to limit the additional modelling required, it was assumed that the overall temperature swing between the hot and cold states for the cold store would be the same for any given discharge pressure. Thus, the heat storage capacity of the cold store varies linearly with its mass.

With this in mind, the cold store was sized for the different quantities of specific cold recycle shown in Figure 5-20 according to the equation:

$$L = 16\frac{CR_m}{320{,}000} \qquad (5\text{-}4)$$

where CR_m is the theoretical maximum specific cold recycle available for the discharge air stream, in Joules, and L is the length of the cold store. In the case of the example discussed in this section, 16 m is the length of the store and 320 kJ/kg is the theoretical maximum cold recycle based on the initial enthalpy difference across the discharge-side heat exchanger.

Altering the theoretical available specific cold recycle similarly increases the required flow rate through the cold store loop. As before, heat exchanger temperature differences were assumed to be equal through the cold store loop side of the discharge heat exchanger, and given that the loop's pressure was also taken to be fixed, it was assumed that the required mass flow rate would also scale linearly with the specific cold recycle using the equation:

$$\dot{m} = 185\frac{CR_m}{320{,}000} \qquad (5\text{-}5)$$

where $\dot{m}$ is the required cold store loop mass flow rate. Here, 185 kg/s is the operating flow rate in the case of the example discussed in this section.

Using these scaling equations, cold store cycling was performed for discharge pressures of between 7.5 and 15 MPa at 0.5 MPa intervals, mirroring the pressures used in section 5.2.3. To determine the theoretical maximum specific cold recycle, the same temperature differences

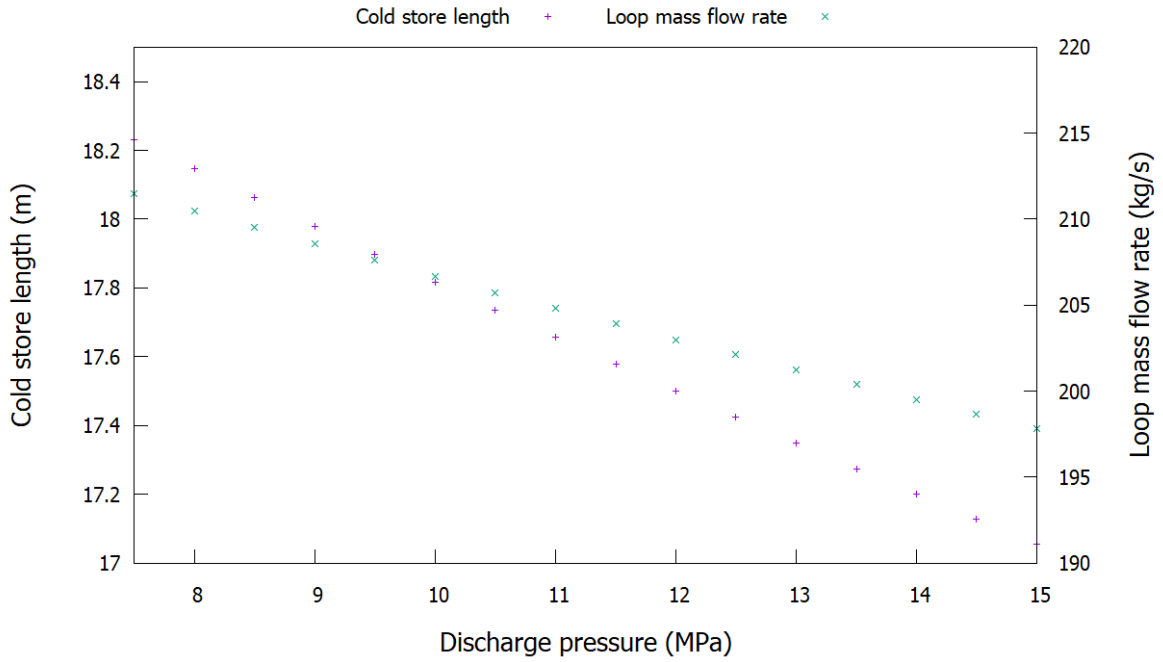

Figure 5-26: Cold store size and loop parameters for different pressures

across the discharge side heat exchanger were assumed as those used in the example in this section, that is the discharge air stream leaving the heat exchanger at 258.5 K.

Cold stores were cycled in the same way as in the example above for the input parameters shown in Figure 5-26. This yielded a set of initial temperature profiles for the cold store which could then be used for modelling the charge an discharge cycles from a point of cyclic equilibrium.

5.2.5. Charge cycle modelling

With potential cold store dynamics understood, and an understanding of operating ranges for the discharge system, the final step was to study the options for liquefaction. Once again, modelling was built up in a modular sense. Because the liquefier cycle bears minimal bearing on the compression and the compressed air is water cooled to a known temperature, a mass flow source was used to define the flow from the compression cycle, allowing optimisation the liquefaction cycles beyond the compression train. Following this, compression trains were modelled to determine the specific energy of liquefaction for each potential configuration. For brevity, cycles considered in this section are denoted C-*y* where *y* is the number of compression stages used. In order to link the system to the discharge cycle, the temperature profiles for the cold store from section 5.2.5 were used as an initial parameter for these simulations.

As discussed in section 2.5, Highview Power and the associated study group at the University of Birmingham provide the most comprehensive, realistic and experimentally verified body of modelling work on the LAES system (Morgan et al., 2015b, Morgan, 2016, Sciacovelli et al., 2017a, Sciacovelli et al., 2017b). Their system is Highview's vision for their commercial design, and is the design on which this study is based. This bears most similarity to the Collins cycle. In its first stage, compressed air is first cooled and then some is diverted away to a warm turbine, which, after being expanded, is combined with the return air stream. A second stage involves the same process, cooling first, then diverting a fraction to a cold turbine and joining it with the return air stream. The incoming air stream is then further cooled by both the return air stream and the cold store loop before being expanded in a J-T valve. Finally, the air is separated into its vapour and liquid fractions. The vapour fraction begins its return journey back through the cycle and the liquid fraction is sent to the tank.

The chosen configuration for study is shown in Figure 5-27. Initial testing showed that the key parameters for study are the pressure from the compression cycle, $p_{\text{peak, charge}}$, and the proportion of the air stream diverted to the turbines following heat exchanger 1, x_1, and heat exchanger 2, x_2.

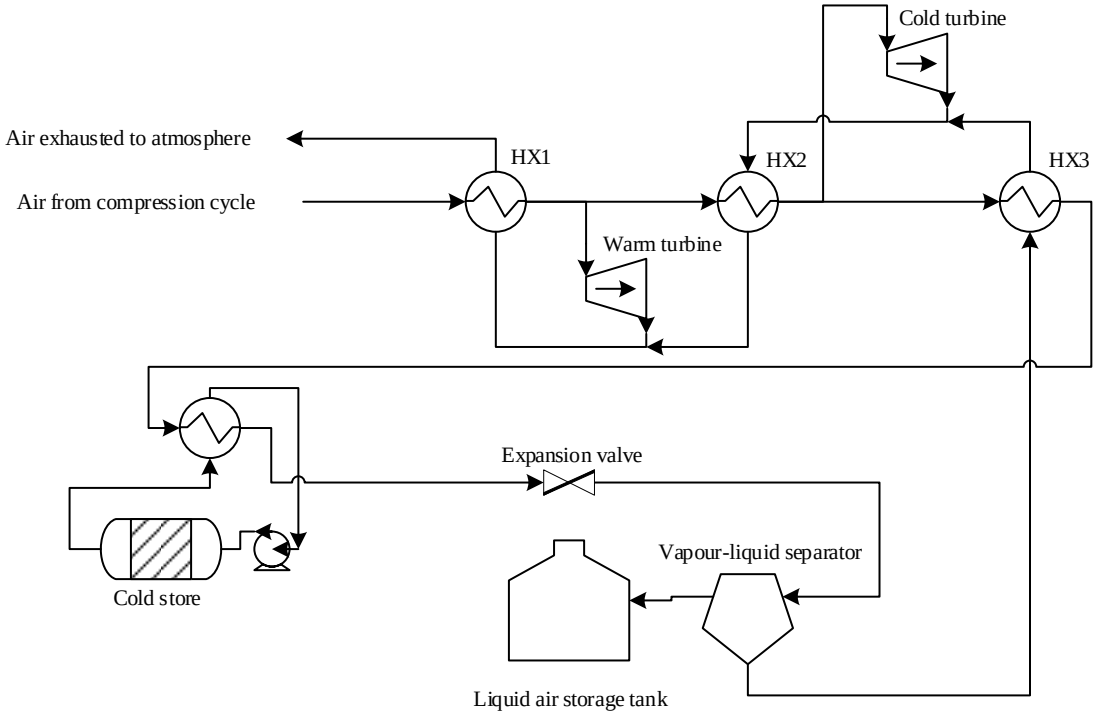

Figure 5-27: Charging liquefier configuration C-y

The liquefaction cycles were modelled in the configurations shown. Parameter sweeps were performed on the peak pressure and diversion ratios mentioned with different quantities of cold recycle available. Idealised heat exchangers were used with high surface areas. Key parameters are shown in Table 5-6. The resulting average liquid production rate, specific cold recycle, net power rating and power available from returning the exhaust to ambient temperature were output.

Parameter	Value	Units
Heat exchanger surface area – all exchangers	200	m^2
Heat transfer coefficient	300	W/m^2K
Air mass flow rate from source	Swept parameter	
Air pressure from source	Swept parameter	
Air temperature from source	298.15	K
Atmospheric pressure	101.3	kPa
Cold store mass flow rate	Results from section 5.2.4	
Cold store initial temperature	Results from section 5.2.4	
Diversion ratio from HX1, x_1	Swept parameter	
Diversion ratio from HX2, x_2	Swept parameter	
Pressure drops	0.01	
Cryoturbine peak efficiency	80	%

Pump efficiency	80	%

Table 5-6: Key parameters for liquefaction cycle models

As discussed above, the compression train was initially modelled separately. It consists of a series of compressor stages with intercooling between each stage. Intercooling is important because as the temperature of air in a compressor increases, so does the energy required to compress it. The availability of exhaust air from the liquefaction cycle complicates the compression train. This air can be used to pre-cool the air prior to each compression stage and reducing power consumption further.

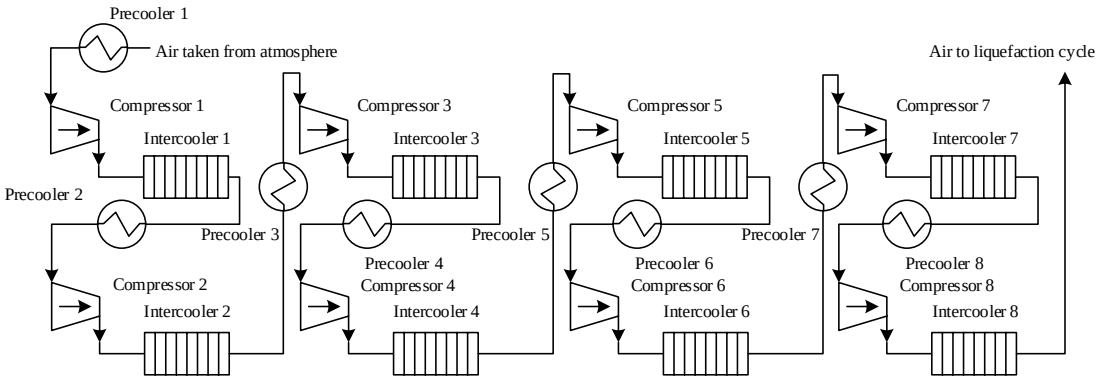

Figure 5-28: Compression train configuration Cx-8 (water flow and air exhaust streams omitted)

The decision was made to model the compression train with between 2 and 8 compression stages, as shown in Table 5-7. Figure 5-28 shows the largest system modelled, with 8 compression stages. Precooling was treated as an input parameter with units of power to enable compression results to be matched with results from the liquefaction cycle modelling. This power was assumed to be equally divided between the precoolers. Initial testing showed that the key parameters for modelling the compression train for a given pressure are the number of turbines and the amount of precooling available.

Configuration	**C*x*-2**	**C*x*-6**	**C*x*-7**	**C*x*-8**
Compression stages	2	4	6	8

Table 5-7: Air liquefier cycle configurations tested

The compression system was modelled with the parameters in Table 5-8. The power consumption, and precooler outlet temperatures for given cooling rate were output.

Parameter	Value	Units
Air mass flow rate from source	Swept parameter	
Air pressure from source (atmospheric pressure)	101.3	kPa
Air temperature from source	293.15	K
Temperature at intercooler outlets	298.15	K
Peak pressure following compression	Swept parameter	
Cooling power at precoolers	Swept parameter	
Pressure drops	0.01	
Compressor peak efficiency	85	%
Pump efficiency	80	%

Table 5-8: Key parameters for compression train models

Following isolated system modelling, model results were collated and impossible results (those with cold recycle exceeding the energy available for a given temperature change, or those with incompatible heat exchange temperatures) were discarded. Of the remaining results, those with the lowest specific energy of production for each configuration were taken forward for final modelling discussed in section 5.2.6, where components were sized and energy balance within the cold store for the combined system was considered.

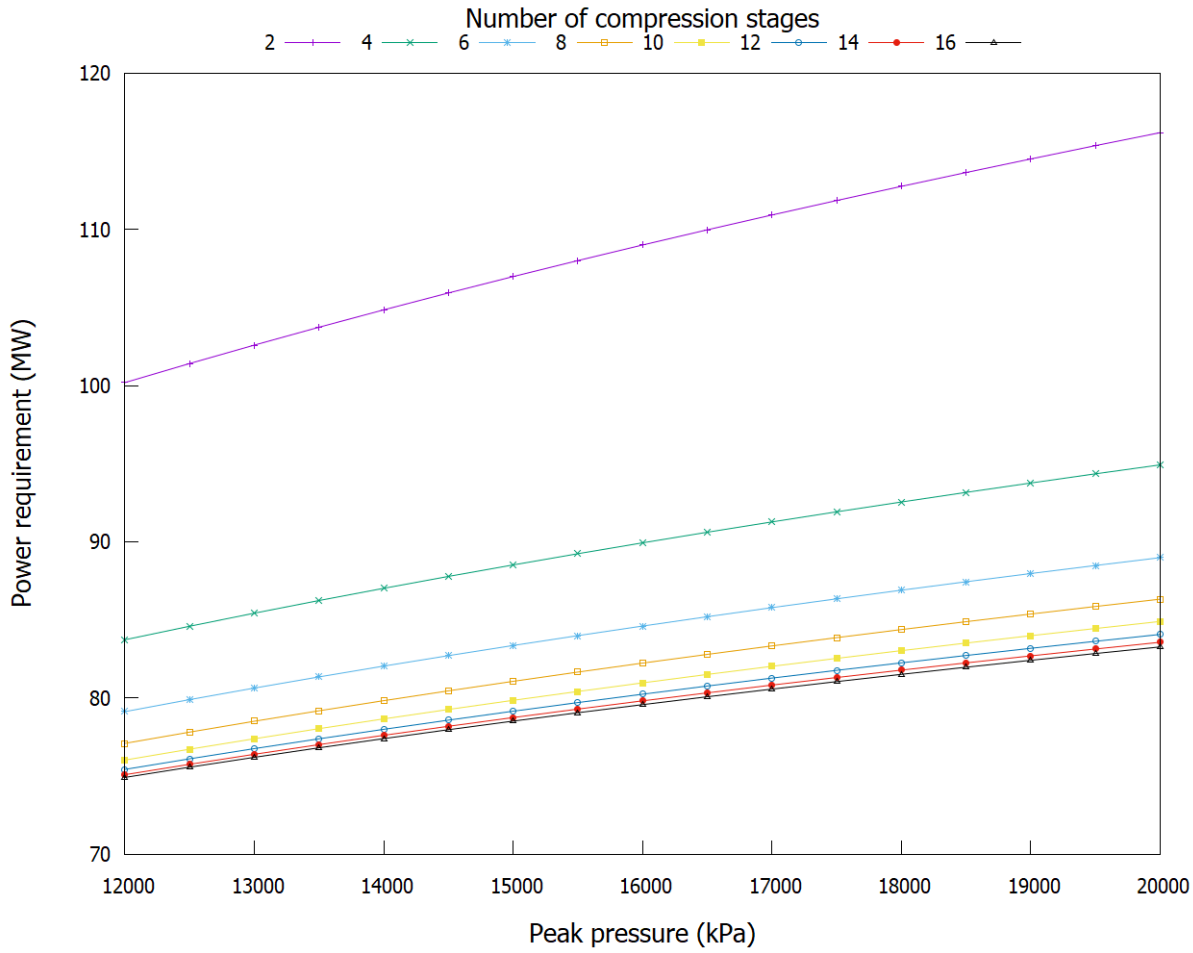

Figure 5-29: Power of compression for 150 kg/s flow rate

These initial investigations revealed some important information. As discussed in section 2.5.2, isothermal compression can theoretically significantly reduce the power requirement over isentropic compression (Li et al., 2014). In reality, the only way to approach isothermal compression with axial compressors is to compress in multiple stages and cool the air in intercoolers between each stage. For the sake of discussion, additional compression stages were modelled up to a total of 16. As shown in Figure 5-29, each successive addition of compression stages achieves a diminishing reduction in the compression power required. This is indicative of the futility in trying to approach isothermal compression with industrial-capacity equipment; 8 compression stages with intercooling is already a large and unwieldy system and the diminishing returns gained by further staging are clearly demonstrable. Ultimately, the decision was made to focus on a maximum of eight-stage compression.

The next consideration was the amount of recycled cold that could be utilised by the liquefier. Obviously, this is an important consideration for the efficiency of the liquefier. The amount of cold that can be utilised is dependent on the pressure, temperature, and mass flow rate of air following heat exchanger 3, and the amount of cold recycle available based on the relevant

discharge pressure. These variables can all be controlled, with varying effectiveness, by the diversion ratios to the hot and cold turbines, x_1 and x_2.

The cold store size and loop mass flow rate for each candidate discharge pressure using the relevant value of specific cold recycle was set via equations (5-4) and (5-5) respectively. Recapped from section 5.2.4:

$$L = 16\frac{CR_m}{320{,}000} \qquad (5\text{-}4)$$

$$\dot{m} = 185\frac{CR_m}{320{,}000} \qquad (5\text{-}5)$$

The relevant temperature profile from the results of section 5.2.4 was also used as an initial parameter for the initial condition of the gravel bed and cold recycle loop mass flow rates, which were both set via table data based on the length of the cold store using the same tables that set the compressor and turbine efficiencies in sections 3.2.6 and 3.2.7 respectively. Parameter sweeps were performed on mass flow rate initially, using a 0.1 bypass ratio for both x_1 and x_2. Of the yielded results, those for which the temperature of the air returning to the cold store in the cold recycle loop was outside 5% of the expected temperature were discarded. Similarly, results for which the liquid yield mass flow rate was less than 100 kg/s were discarded. Withing the remaining results, fine adjustments were made to both the supply mass flow rate and the bypass ratios, via further parameter sweeps, to determine parameters for which the desired cold recycle loop return temperature and the liquid yield target of 101 kg/s were achieved.

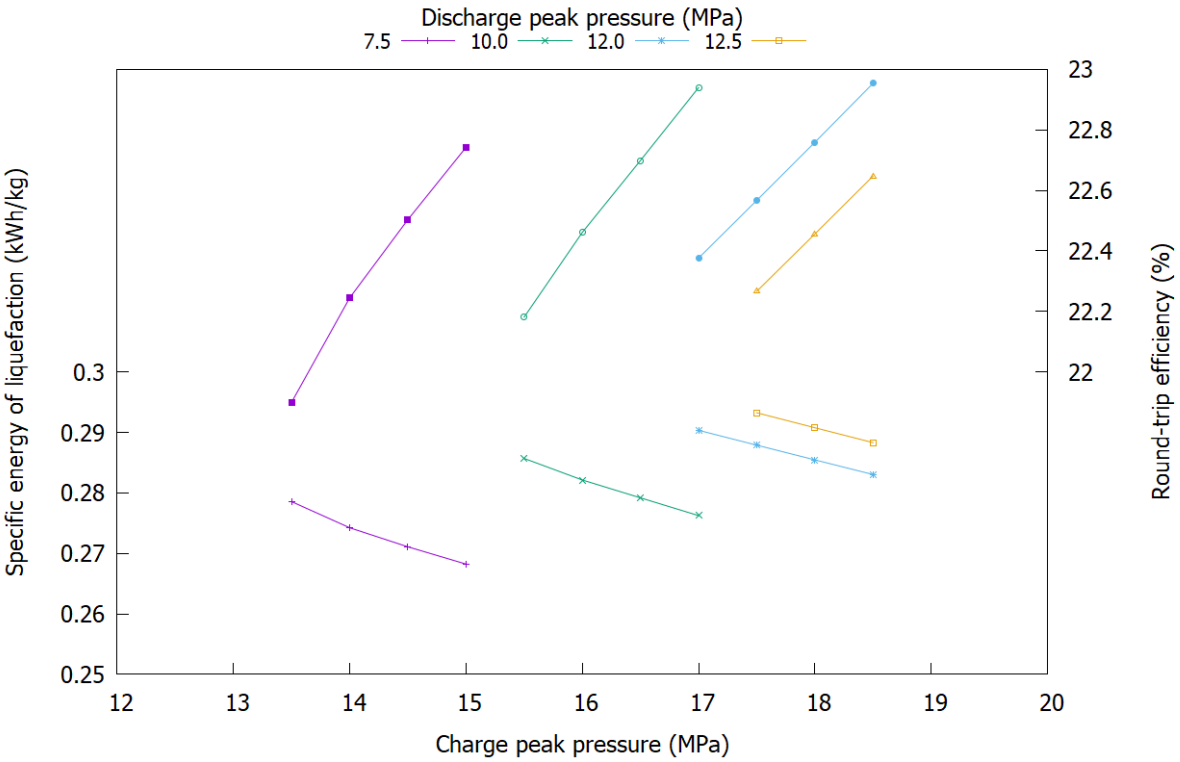

Figure 5-30: specific energy of liquefaction and round-trip efficiency depending on charge and discharge peak pressures (all results net of pumping energy costs)

The results of this process are shown in Figure 5-30. The lower set of lines show the specific energy of liquefaction at the given peak charge pressure. Each line is for a given peak discharge pressure shown in the key. Note that, for brevity, discharge pressures are shown at intervals of 2.5 MPa, along with the optimal peak pressure of 12 MPa. The specific energy cost of liquefaction increases with the discharge pressure, due to the lower specific cold recycle available at these higher discharge pressures as shown in Figure 5-20.

The discontinuity in the results data is important. The lines cover only a small portion of the pressure range used for modelling. This is due to the criteria set on modelling results and the requirement for both mass balance in terms of the liquid yield flow rate, and energy balance in terms of the return temperature of the cold store loop. To the left of each line, the temperature of the air returning to the cold store was too low, meaning that the cold store would not be at a sufficiently high temperature during the following discharge cycle to effectively capture the available cold from the air being discharged. To the right of each line, the air stream was able to effectively capture the available cold from the cold store loop, but the system could not achieve sufficiently high liquid yields to ensure mass balance from charge to discharge.

From the lower set of lines in Figure 5-30, it appears that lower discharge pressures are preferable from the perspective of the charge cycle, due to the greater availability of cold

recycle lowering the specific energy of liquefaction for the system. In the context of LAES however, this is only half of the story. The upper set of lines in the figure show the round-trip efficiency of the system when the increased specific energy yield of the discharge system available at higher pressures is considered. These lines show that the optimal peak discharge pressure occurs at 12 MPa, with the optimal peak charge pressure occurring at 18.5 MPa. It is important to note that these results are all based on discharge mass flow rates of 100 kg/s, which section 5.2.3 shows is very much sub-optimal.

5.2.6. Configurational plant design options

The final step of engineering modelling was to model different plant configurations to be taken forward for economic performance comparison, the subject of Chapter 6. The decision was made to simulate a total of four charge cycles (with 2, 4, 6 and 8-stage compression trains) and three discharge cycles (with 2, 3 and 4-stage expansion trains). These models were simulated in steady-state conditions to reduce the computational time, and to provide sufficient stream data to properly size the required components. The charge cycle is most affected by transient behaviour and, as such, the specific energy cost of liquefaction results were taken from section 5.2.5 to ensure that this behaviour was properly captured rather than using the steady-state data from this round of modelling.

Preliminary work (Wilson et al., 2020) showed that market conditions suitable for a positive NPV for a combined NPP and LAES plant favoured plants with a high discharge rate. This work is discussed in detail in section 6.1.2.With the conclusions of this work in mind, and the fact that there is an optimal discharge rate for a given peak discharge pressure, as shown in section 5.2.3, discharge cycles were modelled at their optimal mass flow rates.

Figure 5-31 shows the round-trip efficiencies of the 12 systems resulting from this round of modelling.

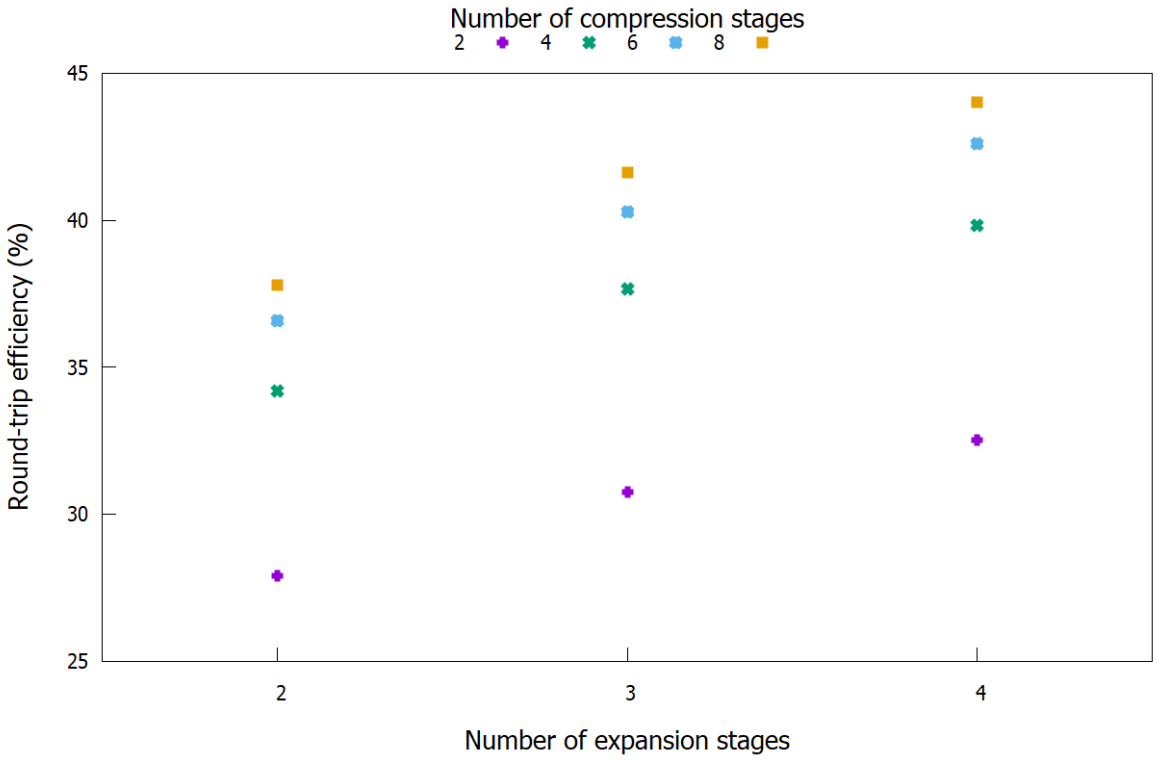

Figure 5-31: round-trip efficiencies of LAES storage systems depending on compression and expansion staging

Chapter 6 - Financially motivated plant design

6.1.1. Introduction

This section discusses the results of the financial modelling and how they influence the overall plant design. Section 6.1.2 discusses the preliminary work performed using an early version of both the engineering and the financial models. Despite some simplifications, there are some important results that were used as a basis of the detailed modelling discussed in the later sections. Section 6.1.3 details the comparison of the economic performance of the different system configurations within the financial model. From these results, a final configuration was taken forward for further modelling. Section 6.1.4 studies the market conditions required for the plant to become profitable.

All results in this chapter are expressed in the form of box-and-whisker plots. These plots are useful for displaying statistical measures of large sets of values that have been output by a model. They consist of two parts: the box and the whisker. The box's upper and lower limits are located at the respective upper and lower quartiles of the dataset. The central bar of the box is located at the mean of the dataset. In this study, the whiskers have been used to show the 10^{th} and 90^{th} percentiles of the data. This is important to note, as the whiskers would typically show the minimum and maximum of the dataset, however in this case, this caused difficulty in scaling plots sufficiently well to present the results clearly.

6.1.2. Preliminary work

Work as part of this project that has been previously published as a peer-reviewed working paper (Wilson et al., 2020) by the Energy Policy Research Group at Cambridge University provides important insights that serve as a starting point for the work in this thesis. This early work was based on early versions of both the engineering and the financial model, both of which had some important differences to the final versions. These are discussed in the following paragraphs.

The early engineering model results assumed a continuous isentropic efficiency for the NPP's steam turbine, meaning that power dropped off linearly, in contrast to the most recent modelling discussed in section 5.2.1. For this reason, the power yield from the discharge system increased linearly with mass flow rate and resulted in a higher overall power output for a given staging configuration and peak pressure. This meant that the resulting specific energy yield and round-trip efficiency of the system was significantly higher than the results discussed in Chapter 5.

Unlike the model described in section 0, the early financial model made no provisions for arbitrage. Any electricity used by the LAES plant while charging the system was assumed to be purchased from the NPP (or to simply reduce the NPP's overall power output), meaning that its cost was always defined by whatever the strike price happened to be for the year in question. Whilst a minor simplification, this meant that varying the charge-side mass flow rate had no effect on the profitability, or otherwise, of the proposed plant design.

The calculation of plant equipment costs used the scaling equation shown in section 2.7.

$$C(A) = C(B)\left(\frac{S(A)}{S(B)}\right)^{X} \qquad (6\text{-}1)$$

The base equipment costs used were the somewhat dated costs taken from the literature (Peters et al., 1968) and adjusted to 2018 prices using CEPCI data. This CEPCI data was collected from the same set of sources (Vatavuk, 2015, 2010, 2008) as that discussed in section 2.7. Using these prices, shown in Table 6-1, resulted in a tendency to underestimate plant capital investment, making the proposed plant appear more attractive than it actually was.

Equipment	Size for comparison	Unit for comparison	Cost for comparison	Year for comparison	CEPCI Price index	2018 Equivalent	Comparison exponent (X)
Turbine	10	MW	£2,000,000	2017	535.3	£2,079,955	0.60
Cryoturbine	745	kW	£113,250	1990	392.2	£160,750	0.69
Water pump	50	kW	£8,500	1990	392.2	£12,065	0.33
Cryo pump	50	kW	£15,000	2014	576.1	£14,495	0.60
H/X - 2 MPa	140	m^2	£107,000	1990	392.2	£151,879	0.44
H/X - 3 MPa	140	m^2	£134,000	1990	392.2	£190,203	0.44
H/X - 7 MPa	140	m^2	£160,000	1990	392.2	£227,109	0.44
H/X - 10 MPa	140	m^2	£202,500	1990	392.2	£287,434	0.44
H/X - 20 MPa	140	m^2	£253,200	1990	392.2	£359,399	0.44
Air tank	400	tonnes	£83,500	1990	392.2	£118,522	0.57

Table 6-1: Equipment cost data for comparison, 2018 equivalent prices and exponents for comparison

Despite these simplifications, the early work provides some important results that are a valuable starting point for the financial modelling discussed herein and will be recapped in this section. The initial uncertain parameters used for the financial model are shown in Table 6-2. As shown in the table, two pricing scenarios were considered: 'high spot market pricing' and 'extreme spot market pricing'.

PERT distribution parameters	FOAK scenario			NOAK scenario		
	Minimum	Most likely	Maximum	Minimum	Most likely	Maximum
NPP spending factor	1	1.7	2	1	1.1	1.3

Binomial distribution parameters	FOAK scenario			NOAK scenario		
	n	p	shift	n	p	shift
NPP construction time – mobilisation	1	0.6	2	0	0.4	2
NPP construction time – critical path	2	0.6	3	1	0.4	3
LAES construction time – mobilisation	1	0.6	1	1	0.2	1
LAES construction time – critical path	1	0.6	1	1	0.4	1

BetaGeneral distribution parameters	α_1	α_2	Minimum /£m	Maximum /£m
CES configuration 1 (slow discharge)	9.8763	16.457	20.9	23.3
CES configuration 2 (moderate discharge)	7.7810	13.202	44.5	51.9
CES configuration 3 (rapid discharge)	10.949	21.242	66.3	80.0

Electricity price amplitudes (NOAK scenario)	Q1	Q2	Q3	Q4
Amplitude factor $\alpha(Q)$	2	2	2	2

ARMA time series parameters	Mean	Volatility	Auto-regressive coefficient	Moving average coefficient
$A(D)$ high spot market pricing	115	8	0.8	-0.2
$A(D)$ extreme spot market pricing	150	8	0.8	-0.2

First order MA parameters	Mean	Volatility	Moving average coefficient	Initial error term
Half-hourly error value ($\varepsilon(P)$)	0	0.12	0.6	0
Consumer Price Index (CPI)	0.225	0.002	0.823	0

Table 6-2: Financial model initial uncertain probability distribution parameters and time series parameters

The plant model used an 8-compressor 4-turbine design and the plant charge/discharge configuration is shown in Table 6-3. The study tested four configurations, the first of which, configuration 0, was a baseload NPP without LAES. The remaining configurations all included LAES systems that discharged and charged over a single half-hour period. The systems in the preliminary work had a round-trip efficiency of 53%, significantly higher than those detailed in Chapter 5, due to the reasons discussed above.

Configuration	0	P1	P2	P3
Charge power (MW)	0	50	50	50
Charge flow rate (tonnes/h)	0	222	222	222
Discharge power (MW)	0	30	150	300
Discharge flow rate (tonnes/h)	0	241.2	1,206	2,412
Storage capacity (tonnes)	0	120.6	603	1,206

Table 6-3: Plant design charge/discharge parameters

The starting point for modelling in both the FOAK and NOAK scenarios was to determine the minimum CfD price that would ensure that the NPP-only plant has a positive NPV in every model iteration. This was considered central to the viability of the project, since NPP financial security is likely to be a major barrier to new build construction. FOAK scenarios required an initial CfD price of £75/MWh or higher for this to be the case. NOAK scenarios required significantly smaller CfD prices of £55/MWh to ensure a positive return on project investment.

The hybrid NPP-LAES plant was then tested for the FOAK scenario. These configurations only became more profitable than NPP-only configurations for extremely high values of mean daily average $A(D)$, in excess of £230/MWh, and with amplitude values of $\alpha(Q) = 3$ for all quarters. The idea of spot market prices reaching this level and a new build NPP plant being able to attract a CfD price of only a third this value seemed unlikely and, as a result, the FOAK scenario was abandoned for the time being.

The FOAK results, whilst not particularly interesting in themselves, go a long way to highlighting the crux of the problem with the preliminary financial model. As discussed above, the power used to charge the LAES plant was always considered to come from the NPP, and as such, always came at whatever CfD price the NPP was being paid. This, given the round-trip efficiency of the plant being just in excess of 50%, meant that the spot market price had to be double the CfD price before the model would allow the system to discharge.

This threshold price for discharging likely had another important effect given the nature of the model construction. Since both the CfD price and the value of $\mu_{A(D)}$ are indexed to the same value of CPI, they will rise in concert. As a result, the threshold price for discharging, being double the CfD price, will rise at a faster rate than the value of $\mu_{A(D)}$. As a result, the likelihood of the plant being able to discharge will lessen over the course of the model. Unfortunately, the preliminary financial model did not track this information.

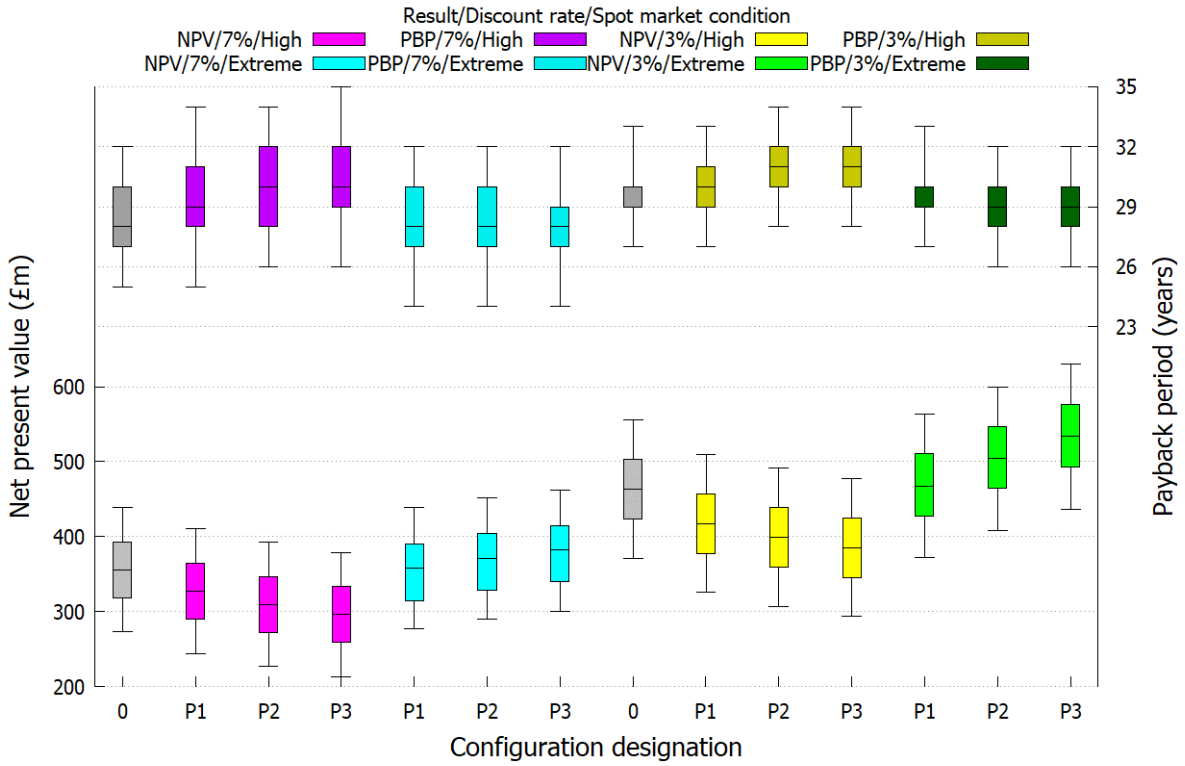

Figure 6-1: Preliminary financial modelling results (NOAK scenario)

The results of the preliminary financial modelling for the NOAK scenario are shown in Figure 6-1. Considering the 'high spot market pricing' first (the purple and yellow bars), these results demonstrate that the construction of a hybrid NPP-LAES plant is an extremely unattractive proposition. In fact, as can be seen from the lower set of bars, moving from right to left, NPV improves as the plant size tends to zero, but always remains lower than that of the NPP-only configuration 0. Similarly, the upper set of bars shows that payback period increases as the plant size increases, and that payback period is always longer for the plants where LAES is included. A smaller discount rate improves plant profitability in all cases, but the overall conclusion remains the same; including LAES in the plant design is detrimental to plant profitability in all cases.

In the 'extreme spot market pricing' (the cyan and green bars), the spot market pricing is sufficient for the LAES to become profitable and start paying for itself. Once spot market prices reach this threshold, the LAES becomes increasingly profitable as plant size rises, shown by the bars appearing higher moving from left to right. It should be noted that the plant configurations in Table 6-3 provide storage such that the plant is fully discharged in a single half-hour period. This was a key system parameter for testing in the early stages of financial modelling, and this demonstrated that, in all cases, this was preferable to having larger storage capacity and allowed the plant to capitalise on the highest electricity prices. This is potentially

due to the constraint the model places that the plant must be charged or discharged continuously, as shown in section 4.5.3; the plant would be unable to stop discharging if the instantaneous price fell below the discharge threshold price if the tank was not already empty.

6.1.3. Plant compression and expansion staging

As seen in section 5.2, charge compression staging and discharge expansion staging have significant effects on the overall efficiency of the plant. Given this information, determining the effect of these design choices on project NPV was the starting point for this round of financial modelling.

As discussed in section 6.1.2, the combined NPP-LAES performed best when the discharge rate was large and discharged the entirety of its store air in a single half-hour period. As a result, this was the starting point for this second round of modelling. Plant discharge rates were chosen such that they coincided with the peak discharge rates discussed in section 5.2.3. The plant designs modelled 2, 4, 6 and 8-stage compression and 2, 3 and 4-stage expansion, resulting in a total of 12 possible staging options for each of the two liquefier configurations considered. The full-plant cycles were modelled for each of these configurations and the components sized in a cost estimation spreadsheet using the equations summarised in section 4.3.1. The same spreadsheet includes the PERT distributions described in section 4.3.2 and uses these in a 100,000-iteration @RISK simulation that results in a distribution of overall plant cost. A BetaGeneral function was then fit to the resultant distribution and used for the LAES cost input into the financial model simulation.

Power ratings for pumps, turbines and compressors were taken directly from the engineering model simulation results. Tanks and cold stores were sized according to the requirements of the given configuration. Single-phase heat exchangers were sized according to the relationship:

$$A = \frac{\dot{Q}}{\gamma \, \Delta T_{LM}} \qquad (6\text{-}2)$$

where $\dot{Q}$ is the heat load in W, γ is the heat transfer coefficient in W/m^{2}K and ΔT_{LM} is the logarithmic mean temperature difference across the heat exchanger calculated by:

$$\Delta T_{LM} = \frac{\Delta T_{\text{hot}} - \Delta T_{\text{cold}}}{\ln \Delta T_{\text{hot}} - \ln \Delta T_{\text{cold}}} \qquad (6\text{-}3)$$

where ΔT_{hot} is the temperature difference between the two streams at the hot end of the heat exchanger and ΔT_{cold} is the temperature difference between the two streams at the cold end of the heat exchanger.

Heat exchangers in which one or both of the fluids exhibited a phase change cannot be sized using equation (6-3) due to the phase change and were hence modelled in isolated models using mass flow sources, pressure sinks and heat exchanger models. The relevant stream data parameters were set using the data from the plant model and the heat exchanger size was reduced progressively until it was at the smallest size for which it could maintain its required heat transfer rate.

Model inputs for the market conditions and other top-level parameters are shown in Table 6-4. The remaining parameters for spending factors, construction times, and time series controls are identical to those shown in Table 6-2. As can be seen in Table 6-4, for the sake of comparing plant configurations, the model assumes a sustained high daily average electricity price and a high amplitude of price fluctuations for the duration of the model. The table also shows the key difference between the A and B simulation sets; a low daily average price is assumed for the A simulations whilst a high price is assumed for the B.

Parameter	**Value**
NPP plant base capital cost (£m)	1,050
Starting CfD price (£/MWh)	55
Plant costs spent during mobilisation	30%
Annual fixed NPP O&M costs (£m)	30
NPP refuel costs (£m)	10
Annual fixed LAES O&M costs as a fraction of plant cost	1.5%
NPP fuel load duration (days)	500
NPP time to refuel (days)	10
Charge window start time	00:30:00
Charge window end time	06:00:00
Discharge window start time	17:30:00
Discharge window end time	23:30:00
Day average $\mu_{A(D)}$, all years, A simulations (£/MWh)	100
Day average $\mu_{A(D)}$, all years, B simulations (£/MWh)	220
Amplitude factor $\alpha(Q)$, all quarters, all years	2

Table 6-4: Model market parameters for A/B simulations investigating the effect of compression/expansion staging

Model parameter inputs for the LAES plant are shown in Table 6-5. The leftmost section of the table shows the simulation designation. Each round of simulations is given an identical letter designation and the simulations in that round are numbered separately in order of increasing number of compression stages, then in order of increasing number of turbine stages. The next section to the right shows the LAES plant characteristics for that simulation including charge

and discharge power ratings. It is important to note that the discharge power is shown as the net power, that is the losses resulting from ramping down the NPP secondary loop are factored in. The next section shows the overall contribution of each subsystem to the overall plant cost:

- charge considers all of the heat exchangers and compressors used in the charge cycle but not the heat exchange with the cold recycle system,
- discharge considers all of the heat exchangers, pumps and turbines used in the discharge cycle but not the heat exchange with the cold recycle system,
- cold recycle cost includes the cold store itself, the pumps and the associated heat exchangers,
- storage cost considers only the air storage tank.

The rightmost section defines the model parameters for the BetaGeneral probability distribution used to model plant cost for each iteration.

Sim #	Compression stages	Expansion stages	Charge power (kW)	Discharge power (kW)	Round trip efficiency	Charge cost	Discharge cost	Cold recycle cost	Storage cost	a_1	a_2	Minimum (£m)	Maximum (£m)
1	2	2	145,179	405,270	27.9%	25.8%	59.3%	9.3%	5.6%	10.398	19.143	101.3	124.5
2	2	3	127,350	391,500	30.7%	23.8%	61.6%	9.2%	5.5%	9.3579	16.216	103.1	125.1
3	2	4	122,256	397,440	32.5%	22.4%	63.5%	8.8%	5.3%	9.4947	17.165	107.3	130.6
4	4	2	118,503	405,270	34.2%	28.5%	57.1%	9.0%	5.4%	9.2377	16.207	105.5	127.9
5	4	3	103,950	391,500	37.7%	26.4%	59.5%	8.8%	5.3%	9.7422	17.77	106.7	130.5
6	4	4	99,792	397,440	39.8%	24.9%	61.5%	8.5%	5.1%	9.01	16.015	111.0	134.4
7	6	2	110,808	405,270	36.6%	30.9%	55.3%	8.7%	5.2%	10.507	19.31	108.6	133.8
8	6	3	97,200	391,500	40.3%	29%	58%	9%	5%	9.5496	17.249	110.1	134.2
9	6	4	93,312	397,440	42.6%	27%	60%	8%	5%	10.851	21.03	113.6	141.0
10	8	2	107,217	405,270	37.8%	33%	54%	8%	5%	10.377	19.066	112.1	137.8
11	8	3	94,050	391,500	41.6%	31%	56%	8%	5%	9.9871	17.527	113.0	137.9
12	8	4	90,288	397,440	44.0%	29%	58%	8%	5%	10.566	20.266	116.8	144.5

Table 6-5: Model LAES parameters for A and B simulations investigating the effect of compression/expansion staging

Table 6-5 shows the financial model input parameters for the 'A' and 'B' simulations of the financial model. These simulations consider the varying the number of compression and expansion stages. It is important to note here that overall efficiency does not necessarily increase according to the number of stages; the charge compression staging appears to have a greater overall contribution to the plant's efficiency than the discharge expansion staging. All simulations were performed according to the parameters in Table 6-4.

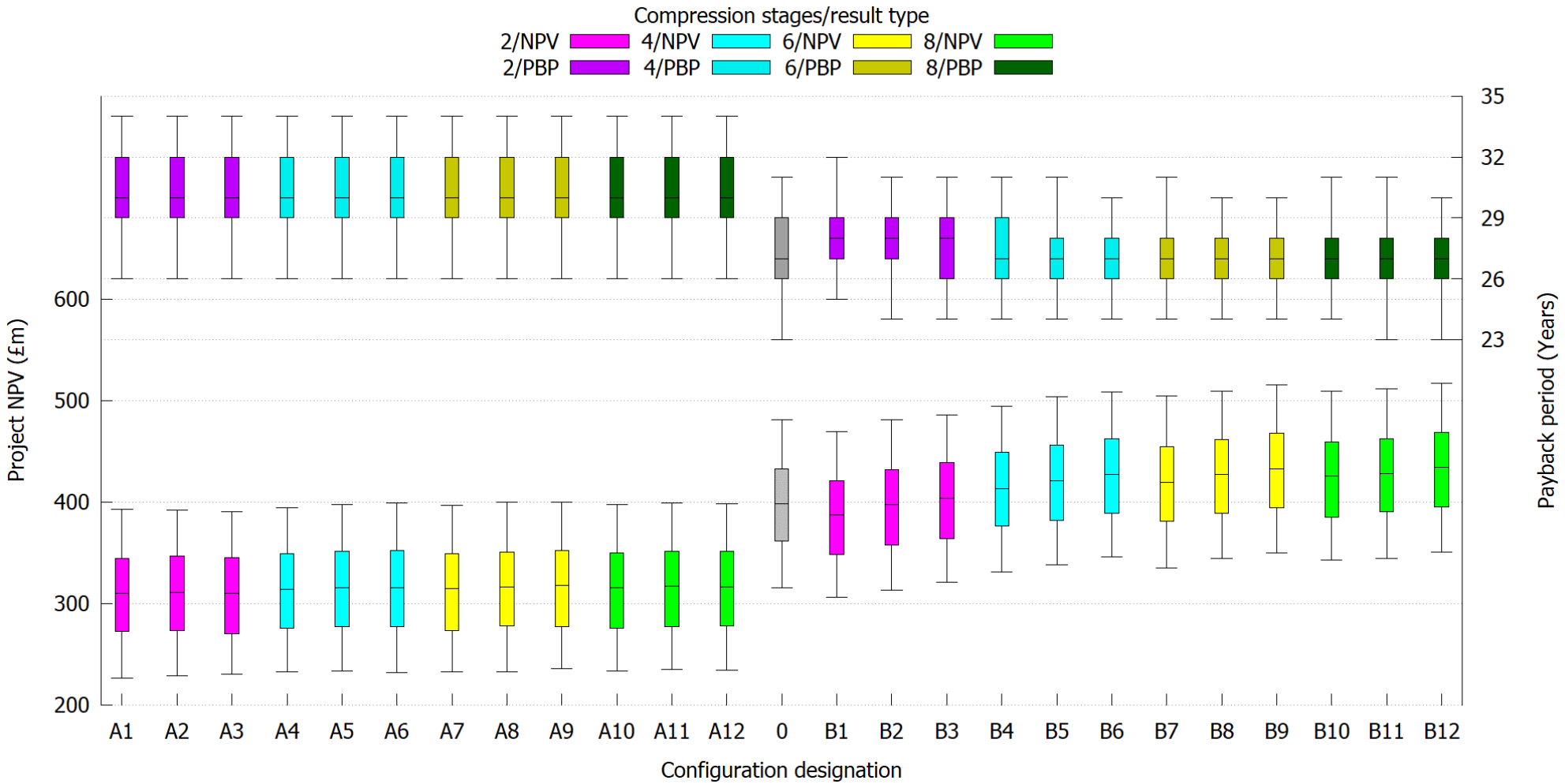

Figure 6-2: A/B simulation results for NOAK scenario

Figure 6-2 shows the results for the A and B simulations for the combined NPP-LAES plant. The A results are, without question, unfavourable to the proposition of the hybrid plant. They show that, under any configuration, the hybrid plant performs extremely poorly. All NPV results are lower than those for an NPV-only configuration, and all payback period results are longer. Interestingly, the difference between results is almost imperceptible, with a very small improvement in more efficient plants. This is an interesting effect of the hybrid plant; the profitability of the NPP is essentially driving the NPV and reducing the losses made by the LAES plant. It is important to note that this is in contrast to the preliminary results in section 6.1.2, whose economic performance worsened with increasing plant cost due to the fact that round-trip efficiency was fixed for all configurations in that work. Here, the round-trip efficiency is not fixed and the difference in results, whilst small, is apparent.

The B results are more favourable. All configurations with LAES perform better than the NPV-only configuration. It is apparent that increasing efficiency, via increasing the number of turbine and expansion stages, improves the economic performance of the plant in all cases. It is important to note that the results also show that improving performance is not solely related to plant output power, as was the conclusion from the preliminary work discussed in section 6.1.2. It is important to bear in mind, however, that this work did not consider designs whose efficiency differed. The effect of efficiency can be most clearly seen when comparing the 2-turbine discharge results with those of the 3- and 4-turbine systems. Despite the fact that the 2-turbine systems power output is significantly higher (by virtue of its peak performance discussed in section 5.2.3), their performance is notably worse due to the decline in round-trip efficiency.

The B results also show an effect of diminishing returns when increasing system efficiency. Increasing the number of compression stages from 2 to 4 offers significant improvement in economic performance but increasing further offers only small benefits. This is a result of the scaling equations used in the plant cost estimation; the nature of these equations favours the cost of large equipment compared to small equipment, so increasing the number of stages also significantly increases the cost of equipment of an equal power rating. Surprisingly, this effect is not apparent when comparing the 2-, 3- and 4-turbine results, despite the fact that not only do the equipment scaling equations favour larger pieces of equipment, but also the fact that the discharge system comprises a much larger part of the overall plant cost, as seen in Table 6-5. This lends credence to the hypothesis that hybrid plant efficiency and overall output power are both important drivers of plant economic performance.

The overarching conclusion of this section is then that the most efficient 4-turbine, 8-compressor LAES plant design offers the best chance of hybrid plant profitability, but that, much as the preliminary results have shown, very high spot market pricing is required for profitability. With this in mind, configuration 12 from table Table 6-5 was taken forward for additional modelling, with the intention of studying exactly how high market pricing had to be, and for how long it needed to be sustained.

6.1.4. Market conditions

The final set of simulations all used LAES configuration 12 from section 6.1.3 and were aimed at determining the threshold market conditions for LAES plant profitability. The plant design model input parameters are recapped in Table 6-6. The market parameters are shown in Table 6-7. Much as was the case for the A simulations, these market conditions are assumed to run throughout the 30-year course of the model for these simulations. Table 6-7 shows that the value of $\mu_{A(D)}$ was varied and that for each value taken, the effect of the changing the value of $\alpha(Q)$ was investigated for three separate cases. From this point onward, all modelling is performed with the assumption of an NOAK scenario.

Parameter	**Value**
Charge power (kW)	90,288
Discharge power (kW)	397,440
Storage capacity (kWh)	198,720
α_1	10.566
α_2	20.266
Minimum (£m)	116.8
Maximum (£m)	144.5

Table 6-6: LAES parameters for C/D simulations investigating the effect of market conditions

Simulation	Day average $\mu_{A(D)}$	Amplitude factor $\alpha(Q)$
C1	190	2
C2	190	2.5
C3	190	3
C4	180	2
C5	180	2.5
C6	180	3
C7	170	2
C8	170	2.5
C9	170	3
C10	160	2
C11	160	2.5
C12	160	3
C13	150	2
C14	150	2.5
C15	150	3

Table 6-7: Market parameters for C simulations investigating the effect of market conditions

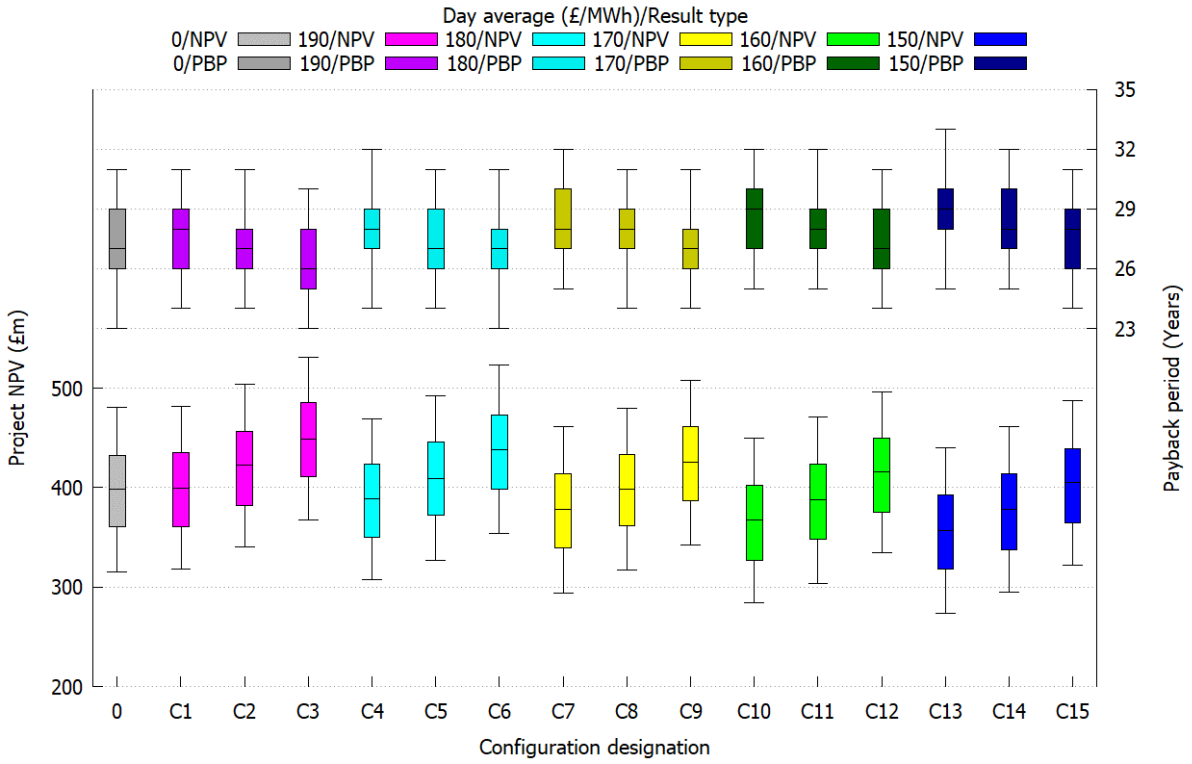

Figure 6-3: C simulation results for NOAK scenario

Figure 6-3 shows the simulation results for the C set of simulations. The groups of coloured bars are sets of results for the same day average price. Each new set from left to right represents a decline of £10/MWh in this price. The effect of this is clearly visible: with less revenue available when discharging the system, the NPV falls and the payback period rises.

Within each set the effect of varying the amplitude of the day profile curves can be seen. A larger amplitude results in a greater difference between the high and low electricity prices and thus an improved opportunity for arbitrage. This is shown by the rise in NPV and the fall in payback period from left to right within each set. This is particular shows the importance of considering arbitrage within the financial model. The increase in day profile shows a marked improvement in NPV by increasing the amplitude of the day curves by 50%.

It should be noted, however, that the value of $\mu_{A(D)}$ remains the more powerful driver of the output results. This can be seen when comparing C3 with C15, for example. This increase of around 25% in the value of $\mu_{A(D)}$ from C15 to C3 results in an improvement in mean NPV from £400m to £450m; around 12.5%. Comparing C13 with C15, for example shows that increasing the value of $\alpha(Q)$ by 50% improves the NPV by a similar amount. Clearly then, despite the additional opportunity greater arbitrage margins present, $\mu_{A(D)}$ remains a more important driver of NPV than $\alpha(Q)$.

DCF analysis is one that favours revenues early in a project's lifecycle to revenues generated later. The next set of simulations explore this effect by varying how long the high spot market prices are sustained. Figure 6-5 shows the input parameters for $\mu_{A(D)}$, whilst Figure 6-4 shows the input parameters for $\alpha(Q)$ for the D set of simulations.

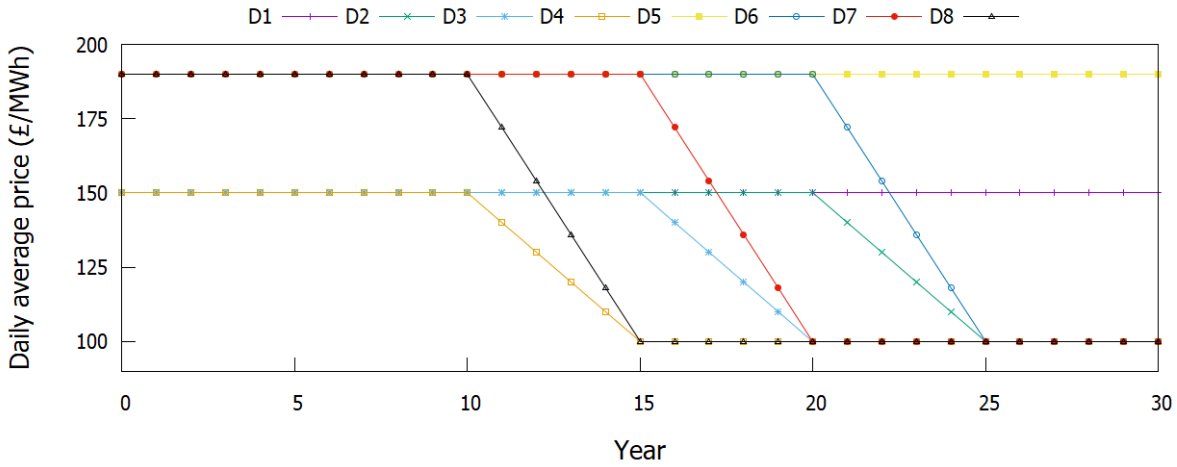

Figure 6-5: $\mu_{A(D)}$ values by year for D simulations

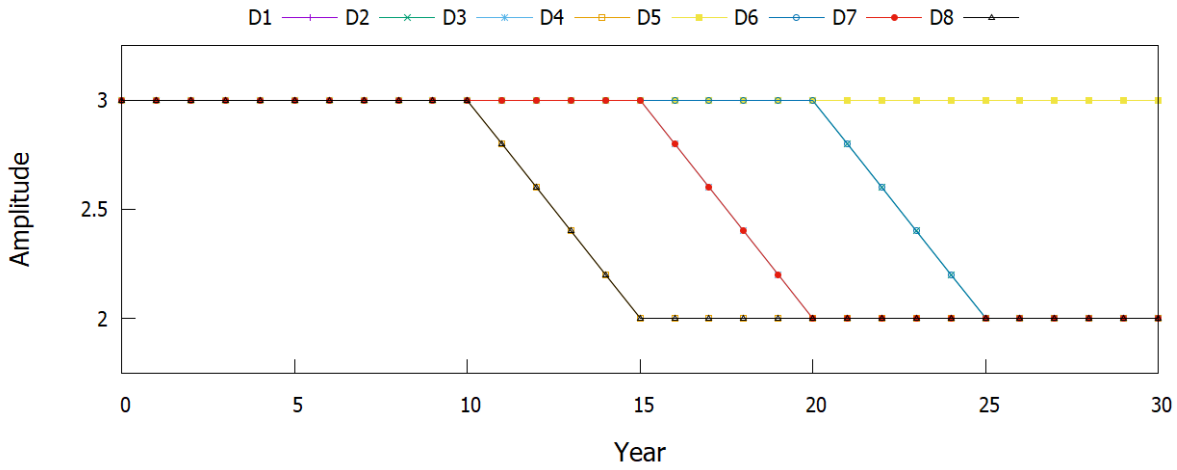

Figure 6-4: $\alpha(Q)$ values by year for D simulations

As the figures show, simulations D1-D4 begin with the same parameters as simulation C15 and simulations D5-D8 begin with the same parameters as simulation C3. For each of the sets of four, the first simulation is the same as the relevant C simulation, with prices remaining high throughout the duration of the simulation. For the remaining three in each set, the market parameters are curbed after a period of either 20, 15, and 10 years. The parameters are otherwise the same as the C set of simulations as shown in Table 6-6.

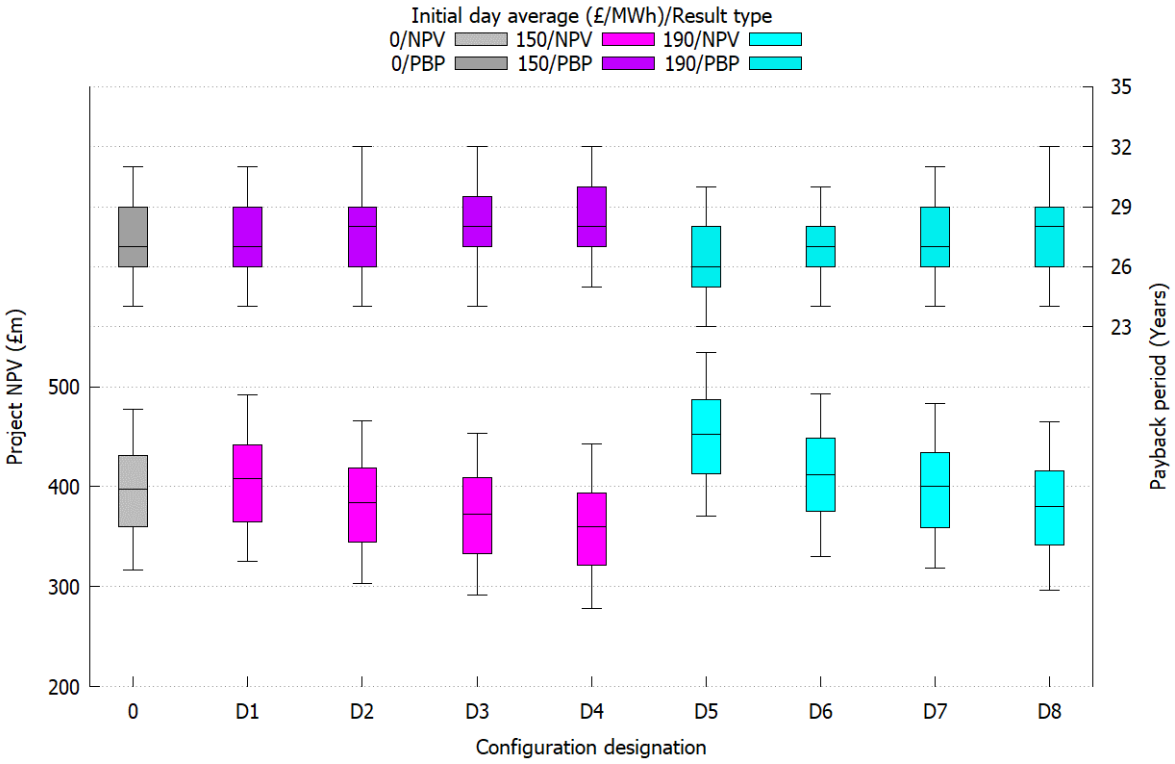

Figure 6-6: D simulation results for NOAK scenario

Figure 6-6 shows the simulation results for the D set of simulations. Neither set of results is particularly surprising; in both cases, NPV falls and payback period lengthens as the period for which high prices are sustained is shortened. Looking at the £150/MWh average price data first, the D1 simulation shows and NPV distribution that is slightly higher than the NPP-only result. This is consistent with the C set of simulation results, where £150/MWh was the threshold price above which the combined NPP and LAES plant would be profitable. As the duration for which this price is sustained is reduced below 20 years, the resultant NPV distribution falls below the NPP-only results and the payback period increases to longer than the NPP-only results.

The £190/MWh results are a little less damning to the prospect of a combined NPP and LAES plant. Simulation D7 shows that prices that are sustained for a period of at least 15 years are sufficient to bring NPV and PBP distributions to parity with the NPP-only scenario. This, however remains a long period for which extreme spot market pricing must prevail.

6.2. Summary and discussion

This chapter has discussed the published preliminary work (Wilson et al., 2020) as part of section 6.1.2. This work comprised the foundation of the bulk of the work in this thesis and helped to define the approximate parameter ranges of interest for further financial modelling. This preliminary work has two fundamental conclusions. Firstly, large capacity LAES plants

that discharge their entire inventory of liquid air in a single period perform better economically than any other scale of combined LAES and NPP plants. Secondly, spot market parameters must be pushed into ranges that are without doubt extreme in order for such plants to become preferable to NPP-only scenarios.

The remaining data analysis in this chapter can be split into two parts; plant configurational analyses in section 6.1.3 and market condition analyses in section 6.1.4. The plant configurational discussion is one of the cornerstones of this work and arguably its largest contribution to the field of techno-economic analyses. This is the only example, as far as this author is aware, where detailed engineering modelling has been performed in tandem with financial modelling allowing plant design decisions to be driven by market factors. The implications and applicability of this are important and are the subject of Chapter 7 and 0.

The results of the B simulations showed that the most complex (and most efficient) plant configuration boasted the most attractive NPV distribution, provided that spot market prices were sufficiently high for the hybrid plant to be preferable to the NPP-only plant. It is important not to read this as a direct endorsement of this technology, however; situations where $\mu_{A(D)}$ is £220/MWh are unheard of in the dataset to which the financial model was fit and would seem to be highly unlikely at best. The results of the A simulations were perhaps a little more surprising. With results less attractive than those of an NPP-only plant, the hybrid plant designs all perform equally poorly for the most part. This is a consequence of the guaranteed income from the NPP's CfD price providing something of an offset to the financial losses from the LAES part of the plant.

Finally, the C and D simulations sought to determine threshold market prices above which the hybrid plant would be profitable. The C simulations showed that a $\mu_{A(D)}$ value of £190/MWh was sufficient to ensure profitability at $\alpha(Q)$ amplitudes of 2 or greater, comparable to at least some of the historical dataset. Where $\mu_{A(D)}$ was reduced to £150/MWh, more extreme $\alpha(Q)$ amplitudes of at least 3 are required to ensure profitability, these being well in excess of any seen in the historical dataset. The D simulations showed that, at the lower prices of £150/MWh, prices had to be maintained for the full 30-year duration of the model to prevent the hybrid plant results falling below those of the NPP-only plant. For the £190/MWh results, periods of 15 years or more were sufficient to bring NPV distributions into line with those for the NPP-only configuration.

In summation, the results of financial modelling would appear particularly critical of the proposed hybrid plant. Without pushing financial modelling parameters to the extreme and

having these extreme prices sustained for long periods, the case for the hybrid plant is always weaker than the NPP-only proposition. The fundamental conclusion of this chapter must then be that without significant subsidy to guarantee favourable storage prices, and without having these prices guaranteed for a long period, the proposed plant would be impossible to justify to potential investors.

Chapter 7 - Project discussion

7.1. Introduction

This chapter discusses the successes and limitations of this work, as well as suggesting some additional work that might be useful as a follow-up to this project. It should, however, be noted at this stage that the results of Chapter 6 are particularly damning of the proposed system. The only results in which the system is profitable involve spot market prices well over double the market average price, and swings between high and low price more significant than any of those seen in the historical electricity price dataset used. The inescapable conclusion of this work is that coupling an LAES system to an NPP in the way proposed is, at best, an extremely weak proposition. It would be extremely difficult to persuade any investor to buy into this concept.

This is not to say that this application of the methodology is without value. As section 7.2 discusses, there are a number of practically useful conclusions that can be drawn from this study. Furthermore, the financial model itself, as well as the methodology in which it is used, could be applied to other asymmetrical ESSs, as well as to alternative design options for the LAES system. Section 7.3 discusses the limitations of the project, especially with regard to the design choices for the LAES plant and the approach to engineering modelling. It notes that whilst there is some room for potential improvements in the liquefier design in particular, these are unlikely to make the overall conclusions of this work any less problematic for proponents of the proposed system. In closing, section 7.4 proposes potential follow-up work for this project.

7.2. Project successes

This project has demonstrated difficulties associated with coupling an NPP to and LAES system. As section 5.2.3 concludes, the optimal LAES system discharge rate is set by the maximum diversion ratio of steam from the NPP. This is an inherent limitation on the system and presents something of a hurdle to the practical applicability of such a system. LAES is a highly flexible system, especially with regard to the decoupling of the charge and discharge rates. Coupling it to an NPP either locks the system into a given discharge rate or means running the system at sub-optimal conditions. This is an important result for design engineers and one not considered in either the existing literature on the subject (Li et al., 2014) or the preliminary work for this study (Wilson et al., 2020). These novel conclusions have arisen as a consequence of a more detailed engineering modelling approach with fewer simplifying assumptions. The

consideration of reduced efficiency for off-design steam turbine operation as discussed in section 5.2.1 was a key contributor to these conclusions.

Perhaps the most attractive reason for coupling LAES to an NPP is the ability to use low-grade heat from the condenser. As section 5.2.3 notes, only some of the available heat is used by the LAES plant. Only using condenser heat is arguably a more sensible option than using a combination of condenser heat and NPP secondary loop steam. If the LAES concept of warm recycle can be proven, the use of condenser heat might provide a means of bridging the temperature gap between the vaporised air leaving the cold store heat exchange system and it being superheated by the recycled heat of compression. Such a system might, however, turn the conclusions of this project on their head. As (Morgan et al., 2015a) notes, increasing the number of compression stages reduces the temperature of compressed air leaving each compressor. This in turn results in a lower peak warm recycle temperature and a lower temperature inlet temperature during the discharge cycle. Thus, the results of section 6.1.3 might well no longer be valid in this context, and the preference might be for a system with fewer compression stages.

There are additional drawbacks to coupled LAES and NPP systems associated with the ramping rates possible with steam turbines. Several of the studies discussed in section 2.5.3 assumes the plant operators are able to garner additional revenue from ancillary service payments associated with the provision for STOR services to the UK grid. Doing so, however, requires the systems to be able to ramp quickly; something not possible with steam turbines as section 2.3 notes. It may transpire that this is a key characteristic of ESSs in the future and that this presents an additional barrier to coupling LAES and NPP plants.

The financial model itself, and the methodology used for market-led system design are arguably the crowning achievement of this thesis and the ones with the greatest applicability to other systems. With some minor modification, the financial model could be used to simulate any asymmetric ESS within spot markets. It contains many features that such modelling would require; a means of tracking current stored energy, a means of making decisions as to whether to charge, discharge or hold the system, and a means to analyse different market scenarios.

LCOS (Tafone et al., 2020) is a useful metric that was introduced at around the same time that this work was started. This author was not aware of it until late in the project and as such, the modelling approach does not include calculation of LCOS. With some additional capture of data in the financial model, this is potentially a metric that could be calculated, however. The period-by-period approach this model takes to electricity sales potentially offers a number of advantages over the LCOS approach, as is discussed in the following paragraphs.

Firstly, the model tracks the ongoing mass of liquid air stored over the duration of the model and simulates a real-world plant bidding into the spot market. With LCOS, the number of charge/discharge cycles the plant achieves is a model assumption and input parameter; here it is one of the model outputs. This gives designers the opportunity to understand expected cycling requirements of the system under different market conditions at the design stage.

Secondly, the model in this study allows designers to test a variety of market scenarios, as section 6.1.4 attempts to do. Again, this is in contrast to LCOS, which outputs a required average electricity price necessary for a storage plant to break even; here the market conditions are a model parameter. Whether one is more useful over the other is contentious, however there is arguably significant value in designers being able to determine not only what kind of market conditions would be conducive to plant profitability, but how long these need to last for a system to remain viable. Whilst the model does not consider a subsidy incentive for operating the LAES plant, this modelling could potentially be used to determine how long such a subsidy would need to be guaranteed for; something which LCOS cannot.

One of the biggest successes of the financial model is that, unlike the studies discussed in section 2.5.3, it is not reliant on perfect prediction of electricity prices. By contrast, the decision-making framework within the financial model only requires known information. That is, that plant operators would know what price was paid to charge the system and would be able to bid into the spot market in such a way that they could ensure system profitability. In reality, operators would have more recent electricity price data and would arguably have a significantly better understanding of potential market prices than the hypothetical operators in this study, allowing them to make better-informed decisions on how to operate the plant.

7.3. Project limitations

This thesis, like any that attempts to model real-world problems, is reliant on assumptions to simplify models and achieve objectives within the limited time available. Section 7.3.1 discusses the key assumptions in the approach to modelling and discusses them in turn. Section 7.3.2 discusses a potential size mismatch in the cold recycle system between the charge and discharge cycles and its implications for the results of the engineering model. Section 7.3.3 discusses additional systemic limitations in the thesis that are not the direct result of assumptions.

7.3.1. Modelling assumptions

The major assumptions made by both the engineering and by the financial model will be discussed here in detail and, where possible, attempts made to quantify their implications and highlight the ways the approach to modelling might be improved. This is by no means an exhaustive list but highlights the key assumptions made by the modelling approach.

Assumption: there is no conduction along the axis of the cold store.

During the early stages of the engineering modelling, the assumption was made that the conduction along the cold store was zero. The reasoning behind this was simple. The thermal cycling of the cold store is a complex thermodynamic system and, at the time, it was not known how long the LAES system would be standing by (the periods where the NPP operates at baseload). In fact, the financial modelling would later show that the plant would have to operate daily charge-discharge cycling in order to remain profitable. That is, the NPV becomes negative before the capacity factor for the LAES drops below 100%.

A more realistic duty cycle for the cold store is shown in Figure 7-1. The temperature states of the cold store are shown in ellipses at the corners of the diagram and the processes by which the cold store is heated or cooled are shown by the arrows. As seen in the figure, the cold store is heated during charge and cooled during discharge. Also important are the processes labelled hold. Between periods of charge and discharge, the cold store temperatures will approach

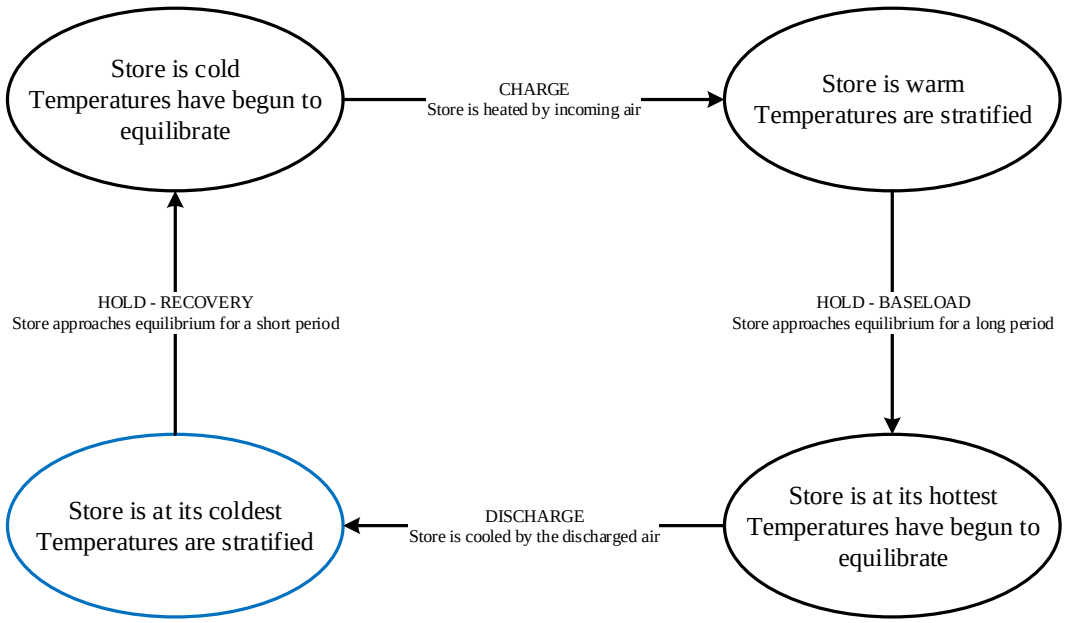

Figure 7-1: Expected duty cycle from the perspective of the cold store

equilibrium as conduction between volumes takes place. As discussed in section 5.2.6, the specific energy of liquefaction increases as the temperature of the cold store increases.

With the knowledge of the periods during which the system would be charged and discharged, attempts could be made to determine the effect of temperature equilibration over the holding periods between the charge and discharge cycles. This would likely have a more significant effect on the charging cycle, since the lowest temperature point in the cold store would not be as low as was assumed in section 5.2.2, meaning that the energy cost of liquefaction would be higher. The effect on the discharge cycle would also be non-negligible, with a lower peak temperature in the cold store meaning that cold capture from the discharge stream and the resulting specific cold recycle would be lower.

The model of the cold store itself, discussed in sections 3.2.8 and 3.2.9, is in fact capable of modelling axial conduction in the cold store. To reduce the complexity of modelling, the thermal conductivity coefficient of the gravel, κ, was set to zero when cycling the cold store. Armed with a greater understanding of the demands of plant profitability on system cycling, attempts could be made to investigate the effect of temperature equilibration in the cold store during the holding periods between charge and discharge.

Assumption: pressure drops in heat exchangers are proportional to inlet pressure.

This assumption is at the heart of the engineering model, and is one that is not without precedent; almost all of the engineering modelling studies discussed in section 2.5.2 make the same assumption, with the exception of those that omit pressure losses entirely. As with any model of a real-world system, there is a trade-off between prediction accuracy and modelling complexity. The system design in this study did not consider the detailed design of heat exchangers. Once the plant reached a detailed design stage, this would become a far more significant concern. The bulk of the liquefaction plant would comprise plate-and-fin heat exchangers, in which subtle changes in plate size, shape and orientation can have implications for heat transfer rates, flow regimes, and ultimately cost (Guo et al., 2018). Such detailed design work is beyond the scope of this study to allow for a more top-level study of system configurations. Furthermore, given the results of financial modelling, significant improvements in plant efficiency would be required to substantially improve profitability rather than the incremental improvements that would likely result from detailed heat exchanger design.

Assumption: the subsystems of the LAES plant can be safely modelled in isolation.

This is perhaps the most contentious assumption of the engineering model, not least because it contributed to the error in the cold recycle system discussed in more detail in section 7.3.2. This assumption was a product of necessity. The basis of the engineering model is discussed in Chapter 3 and its implementation in Chapter 5. In section 3.2.1, the finite volume flow models are discussed and the way these are built into heat exchanger models is discussed in section 3.2.4. Finite volume approaches to process modelling are inherently computationally intensive, and this is compounded when multiple heat exchangers are used in a single model. The approach taken to reduce computational load was to divide the overall plant model into separate components in order to simulate the distinct parts of the cycle in isolation.

The fundamental issue with this is the interconnection between the charge and discharge systems; the cold store. In order to accurately predict axial temperature profiles of the cold store at the beginning of the charge and discharge cycles, the cold store had to be simulated to a point of cyclic equilibrium. This process is discussed in section 5.2.4 and resulted in a series of temperature profiles for the cold store, as well as store sizes and loop mass flow rates, for a range of peak discharge pressures. These were then used as initial parameters when modelling the charge and discharge cycles of the final symmetrical plant design discussed in section 5.2.6.

The implications of doing this on the modelling of the discharge are not too severe. As section 5.2.6 shows, the air temperature following heat exchange with the cold store does fall during the discharge cycle, however there is sufficient low-grade heat available from the NPP condenser coolant to maintain a steady air stream temperature as it enters the expansion train. As a result, errors introduced here should not have an effect on discharge power ratings; these are primarily a function of the system flow rate and the utilisation of the NPP's steam.

Errors introduced in the charge cycle will, however, have a far more significant effect. The effectiveness of the liquefier is ultimately dependent on the thermodynamic state of the air as it enters the J-T valve. The lower the enthalpy at this point, the greater the liquid yield, and the lower the energy cost of liquefaction for a given pressure and mass flow rate. Since the cold store is the key source of refrigeration for the incoming airstream prior to the J-T valve, any errors introduced will have a significant effect on the energy cost of liquefaction, and hence the round-trip efficiency of the system as a whole. The implications of such errors are discussed in more detail in section 7.3.2.

As discussed, the decision to divide the LAES plant into subsystems for engineering modelling was born of necessity; a system this complex would require more computing power and a more sophisticated code to model in its entirety than this project had available. Ultimately, the

approach to modelling allowed some important insights into coupling LAES and NPP plants that would not otherwise have been possible. These include the steam diversion ratio optimising during discharge discussed in section 5.2.3, the results of the cold store cycling in section 5.2.4 and the results of the charge cycle modelling in section 5.2.5. All required detailed modelling that would have been too time consuming to perform without being able to model the respective systems in isolation.

Assumption: the number of finite volumes was sufficient for an accurate assessment of plant performance.

This is another contentious assumption made by the engineering modelling approach. Beyond 200 nodes, heat exchanger temperatures approached convergence, but cannot be said to have fully converged, even to the point of 500+ nodes being used. Once again, there is a trade-off here between computing time and accuracy that cannot be avoided without access to greater computing power. This can be seen in convergence testing performed on the cold store average

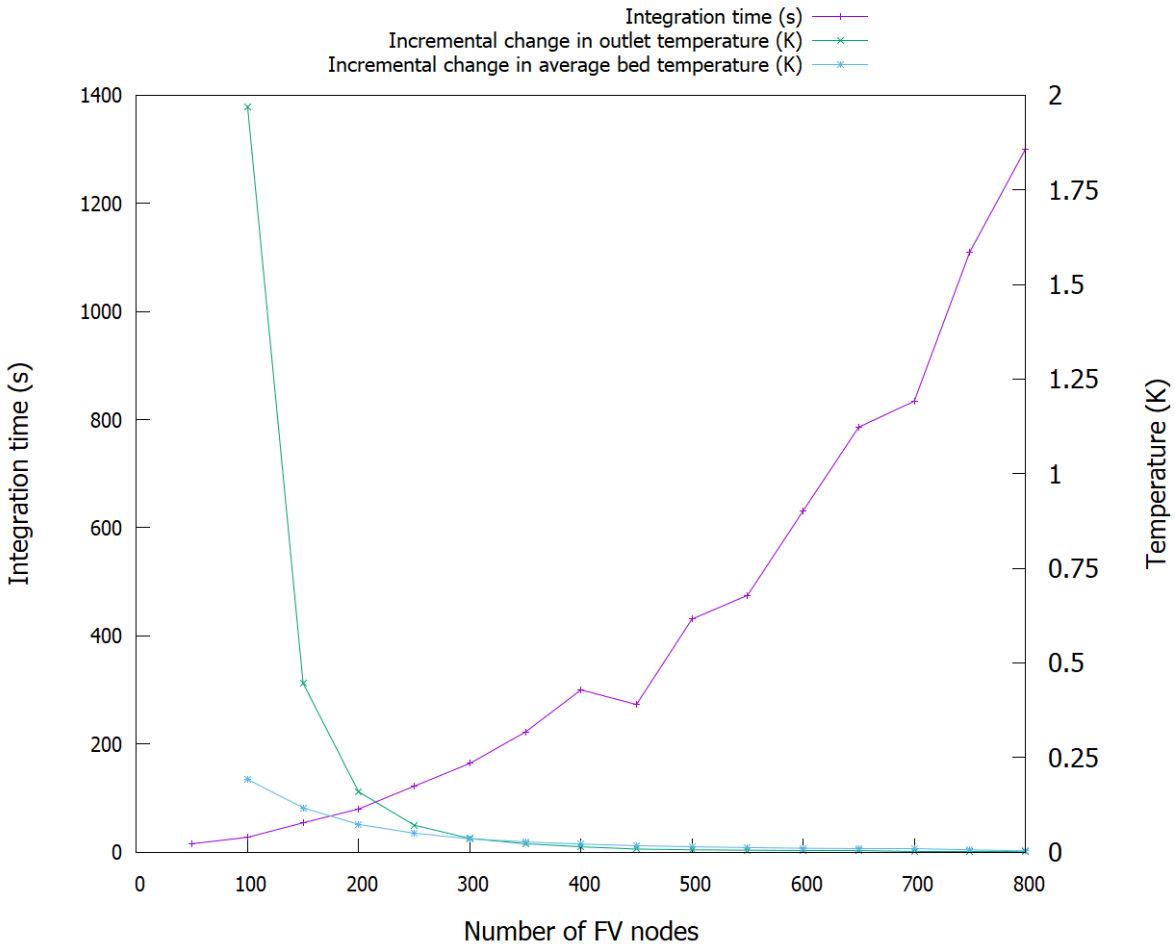

Figure 7-2: Convergence testing for the number of FV nodes

temperature and outlet temperature performed on the plant charge model results shown in section 5.2.2, Figure 5-9.

Figure 7-2 shows the convergence testing results based on increasing the number of FV nodes. The rising line shows the integration time for the simulation. Note that this does not include the initialisation time for the model. The falling lines show the incremental change in outlet temperature achieved by increasing the number of nodes. As the shows, incremental improvements to outlet temperature accuracy fall to less than a tenth of a Kelvin with 250 nodes or more used in the cold store's gravel bed. By contrast, the integration time for a single simulation increases exponentially as the number of nodes is increased. Interestingly, this increase is not continuous; presumably, a result of different computer operating conditions between model runs. Any time increases are compounded during both the initialisation and the results phases of the simulation as additional components that rely on FV modelling are introduced.

One of the major pitfalls of an insufficient number of nodes manifested in heat exchangers during early engineering modelling. When the number of nodes in a heat exchanger is sufficiently small, and temperature differences are sufficiently large, heat flow rates between the two sides of the heat exchanger can be so large that the direction of heat flow changes from one volume to the next as a result of temperature changes being too great. This is obviously indicative of a fundamental error being introduced and was one of the key considerations when checking engineering model results. A similar pitfall occurs with insufficient numbers of nodes in the cold store, where it can make the cold store appear more effective than it actually was.

The decision was made to use 250 nodes for simulation models. Whilst this does not result in convergence of results, it does ensure that the results are at least approaching convergence. The 0.1 K improvement shown in Figure 7-2 beyond this point amounts to a tenth of a percent change in temperature and this was deemed sufficient for the purposes of what is a very early stage assessment of plant profitability. It remains an important assumption to be aware of given that the calculation of plant costs, especially of its heat exchangers, is dependent on the system temperatures resulting from the engineering model.

Assumption: the cold store size and the flow rate required in its loops can be accurately scaled using the theoretical maximum specific cold recycle of the discharge air stream.

As discussed at the end of section 5.2.4, the cold store size and mass flow rate were scaled using linear equations from the detailed cold store modelling performed on the 4000 kWh simulated

in detail in that section. The reasons for this are discussed in that section but, in brief, it is assumed that the amount of energy the cold store is capable of storing is defined by:

$$Q = MC_{\mathrm{m}}\Delta T \qquad (7\text{-}1)$$

where M is the mass of gravel in the cold store, C_{m} is its specific heat capacity and ΔT is the temperature difference between the charged state and the discharged state.

On the face of it, this is a reasonable assumption, however it does not consider the fact that the enthalpy, and hence temperature, of the air following the pump in the discharge cycle will change depending on the peak pressure of that cycle. This will affect the minimum temperature of the cold store following a discharge cycle. As a result, equation (7-1) is not entirely valid. It is, however, the case that the temperature of the air following pumping varies only by a small amount with increasing peak pressure, as shown in Figure 7-3.

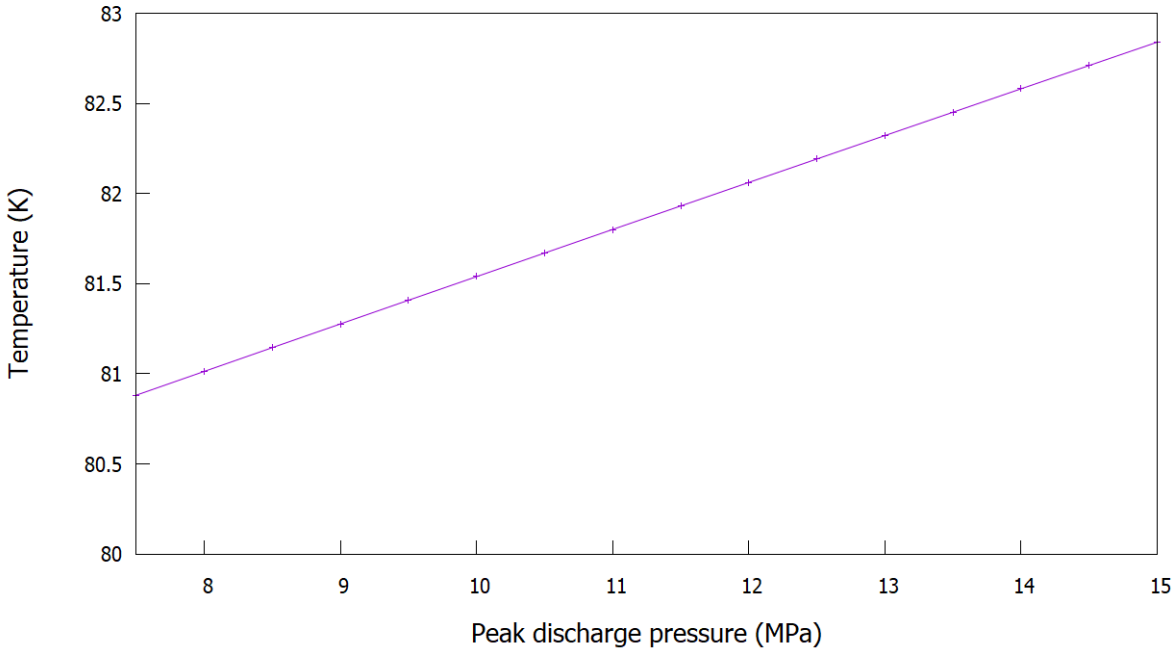

Figure 7-3: Temperature of discharge air following pumping

Once again this is a trade-off, this time between being able to model the dynamics of the charging cycle for as many discharge peak pressure (and hence cold store states) as possible and being able to obtain the initial temperature profiles of those cold store states. This is no doubt a flawed assumption but has made possible a greater search of the possible design space for the system.

Assumption: steady-state simulation of the charge cycle is sufficient for parametric comparison.

Section 5.2.5 discusses how the charge cycle was modelled first in a steady-state simulation before the transient behaviour was modelled, as discussed in section 5.2.6. The steady-state modelling was deemed sufficient to compare the effects of parameters on the performance of the liquefaction system. As the results of the transient modelling in section 5.2.6 show, the transient behaviour occurs for only a small part of the half-hour period of system charging and has only a small effect on the overall energy cost of liquefaction. It would seem, then, that assuming steady-state behaviour is an acceptable means of parametric comparison.

Assumption: the charge cycle can be scaled according to the specific cost of liquefaction from the symmetrical plant modelling.

As discussed in section 6.1.3, the larger power consumption (above 100 kg/s flow rate) charge systems were exclusively modelled in steady-state simulations in order to determine the sizes of components for the cost estimations. The actual specific cost of liquefaction was taken from the results of section 5.2.6, where transient behaviour was modelled. When determining system costs, it was assumed that as long as the modules of the cold store were of smaller size than the asymmetric system, that the performance of the liquefier would be the same or better than that of the symmetric plant. Whilst this is, again, a simplifying assumption, it is one that allowed for a greater exploration of the design space than would otherwise have been possible. By ensuring that the modules of the cold store were always smaller than those used for the symmetric system modelling in section 5.2.6, this approach ensured that both the energy cost of liquefying air, and the cost estimation of the plant would always err on the side of pessimism.

Assumption: the plant will always fully charge or discharge continuously.

The assumption that the plant would always fully charge or discharge in a single continuous process is one that underpins the workings of the financial model. For selling into the spot market, this is a perfectly acceptable assumption for the discharge cycle given the results of the financial modelling. As section 6.1.2 discusses, plant designs that discharge fully in a single half-hour period had greater profitability than those that discharged over two or more periods, and given the half-hour granularity of the financial model, and indeed of the UK stock market, this assumption would seem acceptable.

The same is not necessarily true for the charge cycle. Where the plant operators can take advantage of arbitrage opportunities, it is not necessarily the case that the cheapest electricity

prices will occur during consecutive spot market balancing periods. Taking advantage of these periods by stopping and starting the plant would require perfect forecasting of electricity prices, something which the model assumes is not possible. In the context of the model, then, this assumption would seem to be acceptable for both the charge and the discharge cycles.

Assumption: prices for buying and selling on the spot market are equal.

In the market data that was available to this project, the buying and selling prices for electricity in the wholesale market were the same, except for a very small number of days. As renewable penetration increases, however, this may not be the case. It may become just as important to grid operators that excess power is disincentivised just as much as energy shortfalls are. This could present additional challenges, or additional opportunities, to ESS plant operators and is something that could be considered in further work based on this thesis.

There would be two approaches to such an amendment to the model. The simpler of these would be to set a ratio of the price for buying electricity from the spot market to the price of selling electricity to the spot market. This would require some amendment to the individual sheets of the model but would entail little additional computing power. The more complicated, but arguably better approach would be to introduce a second set of time series to the model dedicated to modelling the price for buying electricity from the spot market. The benefit of this latter approach would be that the buy and sell price time series parameters could be set independently of one another based on market data. A major hurdle to this, however, would be that it would entail significant additional computation load in both the modelling of prices, and the decision-making process within the model. The model developed as part of this thesis is already pushing towards the limits of both the capacity of a single Excel workbook, and the capabilities of the @RISK software. Given these considerations, if such a model was desired, a preferable approach might be to develop a new model in either MATLAB or R.

7.3.2. Cold recycle size mismatch

Section 5.2.5 discusses how duty cycling of the gravel bed was modelled. This is a particularly lengthy process, requiring charge and discharge simulations to be run sequentially with the end-state values of the temperature profile of the cold store being used as the input parameters for the following simulation. After several iterations of this process, the cold store converges on a state of cyclic equilibrium where the end state of the cold store's temperature profile is the same at the end of each consecutive charge cycle, and each consecutive discharge cycle.

In order to avoid having to perform this process of iterating the model to a state of cyclic equilibrium when it came to modelling the charge cycle and the full plant, as discussed in section 5.2.6, the known end-state temperature profiles were used as initial parameters for the cold store's temperature profile for the charge and discharge simulation. This is a valid assumption only if the gravel bed is of identical size as it was in the isolated models from which the temperature profiles were taken. Unfortunately, this was not the case. In an error made when writing the simulation code, the cold store length for the charge loop was set at 1.2 times that of the isolated model from which the temperature profiles were generated. The amount of cold stored by the cold store is a function of the mass of its storage medium, which for a given particle size and density, is determined by the length of the gravel bed. In short, increasing the length of the gravel bed has the effect of increasing its volume by the same amount, ultimately increasing the quantity of cooling available at the heat exchanger with the cold store loop.

This is a not insignificant effect. Because the simulation was optimised by increasing the mass flow rate of the cold store loop until the required rate of heat transfer was reached, and because this heating rate was divided by the mass of the cold store to arrive at a quantity in terms of specific energy, this error was not picked up on until the late stages of this project, by which time it was too late to make significant changes to the model. On a further note, this error allows a greater rate of cooling for a smaller temperature difference across the two ends of the cold store heat exchanger on the side of the cold recycle loop. This in turn allows for a smaller temperature difference on the liquefier side of this heat exchanger. Since this is the key bottleneck for heat exchange in the simulation (the lower the temperature of the air following heat exchanger 2, the less efficient the heat exchanger becomes at cooling the air stream), this improves both the available cold recycle and hence the specific energy cost of liquefaction. This is likely the reason the simulated plant was able to achieve modest air liquefaction energy requirements without multi-stream heat exchange. This latter point is discussed further in section 7.3.3.

This has additional effects for the financial model. Clearly, the most fundamental issue is that the assumed charge power consumption is too low meaning the revenue losses during discharge are less than they should be. In addition to this, because the size of heat exchanger has been calculated using the log mean temperature difference method, the larger temperature difference at the two ends of the heat exchanger means that a smaller heat exchanger cost would have been calculated.

Further review of the engineering modelling showed that this error amounted to less than 1% in terms of plant performance and translated to a cost change of less than 0.1% in overall system

cost. Ultimately, this error is lost in the uncertainty introduced by the financial modelling, especially with respect to the cost estimation process discussed in section 4.3, where the cost estimation factors used have a maximum mean value of 2%. It is safe, then, to assume that these errors are negligible when considered relative to the uncertainty inherent to the financial modelling approach.

7.3.3. Other limitations

A key limitation of the engineering model is its treatment of the air liquefier as using two-stream heat exchangers. The majority of the work discussed in section 2.5.2 uses multi-stream heat exchangers where three air streams exchange heat with one another. This allows the incoming compressed air to be cooled by both the return air (from the turbine outlet and the vapour fraction from the vapour-liquid separator) and by the air stream from the cold store simultaneously. This allows a significantly large temperature difference across the two ends of the cold store when charging the system, in turn allowing a larger temperature difference when discharging and a corresponding increase in the specific cold recycle for the system. As seen in section 5.2.6, improving specific cold recycle improves the specific energy of liquefaction. In addition a greater temperature difference across the cold store also allows for the same specific cold recycle even as peak discharge pressure is increased.

This omission was primarily a result of the time constraints of the project. Once the model components had been coded, engineering modelling had to begin in earnest in order to meet deadlines. The time necessary for developing a model for a multi-stream heat exchanger was simply unavailable. The approach to heat exchanger modelling does, however, lend itself to the development of a multi-stream heat exchanger. Much like a heat exchanger involving a phase transition in one of its streams, a multi-stream heat exchanger can have a point of minimum approach temperature along its length rather than at one end. Thus, it is important that any model of such a heat exchanger be analysed in axial sections. The FV flows and metal tubes discussed in sections 3.2.1 and 3.2.3 respectively should lend themselves well to such a model. With some minor modifications, the metal tube model could be used as the metal matrix of the heat exchanger and the FV flow model should work as is.

As discussed in sections 2.6 and 2.7, access to the ESDU heat exchanger data (IHS Markit, 2019) could have provided more detailed heat transfer coefficients and cost data to inform both the engineering and the financial model. It is worth bearing in mind, however, that the system in question ultimately performed poorly in all but the most extreme spot market conditions. There is little sense in increasing the accuracy of modelling and plant costing when this project

has demonstrated that the plant would be an unattractive investment in any likely market scenario. Any reductions in cost resulting from higher accuracy are unlikely to be significant enough to change this fact. Indeed, the scope of the design work for any project must have its limits, and the minutiae of engineering design that is possible is almost limitless. Without being able to demonstrate additional gains by an engineering redesign, or without some sort of incentive for such a plant (such as a subsidy or capacity payment), there is little point in further refining the modelling regimen.

The version of Dymola used also contributed to some of the limitations of the engineering model. The full industrial version features multi-parameter optimisation algorithms that could have potentially been used to provide further optimisation than has been possible with this project. Whilst the optimisation methodology used (performing wide parameter sweeps to define the search space, followed by fine parameter sweeps for the optimal regions) was sound, such an approach is ultimately limited to the resolution of the parameter sweep. Ultimately, some 12 configurations were modelled in the early stages of this project, and whether or not algorithmic optimisation could have covered as much ground in the same time is unclear, but potentially warrants further study.

Initialisation of Dymola models was also problematic at times. This is most apparent in the sizing of the cold store discussed in section 5.2.6. The air flow through the cold store needs to be initialised at a steady state to prevent failures in simulating the engineering model. As such, when modelling whole-plant systems, the engineering model was run for a full discharge cycle, stopped, had its parameters reset for a charging cycle and then restarted, allowing initialisation to be performed again prior to simulation. This made this stage of the work particularly labour-intensive with pulling end variables from the simulation results and re-entering them as parameters for the next stage of the simulation. It is however possible that some additional scripting within Dymola could have reduced the level of user interaction required.

Perhaps the most important omission in the engineering modelling is the lack of exploration of a warm recycle system for the plant. As many of the papers discussed in section 2.5.2 note, warm recycle is an important way to improve system efficiency. It was omitted from this project in this case because it was expected that the combination of waste and medium-grade heat from the NPP would be sufficient to develop a competitively efficient system. This was partially due to early investigations not considering the efficiency lost when ramping down the NPP's secondary loop, as discussed in sections 5.2.1 and 6.1.1, and partially due to the over-optimistic preceding work (Li et al., 2014) implying a greater improvement in energy yield using NPP heat than is actually possible.

It is worth noting that warm recycle is the most nebulous part of the LAES plant modelling performed so far. As several of the papers in section 2.5.2 note, cold recycle is a far more important part of improving plant round-trip efficiency than warm recycle. Indeed, the many of these studies have not even selected the medium for warm recycle, typically referring to it as simply 'hot oil'. The reasons for this are relatively easy to understand; the studies in question generally rely on either RefProp, CoolProp, or Aspen's inbuilt thermophysical property database for calculation of fluid properties. Neither of the first two property databases features fluids that are liquid throughout the 300-600 K range that would be required of a warm recycle medium, generally focusing on refrigerants and power cycle fluids. Aspen's property database was not available to this project. As a result, all of the papers that study warm recycle typically define nominal values of density and specific heat capacity to the warm recycle fluid media in their models.

As section 6.1.2 notes, the construction of the financial model places the constraint that whenever the plant charges or discharges, it must do so fully within the limits of the storage tank size. This could potentially favour single-period discharge designs as the preliminary financial modelling investigations demonstrated and is a key limitation of the model. The effect of only partially discharging the system has potentially significant implications for the cold store temperatures at the end of the discharge cycle and its potential effectiveness during subsequent charge cycles. As a result, these effects would require extensive additional engineering modelling to allow part charging and discharging to be incorporated into the financial model.

7.4. Further work

Following on from the discussion in section 7.3, arguably the most important and immediate improvements that could be made to the engineering work are the development of a multi-stream heat exchanger model and the modelling of warm recycle. For the former, this work provides a solid foundation on which to build a multi-stream heat exchanger, as discussed in section 7.3.3. As that section notes, this omission is not a major hurdle to the design of an LAES plant but is representative of an area in which plant performance is likely sub-optimal. Multi-stream heat exchange would allow the utilisation of additional cold from the discharge system and could have a significant effect on plant round-trip efficiency by reducing the energy cost of liquefaction.

There are also opportunities to develop a model for a warm recycle system within the engineering model. There is a major obstacle to this discussed in section 7.3.3. That is that the

thermophysical property databases available for integration into the engineering model do not provide data for fluids that are liquid in the required temperature ranges. A fluid model would not need to be overly complex to come in line with the available literature (whose fluids are assumed to be of continuous phase and specific heat capacity) but its development is a significant undertaking and one which was beyond the scope of this particular project.

There are also opportunities to improve the financial modelling. The model itself operates with no preference for a given purchase price for electricity. The reasoning behind this is simple. The electricity price dataset shows a period of reconciliation of weeks to months, where the final system price is subject to change. Whilst the price rarely changes during this period, it was assumed that the plant operators would not have perfect knowledge of the instantaneous electricity price. Their best option would then be to charge the system over a long period overnight, when the electricity prices are generally at their cheapest. In doing so, the electricity price would be subject to variation during the period of charging, but the cost of charging the system would be governed not by a single period but by the average price over the whole period during which the system was charged. In charging this way, the operators would essentially be hedging their cost of charging by spreading the time spent charging over several half-hour periods when prices are expected to be at their lowest.

The operators of a real plant would have access to more recent electricity price data than the hypothetical operators of the plant in this model, however. This information, and the improvements it could make to electricity price forecasting, might provide an opportunity for the operators to strategically charge the system at specific periods when the electricity price was expected to be at its lowest. The way the financial model operates during discharge points to a way this could be simulated. Much as the model sets a threshold price for discharging the system based on the cost to charge and the round-trip efficiency, a threshold charging price could be set, based perhaps on a rolling average. The model would then only charge the system during periods when the instantaneous electricity price was below this threshold price. This would require significant changes to be made to the financial model to allow for discontinuous charging. It would also likely require a faster charge rate (higher power consumption) in order to ensure that the system was always fully charged given its reduced opportunity to do so.

Chapter 8 - Conclusions

Section 1.4 summarised the objectives of this thesis. Each of these objectives is discussed in turn in this section and the successes of the project in achieving them.

- Develop an engineering model and library of components in the Modelica language for plant process modelling of the combined NPP and LAES system.

The development of a Modelica library of components for the simulation of an LAES system was successfully achieved as part of this project, as detailed in section 3.2. This library has been made available to the wider community via Open Research Data Online (Wilson, 2020b). This is a significant contribution to the wider Modelica community.

- Use the engineering model to determine operating parameters for a range of proposed plant configurations.

The engineering model was used to determine the performance of a variety of system configurations for a hybrid NPP and LAES plant. This is a key novel contribution of this thesis to the field. This furthermore represents a significant improvement on the previous work on this plant design (Li et al., 2014). Interim results have been presented as a peer-reviewed working paper (Wilson et al., 2020) and efforts are underway to have a second paper published on the broader conclusions of the work.

There are several major novel conclusions of the engineering modelling approach. The first of these is a consequence of the treatment of the steam turbine of the NPP as having a variable isentropic efficiency when operating away from its design power rating. As section 5.2.3 shows, this has a major effect on the discharge power rating of the LAES plant, with an peak discharge power rating coinciding with the point at which the NPP is operating at 50% capacity. This essentially forces system designers to trade-off between operating the LAES plant at a set discharge power rating or allowing more flexible operation at the cost of plant efficiency.

The second major novel conclusion is that waste heat from the condenser is sufficiently abundant that none of the plant designs described in this thesis are unable to fully utilise it. Indeed, the aforementioned NPP operating range is the most important limiting factor on LAES plant operating conditions and place a prohibitive energy cost on discharge flow rates well before the heat available at the condenser can be fully utilised by the discharge air stream. This is an important conclusion in itself that points the way to a better coupling regime for LAES and NPPs; that of simply using the NPP's condenser as a waste heat source and making no

changes to the NPP's secondary loop operating conditions. Whether such an approach would be preferable to other potential waste heat sources would need to be the subject of further study.

A third novel conclusion can be garnered as to the importance of compression and expansion train staging to the efficiency of the LAES plant. That being said, these conclusions are unsurprising from a thermodynamic perspective alone, and are much more interesting when considered in the context of financial modelling, as discussed below.

A fourth important conclusion is the importance of warm recycle to such a system. Previous work on a comparable system (Li et al., 2014) implied that this was not the case, and that the supplemental heat available when coupling to a nuclear plant was sufficient for round-trip efficiencies approaching 70%. This thesis unequivocally refutes this conclusion and section 2.5.2 attributes these erroneous conclusions to a number of inappropriate assumptions made by the aforementioned study's thermodynamic model. Conversely, this thesis asserts that a warm recycle system is an integral part of any LAES plant, whether or not supplemental heat is available. This conclusion is in line with the bulk of the work discussed in section 2.5.2, and is reinforced by the compatibility issues associated with the proposed plant coupling. Specifically, these are the NPP secondary loop pressures and the resultant inefficiencies encountered during heat exchange with the LAES discharge cycle, as discussed in section 7.2. Any further work on this plant design should consider this point.

- Size components for the given plant configurations and use these to evaluate asset costs for the LAES plant.

The approach taken to sizing components, evaluating key asset costs, and using these to estimate the total cost of the LAES plant is not a novel one and one that has been demonstrated in several studies referenced in section 2.7. Nevertheless, the success of the approach in this thesis, not least the closeness of the resulting estimates to Highview Power's own (Highview Power) lends credence to this approach. The results of this approach themselves are representative of new knowledge due to the additional plant equipment that the proposed design necessitates.

- Develop a financial model for determining relative economic performance of the plant designs in the face of uncertain market conditions using Excel and the Palisade @RISK plugin.

The financial model was successfully developed. This model represents, to this author's knowledge, the only financial model of its type to simulate plant performance within the UK

electricity spot market to the resolution of half hour periods. Other comparable work is reliant on data resampling to achieve a similar level of resolution. As section 7.2 discusses, time series modelling allows far greater flexibility in the exploration of hypothetical markets than simple data resampling. Furthermore, such an approach allows models to be updated as new data becomes available and the effect of the changing face of UK generating assets on the market becomes better understood. This financial model is, in itself, a major novel contribution to the field and one that has been made publicly available via Open Research Data Online (Wilson, 2020a).

- Use the financial model to determine the relative economic performance and investment risk of the plant design outputs from the engineering model.

The financial model was successfully demonstrated. The conclusions drawn from the results of this demonstration once again represent a major novel contribution to the field. As with the engineering work, interim results have been presented as a peer-reviewed working paper (Wilson et al., 2020) and efforts are underway to have a second paper published on the broader conclusions of the work.

There are many conclusions that can be drawn from the financial model results and are unique to this work. The very real effect that chasing plant efficiency has on the LAES plant asset cost, and thus its economic risk can be demonstrably seen in the content of section 6.1.3. This section shows that as the number of compression and expansion stages are increased, the diminishing returns of plant efficiency are also manifested in diminishing improvements of economic performance and the corollary reduction of risk.

The suitability of this system for the market is also an important consideration. Only by pushing market parameters to extremes, and only by assuming the most modest of overspends in plant cost does the proposed system become viable. It is important to concede that by virtue of its design, this plant is less efficient than others proposed in literature. That being said, the conclusion of this thesis must be that not only is this plant not economically viable in current market conditions, nor in the most extreme of hypothesised conditions. This is not to say that improvements in efficiency are not worth chasing, but it would support the conclusion that more detailed engineering modelling of the proposed system is unwise. The incremental improvements more detailed optimisation would provide will not be sufficient to make this plant viable; only a ground-up configurational redesign with a warm recycle system could render the improvements necessary. These points are discussed in detail in section 7.3.

In summation, this thesis asserts that there are several novel contributions to the fields of both engineering and financial modelling in this work. Furthermore, the open nature and public availability of the models it has yielded should speak to the transparency and replicability that should be required of academic work at this level. Furthermore, their availability presents opportunities for those who might want to build on this work. Some suggestions of further work relevant to this thesis are discussed in section 7.4.

8.1. Further discussion

Perhaps the most significant contribution of this work relates not directly to the objectives themselves, but in an understanding of how this project fits into a broader whole. As discussed during the introductory remarks of this thesis, it is a core assumption that the world will, as a whole, move towards the decarbonisation of energy. In this sense, the combined approach taken might seem like something of a coarse tool. Indeed, there are broader societal benefits to both power grid balancing and displacement of carbon in generation to be gained by the construction of the plant described herein. Viewed through this lens, it could be argued that the economics of a proposal should matter less if it helps us with the issues associated with decarbonisation.

This is an argument that this author is not unsympathetic to and would indeed agree that a more holistic approach exploring routes to decarbonisation is required than simply considering economics. With that being said, the wholesale decarbonisation of energy (even if only the electricity generating network is considered) will be one of the largest and most resource-hungry endeavours mankind has ever undertaken and will most likely require the mass deployment of ESSs. In light of this, the real financial cost to society must be part of this holistic approach. It might be argued that energy and its consumption are a major hallmark of developed society. With this in mind, decarbonisation should not come at such a cost that the poor are priced out of access to clean energy. In this sense, financial analyses like those described in this thesis are indeed just a piece of a larger puzzle but are nevertheless an important one.

It is in this area that the methodology developed in this thesis is perhaps of its greatest value. The LCOS approach to assessing the financial cost of energy storage is a metric that has come to the fore over the years that this project was developed. In its simplest form, it represents the sale price of electricity required for an ESS to become economically viable. This is very useful if one wants to subsidise the construction of an ESS that will sell electricity into the spot market. It is possible that such a subsidy might work in a similar way to CfD pricing, wherein the operator is guaranteed a sale price and any shortfall is ultimately made up by the ratepayer. It is here where energy storage might become extremely expensive.

LCOS provides an understanding of how high a subsidy might need to be for a given proposition. Conversely, it does little to assess the ultimate cost of providing such a subsidy. Such insights are only available by testing the proposition in a simulated electricity market in order to determine the shortfall. This thesis has yielded a first of its kind tool to do just that. Used in concert with LCOS, the approach can yield insights into the real financial cost of subsidising a given ESS. Whilst the probabilistic nature of the model means that only speculative conclusions can be drawn for a given ESS in a hypothetical market, the comparison of the relative risk of several competing systems in multiple proposed markets will provide real and practical insights into which might be better suited for the majority of proposed markets.

A further ancillary benefit is a novel understanding of the interplay of engineering and economic factors. The conclusions regarding the effect that coupling an NPP has on locking the LAES plant into a specific discharge rate is an unexpected one and one which has important consequences. The previous paragraphs discuss the likely significant need for grid-scale energy storage, the necessity for this storage to be suitable for the market, and the ways in which this suitability will define its cost. Related to this point is the question of flexibility and consideration of whether a given system is able to adjust its charge/discharge profile to respond to changing market conditions. In light of this consideration, the hurdles to flexibility encountered when coupling systems, and their real economic consequences, are an important consideration.

8.2. Closing remarks

This thesis set out to explore a coupled engineering and financial modelling approach that would allow a combined NPP and LAES plant to be optimised from a market-led perspective. Unlike the previous work discussed in section 2.5, which are either solely engineering-focused optimisation studies, or seek to determine the economic viability of an already-designed engineering system, this thesis has proposed a novel methodology in which exploration of hypothetical markets has directly influenced the engineering design of the LAES plant.

This methodology is the core novel contribution of this thesis to the field of study and one that has important features that set it apart from comparable work. In contrast to previous studies discussed in section 2.5.3, the financial model is not reliant on perfect forecasting of electricity prices. The approach to financial modelling simulates a practical method by which operators could conceivably run the plant. With the knowledge of the price they had paid to charge the system, and a knowledge of the round-trip efficiency of the plant, the operators can bid into the spot market at a level that ensures profits are made via arbitrage of the electricity price. The

nature of the UK spot market, where all successful bidders are paid at the highest successful bid price facilitates this.

The financial model also allows exploration of hypothetical markets and their effect on plant profitability. In doing so, it provides a means for investors to assess the type of market in which a plant will become profitable, allowing them a greater understanding with which to make decisions. It could, with some additional development, also provide governments a means to assess what subsidisation might be required to incentivise such a plant. It would similarly allow an understanding of how such a subsidy would need to respond to market conditions and enable simulation of the probable costs of such a subsidy given market conditions.

In summation, this thesis has been successful in developing and demonstrating a novel approach to techno-economic analysis in the context of a combined LAES and NPP system. The financial model especially, however, could be applied to different ESS systems in different markets and contexts with little modification. As part of the demonstration of this approach, a library of components has been developed for the Modelica language that facilitates the engineering modelling of liquefaction systems and could be of use to other researchers in the field. This thesis has revealed the importance of, and demonstrated the practicality of, engineering design co-optimised with market performance. Advanced software modelling and further development of the techniques demonstrated in this thesis could reveal additional insights and opportunities that might otherwise be neglected.

References

2008. Chemical Engineering Plant Cost Index (CEPCI). *Chemical Engineering.*

2010. Chemical Engineering Plant Cost Index (CEPCI). *Chemical Engineering,* 117**,** 80.

2015. Chemical Engineering Plant Cost Index (CEPCI). *Chemical Engineering.*

ALEXANDER, M. J., RICHARDSON, N. & JAMES, P. 2015. Energy storage against interconnection as a balancing mechanism for a 100% renewable UK electricity grid. *IET Renewable Power Generation,* 9**,** 131-141.

ANALYCORP. *XLSim* [Online]. Available: https://xlsim.software.informer.com/download/ [Accessed].

ANEKE, M. & WANG, M. 2016. Energy storage technologies and real life applications – A state of the art review. *Applied Energy,* 179**,** 350-377.

ANTONELLI, M., BARSALI, S., DESIDERI, U., GIGLIOLI, R., PAGANUCCI, F. & PASINI, G. 2017. Liquid air energy storage: Potential and challenges of hybrid power plants. *Applied Energy,* 194**,** 522-529.

AREVA 2013. Chapter Ten: Steam and Power Conversion System. *U.S. EPR FINAL SAFETY ANALYSIS REPORT.*

ASPENTECH. *Aspen HYSYS* [Online]. Available: https://www.aspentech.com/products/engineering/aspen-hysys [Accessed].

ASPENTECH. *aspenONE Product Portfolio* [Online]. Available: https://www.aspentech.com/en/products/full-product-listing [Accessed 14 January 2020].

BARBOOTI, M. M. & AL-ANI, R. R. 1984. The copper—chlorine thermochemical cycle of water splitting for hydrogen production. *Thermochimica Acta,* 78**,** 275-284.

BARBOUR, E., WILSON, G., HALL, P. & RADCLIFFE, J. 2014. Can negative electricity prices encourage inefficient electrical energy storage devices? *International Journal of Environmental Studies,* 71**,** 862-876.

BARBOUR, E., WILSON, I. A. G., BRYDEN, I. G., MCGREGOR, P. G., MULHERAN, P. A. & HALL, P. J. 2012. Towards an objective method to compare energy storage technologies: development and validation of a model to determine the upper boundary of revenue available from electrical price arbitrage. *Energy Environ. Sci.,* 5**,** 5425-5436.

BARBOUR, E., WILSON, I. A. G., RADCLIFFE, J., DING, Y. & LI, Y. 2016. A review of pumped hydro energy storage development in significant international electricity markets.(Report). *Renewable and Sustainable Energy Reviews,* 61**,** 421.

BARRY, W. B., TOM, B., TOM, M. L. W. & SANGHYUN, H. 2018. Silver Buckshot or Bullet: Is a Future "Energy Mix" Necessary? *Sustainability,* 10**,** 302.

BELL, I. H., WRONSKI, J., QUOILIN, S. & LEMORT, V. 2014. Pure and Pseudo-pure Fluid Thermophysical Property Evaluation and the Open-Source Thermophysical Property Library CoolProp. *Industrial & Engineering Chemistry Research,* 53**,** 2498-2508.

BERTHÉLEMY, M. & RANGEL, L. 2015. Nuclear reactors' construction costs: The role of lead-time, standardization and technological progress. *Energy Policy,* 82**,** 118.

BOLDON, L., SABHARWALL, P., PAINTER, C. & LIU, L. 2014. An overview of small modular reactors: status of global development, potential design advantages, and methods for economic assessment. *International Journal of Energy, Environment and Economics,* 22**,** 437-459.

BROWN, R. C., BROWN, T., DALE, B., EDWARDS, D., ESTES, V., GRANDA, C., HOLTZAPPLE, M., LONKAR, S. & WYMAN, C. 2015. Lignocellulosic Biofuels. *In:* ENGINEERING, S. F. B. (ed.). American Institute of Chemical Engineers.

BUONGIORNO, J., CORRADINI, M., PARSONS, J. & PETTI, D. 2018. The Future of Nuclear Energy in a Carbon-Constrained World. Massachusetts Institute of Technology.

CASELLA, F. 2014. *ThermoPower* [Online]. Politecnico di Milano. Available: http://thermopower.sourceforge.net/ [Accessed 2 September 2016].

CASELLA, F. & LEVA, A. 2003. *Modelling of Distributed Thermo-Hydraulic Processes Using Modelica*.

CASELLA, F. & LEVA, A. 2009. *ThermoPower library* [Online]. Available: https://github.com/casella/ThermoPower [Accessed].

CASELLA, F. & RICHTER, C. *ExternalMedia* [Online]. Available: https://github.com/modelica-3rdparty/ExternalMedia [Accessed].
CASELLA, F. & RICHTER, C. ExternalMedia: a library for easy re-use of external fluid property code in Modelica. Proceedings 6th International Modelica Conference, Bielefeld, Germany, March, 2008. 3-4.
CHART INDUSTRIES. 2018. *Cryogenic Storage Tanks and Regasification* [Online]. Available: http://www.chartindustries.com/Energy/LNG-Solutions-Equipment/Storage [Accessed 16th October 2018].
CHESSHIRE, J. 1992. Why nuclear power failed the market test in the UK. *Energy Policy,* 20**,** 744-754.
CLACK, C. T. M., QVIST, S. A., APT, J., BAZILIAN, M., BRANDT, A. R., CALDEIRA, K., DAVIS, S. J., DIAKOV, V., HANDSCHY, M. A., HINES, P. D. H., JARAMILLO, P., KAMMEN, D. M., LONG, J. C. S., MORGAN, M. G., REED, A., SIVARAM, V., SWEENEY, J., TYNAN, G. R., VICTOR, D. G., WEYANT, J. P. & WHITACRE, J. F. 2017. Evaluation of a proposal for reliable low-cost grid power with 100% wind, water, and solar. *Proceedings of the National Academy of Sciences,* 114**,** 6722-6727.
CONNOLLY, D., LUND, H., FINN, P., MATHIESEN, B. V. & LEAHY, M. 2011. Practical operation strategies for pumped hydroelectric energy storage (PHES) utilising electricity price arbitrage. *Energy Policy,* 39**,** 4189-4196.
COOPER, M. 2010. Policy challenges of nuclear reactor construction: cost escalation and crowding out alternatives. *Institute for Energy and the Environment, Vermont Law School, September*.
CORBAN ENERGY GROUP. 2018. *LNG Tanks* [Online]. Available: https://www.corbanenergygroup.com/lng-storage-tanks/ [Accessed 16 October 2018].
COUPER, J. R. 2012. *Chemical process equipment : selection and design,* Waltham, Mass., Waltham, Mass. : Butterworth-Heinemann.
CUMMINS, W. 2013. Passively Safe Plant. *Nuclear Plant Journal,* 31**,** 28-29.
DAMES AND MOORE 1981. An Assessment of Hydroelectric Pumped Storage. *In:* NATIONAL HYDROELECTRIC POWER RESOURCES STUDY (ed.).
DASSAULT SYSTEMES. *Dymola (Dynamic Modelling Laboratory)* [Online]. Available: http://www.3ds.com/products-services/catia/products/dymola/ [Accessed].
DELUCCHI, M. A. & JACOBSON, M. Z. 2011. Providing all global energy with wind, water, and solar power, Part II: Reliability, system and transmission costs, and policies. *Energy Policy,* 39**,** 1170-1190.
DEPARTMENT OF ENERGY AND CLIMATE CHANGE 2013. Annex B: Strike price methodology. London.
DUNBAR, A., WALLACE, A. R. & HARRISON, G. P. 2016. Energy storage and wind power: sensitivity of revenue to future market uncertainties. *IET Renewable Power Generation,* 10**,** 1535-1542.
EAMES, P., LOVEDAY, D., HAINES, V. & ROMANOS, P. 2014. The Future Role of Thermal Energy Storage in the UK Energy System: An Assessment of the Technical Feasibility and Factors Influencing Adoption. London: UK Energy Research Centre.
ELA, E., KIRBY, B., BOTTERUD, A., MILOSTAN, C., KRAD, I. & KORITAROV, V. 2013. The role of pumped storage hydro resources in electricity markets and system operation. *Proceedings of the Hydro Vision International, Denver, CO, USA,* 2326**,** 110.
ENERGY STORAGE ASSOCIATION. 2016. *Compressed Air Energy Storage (CAES)* [Online]. Available: http://energystorage.org/compressed-air-energy-storage-caes [Accessed 27 June 2016].
F-CHART SOFTWARE. *Engineering Equation Solver* [Online]. Available: http://fchartsoftware.com/ees/index.php/ [Accessed].
FARRELL, S. & MACALISTER, T. 2015. *Work to begin on Hinkley Point reactor within weeks after China deal signed* [Online]. The Guardian. Available: https://www.theguardian.com/environment/2015/oct/21/hinkley-point-reactor-costs-rise-by-2bn-as-deal-confirmed?CMP=twt_gu [Accessed 15 October 2018].
FORSBERG, C. 2011. Thermal Energy Storage Systems for Peak Electricity from Nuclear Energy.

FORSBERG, C., RICHARD, J., POUNDERS, J., KOCHENDARFER, R., STEIN, K., SHWAGERAUS, E. & PARKS, G. 2015. Development of a Fluoride-Salt-Cooled High-Temperature Reactor (FHR) Using Advanced Gas-Cooled Reactor (AGR) Technology. *Transactions of the American Nuclear Society Annual Meeting*. San Antonio.
FORSBERG, C. W. 2004. Hydrogen, nuclear energy, and the advanced high-temperature reactor. *International Journal of Hydrogen Energy,* 28**,** 1073-1081.
FORSBERG, C. W. 2009. Sustainability by combining nuclear, fossil, and renewable energy sources. *Progress in Nuclear Energy,* 51**,** 192-200.
FORSBERG, C. W. 2015. Strategies for a Low-Carbon Electricity Grid with Full Use of Nuclear, Wind, and Solar Capacity to Minimize Total Costs. MIT.
FRITZ, K. & GILLI, P. V. Nuclear Power Plants with Integrated Steam Accumulators for Load Peaking. IAEA Symposium on Economic Integration of Nuclear Power Stations in Electric Power Systems, 1970 Vienna.
FUJIWARA, S., KASAI, S., YAMAUCHI, H., YAMADA, K., MAKINO, S., MATSUNAGA, K., YOSHINO, M., KAMEDA, T., OGAWA, T., MOMMA, S. & HOASHI, E. 2008. Hydrogen production by high temperature electrolysis with nuclear reactor. *Progress in Nuclear Energy,* 50**,** 422-426.
GE NUCLEAR ENERGY 1997. ABWR Design Control Document.
GE POWER & WATER, G. H. N. E. 2015. *GE Hitachi PRISM* [Online]. Available: http://gehitachiprism.com/ [Accessed May 2015].
GEN IV INTERNATIONAL FORUM 2014. Technology Roadmap Update for Generation IV Nuclear Energy Systems. OECD Nuclear Energy Agency.
GILLI, P. V. & BECKMAN, G. 1973. Steam Storage Adds Peaking Capacity to Nuclear Plants. *Energy International,* 10**,** 16-18.
GOODING, P. 2018. Consumer price inflation tables. *In:* OFFICE FOR NATIONAL STATISTICS (ed.).
GORENSEK, M. B. & FORSBERG, C. W. 2009. Relative economic incentives for hydrogen from nuclear, renewable, and fossil energy sources. *International Journal of Hydrogen Energy,* 34**,** 4237-4242.
GREEN, M., SABHARWALL, P., YOON, S., BRAGG-SITTON, S. & STOOTS, C. 2013. Nuclear Hybrid Energy Systems: Molten Salt Energy Storage. INL/EXT-13-31768, November.
GRUBLER, A. 2010. The costs of the French nuclear scale-up: A case of negative learning by doing. *Energy Policy,* 38**,** 5174-5188.
GRÜNEWALD, P., COCKERILL, T., CONTESTABILE, M. & PEARSON, P. 2011. The role of large scale storage in a GB low carbon energy future: Issues and policy challenges. *Energy Policy,* 39**,** 4807-4815.
GUITTET, M., CAPEZZALI, M., GAUDARD, L., ROMERIO, F., VUILLE, F. & AVELLAN, F. 2016. Study of the drivers and asset management of pumped-storage power plants historical and geographical perspective. *Energy,* 111**,** 560-579.
GUIZZI, G. L., MANNO, M., TOLOMEI, L. M. & VITALI, R. M. 2015. Thermodynamic analysis of a liquid air energy storage system. *Energy,* 93**,** 1639-1647.
GUO, K., ZHANG, N. & SMITH, R. 2018. Design optimisation of multi-stream plate fin heat exchangers with multiple fin types. *Applied Thermal Engineering,* 131**,** 30-40.
HANLEY, E. S., GLOWACKI, B. A., NUTTALL, W. J. & KAZANTZIS, N. 2015. Natural gas - Synergies with hydrogen. *Proceedings of Institution of Civil Engineers: Energy,* 168**,** 47-60.
HENTSCHEL, J., BABIĆ, U. A. & SPLIETHOFF, H. 2016. A parametric approach for the valuation of power plant flexibility options. *Energy Reports,* 2**,** 40-47.
HEWITT, G. F. & PUGH, S. J. 2007. Approximate Design and Costing Methods for Heat Exchangers. *Heat Transfer Engineering,* 28**,** 76-86.
HIGHVIEW POWER. *Cost Estimator* [Online]. Available: https://www.highviewpower.com/#calc-jumper [Accessed 17 March 2018].
HIGHVIEW POWER 2015. Liquid Air Energy Storage (LAES).
HIGHVIEW POWER STORAGE. 2016. *Pilot Demonstrator* [Online]. Available: http://www.highview-power.com/pilot-demonstrator-january-2010-february-2011/ [Accessed 25 June 2016].

HORI, M. 2008. Nuclear energy for transportation: Paths through electricity, hydrogen and liquid fuels. *Progress in Nuclear Energy,* 50**,** 411-416.
HORI, M., MATSUI, K., TASHIMO, M. & YASUDA, I. 2005. Synergistic hydrogen production by nuclear-heated steam reforming of fossil fuels. *Progress in Nuclear Energy,* 47**,** 519-526.
HU, Y., LI, X., LI, H. & YAN, J. 2013. Peak and off-peak operations of the air separation unit in oxy-coal combustion power generation systems. *Applied Energy,* 112**,** 747-754.
IHS MARKIT. 2019. *ESDU* [Online]. Available: https://www.esdu.com/ [Accessed 18 December 2019].
INGERSOLL, D. T., COLBERT, C., HOUGHTON, Z., SNUGGERUD, R., GASTON, J. W. & EMPEY, M. 2016a. Integrating nuclear and renewables. *Nuclear Engineering International.*
INGERSOLL, D. T., COLBERT, C., HOUGHTON, Z., SNUGGERUD, R., GASTON, J. W. & EMPEY, M. 2016b. Integrating nuclear and renewables (Operation & safety: Load following). Nuclear Engineering International.
INSTITUTION OF MECHANICAL ENGINEERS 2012. Electricity Storage. London: Institution of Mechanical Engineers.
JACOBSON, M. Z. & DELUCCHI, M. A. 2011. Providing all global energy with wind, water, and solar power, Part I: Technologies, energy resources, quantities and areas of infrastructure, and materials. *Energy Policy,* 39**,** 1154-1169.
JACOBSON, M. Z., DELUCCHI, M. A., CAMERON, M. A. & FREW, B. A. 2015. Low-cost solution to the grid reliability problem with 100% penetration of intermittent wind, water, and solar for all purposes. *Proceedings of the National Academy of Sciences,* 112**,** 15060-15065.
JENKINS, S. 2018. The CE Plant Cost Index: An Update. *Chemical Engineering,* 125**,** 76-77.
JIA, G., CAI, M., XU, W. & SHI, Y. 2018. Energy conversion characteristics of reciprocating piston quasi-isothermal compression systems using water sprays. *Science China Technological Sciences,* 61**,** 285-298.
KARAKURT, A. S. & GUNES, U. 2017. Performance Analysis of a Steam Turbine Power Plant at Part Load Conditions. *Journal of Thermal Engineering,* 3**,** 1121-1128.
KARL ZACH, H. A., GEORG LETTNER 2012. Facilitating energy storage to allow high penetration of intermittent renewable energy. *In:* STORE (ed.).
KERRY, F. G. 2007. *Industrial Gas Handbook: Gas Separation and Purification*, CRC Press.
KESSIDES, I. N. 2010. Nuclear power: Understanding the economic risks and uncertainties. *Energy Policy,* 38**,** 3849-3864.
KHAYYAM, H., RANJBARZADEH, H. & MARANO, V. 2012. Intelligent control of vehicle to grid power.(Report). *Journal of Power Sources,* 201**,** 1.
KIDD, S. 2009. Nuclear in France--what did they get right? With its fleet of standardised, load-following nuclear reactors and range of domestic fuel cycle facilities, the French nuclear programme is certainly unique. But it is not without critics.(COMMENT). *Nuclear Engineering International,* 54**,** 14.
KIDD, S. 2010. SMRs--what are their prospects? Although small reactors overcome one of the biggest hurdles of nuclear power--its great up-front cost--the designs' cost claims should be viewed with caution, since they have not yet been tested by regulatory design review.(Comment). *Nuclear Engineering International,* 55**,** 12.
KIM, J., NOH, Y. & CHANG, D. 2018. Storage system for distributed-energy generation using liquid air combined with liquefied natural gas. *Applied Energy,* 212**,** 1417-1432.
KING, A. 2020. CPI Annual Rate 00: All Items. *In:* OFFICE OF NATIONAL STATISTICS (ed.).
KIS, Z., PANDYA, N. & KOPPELAAR, R. H. E. M. 2018. Electricity generation technologies: Comparison of materials use, energy return on investment, jobs creation and CO2 emissions reduction. *Energy Policy,* 120**,** 144-157.
KOC, R., KAZANTZIS, N. K., NUTTALL, W. J. & MA, Y. H. 2012. Economic assessment of inherently safe membrane reactor technology options integrated into IGCC power plants. *Process Safety and Environmental Protection,* 90**,** 436-450.
KOC, R., KAZANTZIS, N. K., NUTTALL, W. J. & MA, Y. H. 2013. An economic evaluation framework for inherently safe membrane reactor modules in the presence of uncertainty: the case for process safety investment and risk reduction. *Journal of Loss Prevention in the Process Industries,* 26**,** 468-477.

KOOHI-KAMALI, S., TYAGI, V. V., RAHIM, N. A., PANWAR, N. L. & MOKHLIS, H. 2013. Emergence of energy storage technologies as the solution for reliable operation of smart power systems: A review. *Renewable and Sustainable Energy Reviews,* 25**,** 135-165.
KUMAR, N., BESUNER, P., LEFTON, S., AGAN, D. & HILLEMAN, D. 2012. Power plant cycling costs. National Renewable Energy Lab.(NREL), Golden, CO (United States).
KUPPAN, T. 2013. *Heat exchanger design handbook*, Boca Raton, Fla., Boca Raton, Fla. : CRC Press.
KURAVI, S., TRAHAN, J., GOSWAMI, D. Y., RAHMAN, M. M. & STEFANAKOS, E. K. 2013. Thermal energy storage technologies and systems for concentrating solar power plants. *Progress in Energy and Combustion Science,* 39**,** 285-319.
LANDAURO, I. 2012. *Costs of Finland's Olkiluoto nuclear reactor go up yet again* [Online]. nuclear-news. Available: https://nuclear-news.net/2012/12/14/costs-of-finlands-olkiluoto-nuclear-reactor-go-up-yet-again/ [Accessed 15 October 2018].
LAWRENCE LIVERMORE NATIONAL LABORATORY. 2019. *Energy Flow Charts* [Online]. Available: https://flowcharts.llnl.gov/ [Accessed 16 August 2019].
LAZARD 2015. Lazard's Levelized Cost of Storage Analysis - Version 1.0. Lazard.
LEE, D.-H. 2012. Toward the clean production of hydrogen: Competition among renewable energy sources and nuclear power. *International Journal of Hydrogen Energy,* 37**,** 15726-15735.
LEMMON, E. W., JACOBSEN, R. T., PENONCELLO, S. G. & FRIEND, D. G. 2000. Thermodynamic properties of air and mixtures of nitrogen, argon, and oxygen from 60 to 2000 K at pressures to 2000 MPa. *Journal of physical and chemical reference data,* 29**,** 331-385.
LÉVÊQUE, F. 2015. *The Economics and Uncertainties of Nuclear Power,* Cambridge, Cambridge University Press.
LI, Y. 2011. *Cryogen based energy storage: process modelling and optimisation.* The University of Leeds.
LI, Y., CAO, H., WANG, S., JIN, Y., LI, D., WANG, X. & DING, Y. 2014. Load shifting of nuclear power plants using cryogenic energy storage technology. *Applied Energy,* 113**,** 1710-1716.
LIN, B., WU, W., BAI, M., XIE, C. & RADCLIFFE, J. 2019. Liquid air energy storage: Price arbitrage operations and sizing optimization in the GB real-time electricity market. *Energy Economics,* 78**,** 647-655.
LOISEL, R., ALEXEEVA, V., ZUCKER, A. & SHROPSHIRE, D. 2018. Load-following with nuclear power: Market effects and welfare implications. *Progress in Nuclear Energy,* 109**,** 280-292.
LOKHOV, A. 2011a. Load-following with nuclear power plants. *NEA News,* 29**,** 18.
LOKHOV, A. 2011b. Technical and economic aspects of load following with nuclear power plants. *NEA, OECD, Paris, France,* 2.
LUO, X. & WANG, J. 2013. Overview of current development on compressed air energy storage. *School of Engineering, University of Warwick,, Coventry, UK*.
MACLEOD, F. 2014. *See The Most Over Budget Projects of All Time Ranked in this Infographic* [Online]. archdaily. Available: https://www.archdaily.com/555907/see-the-most-over-budget-projects-of-all-time-ranked-in-this-infographic [Accessed 15 October 2018].
MATHWORKS. *MATLAB* [Online]. Available: https://uk.mathworks.com/products/matlab.html [Accessed].
MATHWORKS. *Simulink* [Online]. Available: https://uk.mathworks.com/products/simulink.html [Accessed].
MATSUMURA, Y. & NAKAMORI, T. 2004. Steam reforming of methane over nickel catalysts at low reaction temperature. *Applied Catalysis A: General,* 258**,** 107-114.
MATTSSON, S. E. & ELMQVIST, H. Modelica–An international effort to design the next generation modeling language. 7th IFAC Symposium on Computer Aided Control Systems Design, Gent, Belgium, 1997. 1-5.
MAURICIO, B. C. S., JUNLING, H., MICHAEL, J. A. & WILLIAM, W. H. 2017. Potential Arbitrage Revenue of Energy Storage Systems in PJM. *Energies,* 10**,** 1100.
MCCOMBIE, C. & JEFFERSON, M. 2016. Renewable and nuclear electricity: Comparison of environmental impacts. *Energy Policy,* 96**,** 758-769.
MICROSOFT. *Excel* [Online]. Available: https://products.office.com/en-us/excel [Accessed].
MIZIA, R. E. 2008. Next Generation Nuclear Plant Reactor Pressure Vessel Acquisition Strategy. Idaho.

MORGAN, R., NELMES, S., GIBSON, E. & BRETT, G. 2015a. An analysis of a large-scale liquid air energy storage system. *Proceedings of the Institution of Civil Engineers - Energy,* 168**,** 135-144.
MORGAN, R., NELMES, S., GIBSON, E. & BRETT, G. 2015b. Liquid air energy storage – Analysis and first results from a pilot scale demonstration plant. *Applied Energy,* 137**,** 845-853.
MORGAN, R. E. 2016. Liquid air energy storage – from theory to demonstration. *International Journal of Environmental Studies,* 73**,** 469-480.
NAKHAMKIN, M., CHIRUVOLU, M. & DANIEL, C. 2010. Available compressed air energy storage (CAES) plant concepts. *Energy,* 4100**,** 0.81.
NATERER, G., SUPPIAH, S., LEWIS, M., GABRIEL, K., DINCER, I., ROSEN, M. A., FOWLER, M., RIZVI, G., EASTON, E. B., IKEDA, B. M., KAYE, M. H., LU, L., PIORO, I., SPEKKENS, P., TREMAINE, P., MOSTAGHIMI, J., AVSEC, J. & JIANG, J. 2009. Recent Canadian advances in nuclear-based hydrogen production and the thermochemical Cu–Cl cycle. *International Journal of Hydrogen Energy,* 34**,** 2901-2917.
NATERER, G. F., SUPPIAH, S., STOLBERG, L., LEWIS, M., WANG, Z., DAGGUPATI, V., GABRIEL, K., DINCER, I., ROSEN, M. A., SPEKKENS, P., LVOV, S. N., FOWLER, M., TREMAINE, P., MOSTAGHIMI, J., EASTON, E. B., TREVANI, L., RIZVI, G., IKEDA, B. M., KAYE, M. H., LU, L., PIORO, I., SMITH, W. R., SECNIK, E., JIANG, J. & AVSEC, J. 2010. Canada's program on nuclear hydrogen production and the thermochemical Cu–Cl cycle. *International Journal of Hydrogen Energy,* 35**,** 10905-10926.
NATERER, G. F., SUPPIAH, S., STOLBERG, L., LEWIS, M., WANG, Z., DINCER, I., ROSEN, M. A., GABRIEL, K., SECNIK, E., EASTON, E. B., PIORO, I., LVOV, S., JIANG, J., MOSTAGHIMI, J., IKEDA, B. M., RIZVI, G., LU, L., ODUKOYA, A., SPEKKENS, P., FOWLER, M. & AVSEC, J. 2013. Progress of international hydrogen production network for the thermochemical Cu–Cl cycle. *International Journal of Hydrogen Energy,* 38**,** 740-759.
NATIONAL GRID 2019a. Fast Reserve Market Information Delivery from February 2020. Warwick: National Grid,.
NATIONAL GRID 2019b. TR39 Results Appendix.
NATIONAL GRID. 2020a. *Fast reserve* [Online]. Available: https://www.nationalgrideso.com/balancing-services/reserve-services/fast-reserve?overview [Accessed 14 January 2020].
NATIONAL GRID. 2020b. *Short-term operating reserve* [Online]. Available: https://www.nationalgrideso.com/industry-information/balancing-services/reserve-services/short-term-operating-reserve-stor?overview [Accessed 14 January 2020].
NEWBERY, D. M. 2016. Towards a green energy economy? The EU Energy Union's transition to a low-carbon zero subsidy electricity system – Lessons from the UK's Electricity Market Reform. *Applied Energy,* 179**,** 1321-1330.
NIEVA, M. A., VILLAVERDE, M. M., MONZÓN, A., GARETTO, T. F. & MARCHI, A. J. 2014. Steam-methane reforming at low temperature on nickel-based catalysts. *Chemical Engineering Journal,* 235**,** 158-166.
NORMAN, J. H., BESENBRUCH, G. E., BROWN, L. C., O'KEEFE, D. R. & ALLEN, C. L. 1982. Thermochemical water-splitting cycle, bench-scale investigations, and process engineering. Final report, February 1977-December 31, 1981. *Other Information: Portions of this document are illegible in microfiche products.*
NUSCALE. *A cost competitive nuclear option for multiple applications* [Online]. Available: https://www.nuscalepower.com/benefits/cost-competitive [Accessed 6 July 2018].
NUSCALE POWER LLC 2018a. Chapter Five: Reactor Coolant System and Connecting Systems. *NuScale Standard Plant Design Certification Application.*
NUSCALE POWER LLC 2018b. Chapter Ten: Steam and Power Conversion System. *NuScale Standard Plant Design Certification Application.*
O'BRIEN, P. T. & PYE, J. Exergetic analysis of a steam-flashing thermal storage system. Proceedings of Solar2010, 48th AuSES conference. Canberra, Australia, 2010. Citeseer.
OPEN SOURCE MODELICA CONSORTIUM. *OpenModelica* [Online]. Available: https://www.openmodelica.org/ [Accessed].

ORHAN, M. F., DINCER, I., ROSEN, M. A. & KANOGLU, M. 2012. Integrated hydrogen production options based on renewable and nuclear energy sources. *Renewable and Sustainable Energy Reviews,* 16**,** 6059-6082.
OSAKA GAS. 2017. *Project to construct one of the world's largest LNG storage tank* [Online]. Available: https://www.osakagas.co.jp/en/company/enterprise_future/article2/ [Accessed 16th October 2018].
PALISADE. *@RISK* [Online]. Available: https://www.palisade.com/risk/ [Accessed].
PAVLOV, G. K. & OLESEN, B. W. 2012. Thermal energy storage—A review of concepts and systems for heating and cooling applications in buildings: Part 1—Seasonal storage in the ground. *HVAC&R Research,* 18**,** 515-538.
PENG, X., SHE, X., CONG, L., ZHANG, T., LI, C., LI, Y., WANG, L., TONG, L. & DING, Y. 2018. Thermodynamic study on the effect of cold and heat recovery on performance of liquid air energy storage. *Applied Energy,* 221**,** 86-99.
PENG, X., SHE, X., LI, C., LUO, Y., ZHANG, T., LI, Y. & DING, Y. 2019. Liquid air energy storage flexibly coupled with LNG regasification for improving air liquefaction. *Applied Energy,* 250**,** 1190-1201.
PERRIER, Q. 2018. The second French nuclear bet. *Energy Economics,* 74**,** 858-877.
PETERS, M. S., TIMMERHAUS, K. D., WEST, R. E., TIMMERHAUS, K. & WEST, R. 1968. *Plant design and economics for chemical engineers*, McGraw-Hill New York.
PONCIROLI, R., WANG, Y., ZHOU, Z., BOTTERUD, A., JENKINS, J., VILIM, R. B. & GANDA, F. 2017. Profitability Evaluation of Load-Following Nuclear Units with Physics-Induced Operational Constraints. *Nuclear Technology,* 200**,** 189-207.
POWER TECHNOLOGY. 2013. Pocket rocket - a new generation of small modular reactors. *Progressive Digital Media Oil & Gas, Mining, Power, CleanTech and Renewable Energy News*, 08/14/2013.
RAMACHANDRAN, R. & MENON, R. K. 1998. An overview of industrial uses of hydrogen. *International Journal of Hydrogen Energy,* 23**,** 593-598.
RANGEL, L. & LÉVÊQUE, F. 2015. Revisiting the Cost Escalation Curse of Nuclear Power: New Lessons from the French Experience. *Economics of Energy & Environmental Policy,* 4.
RICHARDSON, D. B. 2013. Encouraging vehicle-to-grid (V2G) participation through premium tariff rates. *Journal of Power Sources,* 243**,** 219.
ROQUES, F., NEWBERY, D. M. & NUTTALL, W. J. 2008. Fuel mix diversification incentives in liberalized electricity markets: a Mean–Variance Portfolio theory approach.
ROSENDAHL, J. & FORSELL, T. 2017. *Areva's Finland reactor to start in 2019 after another delay* [Online]. Reuters. Available: https://www.reuters.com/article/us-finland-nuclear-olkiluoto/arevas-finland-reactor-to-start-in-2019-after-another-delay-idUSKBN1CE1ND [Accessed 15 October 2018].
ROUINDEJ, K., SAMADANI, E. & FRASER, R. A. 2020. A comprehensive data-driven study of electrical power grid and its implications for the design, performance, and operational requirements of adiabatic compressed air energy storage systems. *Applied Energy,* 257.
ROULSTONE, T. 2015. Economies of scale vs. economies of volume: Tony Roulstone looks at the economics of small modular reactors and the conditions needed for them to become competitive with today's larger reactor designs. *Nuclear Engineering International.*
RUSH, H. J., MACKERRON, G. & SURREY, J. 1977. The advanced gas-cooled reactor: A case study in reactor choice. *Energy Policy,* 5**,** 95-105.
RWE POWER 2010. ADELE - Adiabatic Compressed Air Energy Storage for Electricity Supply. Köln.
RYU, K. H., KIMA, B. D., KIMA, J. H., SOHN, S. H., KO, J. W. & CHO, J. H. Simulation of a Steam Accumulator for the Development of Nuclear Equipment Performance Evaluation System. Korean Nuclear Society Spring Meeting, 2012 Jeju.
SANNER, B., KARYTSAS, C., MENDRINOS, D. & RYBACH, L. 2003. Current status of ground source heat pumps and underground thermal energy storage in Europe. *Geothermics,* 32**,** 579-588.
SCIACOVELLI, A., SMITH, D., NAVARRO, M. E., VECCHI, A., PENG, X., LI, Y., RADCLIFFE, J. & DING, Y. 2017a. Performance Analysis and Detailed Experimental Results of the First Liquid Air Energy Storage Plant in the World. *Journal of Energy Resources Technology,* 140.

SCIACOVELLI, A., VECCHI, A. & DING, Y. 2017b. Liquid air energy storage (LAES) with packed bed cold thermal storage – From component to system level performance through dynamic modelling. *Applied Energy,* 190**,** 84-98.
SHARMA, S. & GHOSHAL, S. K. 2015. Hydrogen the future transportation fuel: From production to applications. *Renewable and Sustainable Energy Reviews,* 43**,** 1151-1158.
SHE, X., PENG, X., NIE, B., LENG, G., ZHANG, X., WENG, L., TONG, L., ZHENG, L., WANG, L. & DING, Y. 2017. Enhancement of round trip efficiency of liquid air energy storage through effective utilization of heat of compression. *Applied Energy,* 206**,** 1632-1642.
SHI, G. 2012. Cost Optimal Selection of Storage Tanks in LPG Vaporization Station. *Natural Resources,* 03**,** 164-169.
SLOCUM, A. H., CODD, D. S., BUONGIORNO, J., FORSBERG, C., MCKRELL, T., NAVE, J.-C., PAPANICOLAS, C. N., GHOBEITY, A., NOONE, C. J., PASSERINI, S., ROJAS, F. & MITSOS, A. 2011. Concentrated solar power on demand. *Solar Energy,* 85**,** 1519-1529.
SMITH, A. Z. P. & HALLIDAY, J. A. 2016. The P114 data set: disaggregate half-hourly demand and supply data on the GB electricity grid. *In:* UK ENERGY RESEARCH CENTRE (ed.).
SMITH, E. 1977. Storage of electrical energy using supercritical liquid air. *Proceedings of the Institution of Mechanical Engineers,* 191**,** 289-298.
SMITH, R. 2005. *Chemical Process Design and Integration,* Chichester, John Wiley & Sons Ltd,.
SPATH, P. & MANN, M. 2001. Life Cycle Assessment of Hydrogen Production via Natural Gas Steam Reforming. National Renewable Energy Laboratory.
STACK, D. & FORSBERG, C. Improving Nuclear System Economics using Firebrick Resistance-Heated Energy Storage (FIRES). American Nuclear Society Annual Meeting, 2015 San Antonio, TX.
STACK, D. C., CURTIS, D., IBEKWE, R. & FORSBERG, C. 2016. Conceptual Design and Market Assessment of Firebrick Resistance Heated Energy Storage (FIRES) – Avoiding Wind and Solar Electricity Price Collapse to Improve Nuclear, Wind, and Solar Economics. *International Congress on Advanced Nuclear Power Plants.* San Francisco, California.
STAFF WRITER. 2014. *Major construction projects that went billions over budget* [Online]. Construction Global. Available: https://www.constructionglobal.com/major-projects/infographic-major-construction-projects-went-billions-over-budget [Accessed 15 October 2018].
STRBAC, G., AUNEDI, M., PUDJIANTO, D., DJAPIC, P., TENG, F., STURT, A., JACKRAVUT, D., SANSOM, R., YUFIT, V. & BRANDON, N. 2012. Strategic assessment of the role and value of energy storage systems in the UK low carbon energy future. Carbon Trust.
TAFONE, A., BORRI, E., COMODI, G., VAN DEN BROEK, M. & ROMAGNOLI, A. 2018. Liquid Air Energy Storage performance enhancement by means of Organic Rankine Cycle and Absorption Chiller. *Applied Energy,* 228**,** 1810-1821.
TAFONE, A., DING, Y., LI, Y., XIE, C. & ROMAGNOLI, A. 2020. Levelised Cost of Storage (LCOS) analysis of liquid air energy storage system integrated with Organic Rankine Cycle. *Energy,* 198.
TAFONE, A., ROMAGNOLI, A., BORRI, E. & COMODI, G. 2019. New parametric performance maps for a novel sizing and selection methodology of a Liquid Air Energy Storage system. *Applied Energy,* 250**,** 1641-1656.
TAKESHITA, T. & YAMAJI, K. 2008. Important roles of Fischer–Tropsch synfuels in the global energy future. *Energy Policy,* 36**,** 2773-2784.
TENG, R., WEIQING, X., MAOLIN, C., XIAOSHUANG, W. & MINGHAN, L. 2019. Experiments on Air Compression with an Isothermal Piston for Energy Storage. *Energies,* 12**,** 3730.
THE R FOUNDATION. *R* [Online]. Available: https://www.r-project.org/ [Accessed].
THOMAS, R. J., GHOSH, P. & CHOWDHURY, K. 2012. Role of heat exchangers in helium liquefaction cycles: Simulation studies using Collins cycle. *Fusion Engineering and Design,* 87**,** 39-46.
VATAVUK, W. M. Updating the CE plant cost index.
WAGNER, W. & PRUß, A. 2002. The IAPWS Formulation 1995 for the Thermodynamic Properties of Ordinary Water Substance for General and Scientific Use. *Journal of Physical and Chemical Reference Data,* 31**,** 387-535.

WANG, Y., ZHOU, Z., BOTTERUD, A., ZHANG, K. & DING, Q. 2016. Stochastic coordinated operation of wind and battery energy storage system considering battery degradation. *Journal of Modern Power Systems and Clean Energy,* 4**,** 581-592.
WANG, Z. L., NATERER, G. F., GABRIEL, K. S., GRAVELSINS, R. & DAGGUPATI, V. N. 2009. Comparison of different copper–chlorine thermochemical cycles for hydrogen production. *International Journal of Hydrogen Energy,* 34**,** 3267-3276.
WANG, Z. L., NATERER, G. F., GABRIEL, K. S., GRAVELSINS, R. & DAGGUPATI, V. N. 2010. Comparison of sulfur–iodine and copper–chlorine thermochemical hydrogen production cycles. *International Journal of Hydrogen Energy,* 35**,** 4820-4830.
WARREN, P. 2014. A review of demand-side management policy in the UK. *Renewable and Sustainable Energy Reviews,* 29**,** 941.
WATERS, L. 2019. Energy Consumption in the UK (ECUK) 1970 to 2018. Department for Business, Energy & Industrial Strategy;.
WEARING, L. 2017. SMRs--a plausible reality for the UK: Lisa Wearing gives an update on the opportunities for small modular reactors (SMRs) in the UK.(SMRs: Power market developments)(Small modular nuclear reactors). *Nuclear Engineering International,* 62**,** 20.
WERON, R. 2014. Electricity price forecasting: A review of the state-of-the-art with a look into the future. *International Journal of Forecasting,* 30**,** 1030-1081.
WESTINGHOUSE ELECTRIC COMPANY 2011. Bellefonte Nuclear Plant, Units 3 & 4
WHITE, C. D. & ZHANG, K. M. 2011. Using vehicle-to-grid technology for frequency regulation and peak-load reduction. *Journal of Power Sources,* 196**,** 3972-3980.
WILSON, A. 2015. *Advanced Gas-cooled Reactors as Precursors to the Very High Temperature Reactor (MSc Thesis).* MSc Nuclear Engineering, Imperial College London.
WILSON, A. 2020a. *Energy Storage System @RISK financial model* [Online]. Available: https://ordo.open.ac.uk/articles/software/Energy_Storage_System_RISK_financial_model/13110011 [Accessed].
WILSON, A. 2020b. *Liquid air energy storage system Modelica components* [Online]. Available: https://figshare.com/s/bb31ed1855362199ebba [Accessed].
WILSON, A., NUTTALL, W. J. & GLOWACKI, B. A. 2020. Techno-economic study of output-flexible light water nuclear reactor systems with cryogenic energy storage. *EPRG Working Papers,* 2020.
WOLF, T. E. 2015. An update on lang factors. *Hydrocarbon Processing,* 2015-.
WORLD NUCLEAR NEWS. 2018. *EDF revises schedule, costs of Flamanville EPR* [Online]. World Nuclear News. Available: http://world-nuclear-news.org/Articles/EDF-revises-schedule,-costs-of-Flamanville-EPR [Accessed].
WU, S., ZHOU, C., DOROODCHI, E. & MOGHTADERI, B. 2020. Techno-economic analysis of an integrated liquid air and thermochemical energy storage system. *Energy Conversion and Management,* 205.
XIE, C., HONG, Y., DING, Y., LI, Y. & RADCLIFFE, J. 2018. An economic feasibility assessment of decoupled energy storage in the UK: With liquid air energy storage as a case study. *Applied Energy,* 225**,** 244-257.
ZEPPIERI, M., VILLA, P. L., VERDONE, N., SCARSELLA, M. & DE FILIPPIS, P. 2010. Kinetic of methane steam reforming reaction over nickel- and rhodium-based catalysts. *Applied Catalysis A: General,* 387**,** 147-154.
ZHANG, P., CHEN, S. Z., WANG, L. J. & XU, J. M. 2010. Overview of nuclear hydrogen production research through iodine sulfur process at INET. *International Journal of Hydrogen Energy,* 35**,** 2883-2887.
ZHU, Q., ZHANG, Y., ZHOU, C., WANG, Z., ZHOU, J. & CEN, K. 2012. Optimization of liquid–liquid phase separation characteristics in the Bunsen section of the sulfur–iodine hydrogen production process. *International Journal of Hydrogen Energy,* 37**,** 6407-6414.